Diss. ETH No. 29581

ENTROPY AND PARTICLE TRANSPORT IN QUANTUM GASES MANIPULATED WITH NEAR-RESONANT LIGHT

A thesis submitted to attain the degree of

DOCTOR OF SCIENCES of ETH ZURICH

(Dr. sc. ETH Zürich)

presented by

PHILIPP FABRITIUS

M.Sc., Ruprecht Karl University of Heidelberg

born on 25.01.1993
citizen of Germany

accepted on the recommendation of

Prof. Dr. Tilman Esslinger, examiner
Prof. Dr. Selim Jochim, co-examiner

2023

PHILIPP FABRITIUS
Entropy and Particle Transport in Quantum Gases Manipulated with Near-Resonant Light,
Diss. ETH No. 29581 © TM 2023

ABSTRACT

Entropy transport and particle transport and their interplay give insight into the transport processes in a complex systems, often intractable with a microscopic simulation. In this thesis, we study a quantum gas of ultracold fermionic ^{6}Li flowing through a mesoscopic junction. The atomic nature of the quantum gas enables us to shape a two-terminal transport geometry with light. The tunability of interactions between atoms allows exploration of the weakly-interacting Fermi gas and the strongly interacting, unitary Fermi gas.

The *first part* of the thesis details the technical upgrades to the apparatus. Degradation of laser powers led us to replace the laser system used for laser cooling, by a more powerful and stable system based on a fiber amplifier and frequency doubling. In addition, the unstable lock of the resonator trap was replaced and a spin-resolved imaging system implemented. These upgrades led to a continuous operability of the experiment, greatly simplifying measurements.

In the *second part* we measure how the quantum nature of transport, characterized by the quantization of conductance, competes with particle losses imposed by near-resonant light. This dissipation mechanism is locally controlled inside the quantum point contact (QPC), under which the conductance plateaus are robust. Additionally, we show that our observations can be described with an extended Landauer-Büttiker model. In a second application of near-resonant light we detune the laser frequency to obtain a spin-dependent optical potential. This effective Zeeman shift in the QPK fully spin-polarizes the currents flowing through it, while marginally reducing the atom-number. Exploring weak interactions we observe that attractive (repulsive) interactions reduce (increase) the effective Zeeman shift visibly. In a third application we use the three-level atom light interaction in the strongly interacting regime to at first dissipatively suppress the fast transport and then restore it via electromagnetically induced transparency.

In the *third part* entropy transport between unitary Fermi gases, superfluid in equilibrium, is studied for varying transport geometries from quasi one-dimensional (1D) to quasi two-dimensional (2D). We find that both entropy and particle currents respond non-linearly to a temperature or chemical potential bias. The transported entropy per particle is much larger than the superfluid entropy per particle in the equilibrium junction. This and the concurrently produced total entropy imply that the current is not a pure supercurrent and that the transport process is irreversible. Varying the geometry changes the timescales of advective and diffusive transport modes while the transported entropy per particle remains constant, independent of geometry. We derive a phenomenological model based on the irreversible, non-linear transport processes fitting the observations. In an equivalent, second experiment we impose dissipation in the junction. We find that dissipation enhances the advective response by counterintuitively reducing the transported entropy per particle. We employ the phenomenological model to demonstrate that dissipation strongly increases the thermal conductance while reducing the excess current in the quasi-1D junction. The extraced Seebeck coefficient reduces with dissipation, confirming our observations.

ZUSAMMENFASSUNG

Entropietransport und Teilchentransport und ihr Zusammenspiel geben Einblick in die Transportprozesse in komplexen Systemen, die mit einer mikroskopischen Simulation oft nicht nachvollziehbar sind. In dieser Arbeit untersuchen wir ein Quantengas aus ultrakaltem fermionischem ^{6}Li, das durch einen mesoskopischen Kontakt fließt. Die atomare Natur des Quantengases ermöglicht es uns, eine zweipolige Transportgeometrie mit Licht zu gestalten. Die Einstellbarkeit der Wechselwirkungen zwischen den Atomen ermöglicht die Erforschung des schwach wechselwirkenden Fermi-Gases und des stark wechselwirkenden, unitären Fermi-Gases.

Der erste Teil der Arbeit beschreibt die technischen Verbesserungen, die wir vorgenommen haben. Nachlassende Laserleistungen veranlasste uns, das zur Laserkühlung verwendete Lasersystem zu ersetzen, durch ein leistungsstärkeres und stabileres System, basierend auf einem Faserverstärker und einer Frequenzverdopplung. Außerdem wurde die instabile Stabilisierung der Resonator-Dipol-Falle ersetzt und ein neues Spin-aufgelöstes Absorptionsabbildungssystem implementiert. Diese Verbesserungen führten zu einer kontinuierlichen Betriebsfähigkeit des Experiments, was unsere Messungen drastisch vereinfachte.

Im zweiten Teil messen wir, wie die kohärente Quantennatur des Transports, charakterisiert durch die Quantisierung des Leitwerts, mit Teilchenverlusten konkurriert, die durch nahezu resonantes Licht verursacht werden. Dieser Dissipationsmechanismus wird lokal innerhalb des Quantenpunktkontakts (QPK) kontrolliert, und wir beobachten, dass die Leitwertplateaus gegenüber diesem Mechanismus robust sind. Außerdem zeigen wir, dass unsere Beobachtungen mit einem erweiterten Landauer-Büttiker-Modell beschrieben werden können. In einer zweiten Anwendung von nahezu resonantem Licht verstimmen wir die Frequenz des Lichtes, um ein spin-abhängiges optisches Potenzial zu erhalten. Dieser effektive Zeeman-Effekt im QPC spin-polarisiert die durch ihn fließenden Ströme vollständig, während er nur geringe Auswirkungen auf die Reservoire hat. Bei der Untersuchung schwacher Wechselwirkungen stellen wir fest, dass anziehende (abstoßende) Wechselwirkungen den effektiven Zeeman-Effekt sichtbar verringern (erhöhen). In einer dritten Anwendung verwenden wir die Drei-Niveau Atom-Licht Wechselwirkung im stark wechselwirkenden Regime, um den schnellen Transport zunächst dissipativ zu unterdrücken und ihn dann durch elektromagnetisch induzierte Transparenz wiederherzustellen.

Im dritten Teil wird der Entropietransport zwischen zwei unitären Fermi-Gasen, superfluid im Gleichgewicht, für verschiedene Transportgeometrien von quasi eindimensional (1D) bis quasi zweidimensional (2D) untersucht. Wir stellen fest, dass sowohl die Entropie, als auch die Teilchenströme nichtlinear auf eine Temperatur- oder chemische Potenzial Differenz reagieren. Die transportierte Entropie pro Teilchen ist viel größer als die superfluide Entropie pro Teilchen im Gleichgewicht. Dies und die gleichzeitig erzeugte Gesamtentropie bedeuten, dass der Strom kein reiner Superstrom ist und, dass der Transportprozess irreversibel ist. Durch die Variation der Geometrie ändern sich die Zeitskalen der advektiven und diffusiven Transportmode während die transportierte Entropie pro Teilchen unabhängig von der Geometrie konstant bleibt. Wir leiten ein phänomenologisches Modell her, das auf irreversiblen, nicht-linearen Transportprozessen basiert und die Beobachtungen beschreibt. In einem zweiten Experiment, das ansonsten gleichwertig ist, führen wir Dissipation in der Kontakt ein. Wir stellen fest, dass die Dissipation die advektive Reaktion verstärkt, indem sie kontraintuitiv die transportierte Entropie pro Teilchen reduziert. Wir verwenden das phänomenologische Modell, um die Transportkoeffizienten zu extrahieren. Daraus ergibt sich, dass die Dissipation die thermische Leitfähigkeit stark erhöht, während sie den Überschussstrom im Quasi-1D-Kontakt reduziert. Der extrahierte Seebeck-Koeffizient nimmt mit der Dissipation ab, was unsere Beobachtungen bestätigt.

CONTENTS

Detailed tables of contents can be found at the beginning of each chapter.

1

INTRODUCTION

Transport is one of the ubiquitous processes in nature with numerous interesting and broadly studied examples. One characteristic example the movement of warm water as a current in the Atlantic Ocean via the Atlantic meridional overturning circulation [1] (AMOC), transporting heat from the southern to the northern Atlantic. The driving force of this current are density gradients. This transport process is happening on an immense scale ranging over thousands of kilometers, transporting millions of liters of water and on a smaller length scale the flow is complicated, only tractable with large climate models [2]. Importantly, the AMOC fundamentally still follows the laws of irreversible thermodynamics in that an intensive, generalized force which is the density gradient drives an extensive flux which is the water current. In this context the entropy of the system is another central quantity, since it gives insight into the status of the system and the nature of the transport process. Entropy, defined by the Second Law of Thermodynamics, can only increase in a closed system and will be maximized in equilibrium. In a transport process between two systems, it is thus possible to define a class of irreversible processes, governed by an increase of entropy. Irreversible thermodynamics is the basis for defining rates or fluxes of a process and provides the basis for understanding and describing most transport processes in nature.

The relation between the thermodynamic forces and fluxes are typically linear such that the proportionality constant, often called the conductance or resistance, characterizes the transport process. For transport processes happening at a macroscopic scale, the underlying system sizes often have a simple influence on the overall transport process [3, 4]. For example in an electronic conductor, where the change of the systems cross-sectional area varies its conductance proportionally. Though the situation drastically changes whenever the width reaches a characteristic quantum length scale like the de Broglie wavelength of the particles. The system is then no longer considered macroscopic but mesoscopic which is an intermediate length scale on which the quantum mechanics of the system matters, but the length scales are still larger than the microscopic size of particles. The paradigmatic effect in mesoscopic transport is the quantized conductance [5, 6]. Whereas in a macroscopic junction the conductance increases linearly with its width, the mesoscopic junction displays quantized steps of conductance when varied in width. It is thus not only pertinent to understand the thermodynamics of the transport system but also to include quantum physics in the description of transport processes.

In this sense transport is not only an observable phenomenon, but also a probe of the properties of the underlying system. One characteristic example of transport as a probe is the drop of resistance [7] in a superconductor or the Josephson effect occurring when connecting two superconductors with a weak link [8]. The study of transport processes become particularly interesting, when the excitations and fluctuations of the system are relevant. One way to achieve this, is to change the dimensionality of the system in order to enhance fluctuations and the effect of excitations. For example in two-dimensional (2D) systems correlated electrons in a magnetic field experience the fractional quantum Hall effect [9], while in one-dimension (1D) electrons can only be excited collectively [10] and in the superconducting quantum wire the Majorana fermions are predicted to be found [11]. Thus, not only is transport a useful probe to detect these effects but reducing the dimensionality of the transport geometry enriches its physics. Naturally, studying transport processes has not only become a major tool of condensed matter physics, but also other fields of physics [12–14].

Quantum gases made of ultracold atoms are an ideal platform to study transport due to their well-controlled interactions, adaptable geometries and enhanced length and reduced time scales compared to electron systems. Naturally quantum gases have limitations for studying transport, for example the smooth optical potentials complicate exploration of friction and the lack of charge requires the engineering of artificial magnetic fields. Depending on the atomic species in use, an atomic cloud can be cooled to reach a degenerate quantum gas following Bose [15] or Fermi [16] statistics. Changing the interactions can then lead to a superfluid state which has been extensively studied emerging both from the Bose-Einstein condensate [17, 18] and the attractive Fermi gas [19–21]. These studies were followed by numerous transport experiments in the superfluid regime, such as the measurement of the propagation of collective excitations [22–24], persistent currents in a ring [25, 26] and diffusion of spins and sound in strongly interacting Fermi gases [27, 28]. The advent of quantum gas microscopy led to studies of microscopic transport processes in optical lattices [29–32] with fermions and bosons. Moreover, mesoscopic transport between two terminals has been studied in the context of Josephson oscillations [33, 34], microscopically patterned junctions [35, 36], the quantum point contact [6] (QPC) and transport between superfluids [37, 38].

Quantum-gas experiments are uniquely suited for experiments requiring isolated conditions such as the controlled study of open systems [39] and irreversible processes [3]. The increase of entropy in an irreversible process in a quantum gas can be directly obtained from the equation of state of the system [40] and the near-closed nature entails that processes which could obscure such measurements, are minimized. The direct measurement of entropy itself is a feature which allows direct comparison to fundamental theories such as the entropy-free flow of superfluids [41]. The transport of entropy between superfluids or superconductors out of equilibrium is a long-standing research topic [42–45] and has both fundamental [46] and technological implications mainly in the context of energy harvesting [47–49]. Traditional condensed-matter experiments do not have direct access to the entropy [50–52] and thus cannot yet fully explore entropy transport.

The interaction between atoms and light provides a tool to engineer not only an open system via dissipation, but also coherently reverse the dissipation [53] and create artificial magnetic fields [54, 55]. Thus providing a well-controlled decoherence or dissipation mechanism enabling the controlled opening of a closed system, competing with the coherent Hamiltonian evolutions of transport. Dissipation is therefore not only destructive to the coherent evolution of a system, but can also lead to new interesting phenomena [56, 57]. Experiments in quantum gases have observed open system effects like the Zeno effect [58, 59] and dissipative crossovers [60].

Here, the fermionic isotope of lithium (^{6}Li) is used to realize a mesoscopic transport geometry with ultracold atoms. Using a combination of patterned light fields and an optical dipole trap we can create a variety of transport junctions ranging from a quasi-1D quantum wire [61] to a quasi-2D [37] weak link. Advances in shaping of light [62] enables us to impose additional, almost arbitrarily shaped light fields in the junction, either to locally manipulate transport [63] or to insert optical lattices [61]. The broad Feshbach resonance [64] of ^{6}Li enables the study of strongly interacting Fermi gases exhibiting the BEC-BCS crossover [65]. Notably, the thermodynamics of the quantum gas at the crossover is well understood and its equation of state has been theoretically calculated and precisely measured [40, 66]. These features have been already used to study the transport of strongly correlated quantum gases [37, 38, 67], the flow of heat and particles in the strongly interacting system [38, 68, 69] as well as the effect of local manipulation of the quantum wire [61, 63].

There has been a tremendous amount of progress in the exploration of transport processes, but many open questions are still remaining. In this thesis we extend these studies on the one hand by measuring entropy transport between two superfluids and, on the other hand, by imposing near-resonant light in the transport junction resulting in atom-light interactions affecting transport dispersively, dissipatively and coherently. The thesis is structured in a way that *Ch. 2 to 4* provide an experimental and theoretical background in order to be able to understand the following three *parts* independently. The content is organized as follows

- *Chapters 2 to 4* present the experiment and give an introduction to the atom-light interaction and superfluid transport concepts later used in the thesis.
  - **Chapter 2** introduces the experimental preparation of the transport system, the thermometry of the quantum gas and the transport measurements in the context of Landauer-Bütikker theory.
  - **Chapter 3** focuses on the atom-light interaction of ^{6}Li at high external magnetic fields and its application in two- and three-level systems.
  - **Chapter 4** offers an overview of superfluid and superconducting transport introducing the concepts in superfluid later used to describe our system.
- The *first part* contains the technical details of this thesis. The experimental apparatus is concisely described, the technical upgrades during this work are presented, and future projects are outlined.
  - **Chapter 5** provides the technical details of the apparatus including the ultra-high vacuum system, the resonator dipole trap and the high-resolution microscope used to project optical potentials. The optical system used to generate the transport geometry is outlined, followed by an introduction to spatial light modulation and a terse overview of the imaging system.
  - **Chapter 6** consists of the technical upgrades of the apparatus. The lasers used to generate the cooling light for the magneto-optical trap were replaced by a new fiber based amplifier in conjunction with a second harmonic generation stage. The resonator dipole trap was upgraded, such that remote operation of the experiment became feasible. Moreover, a new spin-resolved absorption imaging system was introduced. Finally, a new laser setup used to manipulate the atoms with near-resonant light was built also generating light at two frequencies for three-level atom light interactions.

  - **Chapter 7** includes several projects realized during this work which have not yet been implemented in the experiment. This includes a new magnetic field stabilization system, an optical cleaning cavity with high transmission and a low-cost mirror motor system with high accuracy. In addition, long term projects such as a high-precision digital to analog converter system and a fast stereo-camera system providing position feedback via an FPGA are described.

- The *second part* encompasses our measurements of quantized conductance through a weakly interacting QPC competing with near-resonant light. Using an aberration-corrected beam tightly focused into the QPC we study the effect of a local spin filter and local particle dissipation on the conductance quanta $1/h$, the onset of conductance and the effect of weak interactions. Moreover, we show that adding a second beam resonant with the transition from another ground state to the light-matter interaction, we form a three-level system in strongly interacting ^{6}Li to demonstrate electromagnetically induced transparency (EIT) in a mesoscopic transport experiment.
  - **Chapter 8** comprises the results regarding spin-filtering and dissipation in the weakly interacting QPC. We find that the spin filter enables us to create a fully polarized spin current and an effective Zeeman shift larger than the Fermi energy. The weak interactions are shown to have an appreciable effect even though the density in the QPC is low, and the spin filter is highly local. The extended Landauer-Büttiker model is used to model *ab initio* the dissipation using the calibration of the effective Zeeman shift from the spin-filter experiments.
  - **Chapter 9** subsumes our observations when utilizing a three-level system in the superfluid QPC to restore large currents from the dissipative regime using EIT. Moreover, new ideas employing three-level atom-light interactions to study quantum dots and spin-orbit coupling are outlined.

- The *third part* focuses on entropy transport between two superfluids. Preparing the system at low temperatures with biases in temperature and chemical potential we can measure the advectively and diffusively transported entropy. We develop a phenomenological model based on irreversible processes which encompasses the nonlinearity and describes our observations. In a second experiment we impose controlled dissipation and repeat the entropy transport experiments between superfluids.
  - **Chapter 10** consists of the measurements of entropy transport between two superfluids. The geometry of the junction is varied from quasi-1D to quasi-2D and the particle and entropy currents are measured for two different initial conditions. We find that entropy and particle currents respond non-linearly to biases in both temperature and chemical potential. The response is found to be "equal" in that their paths in state-space are equivalent up to differences in the initial state preparation. Extracting the transported entropy per particle, we can conclude, that the current is not a pure supercurrent and that the magnitude of the transported entropy is independent of the geometry. The observations

    are modeled with a phenomenological model describing the nonlinearity and the increase in total entropy typical for irreversible processes. Furthermore, the transport coefficients extracted from a fit, confirm that the transported entropy is independent of geometry, while the current scale and the thermal conductance of the system vary drastically.
  - **Chapter 11** entails the effect of dissipation on the transported entropy per particle. Introducing spin-dependent or spin-independent dissipation locally in the junction with a tightly focused beam, we find that the dissipation leads to an enhanced thermoelectric response and enhanced thermal conductance. The enhanced thermoelectric response is attributed to a decrease of the transported entropy per particle, confirmed by fits with our phenomenological model. The system is again studied for a variety of geometries indicating a consistently reduced entropy transport.

- **Chapter 12** provides a summary of the experiments performed and an overview of possible extensions of the presented work as well as ideas for future experiments.

The work in this thesis has been carried out together with Dominik Husmann, Martin Lebrat, Laura Corman, Samuel Häusler, Jeffrey Mohan, Mohsen Talebi, Meng-Zi Huang, Simon Wili and Prof. Tilman Esslinger.

2

PREPARATION AND MEASUREMENT OF TRANSPORT IN A QUANTUM GAS EXPERIMENT

CHAPTER CONTENTS

In this chapter a concise summary of the experimental sequence, the thermometry and the transport measurements as a basis for the experiments presented later is given. Technical details of the apparatus can be found in Part I. The transport theory and the thermometry has been already described in great detail in the PhD theses of S. Krinner [70] and S. Häusler [71].

2.1 EXPERIMENTAL SEQUENCE OF A TWO-TERMINAL TRANSPORT EXPERIMENT

The discussion of the experimental sequence is divided up into three different parts. Firstly, the cooling sequence from the atomic oven temperature $\sim 450\,^{\circ}\mathrm{C}$ to a degenerate Fermi gas $T/T_F \sim 0.2$ is described in Sec. 2.1.1. Secondly, in Sec. 2.1.2 the optical potentials defining the transport geometry and their alignment are discussed. Thirdly, the measurement, i.e. the absorption imaging, is described in Sec. 2.1.3.

2.1.1 Laser- and Evaporative Cooling

Figure 2.1 shows the cooling sequence of the experiment starting from the Zeeman slower and ending with forced evaporation in the glass-cell. The following sections chronologically describe the cooling sequence depicted in Fig. 2.1.

Zeeman Slower

The Zeeman slower operates with σ_+ polarized light red-detuned by $\sim 14.5\Gamma$ from the cooling transition $2^2S_{1/2}, F = 3/2 \rightarrow 2^2P_{3/2}, F = 5/2$ (see Fig. 2.2), thus Doppler cooling the counter-propagating atoms [72]. The magnetic field applied via the Zeeman slower coils decreases with a square-root behavior from 929 G [73] around the Oven chamber towards the MOT chamber where it smoothly connects to the magnetic field of the MOT. This magnetic field profile provides a constant deceleration by keeping the atoms detuned

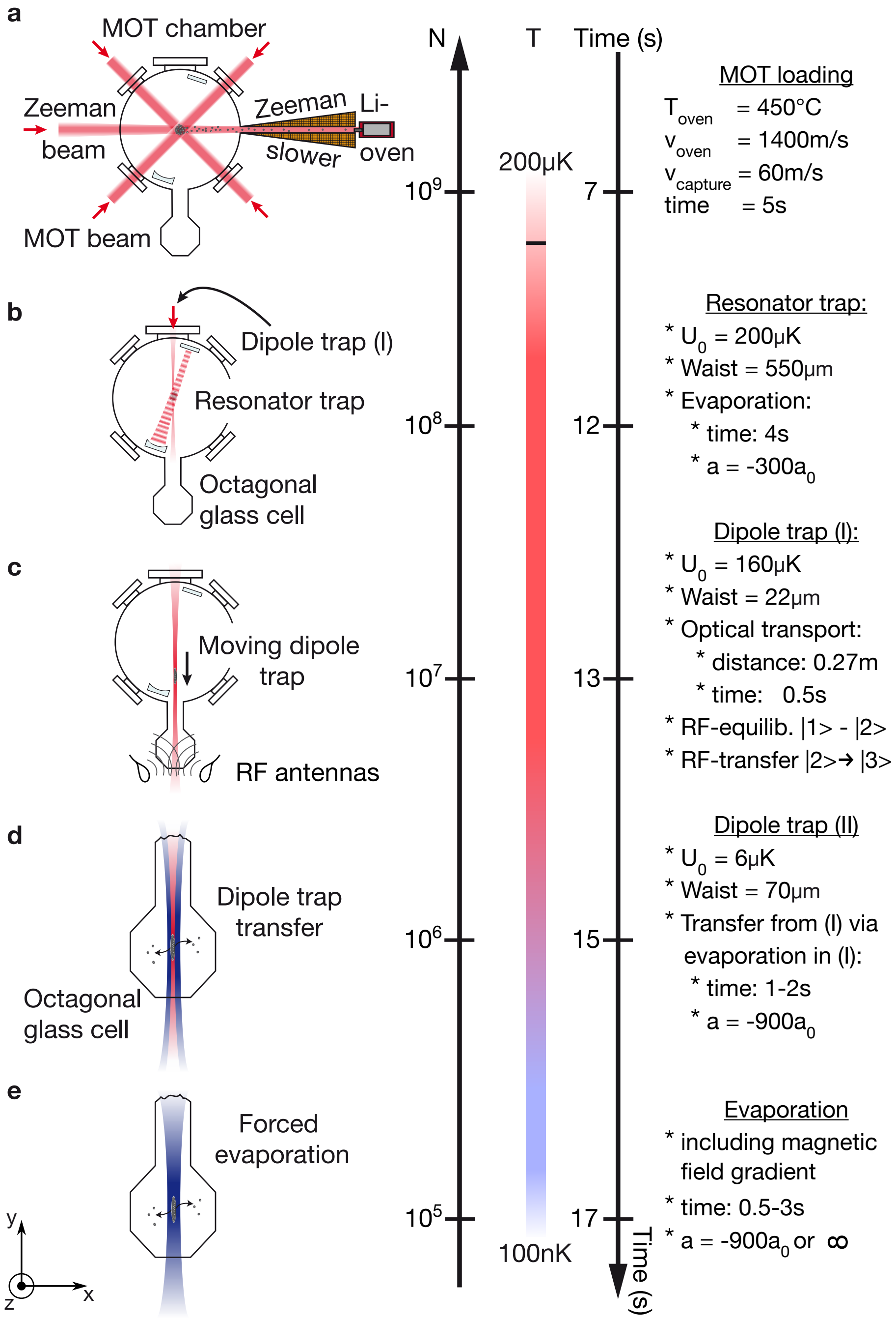

Figure 2.1: Cooling sequence of the Lithium experiment, from atomic oven to ultracold Fermi gas. The cooling sequence starts with the Zeeman slower (a), decelerating the ^{6}Li atoms from the oven in order to be caught by the magneto-optical-trap (MOT). The MOT (b) cools the atomic cloud in order to be loaded into a standing-wave, resonator dipole trap where the first forced optical evaporation takes place. Subsequently, the atoms are transported from the MOT chamber to the glass-cell with the transport dipole trap (c), followed by another evaporation into the final dipole trap (d). The final evaporation – during which the transport geometry is present – is aided by a magnetic gradient and cools the cloud to a degeneracy of $\sim 0.2\,T/T_F$. Adapted from Ref. [70].

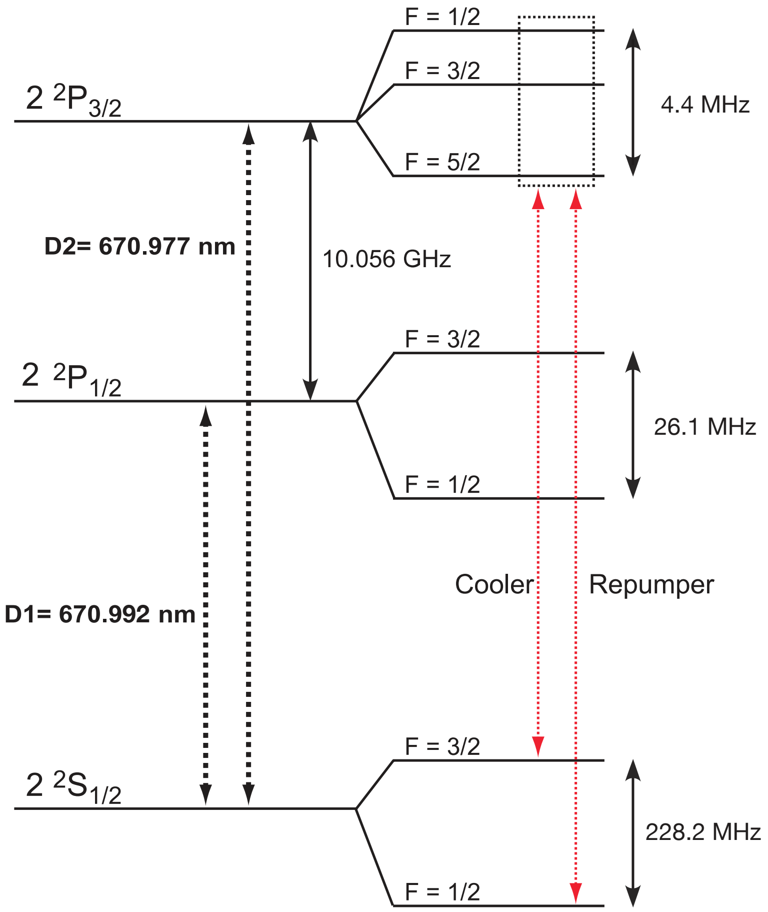

Figure 2.2: Electronic level structure of ^{6}Li. The D1 and D2 transitions of ^{6}Li both have a wavelength of ~ 671 nm and are only split by ~ 10 GHz. The cooler and repumper transition for the magneto-optical-trap (MOT) and the Zeeman slower are using the D2 transition where the excited state hyperfine structure splitting is smaller than the inverse lifetime of the states $\Gamma = 2\pi \cdot 5.8\,\mathrm{MHz}$. In the MOT the cooler and repumper are of equal strength to cool efficiently. Adapted from Ref. [70].

from the laser light via the Zeeman shift. The non-zero field at the Zeeman slower exit lets the atoms propagate towards the MOT at $v_f = 60\,\mathrm{m/s}$. Over the years a visible layer of lithium atoms has been deposited on the entrance viewport of the Zeeman slower which leads to an increased need of laser power. In the current configuration the Zeeman slower is operated at a power of ~ $200mW$ which corresponds to a peak intensity of about $I/I_{\mathrm{sat}} \sim 280$ (assuming 50 % transmission and a minimal beam waist of $w_{\mathrm{min}} = 3\,\mathrm{mm}$ [73]) and a minimal intensity $I/I_{\mathrm{sat}} \sim 25$ (at the maximal waist $w_{\mathrm{max}} = 10\,\mathrm{mm}$ [73]). We find that adding repumper light to the Zeeman slower does not substantially improve the atomic flux, likely due to the substantial power broadening. Depending on the size of the MOT we find that the Zeeman slower pierces a large hole into the atomic cloud, the atomic beam is propagating slightly above the MOT and significantly above the resonator dipole trap position.

Magneto Optical Trap

The magneto optical trap (MOT) is made up of three, retroreflected, red detuned beams each made up of cooler and repumper light. Figure 2.2

shows the electronic structure of ^{6}Li at zero magnetic field, including the cooler and repumper transitions. The cooler light is initially $\sim 6.5\Gamma$ red detuned from the cooling transition $2^2S_{1/2}$, $F = 3/2 \to 2^2P_{3/2}$, $F = 5/2$, while the repumper light is $\sim 6.5\Gamma$ red detuned from the repumping transition $2^2S_{1/2}$, $F = 1/2 \to 2^2P_{3/2}$, $F = 3/2$. The MOT beams diameter is limited by the size of the viewports $2w_0 \sim 38\,\mathrm{mm}$ which leads to an initially large MOT. Nominally, the intensity of the repumper and cooler light are both around $I/I_{sat} \approx 1$ which provides optimal MOT conditions in our experiment. We find that increasing the MOT power to up to $I/I_{sat} \approx 2$ does not substantially improve the final atom number. Figure 2.1 shows the beam configuration with respect to the Zeeman slower. MOT and Zeeman slower are operated for $7 - 10\,\mathrm{s}$ in order to load enough atoms for the experiments. After the MOT loading is finished the MOT is compressed to increase the loading efficiency into the first optical dipole trap. The compression takes place over $\sim 10ms$ during which the MOT field are ramped up and the detuning of cooler and repumper are reduced to $\sim 0.5\Gamma$. The compression leads to a final compressed MOT diameter of $\sim 1\,\mathrm{mm}$ at a temperature of $T_{cMOT} \sim 500\,\mu\mathrm{K}$. The repumper light is used to prepare the atoms in the lowest $F = 1/2$ hyperfine manifold via optical pumping at the end of the compressed MOT. From fluorescence imaging we estimate a final compressed MOT atom number of $N_{cMOT} \sim 2 \times 10^9$ of which only $\sim 0.3\,\%$ get loaded into the following resonator dipole trap.

Resonator Dipole Trap

The standing-wave resonator dipole trap is used to enhance the intensity of the incoming light such that a deep $U_0 \approx 200\,\mu\mathrm{K}$ and large $w_0 \sim 550\,\mu\mathrm{m}$ trap can be formed. Though the height is likely limiting the loading efficiency from the compressed MOT significantly. In longitudinal direction the dipole trap has a lattice structure which limits the loading efficiency, though compensating this lattice [74] did not improve its loading efficiency. The vacuum lifetime in the resonator trap is $\sim 9\,\mathrm{s}$ which is more than enough for optical evaporation. The Feshbach coils in the MOT chamber are used to set the s-wave scattering length to $a_{12} = -300\,a_0$ which allows efficient evaporation. The evaporation is done by reducing the intensity of the resonator laser power over $\sim 3\,\mathrm{s}$ by a factor of ~ 5 which gives a final temperature of $T_{Resonator} \approx 13\,\mu\mathrm{K}$. During evaporation the transport dipole trap is already present which allows efficient loading $\sim 30\,\%$.

Transport Dipole Trap

The transport dipole trap is a strongly focused beam $w_0 = 22\,\mu\mathrm{m}$ which is moved via a lens on a translation stage. The trap depth for transport is $U_0 \approx 160\,\mu\mathrm{K}$ which allows capturing the atoms from the resonator and transporting them within $\sim 0.5\,\mathrm{s}$ over $\sim 27\,\mathrm{cm}$ into the glass-cell. In the transport trap a temperature of $T \approx 22\,\mu\mathrm{K}$ is measured. The atoms are held in the transport dipole trap for the $|1\rangle - |2\rangle$ equilibration and the optional preparation of a spin polarized gas. Subsequently, the atoms are loaded into the final dipole trap, used for the experiments via optical evaporation over $1\,\mathrm{s}$.

Spin Mixture Preparation

In order to prepare well-defined spin-mixtures a magnetic field allowing us to tune the s-wave scattering length, the so-called Feshbach field is switched on. The spin-preparation takes place at a magnetic field of $B_{FB} \sim 375\,\mathrm{G}$.

- **1-2 equilibration.** The $|1\rangle - |2\rangle$ mixture is equilibrated via multiple incomplete Landau-Zener [75, 76] transfers between the two states via an RF transition. The magnetic field is set to $B = 300\,\mathrm{G}$ and the frequency of the RF field is swept back and forth through the avoided crossing of the $|1\rangle - |2\rangle$ transition such that a 50/50 mixture is reached.

- **2-3 transfer.** The $|1\rangle - |3\rangle$ mixture is prepared by an adiabatic transfer of the atoms in state $|2\rangle$ to $|3\rangle$. Here the RF field, coupling $|2\rangle - |3\rangle$, is fixed in frequency while the magnetic field is ramped slowly such that the atoms adiabatically follow the dressed-state from $|2\rangle$ to $|3\rangle$.

The following experiments are predominantly performed in the $|1\rangle - |3\rangle$ mixture for two reasons. Firstly, evaporation around the zero-crossing of the Feshbach resonance is more efficient in the $|1\rangle - |3\rangle$ mixture. This stems from the attraction at the minimum of the s-wave scattering length around the zero-crossing being stronger in the $|1\rangle - |3\rangle$ mixture at $a = -890\,a_0$ compared to the $|1\rangle - |2\rangle$ mixture with $a = -290\,a_0$. Secondly, the Feshbach resonance is located at a lower magnetic field value for the $|1\rangle - |3\rangle$ mixture, i.e. at $B_0 = 689.7\,\mathrm{G}$. Therefore, there is less thermal load on the experiment since lower currents are required to prepare the required fields for both the unitary Fermi gas at B_0 and the BCS limit at $B_{BCS} > B_0$.

A spin-polarized gas can be prepared via narrow p-wave Feshbach resonances [77] which lead to spin-dependent losses. The p-wave resonances are located at $\sim 159\,\mathrm{G}$ [77] for the $|1\rangle - |1\rangle$ interaction and at $\sim 215\,\mathrm{G}$ [77] for the $|2\rangle - |2\rangle$ interaction. Depending on the magnetic field and the duration at which the atoms are held at the p-wave resonance the magnetization of the gas can be arbitrarily adjusted.

Hybrid Dipole Trap

The final dipole trap, which is used for the experiments, has a large waist $w_0 = 70\,\mu\mathrm{m}$, see Fig. 2.1 and is confining the atoms in z- and x-direction, where $\nu_x \approx \nu_z \sim 370\sqrt{P_{trap}}\,\mathrm{Hz/W}^{0.5}$. The confinement along the beam direction (y-direction) is provided by the magnetic field which is produced by the Feshbach coils in a displaced Helmholtz configuration. This configuration leads to a weak harmonic confinement in the radial x- and y-direction of $\nu_y = 20 \ldots 26\,\mathrm{Hz}$ and anti-confinement in z-direction, see Ch. 5. In this trap the last step in the spin-preparation, i.e. the $|2\rangle - |3\rangle$ transfer, is performed before the Feshbach field is ramped up for evaporation. This is followed by the preparation of the biases required for the transport experiments, see Sec. 2.3 for details, and the optical potentials creating the transport geometry are ramped up. The evaporation is performed either at the Feshbach resonance, whenever a strongly interacting gas is prepared or at the minimum of the scattering length close to the zero-crossing, whenever a non-interacting gas is prepared. The optical evaporation is aided by a magnetic gradient in z-direction acting as a tilt [78] and lasts, depending on the interaction, $0.5 - 3\,\mathrm{s}$. The final degeneracy that can be reached when the transport geometry is present is $T/T_F \sim 0.2$, without the transport beams T/T_F is slightly lower. The vacuum limited lifetime in this trap without the

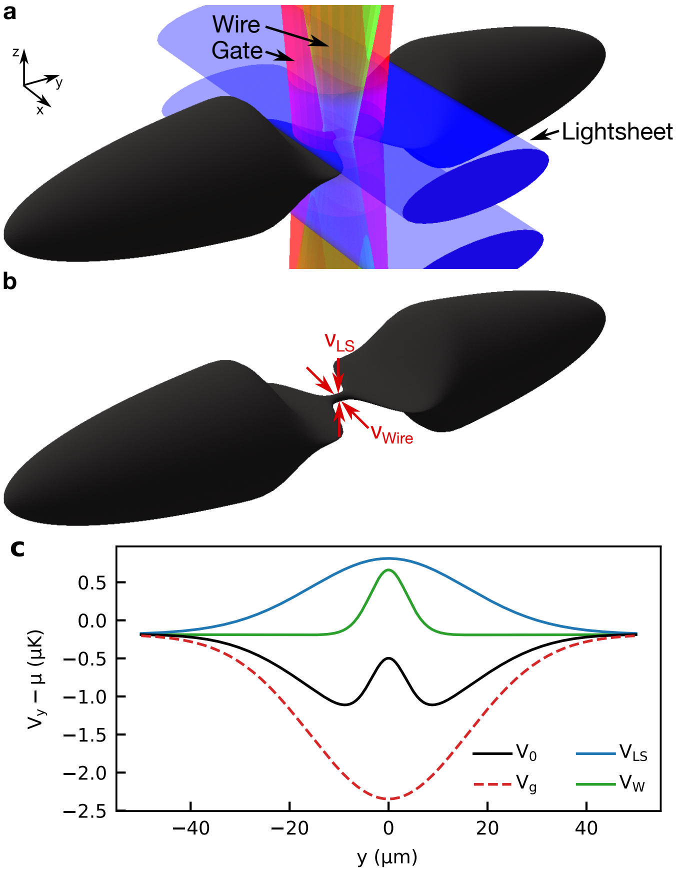

Figure 2.3: Potential landscape in transport configuration. (a) Schematic of the cloud ($L \approx 500\,\mu m$) including the constriction beams creating the 1D transport configuration. The lightsheet (blue, $2w_y \approx 60\,\mu m$) is confining vertically (b) via a TEM_{01}-like beam shape, blue detuned at 532 nm. The wire beam (green, $2w_y \approx 13\,\mu m$) is confining in transversal x-direction (b) also via a TEM_{01}-like shape. The gate beam (red, $2w_y \approx 60\,\mu m$) is a Gaussian beam which attractively raises the local chemical potential around the constriction. The potential landscape $V_i - \mu$ (c) along the transport direction (y) displays the zero-point energy $\sim h/2\nu_i e^{-y^2/w_y^2}$ of the different confining potentials, i.e. lightsheet V_{LS}, wire V_W and gate V_g (red), as well as the combined potential V_0. The lowest potential regions in V_0 next to the wire are the so-called pockets created by the attractive gate.

transport geometry present is ∼ 44s. The transport experiments, following the final evaporation can take up to 6 s limited by the temperature of the Feshbach coils.

2.1.2 Optical Potentials – Alignment

In this section an overview over the optical potentials creating the transport geometry is provided. In addition, the alignment procedure required to get transport through a quantum point contact is outlined. The technical details regarding the optical potentials making up the transport geometry are described in Ch. 5.

Lightsheet Potential

The confinement in vertical direction is achieved via a repulsive TEM_{01} beam at 532 nm propagating along the x-direction. The waist of the beam in vertical direction is $w_z = 9.5(2)\,\mu\mathrm{m}$ and in transport direction $w_y = 30.2(10)\,\mu\mathrm{m}$ which provide a peak confinement within the dark region of

$$\omega_z^2 = \frac{24c^2\Gamma P}{\pi m_{6_{Li}}\omega_l^3 w_z^3 w_y \Delta}, \tag{2.1}$$

where ω_l is the laser frequency, Γ is the natural linewidth and Δ is the laser detuning. The Rayleigh range $z_R = 530\,\mu\mathrm{m}$ of the beam is much larger than the waist of the dipole trap, thus providing a uniform confinement along the lightsheet beams propagation direction. In the experiment the confinement frequency that can be reached is $\nu_z = \sqrt{P} \cdot 10.97(30)\,\mathrm{kHz}/\sqrt{\mathrm{W}}$ with laser powers of up to $P = 0.9\,\mathrm{W}$. This confinement $\nu_z h/k_B = 480\,\mathrm{nK}$ is usually larger than the temperature of the gas and thus creates a two-dimensional transport region between the two three-dimensional reservoirs.

Wire Potential

The one-dimensional transport geometry is obtained by projecting an image of a lithographic mask onto the atoms through the high resolution microscope. The beam is effectively a TEM_{01} shaped repulsive potential at 532 nm. The nodal region has a waist of $w_{\mathrm{dark}} = 1.5\,\mu\mathrm{m}$ while the elliptical beam is larger in x-direction $w_x = 78\,\mu\mathrm{m}$ such that atoms cannot flow around the wire. The length of the wire $w_y = 5.8\,\mu\mathrm{m}$ can be tuned by varying the distance of the collimation lens to the fiber. In this configuration transversal confinement frequencies of $\nu_x = \sqrt{P} \cdot 1.65(3)\,\mathrm{kHz}/\sqrt{\mathrm{mW}}$ can be achieved with possible laser powers in excess of $P = 100\,\mathrm{mW}$. The two transversal confinements lead to a relatively high zero-point energy of the 1D trap $0.5\nu_x + 0.5\nu_z \sim 0.55\,\mu\mathrm{K}$ which is above the usual Fermi energy in the reservoirs $\mu \sim 0.4\,\mu\mathrm{K}$, such that a gate potential is necessary to transport atoms.

Gate Potential

The gate beam is a circular Gaussian beam send through the upper microscope collinear with the wire beam. The light is red detuned at 767 nm thus providing an attractive potential for the atoms. The size of the gate beam is kept similar to the lightsheet waist in y-direction $w_{\mathrm{gate},x} = w_{\mathrm{gate},y} \approx 30\,\mu\mathrm{m}$. This way the chemical potential around the wire can be tuned via $\tilde{\mu} = \mu - (-V_g)$, where V_g can be increased up to $V_g \sim 2.5\,\mu\mathrm{K}$ before the attractive potential pierces the lightsheet trap and losses set in.

Wall Beam

The wall beam provides the mechanism to open and close the transport constriction, thereby starting and stopping transport. The repulsive beam at 532 nm is shaped with a cylindrical lens into a highly elliptical beam with $w_y = 8.6\,\mu\mathrm{m}$ and $w_x = 54\,\mu\mathrm{m}$ such that a high intensity is reached to prevent atoms from flowing over the wall $V_{\mathrm{Wall}} \sim 2.5\,E_R$ while the transversal size prevents atom flowing around it.

Near-Resonant Beam

In some experiments presented here a near-resonant, strongly focused beam is used to manipulate transport. For this purpose a digital micromirror device (DMD) is used to correct aberrations [62] of the objective (and the optics in front of it) in order to project diffraction limited potentials at 671 nm, i.e. $w_{\text{min}} \sim 770\,\text{nm}$ [79]. For a more convenient alignment process the beam size is often kept above the diffraction limit $w_{\text{DMD}} \sim 1-2\,\mu\text{m}$, but smaller than the wire length to act locally.

Alignment

The cloud generally provides the reference position for all optical potentials impinging from different directions. The alignment is then according to the following procedure

1. The lightsheet position is aligned to the clouds center position with a picomotor (*NewFocus Picomotor*), since the alignment by hand is too imprecise.
2. The wire is focused in z-direction with a transport measurement, i.e. atoms only flow if the lithographic mask is sharply imaged on the atoms. The focus is adjusted via the position of the upper microscope.
3. The lighsheet's center in the horizontal plane is determined with absorption imaging through the microscope.
4. The wire is aligned to the center of the lightsheet using the position of the upper microscope in the horizontal $x-y$ plane.
5. The gate is aligned to the wire with a picomotor.
6. The near-resonant beam is aligned to the wire with the tilt aberration providing a focus position shift.
7. The wall can be aligned by hand to the wire.

The alignment of the vertically projected transport beams to the lightsheet can be performed either via the imaging in z-direction or via transport. The near-resonant beam needs to be aligned using transport since the alignment by eye is not reliable. Following the alignment of the transport geometry the magnetic gradient in y-direction is used to align the bias, such that transport ends at zero bias. In recent years the experiment is stable enough to run around the clock which greatly reduced the need for realignment.

2.1.3 Absorption Imaging

The final event in the transport experiment is the in-situ absorption imaging of the cloud either in horizontal or vertical direction.

- **x-imaging.** The full cloud can be imaged in x-direction with a low-resolution, shot-noise limited [80] imaging system, see also Sec. 6.3. The magnification is 3 which results in an effective pixel size of 4.3 µm. This imaging system allows taking spin resolved images of the cloud and is primarily used for atom-number and thermometry measurements.

- **z-imaging.** In z-direction the lower microscope can be used to take absorption images of the center of the cloud, FOV $= 150 \times 150\,\mu\mathrm{m}^2$. The effective pixel size is 296 nm which allows us to measure local density effects, provided the density is high enough.

Technical details of the spin-resolved imaging can be found in Sec. 6.3 while the technical details regarding the high resolution imaging are in Sec. 5.3.

In either case Beer's law is used to estimate the local density via

$$I'(z) = -n\sigma(\omega, I)I(z)\,, \tag{2.2}$$

where I is the intensity of the light and σ is the absorption cross-section of the medium. The absorption cross-section in this case depends on the light frequency and on the light intensity, since the imaging is performed around the saturation intensity which provides the optimal signal-to-noise [81]. The optical depth of the medium $OD(y,z) = \sigma_0 \int n(x,y,z)dx$ is then given by [82]

$$OD = -\alpha \ln\left(\frac{I_f}{I_i}\right) + \frac{I_i - I_f}{I_{s,0}}\,, \tag{2.3}$$

where $I_{i,f}$ is the initial and final picture of the cloud, i.e. the atom and bright image. The parameter α provides a correction due to polarization and the excited state structure, such that $I_s = \alpha I_{s,0}$, where $I_s = 25.4\,\mathrm{W/m^2}$ is the saturation intensity. α is calibrated using the method outlined in Ref. [81].

The challenge when imaging lithium compared to other elements is that the low mass leads to a quick acceleration when photons are scattered. Taking into account the resulting Doppler shift and the diffusion due to the scattering the optimal imaging pulse lengths is $1-3\,\mu\mathrm{s}$ [81]. On the other hand, imaging at high magnetic fields has the advantage that there are closed transitions which do not require repumping during the imaging.

Since there are some fringes in the absorption images due to imperfect optical elements a fringe removal algorithm [83] is used to produce an optimal bright picture which allows us to subtract said fringes in the atom picture.

2.2 THERMOMETRY OF THE FERMIONIC QUANTUM GAS

In order to determine the thermodynamic properties of the atomic cloud beyond the atom-number we use standard thermometry techniques relying on the equation of state of the non-interacting Fermi gas and the unitary Fermi gas. The different techniques are compared in the PhD thesis of S. Krinner [70], while in recent years the technique of choice has been the second-moment method [84].

The second-moment method relies on the virial theorem relating the internal energy to twice the well-known potential energy such that

$$U/N = 3m_{^6Li}\omega_y^2 \langle y^2 \rangle\,, \tag{2.4}$$

where ω_y is the confinement frequency along the y-direction and $\langle y^2 \rangle$ is the second moment. This relation also holds for the unitary Fermi gas [85]. The second-moment is extracted from the 1D density profile of the cloud via

$$\langle y^2 \rangle = \frac{\int n(y)y^2 dy}{\int n(y)dy} \tag{2.5}$$

The image of the cloud is taken in-situ such that both spins can be imaged. The density profile along the y-direction is given by the harmonic confinement of the magnetic trap.

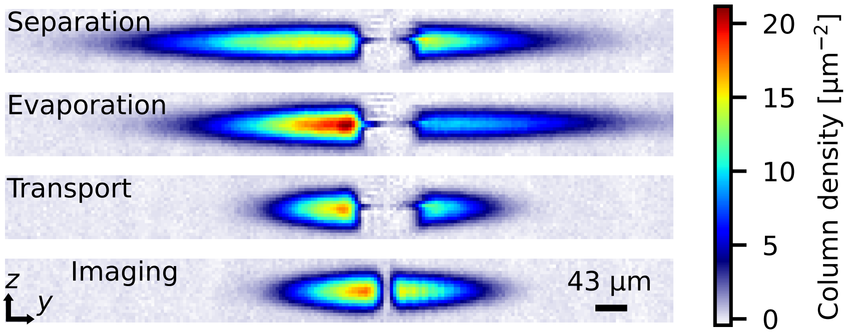

Figure 2.4: Cloud shapes during preparation. For the separation the center of the harmonic trap is shifted creating an imbalance of atom-number between the reservoirs. The following optical evaporation (image taken during evaporation) cools the cloud to degeneracy. During transport the imbalance can relax. Imaging is performed in the harmonic trap given by the radial magnetic confinement.

Experimentally, the transport experiments require us to obtain the degeneracy of two half-harmonic clouds separately. In order to do this the position of the wall, intersecting the cloud is determined via a fit. Then a fixed region around the wall is removed from the picture, where the density too small to be estimated correctly by our imaging system. For the second-moment determination each half-harmonic reservoir is assumed to be mirrored such that its thermodynamic quantities can be determined assuming harmonic reservoirs.

In order to obtain the thermodynamic quantities of each reservoir we take the following steps:

1. **N** – The atom number is determined from the integration of $n(y)$ along the y-direction.

2. $\langle \mathbf{y^2} \rangle$ – The non-interacting density profile is fitted to the density profile $n(y)$ to reduce noise in the wings of the cloud [16]. This density profile fits even in the strongly-interacting gas.

3. $\mathbf{E_F}$ – The atom-number N and the calibrated trap frequencies $\bar{\omega} = (\omega_x \omega_y \omega_z)^{1/3}$ are used to calculate the Fermi energy via

$$E_{F,i} = \hbar\bar{\omega}(6 \cdot 2N_i)^{1/3}\,, \tag{2.6}$$

   where the factor of 2 is included since the atom number N_i (with $i = L, R$) is that of a half-harmonic reservoir.

4. $(\mathbf{U/NE_F})_\mathbf{i}$ – The energy per particle normalized by the Fermi energy is obtained from the second moment via Eq. 2.5 and the Fermi energy.

5. $\mathbf{q_{0,i}}$ – The reduced chemical potential $q_{0,i}$ at the center of the cloud is found from the equation-of-state of the gas [40]. The equation-of-state was previously integrated over the harmonic trap and the relations between $(U/NE_F)_i$ and $q_{0,i}$ are saved in a look-up-table.

6. The remaining thermodynamic quantities, e.g. T/T_F and S/Nk_B, can then be calculated using the equations given in Tab. 2.1.

	Non-interacting	**Unitary**
Central density n_{3D}	$\frac{F_{1/2}(q_0)}{\lambda_T^3}$	$\frac{f_n(q_0)}{\lambda_T^3}$
Atom number N	$\left(\frac{k_B T}{\hbar\bar{\omega}}\right)^3 F_2(q_0)$	$\frac{4}{\sqrt{\pi}}\left(\frac{k_B T}{\hbar\bar{\omega}}\right)^3 N_2(q_0)$
Temperature T/T_F	$(6F_2(q_0))^{-1/3}$	$\left(\frac{24}{\sqrt{\pi}} N_2(q_0)\right)^{-1/3}$
Entropy S/Nk_B	$4\frac{F_3(q_0)}{F_2(q_0)} - q_0$	$\frac{8}{3}\frac{N_4(q_0)}{N_2(q_0)} - q_0$
Internal energy U/NE_F	$\frac{3}{6^{1/3}}\frac{F_3(q_0)}{F_2(q_0)^{4/3}}$	$\left(\frac{\pi}{9}\right)^{1/6}\frac{N_4(q_0)}{N_2(q_0)^{4/3}}$
Compressibility κ/N	$\frac{1}{k_B T}\frac{F_1(q_0)}{F_2(q_0)}$	$\frac{1}{2k_B T}\frac{N_0(q_0)}{N_2(q_0)}$
Dilatation coefficient α_r/k_B	$3\frac{F_2(q_0)}{F_1(q_0)} - q_0$	$6\frac{N_2(q_0)}{N_0(q_0)} - q_0$
Specific heat C_N/Nk_B	$12\frac{F_3(q_0)}{F_2(q_0)} - 9\frac{F_2(q_0)}{F_1(q_0)}$	$8\frac{N_4(q_0)}{N_2(q_0)} - 18\frac{N_2(q_0)}{N_0(q_0)}$

Table 2.1: Thermodynamic properties of a harmonically trapped Fermi gas. Density n_{3D} at the trap center for a single spin, atom number N, temperature T, internal energy U, entropy S, compressibility $\kappa = (dN/d\mu)|_T$, dilatation coefficient $\alpha_r = -(d\mu/dT)|_N$ and specific heat $C_N = T(dS/dT)|_N$ as a function of the reduced chemical potential $q_0 = \mu_0/k_B T$ at the trap center. The atom number N is obtained by integrating the local density for one spin over the entire trap. All other extensive quantities are normalized by N and do not depend on whether one or two spins, or one or two half-traps (reservoirs) are considered. The functions $N_j(q_0) = \int_0^\infty r^j f_n(q_0 - r^2)\,dr$ indicate the dimensionless moments of the dimensionless function f_n introduced in Ref. [86]. The functions $F_j(q)$ are the complete Fermi-Dirac integrals, $\bar{\omega}$ is the geometric mean of the trap frequencies and $\lambda_T = \sqrt{2\pi\hbar^2/mk_B T}$ is the thermal wavelength. Adapted from Ref. [36].

Importantly, the previously discussed quantities are determined during imaging where the atoms are held in a well-calibrated harmonic trap. During transport the shape of the cloud is quite different as can be seen in Fig. 2.4. The thermodynamic quantities during transport are calculated assuming that the transport geometry is ramped down adiabatically such that the entropy per particle S/Nk_B stays constant. The possibly different trap frequencies are then included via the Fermi energy $E_{F,tr}$ while the effect of the lightsheet, pushing the atoms away from the center is included via the equation-of-state.

2.3 BIAS PREPARATION METHODS

One of the advantages of operating in a voltage driven transport configuration is the possibility to easily prepare biases in chemical potential, temperature/entropy and spin/magnetization. The three different preparation methods are sketched in Fig. 2.5 where for each bias the position of the harmonic magnetic confinement in y-direction is varied with respect to the wall to create the biases

$$V_{\mathrm{mag},y} = \frac{1}{2} m_{^6\mathrm{Li}} \omega_y^2(B) y^2 + \mu(B) B_y' y \,, \tag{2.7}$$

with the magnetic moment $\mu(B)$ and the confinement frequency $\omega(B)$ which depend on the Feshbach field and the magnetic gradient B_y' in y-direction. All three biases are prepared before or via evaporation such that the system is in thermodynamic equilibrium before transport.

Chemical Potential Bias

In order to prepare a chemical potential bias, i.e. particle number imbalance, the cloud is first displaced in y-direction (see 2nd step in Fig. 2.5(a)) then the wall is separating the left and right reservoir and the harmonic confinement is recentered. During the following evaporation the center of the confinement is shifted in the opposite direction, such that the reservoirs reach the same temperature even though the initial chemical potential is different.

New Temperature Bias Preparation

Preparing small biases at small temperatures is difficult using parametric modulation of the gate beam inside the reservoirs [87]. This is why we developed a new technique to prepare temperature biases via the compression of the trap. Figure 2.5 shows the temperature bias preparation in its middle column. The cloud is separate with the wall before the magnetic gradient in y-direction is used to shift the center of the magnetic confinement, see 3rd step in Fig. 2.5. Then the cloud is optically evaporated which in our system is more efficient in the decompressed trap, leading to a lower final temperature on the right. Finally, the magnetic gradient is removed such that the left and right reservoir feel the same confinement, but at different temperatures.

Spin Bias

The spin bias is created via the magnetic field dependence of the confinement frequency $\omega_y(B)$ which is different for the three lowest hyperfine states at low magnetic fields. Here, the spin bias is created for the $1-3$

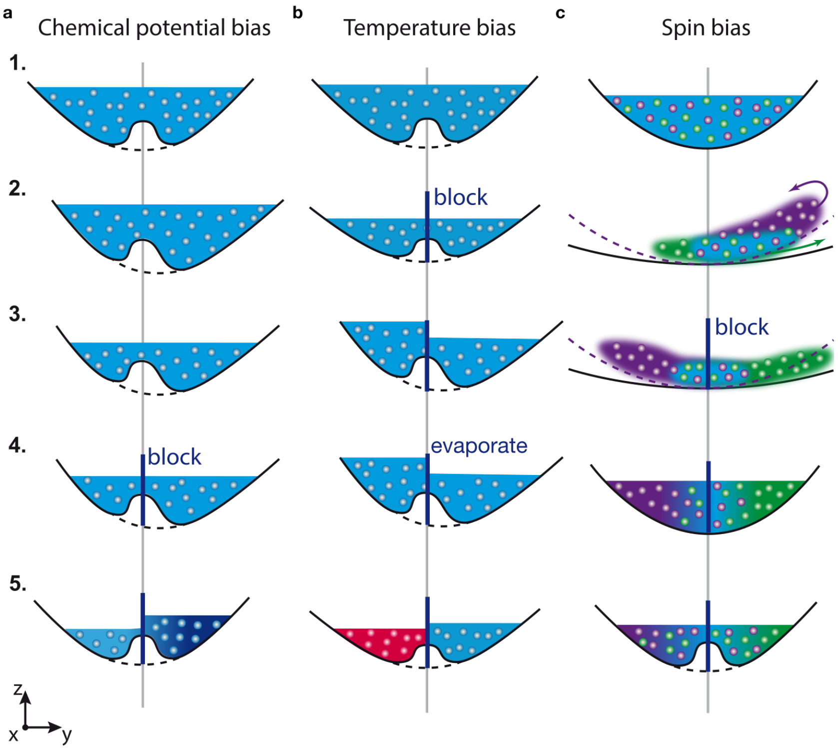

Figure 2.5: Preparation of biases in chemical potential, temperature and spin. (a) The preparation schemes for all three biases rely on shifting the center of the harmonic magnetic confinement using a magnetic gradient in y-direction. The chemical potential bias is created by shifting the cloud, then blocking the constriction with the wall and subsequently shifting the potentials back to their original position. For the temperature bias (b) the wall is separating the reservoirs before shifting, such that the reservoirs are evaporated at different confinements. We find that this leads to a higher temperature in the denser reservoir. This confinement is also used in the case of a chemical potential bias to prevent a temperature difference from building up during evaporation. The spin bias (c) is created via sinusoidal modulation of the magnetic trap position at $B \sim 40\,\mathrm{G}$ where the hyperfine states experience the largest difference in magnetic confinement frequency along y. Stopping the dipole oscillation at the correct time with the wall leads to a spin bias. Adapted from Ref. [70].

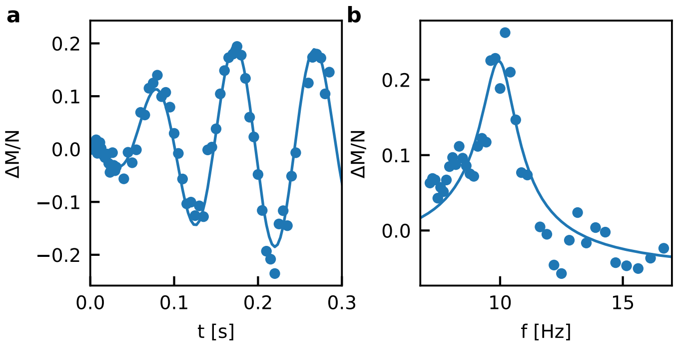

Figure 2.6: Preparation of a spin bias. (a) Sinusoidal modulation of the trap position in y-direction excites the dipole mode which has different resonance frequencies for two spin-states, i.e. $\nu_{y,1} = 10.96(6)\,\mathrm{Hz}$ and $\nu_{y,3} = 9.97(8)\,\mathrm{Hz}$. The oscillations are out-of-phase and a relative magnetization $\Delta M/N$ shows the expected oscillation at the average frequency with a slow envelope at the frequency difference. (b) The system can be described as a damped, driven harmonic oscillator which can be fitted with a damped Lorentzian, the resonance is at $f_c = 9.99(8)\,\mathrm{Hz}$.

mixture. The difference in magnetic moment is maximal at around $B = 52\,\mathrm{G}$. The dipole oscillation is excited via a sinusoidal modulation of the gradient $B'_y \sim \sin(\omega_0 t)$, see Fig. 2.5(c). Figure 2.6(a) shows the resulting dynamics of the relative magnetization $\Delta M/N$ which oscillates at $(\nu_{y,1} + \nu_{y,3})/2 = 10.47(5)\,\mathrm{Hz}$ with an envelope of $(\nu_{y,1} - \nu_{y,3})/2 = 0.49(5)\,\mathrm{Hz}$. The oscillations of the magnetization can be modeled with a driven, damped harmonic oscillator as can be seen in Fig. 2.6(b) where a damped Lorentzian is fitted to the resonance.

2.4 TWO-TERMINAL TRANSPORT MEASUREMENTS

In this section a terse introduction of the transport measurements is provided. First the transport model describing two-reservoir coupled by a resistive junction is introduced and secondly the Landauer theory, governing transport through a quantum point contact is described. For a more thorough discussion of the basics underlying the transport in this experiment the PhD thesis of S. Krinner [70] is detailing particle transport, while the PhD thesis of S. Häusler [71] provides more details regarding the transport of heat.

The RC Model

The transport geometry of two-reservoirs connected by a junction is in the simplest case modeled by an RC-circuit where the capacitance C is the compressibility κ of the reservoirs and the resistance R is the inverse conductance G of the junction. In our system transport is then observed by applying a "voltage" bias, here a chemical potential bias $\Delta\mu = \mu_L - \mu_R$. Alternatively it would be possible to apply a constant current. In the linear regime the bias drives a current via

$$I_N = G\delta\mu\,, \tag{2.8}$$

with G being the conductance of the junction and the particle current $I_N = -0.5\ \partial\Delta N/\partial t\ =$. The chemical potential in each reservoir can be linearized via $d\mu = \partial\mu/\partial N|_T dN = \kappa dN$ such that the equation of motion is obtained

$$\frac{\partial\Delta N}{\partial t} = \Delta N/\tau = \Delta N 2G/\kappa\,, \tag{2.9}$$

which is equivalent to the e.o.m. of an RC circuit. The compressibility is provided by the Pauli principle (the Fermi energy is the electrical potential) such that each reservoir contributes $\kappa/2$ since generally the capacitance is defined for a combination of two plates. In the experiment the exponential solution to the equation of motion of the RC circuit is used to measure the conductance. The conductance is determined by measuring the particle imbalance ΔN at two points via

$$G = \frac{\kappa}{2t}\ln\left(\frac{\Delta N(0)}{\Delta N(t)}\right)\,, \tag{2.10}$$

where t is the time during which the wall is open and $\Delta N(0)$ is determined as an average over measurements where no transport is happening. Figure 2.7(b) shows a measurement of the conductance obtained with the method explained here. The atom number imbalance corresponding to $V_g + \mu < 1\,\mu\mathrm{K}$ is used to determine $\Delta N(0)$. Interestingly, the Landauer formalism works in our system even in the non-interacting regime where thermal equilibration is not obvious [6], though it has been shown that the formalism holds even in a microcanonical limit [88].

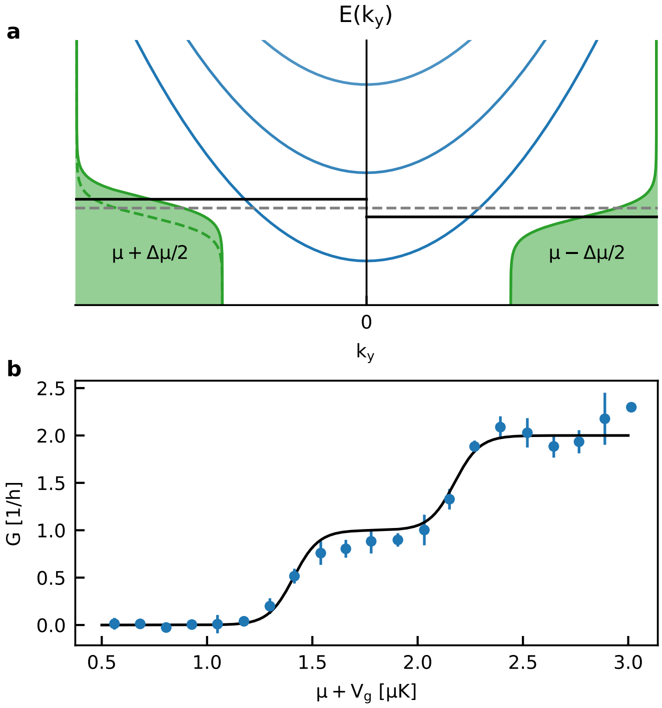

Figure 2.7: Quantized conductance measurement. The schematic energy landscape for a single-particle transmitted through a harmonically confined, ballistic region is shown in (a). The blue parabolas show the possible transmission modes for the fermions. The average chemical potential $\bar{\mu}$ (gray dashed line) determines how many modes are occupied. The bias driving a current is given by the chemical potential difference $\Delta\mu$. (b) The quantized conductance curve shown here was measured using Eq. 2.10. The solid line is a fit which provides the step-size, given by the confinement frequency $\nu_x = 15.8(54)\,\text{kHz}$, and the temperature of the reservoirs via the broadening of the step $T = 59(12)\,\text{nK}$.

Coupled Particle and Heat Transport

As soon as there is coupling between transported currents the dynamics deviate from the simple exponential behavior and in the linear regime are described by a sum of exponentials. The most common coupled transport scenario in our experiment is the thermoelectric transport, where heat/entropy and particle transport interact. Microscopically the coupling stems from an asymmetry in the dispersion relation, i.e. thermoelectricity requires particle-hole asymmetry [44]. The transport is then described by a 2×2 matrix obeying the Onsager relation. The derivation of the matrix coefficients is described in Ref. [71].

The starting point of the thermoelectric transport is a current which transports both heat and particles. In terms of thermodynamics it is most straightforward to begin with an energy current I_E. In the case where the energy current does not do work it can be considered equivalent to the heat current. Generally the heat flow is given by [3]

$$I_Q = I_E - \bar{\mu} I_N \,. \tag{2.11}$$

The entropy current is found from $dQ = TdS$ such that

$$I_S = \frac{1}{T} I_E - \frac{\bar{\mu}}{T} I_N \,. \tag{2.12}$$

In the case of thermoelectric transport we like to use the basis of extensive particle I_N and entropy current I_S, driven by intensive chemical potential $\Delta\mu$ and temperature δT biases. The current-voltage characteristic is then given by

$$\begin{pmatrix} I_N \\ I_S \end{pmatrix} = G \begin{pmatrix} 1 & \alpha_c \\ \alpha_c & L + \alpha_c^2 \end{pmatrix} \begin{pmatrix} \Delta\mu \\ \Delta T \end{pmatrix} , \tag{2.13}$$

with the Lorenz number L and the Seebeck coefficient α_c. The Seebeck coefficient α_c quantifies the coupling between entropy and particle transport, i.e. the transported entropy per particle $\alpha_c = I_N / I_S|_{\Delta T = 0}$. The Lorenz number is the ratio between the Ohmic heat and particle conductance $L = G_T / TG$. One interesting observation is that the entropy current is given by $I_S = \alpha_c I_N + (L + \alpha_c^2)\Delta T$ which implies that each particle transports a certain entropy by itself which means that the thermoelectric power α_c is just the advectively transported entropy, i.e. the transported entropy per particle. The remaining contribution to the entropy current is the diffusive exchange of entropy between the reservoirs.

The overall timescale of transport is given by the conductance G. These equations describe the transport constraints given by the junction, while the reservoirs can also have a significant influence on the observed transport behavior [87] via their response coefficients. The reservoir response coefficients give the linearized chemical potential and temperature bias in units of the measured particle number and entropy bias.

$$\begin{pmatrix} \Delta\mu \\ \Delta T \end{pmatrix} = \frac{1}{\kappa \ell} \begin{pmatrix} \ell + \alpha_r^2 & -\alpha_r \\ -\alpha_r & 1 \end{pmatrix} \begin{pmatrix} \Delta N \\ \Delta S \end{pmatrix} , \tag{2.14}$$

with the compressibility κ, the dilatation coefficient α_r and the reservoir Lorenz number ℓ. The dilatation coefficient is in principle the counterpart to the Seebeck coefficient in the channel. It describes the change of entropy with particle number in the reservoirs via $\alpha_r = -(\partial S/\partial N)|_T$. The reservoir Lorenz number is given by the ratio of specific heat to compressibility $\ell = C_N/T\kappa$, with $C_N = T(dS/dT)|_N$. In analogy to its transport counterpart, the reservoir Lorenz number describes ratio between the "ability" of the reservoir to absorb heat over the ability to absorb particles.

Inserting Eq. 2.14 into Eq. 2.13 gives the equation of motion of the coupled system

$$\frac{d}{dt}\begin{pmatrix}\Delta N\\ \Delta S\end{pmatrix} = -\frac{2G}{\ell\kappa}\begin{pmatrix}\ell - \alpha\alpha_r & \alpha\\ -(L^2+\alpha_c\alpha)\alpha_r + \ell\alpha_c & L^2+\alpha_c\alpha\end{pmatrix}\begin{pmatrix}\Delta N\\ \Delta S\end{pmatrix}, \quad (2.15)$$

alternatively the easier to interpret equations of motion in the ΔN, ΔT basis are

$$\frac{d}{dt}\begin{pmatrix}\Delta N\\ \Delta T\end{pmatrix} = -\frac{2G}{\kappa}\begin{pmatrix}1 & \kappa\alpha\\ \alpha & (L+\alpha^2)/\ell\end{pmatrix}\begin{pmatrix}\Delta N\\ \Delta T\end{pmatrix}. \quad (2.16)$$

The parameter $\alpha = \alpha_c - \alpha_r$ is the effective thermopower which gives the direction of thermoelectric response, i.e. for $\alpha > 0$ the particle transport is from hot to cold while for $\alpha < 0$ it is from cold to hot reservoir. We call these regimes channel dominated if $\alpha > 0$ and reservoir dominated if $\alpha < 0$. The channel dominated regime is termed due to the fact that the channel prefers transport of hot particles (due to the zero point energy) while cold particles are blocked. The reservoir dominated regime exists because the chemical potential of the reservoir has a temperature dependence given by α_r when linearized. The solution to both equations of motion are biexponential functions with two timescales describing the initial response and final relaxation [71].

In the case of a magnetization imbalance there is no coupling between spins and particle current in the channel, but the reservoirs can be used to induce a spin current via $\Delta M = M_L - M_R = (N_{L\uparrow} - N_{L\downarrow}) - (N_{R\uparrow} - N_{R\downarrow})$. In linear response the current voltage relation is again given by

$$I_M = G_M \Delta\mu_M, \quad (2.17)$$

with $\Delta\mu_M = (\Delta\mu_\uparrow - \Delta\mu_\downarrow)/2$. Again, the chemical potential is related to the atom number via a reservoir response coefficient, here the spin susceptibility $\chi = \partial M/\partial\mu_M$, with $\mu_M = (\mu_\uparrow - \mu_\downarrow)$. The equation of motion is thus given by

$$-\frac{d\Delta M(t)}{dt} = \frac{G_M}{\chi}\Delta M. \quad (2.18)$$

The spin-susceptibility has been measured in Ref. [27] and calculated in Ref. [89] for the unitary Fermi gas, thus allowing us to determine the spin-conductance in the experiment. In order to obtain a coupling similar to the Seebeck effect between spin-currents and particle currents it would be necessary to engineer a coupling process, e.g. Raman transition, inside the channel.

2.4.1 Landauer-Büttiker Theory

The previously discussed models are purely phenomenological, i.e. they reproduce our transport experiments but do not have a microscopic origin. In this section the microscopic Landauer-Büttiker theory is introduced which allows us to calculate the transport coefficients of the phenomenological model in the non-interacting regime a priori from the knowledge of the underlying potential landscape and the degeneracy in the reservoirs.

Quasi-1D Potential Landscape

Figure 2.3(c) shows the quasi-1D potential landscape calculated from the confinement potentials provided by the constriction beams. The general idea is that we can separate the atomic wavefunction into different components along the spatial-directions given the confinement variations being adiabatic with respect to the atomic wavefunction [90]

$$\psi(x,y,z) = \phi_n(x)\phi_j(z)e^{iky} \tag{2.19}$$

where ϕ are wavefunctions of the harmonic oscillator. The Schrödinger equation is then given by

$$\frac{\hat{p}^2}{2m}\psi(y) + V_{1D}(y)\psi(y) = E\psi(y)\,, \tag{2.20}$$

where $V_{1D}(y)$ is the quasi-1D potential landscape given by the transversal confinement and the potentials along the y-direction, see Fig. 2.3(c). The confinement as a function of space is described by a Gaussian via

$$\nu(y) = \nu_0 e^{-y^2/w^2} = \nu_0 E(y)\,, \tag{2.21}$$

with the confinement frequency ν_0 and the beam waist w. The total confinement frequencies are then given by

$$\nu_x(y) = \sqrt{\nu_W^2 I_W(y) + \nu_g^2 I_g(y) + \nu_{x,d}^2}\,, \tag{2.22}$$

$$\nu_z(y) = \sqrt{\nu_{LS}^2 I_{LS}(y) + \nu_{z,d}^2}\,, \tag{2.23}$$

with the wire confinement ν_W, the lightsheet confinement ν_{LS}, the dipole trap confinement ν_d and the gate beam confinement ν_g. The corresponding intensity functions are defined as $I_i = e^{-2y^2/w_i^2}$ where $i = \{LS, g, W\}$. The zero-point energy V_0 is the sum over these confinements for the lowest mode

$$V_0(y) = h\nu_x(y)/2 + h\nu_z(y)/2 - h(\nu_{d,x} + \nu_{d,z})/2\,. \tag{2.24}$$

The total quasi-1D potential landscape is ultimately given by the sum over all contributing potentials

$$V_{1D}(y) = V_0(y) - V_g(y) + V_{LS}(y) + V_W(y) + h\nu_x(y)n_x + h\nu_z(y)n_z\,, \tag{2.25}$$

where the higher transversal modes are described by $h\nu_i(y)n_i$. The potentials $V_{LS}(y)$ and $V_W(y)$ are in principle zero at the position where transport takes place, i.e. $x = 0$, $z = 0$, but experimentally it is found that both have a non-zero darkness within the nodal lines of the TEM_{01} due to optical aberrations. This additional zero-point energy is accounted for by $V_{LS}(y)$ and $V_W(y)$. The gate potential on the other hand does provide a desired attractive shift of the potential landscape. The potential landscape of the different beams are displayed in Fig. 2.3(c).

Landauer-Büttiker Formalism

In the adiabatic limit the current through the potential landscape is given by the Landauer-Büttiker formula [91, 92] as a sum over the transversal modes

$$I_N = \frac{1}{h} \sum_{n,j} \int (f_L(E) - f_R(E)) T_{n,j}(E) dE \,, \tag{2.26}$$

where $T_{n,j}$ is the transmission through a mode and $f(E)$ are the Fermi-Dirac distributions of the reservoirs

$$f_i(E, \mu, T) = \left(1 + \exp\left(\frac{E - \mu_i}{k_B T}\right)\right)^{-1} \,, \tag{2.27}$$

with the chemical potential μ_i of the left and right reservoir. In the limit of zero temperature and using the Ohmic current bias relation the conductance can be expressed as

$$G = \frac{1}{h} \sum_{n,j} T_{n,j}(\bar{\mu}) \,, \tag{2.28}$$

where $\bar{\mu}$ is the average chemical potential and $\Delta\mu \ll \bar{\mu}$. This is the well-known formula for quantized conductance [5, 6, 93, 94] in a quantum point contact. At finite temperature the conductance is obtained by weighting the transmission with the Fermi-Dirac distribution of the reservoirs

$$G = \frac{1}{h} \sum_{n,j} \int T_{n,j}(\bar{\mu}) \left(\frac{\partial f(E, \bar{\mu}, T)}{\partial E}\right) dE \,, \tag{2.29}$$

which leads to a broadening of the conductance curves by $4k_B T$. Figure 2.7(a) displays the energy landscape for a fermionic particle being transmitted through a region of quantized harmonic confinement. The measurement of the conductance by varying the average chemical potential, see Fig. 2.7(b), displays the quantized conductance plateaus expected from Eq. 2.28. The length of the plateaus can be used to quantify the transversal confinement while the step length is given by the temperature broadening of the Fermi-Dirac distributions. We also find that the onset of conductance $\sim 1.25\,\mu\text{K}$ is larger than the step size indicating a non-zero darkness of the lightsheet and wire beams.

Beyond the particle transport we can derive the heat, entropy and energy current from the difference of left and right moving energies. The right moving flows are given by

$$I_{E,\rightarrow} = \frac{1}{h} \int \mathcal{T}(E) f_L(E) E dE \,, \tag{2.30}$$

$$I_{Q,\rightarrow} = \frac{1}{h} \int \mathcal{T}(E) f_L(E)(E - \bar{\mu}) dE \,, \tag{2.31}$$

$$I_{S,\rightarrow} = \frac{k_B}{h} \int \mathcal{T}(E) f_L(E) \frac{(E - \bar{\mu})}{\bar{T}} dE \,. \tag{2.32}$$

In the limit of irreversible processes the entropy production rate $\dot{S}$ allows us to identify all fluxes and their thermodynamic forces. The local rate of production of entropy is given by the outflow of entropy from the region and the increase of entropy in the region

$$\dot{s} = \frac{\partial s}{\partial t} + \nabla \cdot \mathbf{J}_S \,, \tag{2.33}$$

where s is the local entropy density and J_S is the current density. Assuming the extensive parameters energy and particle number are conserved, the entropy production can be written as [3]

$$\dot{s} = \sum_k \nabla F_k J_k \,, \tag{2.34}$$

with $F_k = \partial S/\partial X_k$ being the generalized force driving the system towards equilibrium and X_k is an extensive parameter. In the case of an entropy current driven by an intensive chemical potential and temperature bias the entropy production rate is given by

$$\dot{S} = \nabla\frac{1}{T} I_E - \nabla\frac{\mu}{T} I_N \,. \tag{2.35}$$

The currents I_k are tending to zero for infinitesimal small forces such that they can be expanded in powers of those

$$I_k = \sum_j \left(\frac{\partial I_k}{\partial F_j}\right) F_j + \frac{1}{2!}\sum_i\sum_j \left(\frac{\partial^2 I_k}{\partial F_i \partial F_j}\right) F_i F_k + \dots \,, \tag{2.36}$$

with the so-called kinetic coefficients $L_{jk} = \partial I_k/\partial F_j$ and L_{ijk}. This formula can thus be used to write the linear current bias characteristic for thermoelectric transport

$$I_N = -L_{11}\nabla\frac{\mu}{T} - L_{12}\nabla\frac{1}{T} \,, \tag{2.37}$$

$$I_E = L_{21}\nabla\frac{\mu}{T} + L_{22}\nabla\frac{1}{T} \,. \tag{2.38}$$

The Onsager relation then dictates that $L_{12} = L_{21}$ and the kinetic coefficients can be calculated in the non-interacting system from the microscopic Landauer-Büttiker formalism. In addition, the transport coefficients can be related to the kinetic coefficients such that the conductance G, the Seebeck coefficient α_c and the Lorenz number L can be numerically calculated. The details of the derivation can be found in Ref. [71]. For the calculation a general Landauer integral can be defined

$$L_k = \frac{1}{h}\int T(E)(E-\bar{\mu})^k \left(\frac{\partial f(E,\bar{\mu},T)}{\partial E}\right) dE \,. \tag{2.39}$$

Then the transport coefficients are given by

$$G = L_0 \,, \tag{2.40}$$

$$\alpha_c = \frac{1}{\bar{T}}\frac{L_1}{L_0} \,, \tag{2.41}$$

$$L = \frac{1}{\bar{T}^2}\left(\frac{L_2}{L_0} - \frac{L_1^2}{L_0^2}\right) \,. \tag{2.42}$$

The transmission $\mathcal{T}(E)$ can be numerically calculated from solving the 1D Schrödinger equation using Numerov's method for a particle scattering at the 1D potential given by the potential landscape $V_{1D}(y)$. The transport coefficients are then calculated via the kinetic coefficients L_{jk}.

3

LIGHT-MATTER INTERACTION IN LITHIUM AT HIGH MAGNETIC FIELDS

CHAPTER CONTENTS

The atomic level structure of ^{6}Li at high magnetic fields in the Paschen-Back regime [72] is seemingly simple since it mostly consists of "closed" transitions. In this regime the interaction with an external magnetic field is larger than the internal hyperfine interaction such that instead of the quantum number F, m_J and m_I become the good quantum numbers. This leads to 6 degenerate ground-states in the $2S_{1/2}$ manifold and 18 total states in the excited state manifolds $2P_{3/2}$ and $2P_{1/2}$ which are often assumed to have a singular set of quantum numbers. Since light-fields cannot couple to the m_I quantum number of the atoms nuclear angular momentum I the transitions between ground and excited states are considered closed. In this chapter we want to outline how one can use the admixtures of the different hyperfine states, albeit small, to enable many interesting possibilities for atom-light interactions at high-magnetic fields. This implies that strong s-wave scattering interactions between the ground-states can be combined with dissipative, coherent and even spin-coupling atom-light interactions.

We first describe the atomic level structure at high magnetic fields and the resulting dipole matrix elements of the resulting transitions. Additional details regarding the electronic structure of the atom in a magnetic field can be found in the master thesis of L. Bartha [95]. In the second section single photon transitions used for dissipative and dispersive manipulation of transport are discussed. In the last section two-photon transitions between two ground-states forming a lambda system are outlined.

3.1 ATOMIC LEVEL STRUCTURE AT HIGH EXTERNAL MAGNETIC FIELDS

In this section we are going to focus on the ground-state manifold $2S_{1/2}$ and the excited state manifolds $2P_{1/2}$, $2P_{3/2}$ which form the D_1 and D_2 transitions respectively shown in Fig. 3.1(a)-(b). For lithium the fine structure contribution, splitting the excited state manifold by $\Delta E_{FS} = 10.056\,\text{GHz}$ is fairly small since $\Delta E_{FS} \sim Z^2\alpha^2$, where α is the fine-structure constant and Z is the nuclear charge number. Implying that both D_1 and D_2 lines can be accessed with one laser. Figure 3.1(a) displays how the hyperfine splitting further splits each manifold given their respective total angular

Parameter	Value	
ν_{D1}, λ_{D1}	D1 transition	446.789 596 THz, 670.992 477 nm
ν_{D2}, λ_{D2}	D2 transition	446.799 648 THz, 670.977 380 nm
Γ	natural linewidth	5.8724 MHz
$\Delta E_{FS,P}$	fine struct. splitting	10.056 GHz
$\Delta E_S, \Delta E_{P_{1/2}}, \Delta E_{P_{3/2}}$	hyperfine splitting	228.2, 26.1, 4.4 MHz
g_L	orbital gyrom. factor	0.99999587
g_S	spin gyrom. factor	2.0023193043737
g_I	nuclear gyrom. factor	−0.000447654
$g_{J,S}, g_{J,P_{1/2}}, g_{J,P_{3/2}}$	electronic gyrom. factor	2.002301, 0.6668, 1.335
$d_{1/2\to1/2}, d_{3/2\to1/2}$	red. matrix element $d_{J'\to J}$	$-2.812\times10^{-29}, 3.997\times10^{-29}$ Cm

Table 3.1: Atomic properties of ^{6}Li [96].

momentum F, i.e. the ground state manifold is split into $F = 1/2$, $F = 3/2$ by $\Delta E_{HFS} = 228.2$ MHz. The hyperfine interaction is given by

$$H_{HFS} = A\mathbf{I}\cdot\mathbf{J} \tag{3.1}$$

which provides a splitting given by $\Delta E_{HFS} \sim Z\alpha^2$.

Applying an external magnetic field $\mathbf{B} = B\mathbf{e}_z$ leads to an additional interaction $H \sim \boldsymbol{\mu}\cdot\mathbf{B}$ between the atoms magnetic moment $\boldsymbol{\mu}$ and the external field. Taking into account both the atoms electronic moment $g_J\mu_B\mathbf{J}$ and its nuclear moment $g_I\mu_B\mathbf{I}$ the Zeeman interaction is

$$H = \mu_B(g_J\mathbf{J}\cdot\mathbf{B} + g_I\mathbf{I}\cdot\mathbf{B}), \tag{3.2}$$

with the Bohr magneton μ_B and the gyromagnetic factors g_I and g_J. Table 3.1 contains the values for the gyromagnetic factors for ^{6}Li. In the limit where the Zeeman interaction $\mu_B B$ is larger than the hyperfine interaction A the Zeeman interaction cannot be written in terms of $\mathbf{F}\cdot\mathbf{B}$, but the states have to be expressed as $|Im_I Jm_J\rangle$ and the hyperfine splitting is calculated as a perturbation on these eigenstates. This limit of $\mu_B B > A$ is reached at rather low magnetic field values in lithium, since $\mu_B/h = 1.4$ MHz/G and $E_{HFS} \approx 228$ MHz. The interaction in this Paschen-Back limit is then given by

$$H = \mu_B\left(g_J\mathbf{J}\cdot\mathbf{B} + g_I\mathbf{I}\cdot\mathbf{B}\right) + A\mathbf{J}\cdot\mathbf{I}. \tag{3.3}$$

Figure 3.1(a)-(b) shows the resulting atomic level structure calculated at varying magnetic field strength for the states involved in the D1 and D2 transition. The Paschen-Back regime extends up to fields where the orbital angular momentum becomes the valid quantum number, i.e. the Zeeman shift leads to a level crossing between the $P_{1/2}$ and $P_{3/2}$ manifold. This hyper Paschen-Back regime is reached at around 3200 G in lithium [97].

For us, it is particularly interesting how the eigenstates of the interaction Hamiltonian in Eq. 3.3 are composed of the basis states $|Im_I Jm_J\rangle$. The eigenstates can be calculated, assuming $\mathbf{B} = B\mathbf{e}_z$ and the ladder operators $J_\pm = J_x \pm iJ_y$ and $I_\pm = I_x \pm iI_y$ via

$$H = \mu_B B\left(g_J J_z + g_I I_z\right) + A\left(J_z I_z + \frac{1}{2}J_+I_- + \frac{1}{2}J_-I_+\right). \tag{3.4}$$

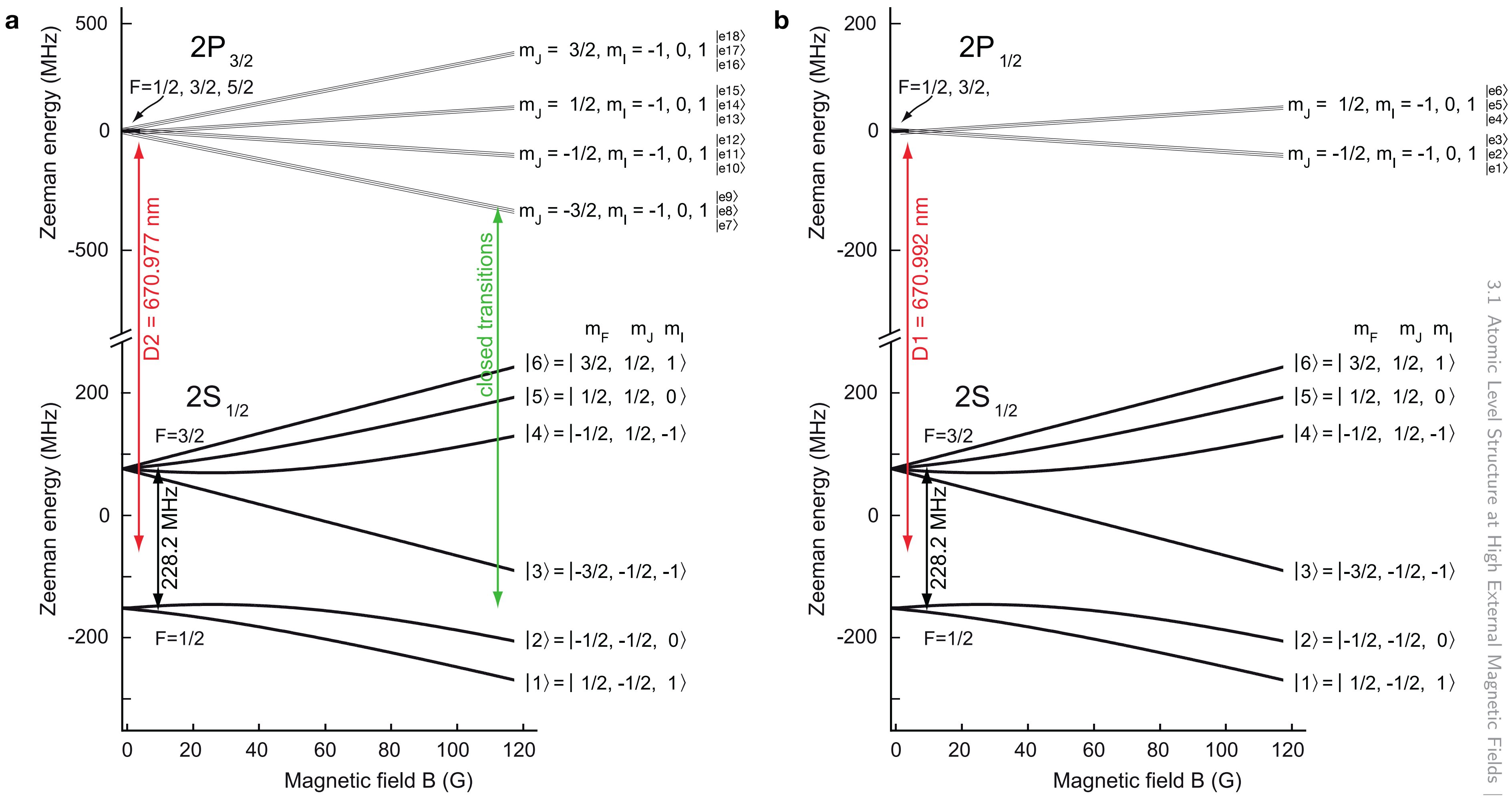

Figure 3.1: Atomic level structure at finite magnetic fields. D2 (a) and D2 (b) transitions in ^{6}Li as a function of the external magnetic field. The ground and excited-states are labeled by numbers $|i\rangle$ and $|ei\rangle$ ordered by energy.

G. states	$S_{1/2}$	Exc. states	$P_{1/2}$, $P_{3/2}$
$\lvert 1\rangle$	$\lvert -1/2,1\rangle - \epsilon_i \lvert 1/2,0\rangle$	$\lvert e1\rangle$	$\lvert -1/2,1\rangle - \epsilon_i \lvert 1/2,0\rangle$
$\lvert 2\rangle$	$\lvert -1/2,0\rangle - \epsilon_i \lvert 1/2,-1\rangle$	$\lvert e2\rangle$	$\lvert -1/2,0\rangle - \epsilon_i \lvert 1/2,-1\rangle$
$\lvert 3\rangle$	$\lvert -1/2,-1\rangle$	$\lvert e3\rangle$	$\lvert -1/2,-1\rangle$
$\lvert 4\rangle$	$\lvert 1/2,-1\rangle + \epsilon_i \lvert -1/2,0\rangle$	$\lvert e4\rangle$	$\lvert 1/2,-1\rangle + \epsilon_i \lvert -1/2,0\rangle$
$\lvert 5\rangle$	$\lvert 1/2,0\rangle + \epsilon_i \lvert -1/2,1\rangle$	$\lvert e5\rangle$	$\lvert 1/2,0\rangle + \epsilon_i \lvert -1/2,1\rangle$
$\lvert 6\rangle$	$\lvert 1/2,1\rangle$	$\lvert e6\rangle$	$\lvert 1/2,1\rangle$
		$\lvert e7\rangle$	$\lvert -3/2,-1\rangle$
		$\lvert e8\rangle$	$\delta_j \lvert -1/2,-1\rangle + \lvert -3/2,0\rangle$
		$\lvert e9\rangle$	$\delta_j' \lvert 1/2,-1\rangle + \delta_j \lvert -1/2,0\rangle + \lvert -3/2,1\rangle$
		$\lvert e10\rangle$	$\lvert -1/2,-1\rangle - \delta_j \lvert -3/2,0\rangle$
		$\lvert e11\rangle$	$\delta_j \lvert 1/2,-1\rangle + \lvert -1/2,0\rangle - \delta_j \lvert -3/2,1\rangle$
		$\lvert e12\rangle$	$\delta_j' \lvert 3/2,-1\rangle + \delta_j \lvert 1/2,0\rangle + \lvert -1/2,1\rangle$
		$\lvert e13\rangle$	$\delta_j \lvert 3/2,0\rangle + \lvert 1/2,1\rangle$
		$\lvert e14\rangle$	$\delta_j \lvert 3/2,-1\rangle + \lvert 1/2,0\rangle - \delta_j \lvert -1/2,1\rangle$
		$\lvert e15\rangle$	$\lvert 1/2,-1\rangle - \delta_j \lvert -1/2,0\rangle + \delta_j' \lvert -3/2,1\rangle$
		$\lvert e16\rangle$	$\lvert 3/2,1\rangle$
		$\lvert e17\rangle$	$\lvert 3/2,0\rangle - \delta_j \lvert 1/2,1\rangle$
		$\lvert e18\rangle$	$\lvert 3/2,-1\rangle - \delta_j \lvert 1/2,0\rangle + \delta_j' \lvert -1/2,1\rangle$

Table 3.2: Eigenstates of the ^{6}Li atom interacting with a strong external magnetic field.

In the S, $P_{1/2}$ manifold the eigenstates are then given by two sets of two and four different states respectively. The first set of states are the uncoupled states which are unaffected by the ladder operators, i.e. the states with $m_F = \pm 3/2$. The second set, of four, are the coupled states, where m_F preserving couplings give rise to a mixture of states. The coupling energy is given by A and consequently the admixture of the states is proportional to $\epsilon_i \sim A/\mu_B B$, continually decreasing with stronger fields.

Table 3.2 contains the eigenstates in the $\lvert m_J, m_I\rangle$ basis, ordered by increasing energy. For the $P_{3/2}$ manifold there are 12 states, again two of which are uncoupled $\lvert e1\rangle$, $\lvert e10\rangle$ here with $m_F = \pm 5/2$ while the remaining states are mixed according to Eq. 3.4. The admixtures δ and δ' are again inversely proportional to the magnetic field $\sim A/\mu_B B$, with δ' being smaller than δ. The precise admixtures ϵ, δ and δ' vary for each individual state, but they can be calculated analytically [95]. For simplicity, we obtain them numerically, i.e. at $B = 900\,\mathrm{G}$ we find $\epsilon_{S_{1/2}} \sim 4 \times 10^{-2}$, $\epsilon_{P_{1/2}} \sim 1 \times 10^{-2}$ while $\delta \sim 1 \times 10^{-4}$ and $\delta' \sim 1 \times 10^{-9}$.

The eigenenergies of the states is calculated via diagonalization of Eq. 3.3 called Breit-Rabi formula [98]

$$E_\pm = \frac{1}{4}\left(-A + 4\mu_B B g_I m_F \pm \sqrt{9A^2 - 8A\mu_B B(g_I - g_J)m_F + 4(\mu_B B(g_I - g_J))^2}\right), \tag{3.5}$$

where $+$ accounts for states with $F = 3/2$ and $-$ for states with $F = 1/2$. The eigenenergies of the $P_{3/2}$ manifold are obtained numerically, though an analytical expression exists [95].

3.2 INTRODUCTION TO TWO-LEVEL SYSTEM

In this section we use the previously obtained atomic level structure combined with the transition rules to find possible transitions at high magnetic fields. Table 3.2 already indicates that there are weak transitions beyond the normally used strong imaging transitions. In order to determine possible transitions and their strength the dipole matrix element in semiclassical approximation is calculated

$$d_{eg} = \sum_q e_q \langle e| d_q |g\rangle \,, \tag{3.6}$$

where e_q is the polarization of the light field and d_q is the polarization dependent dipole moment of the atom. The calculation of d_{eg} can be simplified using the Wigner-Eckart theorem which allows expressing the expectation value in the current basis $|Im_I Jm_J\rangle$ as a multiplication of Clebsch-Gordan coefficient $\langle Jm_J 1q|J'm_J'\rangle$ and reduced matrix element $\langle J'||\mathbf{d}||J\rangle$. The reduced matrix element $\langle J'||\mathbf{d}||J\rangle$ can be even further simplified to $\alpha_{JJ'}\langle L'||\mathbf{d}||L\rangle$ using the Wigner-Eckart theorem a second time. The values for the reduced matrix element are given in tab. 3.1. The Clebsch-Gordan coefficient incorporates the selection rules for the transitions and quantifies the change of angular momentum m_J by a photon

$$d^q_{ij} = \frac{1}{\sqrt{2J'+1}} \delta_{m_I\, m_I'} \langle Jm_J, 1q|J'm_J'\rangle\, \alpha_{JJ'} \langle L'||\mathbf{d}||L\rangle \,. \tag{3.7}$$

The polarization is encoded in q such that the transferred angular momentum is $q = +1$, $q = -1$ or $q = 0$ for σ_+, σ_- and π polarization, respectively. In case of the D_1 transition the Wigner-Eckart theorem gives $\alpha_{1/2\to 1/2} = -\sqrt{2/3}$ while for the D_2 transition $\alpha_{1/2\to 3/2} = \sqrt{4/3}$ [96].

The value of the individual dipole matrix elements quantifies the strength of an optical transition. The spontaneous decay is one example of such a transition where the emission rates Γ_{eg} between the transitions from excited state to different ground states is given by

$$\Gamma_{eg} = \frac{h\nu_{eg}}{3\pi\epsilon_0 c^3 \hbar^3} \sum_q |\langle e| d_q |g\rangle|^2 \,. \tag{3.8}$$

The natural linewidth is then calculated as the sum over all individual decay rates from one excited state, given in Tab. 3.1. Importantly, the spontaneous transition rate Γ_{eg} does not quantify the line-shape when driving an individual transition to this excited state. Table 3.3 contains the possible optical transitions at high magnetic fields for ^{6}Li. The transition strength is quantified in terms of branching ratios defined as

$$\beta = \frac{\Gamma_{eg}}{\sum_g \Gamma_{eg}} \,. \tag{3.9}$$

The individual transition strengths are proportional to the admixture of the involved states to the eigenstate. Comparing Tab. 3.2 and Tab. 3.3 we find that the weak transitions are present due to the mixture of hyperfine states, implying that the transition strength depends on ϵ, δ and δ' and therefore also on the magnetic field strength.

The value of the transition frequency is ν_{eg} calculated from the bare transition frequencies (see Tab. 3.1) including the Zeeman shift at high fields calculated from Eq. 3.5.

	$\vert 1\rangle$	$\vert 2\rangle$	$\vert 3\rangle$	$\vert 4\rangle$	$\vert 5\rangle$	$\vert 6\rangle$
$\vert e1\rangle$	33.2 (π)	2.4e − 02 (σ_+)		7.9e − 05 (σ_+)	0.2 (π)	66.6 (σ_-)
$\vert e2\rangle$	0.2 (σ_-)	33.1 (π)	2.5e − 02 (σ_+)	0.2 (π)	66.5 (σ_-)	
$\vert e3\rangle$		0.2 (σ_-)	33.3 (π)	66.4 (σ_-)		
$\vert e4\rangle$	7.1e − 05 (σ_-)	0.2 (π)	66.6 (σ_+)	33.1 (π)	2.5e − 02 (σ_-)	
$\vert e5\rangle$	0.2 (π)	66.4 (σ_+)		0.2 (σ_+)	33.2 (π)	2.4e − 02 (σ_-)
$\vert e6\rangle$	66.5 (σ_+)				0.2 (σ_+)	33.3 (π)
$\vert e7\rangle$			100.0 (σ_-)			
$\vert e8\rangle$		99.7 (σ_-)	8.0e − 05 (π)	0.3 (σ_-)		
$\vert e9\rangle$	99.7 (σ_-)	8.0e − 05 (π)	1.6e − 11 (σ_+)	2.7e − 07 (π)	0.3 (σ_-)	
$\vert e10\rangle$		0.1 (σ_-)	66.7 (π)	33.2 (σ_-)		
$\vert e11\rangle$	0.1 (σ_-)	66.4 (π)	5.3e − 05 (σ_+)	0.2 (π)	33.2 (σ_-)	
$\vert e12\rangle$	66.5 (π)	5.3e − 05 (σ_+)		1.8e − 07 (σ_+)	0.2 (π)	33.3 (σ_-)
$\vert e13\rangle$	33.2 (σ_+)				0.1 (σ_+)	66.7 (π)
$\vert e14\rangle$	0.2 (π)	33.2 (σ_+)		0.1 (σ_+)	66.5 (π)	5.4e − 05 (σ_-)
$\vert e15\rangle$	1.6e − 07 (σ_-)	0.2 (π)	33.3 (σ_+)	66.4 (π)	5.3e − 05 (σ_-)	
$\vert e16\rangle$						100.0 (σ_+)
$\vert e17\rangle$	0.3 (σ_+)				99.7 (σ_+)	8.0e − 05 (π)
$\vert e18\rangle$	2.3e − 07 (π)	0.3 (σ_+)		99.7 (σ_+)	8.0e − 05 (π)	1.6e − 11 (σ_-)

Table 3.3: Branching ratios and polarization of optical transitions in the D1 and D2 manifold of ^{6}Li. The table contains the branching ratios $\Gamma_{eg}/(\sum_g \Gamma eg)$ in percent and polarization's of the optical transitions coupling the hyperfine states at a magnetic field of $B = 690\,\mathrm{G}$. The excited states of the $P_{1/2}$ and $P_{3/2}$ manifold are sorted by energy and used as the rows of the table, while the ground-states of the $S_{1/2}$ manifold are contained in the columns.

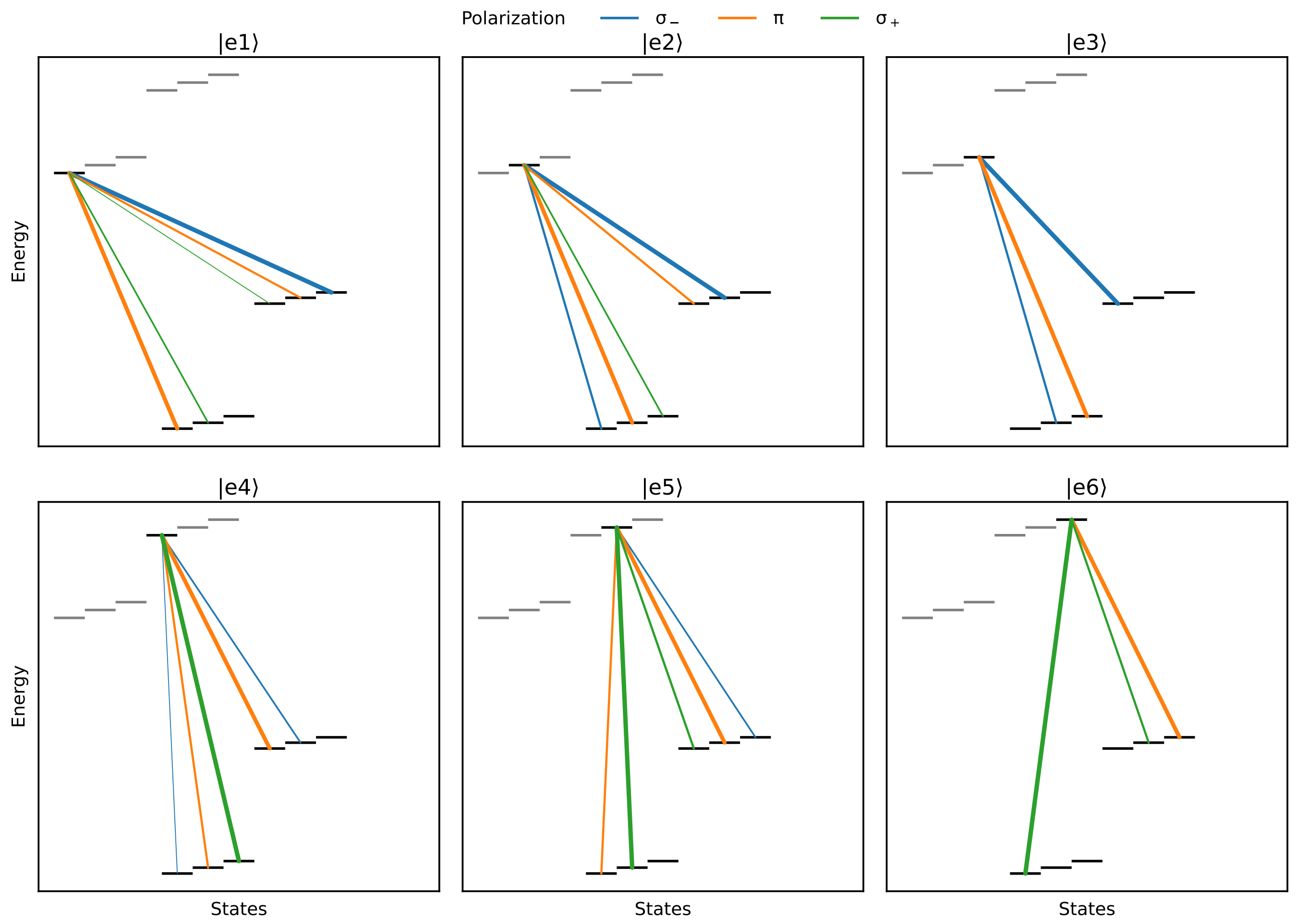

Figure 3.2: $P_{1/2} \leftrightarrow S_{1/2}$ **optical transitions between excited and ground states.** The individual panels display schematically all possible transitions, within the D_1 spectrum, between a single excited state (bold black line), see panel title, and the ground states. The strength of the individual transitions are qualitatively indicated by their line thickness and their polarization is color coded. This schematic overview allows to easily find possible three-level systems in lambda configuration, i.e. the ones coupling the lowest hyperfine states providing a coherent spin coupling.

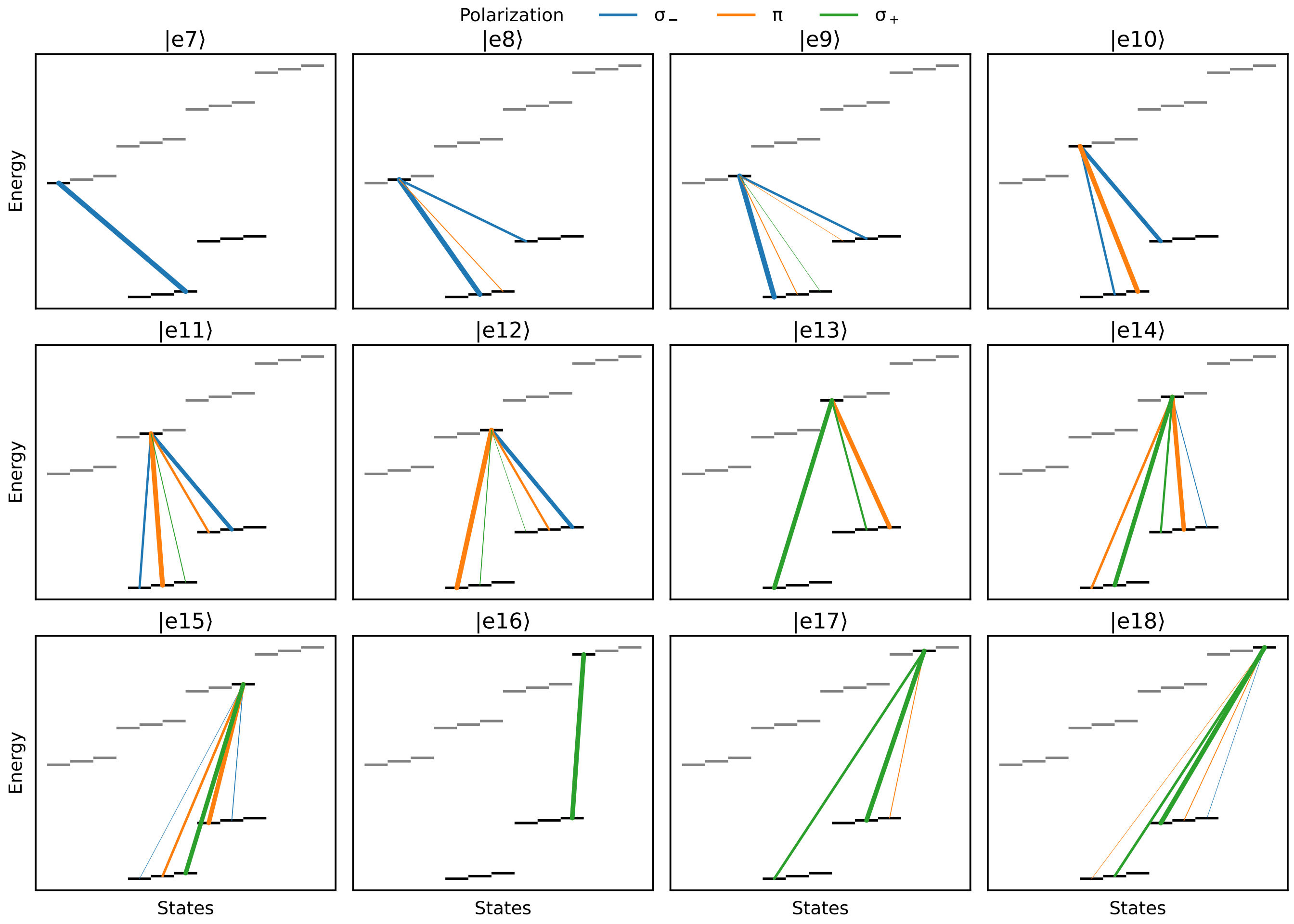

Figure 3.3: $P_{3/2} \leftrightarrow S_{1/2}$ **optical transitions between excited and ground states.** Equivalently to Fig. 3.2, here the possible transitions within the D_2 line spectrum are displayed. The panel titles indicate the excited state while the polarization of the transition is color coded and the transition strength is proportional to the line thickness.

As an additional visualization of the possible transitions in ^{6}Li, Fig. 3.2 and Fig. 3.3 show the possible optical transitions schematically, where the line thickness corresponds to the branching ratio and the color to the polarization of the emitted light.

In the following we would like to calculate both the dispersive and dissipative part of the atom-light interaction for these transitions, i.e. the dipole potential and the scattering rate. The classical atom-light interaction quantifies this interaction via the polarizability of the atom. In analogy to an electric dipole interacting with an electric field the induced dipole moment of the atom is

$$\mathbf{d} = \alpha \mathbf{E}\,, \tag{3.10}$$

with the polarizability α and the electric field $\mathbf{E}$. In a dilute medium this polarizability contributes to the polarization density $\mathbf{P} = N\mathbf{d}$ which determines its susceptibility via

$$\chi = \frac{N}{\epsilon_0}\alpha\,. \tag{3.11}$$

The optical susceptibility determines the refractive index and absorption of a medium implying the importance of the real and imaginary part of the polarizability. In the case of an atom interacting with an electromagnetic field the potential energy, i.e. dipole potential, of the induced dipole is

$$V = -\frac{1}{2}\mathbf{d}\cdot\mathbf{E}\,, \tag{3.12}$$

inserting the oscillating electric field and applying the Rotating-Wave approximation the dipole potential can be derived as

$$V = -\frac{I}{2\epsilon_0 c}\mathrm{Re}(\alpha)\,, \tag{3.13}$$

also known as the ac Stark shift. The repulsive and attractive limit of the dipole potential can again be understood in close analogy to a dipole, where depending on the detuning the dipole lags behind the field with an angle either aligned ($\Delta < 0$) or opposed ($\Delta > 0$) to the field leading to attraction or repulsion, respectively. The photon scattering rate for the atom interacting with a field can be derived from the radiated power from the atom

$$P_{\mathrm{rad}} = \int d\Omega\, r^2 \langle \mathbf{S} \rangle \cdot \hat{r} = \frac{|\ddot{d}|^2}{3\pi\epsilon_0 c^3}\,, \tag{3.14}$$

with the Poynting vector $\mathbf{S}$. Dividing the radiated power by the photon energy gives the scattering rate

$$R = \frac{P_{\mathrm{rad}}}{h\nu} = \frac{I}{\hbar\epsilon_0 c}\mathrm{Im}(\alpha)\,, \tag{3.15}$$

for a single resonance which is closely related to the absorption of a dilute medium.

Importantly, these results are only applicable for small intensities where the excited state population can be ignored. The saturation intensity I_s is introduced as an intensity scale which allows distinguishing between the previously discussed classical limit and the behavior at large intensities. The saturation intensity is defined as

$$I_{s,j} = \frac{\hbar^2 \epsilon_0 c \Gamma^2}{4 d_j^2}\,, \tag{3.16}$$

and the saturation parameter as

$$\frac{I}{I_{s,j}} = \frac{2\Omega_j^2}{\Gamma^2}, \tag{3.17}$$

where the index j represents the specific transition and Ω_j is the Rabi frequency of the transition. The index j is here used as an abbreviation of i, j, q used in Eq. 3.7. In order to take saturation effects into account the atom-light interaction has to be solved using the optical Bloch equations [72, 99]. This is considered the semiclassical solution to the atom-light interaction, where the light-field is still classical while the dipole becomes an operator. The Bloch equations are derived by using a density matrix operator $\hat{\rho}$ approach where the equations of motion can be deduced from the von-Neumann equation

$$\frac{\partial}{\partial t}\hat{\rho} = -\frac{i}{\hbar}\left[\hat{H}_A + \hat{H}_{AL}, \hat{\rho}\right]. \tag{3.18}$$

In the Rotating wave approximation the atom is described by H_A and the atom-light interaction by H_{AL}

$$H_A = -\hbar\Delta \left|e\right\rangle\left\langle e\right| \tag{3.19}$$

$$H_{AL} = \frac{\hbar}{2}\left(\Omega^* \left|g\right\rangle\left\langle e\right| + \Omega \left|e\right\rangle\left\langle g\right|\right), \tag{3.20}$$

with the detuning $\Delta = \nu - \nu_{eg}$ and the coupling between the ground and excited state given by the Rabi frequency Ω

$$\Omega(\mathbf{r}) = \frac{\langle\hat{d}\rangle\, E(\mathbf{r})}{\hbar} = |\Omega(\mathbf{r})| e^{i\phi(\mathbf{r})}. \tag{3.21}$$

The solutions of the resulting Bloch equations describe undamped oscillations of the atom population ρ_{ii} between the excited and ground-state at a frequency of $\Omega_r = \sqrt{\Omega^2 + \Delta^2}$, the generalized Rabi frequency. The damping of the oscillation, leading to the natural linewidth of the atomic transition is not described by these undamped optical Bloch equations (OBE). The OBEs are further refined by including the interaction of the atom with its environment, i.e. the open system. The consequence of interest here is the spontaneous emission which is one of the damping mechanisms which can be described with the Lindblad master equation [39, 100]

$$\frac{\partial}{\partial t}\rho = -\frac{i}{\hbar}\left[H_A + H_{AL}, \rho\right] + \sum_j \Gamma_j \left(L_j \rho L_j^\dagger - \frac{1}{2}\left\{L_j L_j^\dagger, \rho\right\}\right). \tag{3.22}$$

The Lindblad operator L_j for spontaneous emission is given by $L_j = \left|e\right\rangle\left\langle g_j\right|$, the rate of such an event is given by Γ_j.

In order derive the spectrum of a transition we are going to continue in the steady-state limit $\frac{\partial}{\partial t}\rho = 0$, i.e. at long times $t \to \infty$, of the damped oscillations. This allows solving the Lindblad master equation analytically for the steady-state excitation ρ_{ee} and the steady-state coherence ρ_{eg}

$$\rho_{ee} = \frac{\Omega^2/\Gamma^2}{1 + \frac{4\Delta^2}{\Gamma^2} + 2\frac{\Omega^2}{\Gamma^2}}, \tag{3.23}$$

$$\rho_{eg} = -\frac{i\Omega}{\Gamma}\frac{1 + i2\Delta/\Gamma}{1 + \frac{4\Delta^2}{\Gamma^2} + 2\frac{\Omega^2}{\Gamma^2}}, \tag{3.24}$$

with the detuning Δ, the Rabi frequency Ω and the natural linewidth Γ, i.e. the damping rate. The scattering rate is then the photon scattering out of the original light field via the excited state by spontaneous emission, given by

$$R = \Gamma\rho_{ee}\,, \tag{3.25}$$

where ρ_{ee} is the steady-state population of the excited state. Interestingly the absorption line shape contains the saturation intensity via

$$R_j = \Gamma\frac{1}{2}\frac{I/I_{s,j}}{1+4\Delta_j^2/\Gamma^2+I/I_{s,j}}\,, \tag{3.26}$$

which introduces the concept of power broadening. In this limit the strong coupling between atom and field increases the width of the transition to FWHM $= \sqrt{2}\Omega_j$. Importantly, the properties of the transition, i.e. its dipole matrix element, polarization dependence, selection rules, are included via its saturation intensity $I_{s,j}$ and detuning Δ_j. In the limit of weak intensities the line-shape is equivalent to the one given by the imaginary part of the polarizability α. The broadening in this limit is given by the decay rate Γ which is called homogeneous broadening. The susceptibility of the medium in the weak intensity approximation can also be related to the dipole matrix elements. The expectation value of the dipole operator is given by $\langle e|\,\hat{d}\,|g\rangle = d\cdot\rho_{eg}$ which means the coherences ρ_{eg} in the dipole matrix determine the susceptibility via

$$\chi = \frac{2Nd}{\epsilon_0 E}\rho_{eg}\,. \tag{3.27}$$

In the semiclassical picture the dipole potential felt by the atom can also be obtained from the optical Bloch equations. The equations of motion are simplified by comparing the internal oscillations at the generalized Rabi frequency $\Omega_r = \sqrt{\Omega^2+\Delta^2}$ and the motion of the atom which is slow. It is thus possible to assume that the internal dynamics have been damped on the external timescales due to the damping rate Γ, i.e. the steady-state. The dipole potential is then derived in the Heisenberg picture via the force $\mathbf{F}$ given by

$$\mathbf{F} = \frac{i}{\hbar}\left[H,\mathbf{p}\right]\,, \tag{3.28}$$

with $\mathbf{p} = -i\hbar\nabla$. We are thus interested in gradients of the atom-light interaction Hamiltonian which are only present in the Rabi frequency $\Omega(\mathbf{r})$, see Eq. 3.21. The gradient of the atom-light interaction Hamiltonian H_{AL} (the atomic Hamiltonian has no gradient) then gives two forces, i.e. the dipole and the radiation force given by

$$\langle\mathbf{F}\rangle = \frac{\hbar\Omega^*(\mathbf{r})}{2}\left(\nabla\log|\Omega(\mathbf{r})| - \nabla\phi(\mathbf{r})\right)\rho_{eg} + \text{c.c.} = \langle\mathbf{F}_{\text{dip}}\rangle + \langle\mathbf{F}_{\text{rad}}\rangle\,, \tag{3.29}$$

assuming the atom is slow w.r.t to the decay rate Γ. Inserting the coherence ρ_{eg} the force is

$$\langle\mathbf{F}\rangle = \frac{\hbar s(\mathbf{r})}{1+s(\mathbf{r})}\left(-\Delta\nabla\log|\Omega(\mathbf{r})| + \frac{\Gamma}{2}\nabla\phi(\mathbf{r})\right)\,, \tag{3.30}$$

with the saturation parameter s

$$s(\mathbf{r}) = \frac{|\Omega(\mathbf{r})|^2}{2\left((\Gamma/2)^2+\Delta^2\right)}\,. \tag{3.31}$$

The dipole potential can be derived from the force and is given by

$$V_j = \frac{\hbar\Delta_j}{2} \log\left[1 + \frac{I(\mathbf{r})/I_{s,j}}{1+4\Delta_j^2/\Gamma^2}\right] . \tag{3.32}$$

3.2.1 *Dissipation via Optical Pumping*

In this section we are going to use the previously derived scattering rate to characterize the transitions used for optical pumping in ^{6}Li at high magnetic fields. In particular, we are interested in the weak transitions which can be used to pump atoms from the ground-state manifold $|1\rangle, |2\rangle, |3\rangle$ used in the experiment to the low-field seeking ground states $|4\rangle, |5\rangle, |6\rangle$. These transitions are interesting for us since they provide a way of removing atoms from the system via the recoil kick $\mathbf{p_r}$ while simultaneously transferring them to an auxiliary state. The idea being that the fast atom, accelerated by the recoil kicks, is in a state $|5\rangle$ which does not interact with the superfluid pairs, i.e. $|1\rangle, |3\rangle$, and leaves the system since it is not trapped by the magnetic gradient. In Ch. 8 the effect of dissipation on transport through a non-interacting QPC is discussed. In Ref. [101] and Ch. 11 optical pumping was used to dissipate atoms from a superfluid without heating the system via secondary interactions.

Figure 3.4 shows all transitions between the $S_{1/2}$ ground-state manifold and the excited state manifolds $P_{1/2}$ (D_1) and $P_{3/2}$ (D_2). The spectrum was calculated at a magnetic field of $B = 692\,\mathrm{G}$ for the three different polarization's σ_+, σ_- and π. The detuning Δ_{D2} on the x-axis is calculated as the energy difference from the D2 line at zero magnetic field. The scattering rate on the y-axis calculated in the weak intensity limit. The spectrum shows that there are many additional transitions besides the shifted D1 and D2 lines which can be used for our purposes. Importantly, the mixing of hyperfine states already seen in Tab. 3.2 provides transitions between states of seemingly different nuclear magnetic moment m_I which cannot be changed by electric fields.

The optical pumping transition of interest for us is at a detuning $\Delta_{D2} \approx 2.95\,\mathrm{GHz}$ for σ_+ polarized light. This weak transition excites the ground-state $|1\rangle$ to the excited state $|e17\rangle$ which preferentially decays to the low field seeking ground-state $|5\rangle$. Figure3.5(a)-(b) shows the spectrum of this transition and of the nearby D2 line for comparison in Fig. 3.5(c)-(d). The excited state $|e17\rangle = |m_J = 3/2, m_I = 0\rangle - \delta_j |1/2, 1\rangle$ has several decay channels which are dominated by the emission into $|5\rangle = |1/2, 0\rangle + \epsilon_i |{-1/2}, 1\rangle$ with a branching ratio of $\Gamma_{e17,5}/\Gamma \approx 99.7\,\%$. The decay into the lowest hyperfine state $|1\rangle = |{-1/2}, 1\rangle - \epsilon_i |1/2, 0\rangle$ has a branching ratio of $\lesssim 0.3\,\%$. The reason being that the admixture to $|1\rangle$ is weak, i.e. $|1\rangle \sim \epsilon_i |1/2, 0\rangle$, while the decay happens preferentially to $|5\rangle \sim |1/2, 0\rangle$.

Importantly, the difference in branching ratio and equivalently in dipole matrix elements of the transitions has no effect on the linewidth of the transition at weak intensities. The homogeneous linewidth is always given by the inverse lifetime of the excited state. Conversely, the small dipole matrix element of the $|1\rangle \rightarrow |e17\rangle$ transition has a strong effect on the saturation intensity of the weak transition, see Fig. 3.5(b). The line-shape is calculated for different intensities below and above the saturation intensity of the D2 transition leading to power broadening of the strong D2 transition. The weak transition is not power broadened since its saturation intensity is large $I_s \approx 8.8\,\mathrm{kW/m^2}$. This becomes clear when relating the saturation intensity

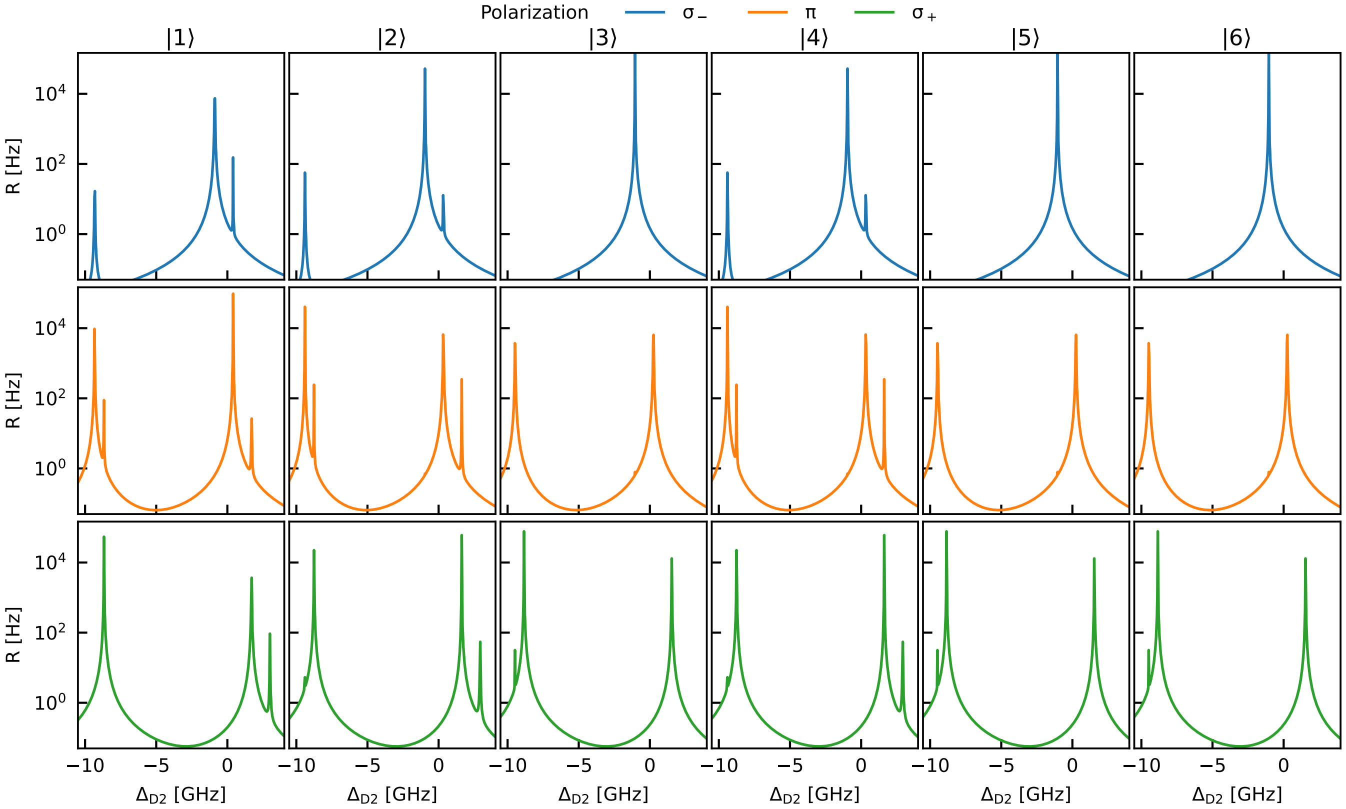

Figure 3.4: Scattering rate of $P_{3/2} \leftrightarrow S_{1/2}$ **optical transitions driven from ground to excited states.** Equivalently to Fig. 3.2 and Fig. 3.3, here the possible transitions in the D1 (around $\Delta_{D2} \sim -10$GHz) and D2 (around $\Delta_{D2} \sim 0$GHz) manifold are displayed. The scattering rates of the "weak" transitions are lower due to their lower dipole matrix element.

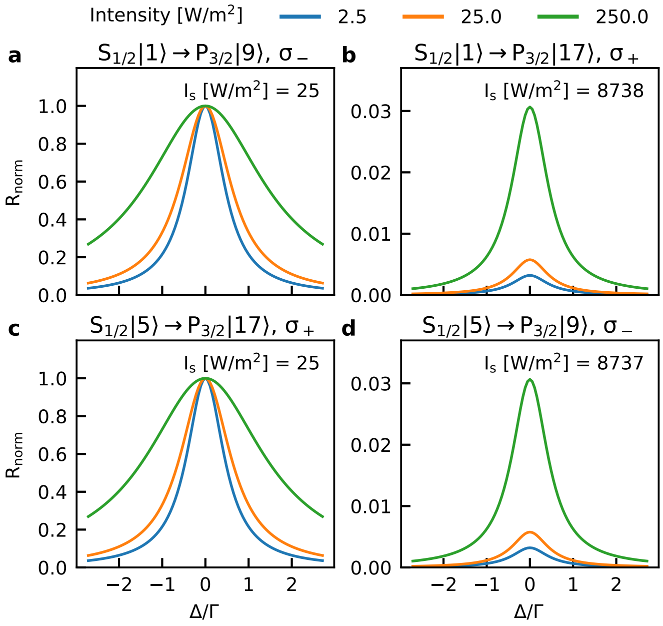

Figure 3.5: Optical pumping and power broadening. (a)-(d) show photon-atom scattering rates as a function of the detuning from the respective optical transition indicated in the title. The colors correspond to different optical intensities which have a distinct effect depending on the saturation intensity of the respective transition, displayed in each panel. The vertical axis is normalized by the peak scattering rate of the strong transitions presented in (a), (c) such that the weaker transitions presented in (b), (d) display the reduced scattering rate. We find that the weak transitions are homogeneously broadened $\sim \Gamma$ by the inverse lifetime of the excited state, while power broadening these transitions is difficult due to their large saturation intensity. The strong transitions (a), (c) display a broadening of $\sim \sqrt{\Omega}$ whenever $I/I_s > 1$. The difference in saturation intensity, i.e. spontaneous emission rates, between (a), (d) and (b), (c) implies optical pumping paths from $|1\rangle \to |5\rangle$ and vice-versa.

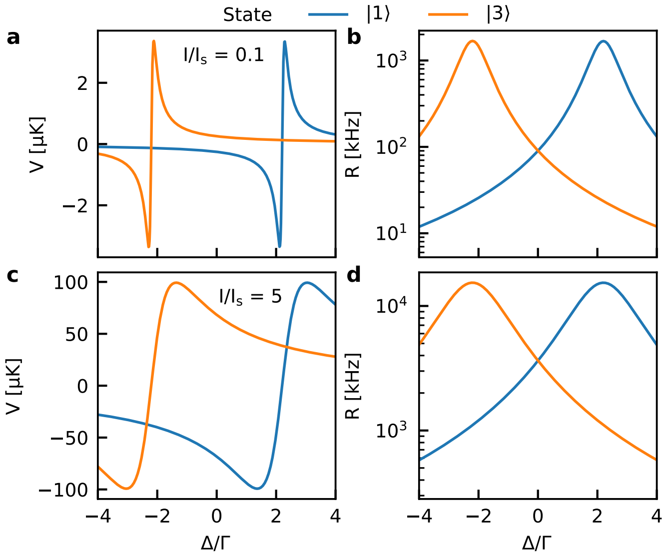

Figure 3.6: Optical dipole potential around the D2 transition. (a)-(b) display the optical dipole potential and the scattering rate for the lowest and third-lowest hyperfine state in lithium at $B = 568\,\mathrm{G}$, the zero-crossing of the hyperfine states' Feshbach resonance. Both quantities are calculated in the weak intensity limit for σ_- polarized light. The energy difference of the transitions leads to dipole potentials of opposite sign in-between the transitions. This effective Zeeman shift can be used to create spin-dependent optical potential, though the optical scattering rate will lead to continuous loss which has to be accounted for. (c)-(d) show the same calculation for strong intensities. In this limit the high intensity saturates the transition, i.e. the scattering rate approaches $\sim \Gamma/2$ for all detunings (see Eq. 3.26), while the dipole potential can continuously grow, though only logarithmically, see Eq. 3.32.

to the ability of observing Rabi oscillations between the two states involved in the transition. Due to the unfavorable branching ratios it requires remarkable intensities to drive Rabi oscillations which are not immediately damped via the decay to $|5\rangle$, i.e. to saturate the specific transition $\rho_{ee} \to 0.5$.

Figure 3.5(c)-(d) shows the equivalent transitions starting from the $|5\rangle$ state, where the figure panels on the diagonals describe two possible optical pumping configurations starting in different ground-states. Interestingly this kind of configuration where optical pumping is involving two accessible ground-states motivates the following discussion/application adding a second laser to form a three-level lambda system, see Sec. 3.3 and Ch. 9.

3.2.2 Spin-Dependent Potentials

The previously derived dipole potential is used here to calculate the optical dipole potential for the hyperfine states present in the Fermi gas. The particularly interesting regime is where the detuning of the light is chosen such that the spin-states of the system feel different optical potentials, i.e. an effective Zeeman shift. The experimental results when applying such a shift on a weakly interacting QPC is discussed in Ch. 8.

One possible configuration to create spin-dependent optical potentials is shown in Figure 3.6 for the lowest and third-lowest hyperfine state. The dipole potential is calculated for σ_- polarized light around the respective D2 transition for $|1\rangle$ and $|3\rangle$. At the center between the two transitions the dipole potentials have opposite sign leading to an effective Zeeman potential

$V_Z = V_1 - V_3$. This effective potential can be understood as a magnetic shift in z-direction, shifting the energy of the states depending on their alignment with the effective field. For the given intensity $I \approx 2.54\,\mathrm{W/m^2}$ the effective potential is around $\sim 0.5\,\mu\mathrm{K}$ which corresponds to an energy shift of $\sim 2E_F$. Increasing the intensity (see Fig. 3.6(c)-(d)) beyond the saturation intensity augments both the dipole potential and the scattering rate. Notably, in the high intensity limit the scattering rate at a given detuning is limited to the inverse lifetime of the excited state, while the dipole potential can grow logarithmically.

3.3 INTRODUCTION TO THREE-LEVEL SYSTEMS

In this section we expand the discussion of light-matter interaction to three-level systems in ^{6}Li at high magnetic fields. The coupling of an additional level with a new light field drastically alters the dispersion and dissipation behavior of the atom-light interaction, leading to a plethora of new applications like Raman spectroscopy, electromagnetically-induced-transparency [53], Raman transitions, subwavelength potentials [102] etc.

In the following we are going to introduce the different possible lambda systems and their properties. In addition, we introduce the weak probe solution of the three-level atom-light interaction and its consequences for our system. The applications of spin-rotations and subwavelength potentials are introduced in Ch. 9, while the experimental results when introducing a Dark state in a superfluid QPC will also be described in Ch. 9.

3.3.1 *Lambda Systems*

Here, we are mainly interested in the so-called lambda systems which are three-level-systems connecting two-states which are close-by in energy, i.e. within the radio-frequency range, via a third excited state which is energetically far away. In our case these lambda systems are made up out of two hyperfine ground-states from the $S_{1/2}$ manifold and one excited state from the $P_{1/2}$ or $P_{3/2}$ manifold. There are two types of lambda systems which are of particular interest here. The first being a lambda system connecting a state from the high field seeking ground-states with a state from the low-field seeking ground-states, e.g. $|1\rangle - |e17\rangle - |5\rangle$. The second being a lambda system made up of two high field-seeking states, e.g. $|1\rangle - |e2\rangle - |2\rangle$. Additional lambda-systems can be found in Tab. 3.3, Fig. 3.2 and Fig. 3.3.

The lambda systems we are interested in here have the peculiarity that the two involved transitions have considerably different dipole matrix elements. It is thus important to consider the application of the lambda system due to an implicit population trapping in the ground-state of the strong transition, see Sec. 3.3.2. The relative dipole matrix elements are given by

$$\tilde{d}_{qge} = \frac{|d_{qge}|}{\sum_{q,g} |d_{qge}|} \,. \tag{3.33}$$

For the lambda systems displayed in Fig. 3.7 and their counterparts in terms of transition strength the relative dipole matrix elements are

We find that the lambda system Λ_{15} is almost closed, i.e. the excited stay preferentially decays to the involved ground-states. The second lambda system Λ_{12} is not closed which means that it is important to keep the excited state population small such that spontaneous emission out of the system is suppressed. Figure 3.7 displays the lambda systems schematically.

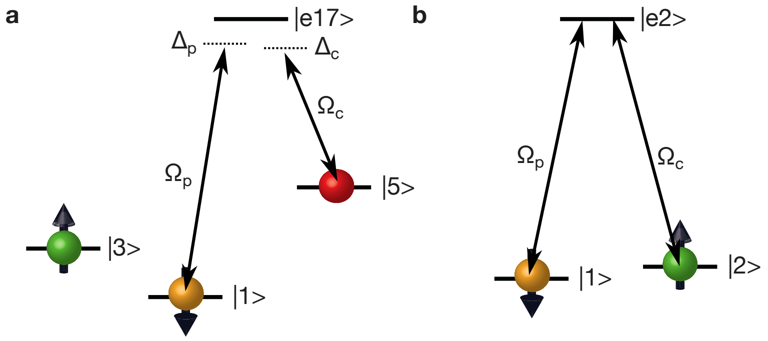

Figure 3.7: Three-level lambda systems at high magnetic fields in ^{6}Li. The lambda system sketched in (a) consists of two ground-states one of which is in the spin manifold $|1\rangle$, $|3\rangle$ of the interacting system. This system allows probing effects of three-level atom-light interaction in a differential way, where only one of the two states involved in the transport experiments are affected. The three-level system shown in (b) includes ground-states which are both part of the experimental spin-system. This system allows for spin-rotations between directly interacting spins and narrow Raman transitions allowing to probe the many-body spectrum of the interacting Fermi gas.

Λ_{15}	$\|1\rangle$	$\|5\rangle$	Λ_{12}	$\|1\rangle$	$\|2\rangle$
$\|e17\rangle$	5.1 (σ_+)	94.8 (σ_+)	$\|e1\rangle$	2.9 (π)	38.5 (σ_+)
$\|e9\rangle$	94.8 (σ_-)	5.1 (σ_-)	$\|e2\rangle$	39.7 (σ_-)	1.1 (π)

The choice of the system in Fig. 3.7(a) was motivated by the application of electromagnetically-induced-transparency (EIT) where the spin ground-state $|1\rangle$ becomes a dark-state and thus does not feel an optical potential at the EIT resonance. In order to probe the EIT spectrum it is useful to have a second ground-state which is not within the spin ground-state manifold since off-resonant scattering will lead to heating which in the case of a spin ground-state will be deposited in the atom cloud via the interactions. The second lambda system in Fig. 3.7(b) is chosen due to the involved ground-states. On the one hand this choice allows to have narrow Raman resonance since the involved ground-states have a common-mode energy shift due to the magnetic field which means fluctuations of the external magnetic field do not affect the energy splitting between the spin-states, i.e. the two-photon detuning is insensitive to the magnetic field. On the other hand it allows for rotations between two spin-states which can be made momentum dependent, see Ch. 9.

3.3.2 Electromagnetically Induced Transparency

In this section the optical susceptibility of the dilute atomic cloud is calculated in order to discuss the effects of a three-level atom-light interaction on the dispersion and absorption of the cloud. The susceptibility is derived by analytically solving the three-level atom-light interaction Hamiltonian in the weak probe limit $\Omega_p \ll \Omega_c$. The Hamiltonian is given by

$$H_\Lambda = -\frac{\hbar}{2}\begin{pmatrix} 0 & \Omega_p & 0 \\ \Omega_p & -2\Delta_p & \Omega_c \\ 0 & \Omega_c & -2(\Delta_p - \Delta_c) \end{pmatrix}, \tag{3.34}$$

with the basis given by $(|1\rangle, |e\rangle, |5\rangle)$. The probe Rabi frequency Ω_p quantifies the coupling for the $|1\rangle - |e\rangle$ transitions while the control Rabi frequency Ω_c gives the $|5\rangle - |e\rangle$ coupling. The detunings Δ_p and Δ_c are the single photon detunings from the individual transitions. The two photon detuning is defined as $\delta = \Delta_p - \Delta_c = \omega_{5e} - \omega_{1e} + \omega_p - \omega_c$ which becomes resonant when the light frequency difference matches the ground-state energy difference, independently of the absolute frequency of the light. This resonance condition $\delta = 0$, called two-photon resonance, allows Raman spectroscopy far detuned from the excited state, i.e. allowing an adiabatic elimination of $|e\rangle$.

Diagonalizing the Hamiltonian at the two-photon resonance gives the eigenstates and their energies which can be expressed in terms of their mixing angles $\theta = \arctan(\Omega_p/\Omega_c)$ and ϕ. Importantly there exists an eigenstate which has no contribution from the excited-state and has zero energy, its energy is independent of the Rabi frequencies and single photon detuning Δ, since the Dark state requires $\delta = 0$. This dark-state is given by

$$|D\rangle = \cos\theta\,|1\rangle - \sin\theta\,|5\rangle\ , \tag{3.35}$$

while the bright states $|\pm\rangle$ retain a contribution of the short-lived excited state $|e\rangle$ allowing light scattering. In addition, the bright states are energy shifted from zero by $E_\pm = (\Delta \pm \sqrt{\Delta^2 + \Omega_p^2 + \Omega_c^2})/2$, with $\Delta = \Delta_p = \Delta_c$. The energy of the dark-state implies that it does not feel an optical potential from the light fields, while the eigenstate structure does not allow light scattering via spontaneous emission, thus the state is dark.

Analogously to previous calculations for the two-level system, the three-level system can be solved analytically in the weak probe approximation. First the master equation for the three level system is used to derive the optical Bloch equations which then are simplified via perturbation of first order in Ω_p. The master equation is given by

$$\partial\hat{\rho}/\partial t = -\frac{\hbar}{i}[H, \hat{\rho}] + \begin{pmatrix} \Gamma_{e1}\rho_{ee} & -\Gamma_{e1}\rho_{1e}/2 & 0 \\ -\Gamma_{e1}\rho_{e1}/2 & -(\Gamma_{e1}+\Gamma_{e5})\rho_{ee} & -\Gamma_{e5}\rho_{e5}/2 \\ 0 & -\Gamma_{e5}\rho_{5e}/2 & \Gamma_{e5}\rho_{ee} \end{pmatrix}\ , \tag{3.36}$$

with the spontaneous emission rates from excited state to the respective ground-states Γ_{e1} and Γ_{e5}. The optical Bloch equations for the coherences – determining the susceptibility – are then given by

$$\dot{\rho}_{e1} = (i\Delta - \Gamma e)\rho_{e1} + i\Omega_p(\rho_{ee} - \rho_{11}) - i\Omega_c\rho_{51}\ , \tag{3.37}$$

$$\dot{\rho}_{51} = i\Delta\rho_{51} + i\Omega_p\rho_{5e} - i\Omega_c\rho_{e1}\ , \tag{3.38}$$

$$\dot{\rho}_{5e} = -\Gamma_e\rho_{5e} - i\Omega_c(\rho_{ee} - \rho_{55}) + i\Omega_p\rho_{51}\ , \tag{3.39}$$

with $\Gamma_e = (\Gamma_{e1} + \Gamma_{e5})/2$. To zeroth order in Ω_p, i.e. $\Omega_p = 0$ these equations correspond to the optical pumping configuration seen previously, i.e. in the steady state $\rho_{11}^{(0)} = 1$, $\rho_{ee}^{(0)} = 0$, $\rho_{55}^{(0)} = 0$ and $\rho_{ij}^{(0)} = 0$ for $i \neq j$. In first order Ω_p, i.e. weak probe approximation, the optical Bloch equations are

$$\dot{\rho}_{e1}^{(1)} = (i\Delta - \Gamma e)\rho_{e1}^{(1)} + i\Omega_p(\rho_{ee}^{(0)} - \rho_{11}^{(0)}) - i\Omega_c\rho_{51}^{(1)}\ , \tag{3.40}$$

$$\dot{\rho}_{51}^{(1)} = i\Delta\rho_{51}^{(1)} + i\Omega_p\rho_{5e}^{(0)} - i\Omega_c\rho_{e1}^{(1)}\ , \tag{3.41}$$

$$\dot{\rho}_{5e}^{(1)} = -\Gamma_e\rho_{5e}^{(1)} - i\Omega_c(\rho_{ee}^{(1)} - \rho_{55}^{(1)}) + i\Omega_p\rho_{51}^{(0)}\ . \tag{3.42}$$

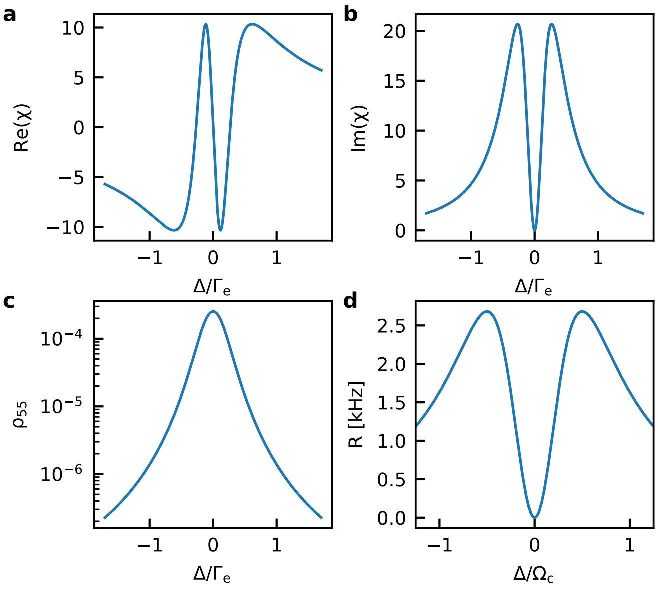

Figure 3.8: Resonant EIT spectrum and steady-state populations. (a)-(b) shows the real and imaginary part of the optical susceptibility χ of the probe transition as a function of the probe detuning Δ. The spectra are calculated in the weak probe approximation $\Omega_p \ll \Gamma_e$ and for a resonant single photon detuning $\Delta_c = 0$. The real part of the susceptibility shows a negative slope on resonance indicating the possibility of slowing light, while the imaginary part shows the typical absorption dip indicative of the electromagnetically induced transparency. The steady-state population of the ground-state $|5\rangle$ displayed in (c) indicates the imbalance of dipole matrix elements of the involved transitions. (d) The scattering rate displays the broadening of the transparency window by Ω_c, as indicated by the scale of the x-axis. Each individual peak is still broadened by Γ_e.

This set of equations can be solved for the probe field coherence ρ_{e1}

$$\rho_{e1} = \frac{-\Delta}{\Omega_c^2 - \Delta^2 - i\Delta\Gamma_e}\Omega_p + O(\Omega_p^2), \tag{3.43}$$

which in turn gives the probe susceptibility via $\chi = \frac{2Nd_{e1}}{\epsilon_0 E_p}\rho_{e1}$.

The two main observations from the susceptibility are the dip in the absorption spectrum, see Fig. 3.8(b), i.e. the signature of EIT and the slope of the dispersive response $\mathrm{Re}(\chi)$ in Fig. 3.8(a). The dispersive response is directly related to the group velocity of the light field which means that light can be slowed in the EIT transparency window [53, 103].

For us the effect on the atom is of more interest, i.e. the reduction of scattering rate in the transparency window shown in Fig. 3.8(d). The optical Bloch equations are solved numerically in the steady-state limit $t \to \infty$ with all initial population in state $|1\rangle$, to obtain the behavior of the system independently of the intensity of the probe beam. Figure 3.8(c)-(d) show the solutions of the equations for the steady-state population of state $|5\rangle$ and the scattering rate $R = \Gamma_e \rho_{ee}$, representing the bright-state population. The spectra are obtained for a resonant single photon detuning $\Delta_c = 0$, with $\Delta = \Delta_p$ and Rabi frequencies of $\Omega_c = \Gamma_e/2$ and $\Omega_p \ll \Gamma_e$ in the weak probe limit. The interesting observation here is that the previously noted large difference between the dipole matrix elements of the probe and control transitions is reflected in the steady-state population of the second

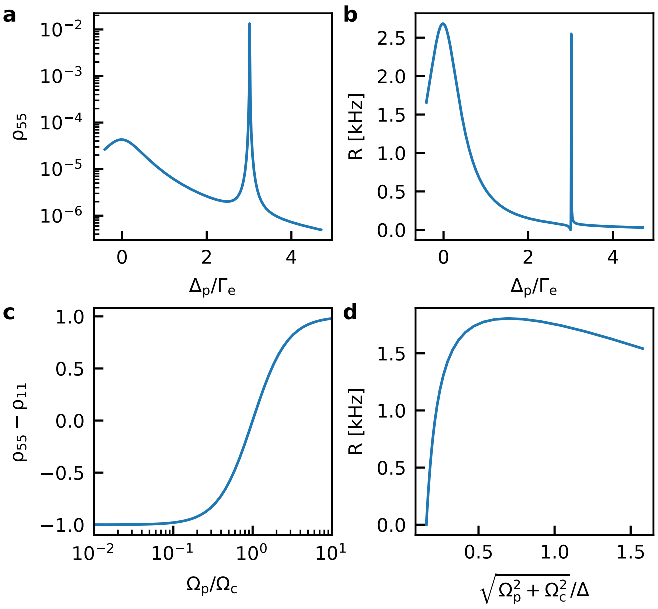

Figure 3.9: Off-resonant lambda system excitation spectrum and steady-state population. The off-resonant spectrum (a)-(b), i.e. $\Delta_c = 3\Gamma_e$, shows the broad single photon transition at $\Delta_p = 0$ as well as the narrow two-photon peak at $\Delta_p = \Delta_c$. Again the population of the auxiliary ground-state $|5\rangle$ is low due to the unequal dipole elements, while width of the transition is reduced compared to the transparency window in Fig. 3.8(b). (c)-(d) show the steady-state populations of the ground-states (c) and the excited state (d) where $R = \Gamma_e \rho_{ee}$. The ground-state population displays the expectation that the mixing angle is proportional to the ratio of Rabi frequencies. The scattering rate indicates the population of the excited state in the bright-state which is decreasing for large Rabi frequencies.

ground-state $|5\rangle$. The mixing angle for the lambda system $|1\rangle - |e17\rangle - |5\rangle$ displayed in Fig. 3.7(a) is given by

$$\theta = \arctan\left(\frac{\Omega_p}{\Omega_c}\right) = \arctan\left(\frac{\sqrt{I_p}\,d_p}{\sqrt{I_c}\,d_c}\right) \approx \arctan\left(\frac{1}{20}\sqrt{\frac{I_p}{I_c}}\right), \tag{3.44}$$

implying that for the experimental realization the probe intensity I_p has to be much larger than the control intensity I_c to reach an equal superposition of the two ground-states. The fact that population remains in the initial state in the weak probe limit also helps, in that switching on the control beam can be seen as a pure transparency effect since changes of the dark-state admixture are not expected. On the other hand this also means that in order to achieve coherent rotations between the involved ground-states large probe intensities are necessary. This will lead to more off-resonant scattering from other, close-by single photon transitions. One way to overcome this is to detune from the single-photon resonance $\Delta = 0$ while keeping the two-photon transition resonant $\delta = 0$.

Figure 3.9(a)-(b) shows the spectrum of the lambda system for off-resonant excitation, i.e. $\Delta_c = 3\Gamma_e$ and $\Omega_c = \Gamma_e/2$ in the weak probe limit. The spectrum includes the broad resonance due to optical pumping at $\Delta_p = 0$ and the narrow Raman transition at $\Delta_p = \Delta_c$. This behavior is reflected in the scattering rate R (see Fig. 3.9(b)) where the incoherent optical pumping leads to a larger scattering rate compared to the coherent Raman transition at the two-photon detuning $\delta = 0$. The population of the two ground-states at the two-photon resonance $\delta = 0$ is displayed in Fig. 3.9(c), calculated as a function of the Rabi frequency ratio Ω_p/Ω_c. The states are equally populated at $\Omega_c = \Omega_p$ which would be achieved at an intensity ratio of $I_p/I_c = 400$. The scattering rate shown in Fig. 3.9(d) shows that the scattering rate is maximal when the admixture of the excited state to the bright-state is maximal.

Importantly, the mentioned downsides of the lambda system given by $|1\rangle - |e17\rangle - |5\rangle$ in terms of dipole element differences can be completely inverted by using the equivalent, symmetric lambda system $|1\rangle - |e9\rangle - |5\rangle$ which involves σ_- polarized light. In this lambda system the probe transition $|1\rangle - |e9\rangle$ has a large dipole matrix element while the control transition has a small dipole matrix element. Thus using this system would give a mixing angle of

$$\theta = \arctan\left(\frac{\Omega_p}{\Omega_c}\right) \approx \arctan\left(20\sqrt{\frac{I_p}{I_c}}\right) , \tag{3.45}$$

such that weak probe intensities would be required to achieve rotations between the two states.

Beyond these calculations it is possible to include all states of the hyperfine manifold of lithium at high magnetic fields to take into account off-resonant excitations and their influence on the three-level system of interest. The theory behind these calculations is presented in Ref. [104], which will allow to get a better understanding of multi-level systems in lithium. In addition, up to now the linewidth of the lasers and magnetic field fluctuations have not been taken into account. The theoretical considerations for including these effective fluctuations of the energies of the ground-states are discussed in Ref. [105].

4

INTRODUCTION TO SUPERFLUID TRANSPORT

CHAPTER CONTENTS

Superfluid and superconducting transport is the cornerstone of many intriguing transport processes such as the Josephson effect [8, 106] or Andreev reflections [42, 107]. Here, we want to provide an introduction to several effects in superfluid and superconducting transport. The main microscopic pictures discussed are, on the one hand, the multiple Andreev process which has been used to describe previous experiments [38] and ,on the other hand, the so-called phase-slips which are considered to be one of the main dissipation mechanisms in superconductors [108]. In this sense both effects are important to compare to our observations discussed in Ch. 11, Ch. 10 and Ch. 9. The words superconducting and superfluid are in most cases interchangeable for the discussion here, wherever this it not the case it will be indicated.

In Sec. 4.2 we are going to introduce several concepts of superfluid transport such as the current-phase relation which help to understand the different transport settings one can find in experiments. Then the effects of a pure phase bias, i.e. the DC Josephson effect, is discussed in Sec. 4.3 followed by the case of a chemical potential bias and its implications on the transport in Sec. 4.4. Finally, a terse overview of superfluid transport between fermionic two-terminal quantum gases is provided in Sec. 4.5.

4.1 DEFINITION OF SUPERFLUIDITY

From a transport perspective the definition of superfluidity is the frictionless flow of a non-viscous liquid through a pipe or capillary [41]. Implying that there is no movement of the superfluid whenever a capillary would be moved through a stationary superfluid. If the liquid is not at zero temperature there are excitations above the superfluid ground-state which behave like a normal gas. This normal gas will have friction with the capillary and thus will be accelerated via interactions with the surface. Importantly, the two-fluids do not exchange momentum with each other [41]. This model of two-fluids is characterized by their density given by

$$\rho = \rho_n + \rho_s \,, \tag{4.1}$$

the sum of superfluid ρ_s and normal density ρ_n. The phase transition from normal to superfluid takes place whenever $\rho_s \neq 0$ such that the total liquid has some superfluid properties. In the zero temperature limit $T = 0$ the normal density is zero $\rho_n = 0$ and the gas is completely superfluid.

Starting from the density of the liquid the current in a two-fluid model can be expressed as

$$\mathbf{j} = \rho_s \mathbf{v}_s + \rho_n \mathbf{v}_n \,, \tag{4.2}$$

where the superfluid part behaves ideal, i.e. it does not carry entropy and does not produce entropy while being transported. The entropy is transported by the normal fraction, either in terms of collective excitation waves, like phonons or rotons or in terms of particle excitations, like quasi-particles. In addition, the Landau two-fluid model assumes the superfluid flow to be irrotational

$$\nabla \times \mathbf{v}_s = 0 \,. \tag{4.3}$$

Finally, Landaus two-fluid model includes a critical velocity v_c beyond which the flow is no longer dissipationless. Within the two-fluid model the critical velocity is defined via the exchange of momentum and energy of the superfluid with an interface. It is assumed that the exchange can only take place whenever the momentum/energy of the obstacle matches exactly the energy of an elementary excitation of the superfluid, whenever the velocity of the superfluid is non-zero this condition is fulfilled at lower momenta. The critical velocity in terms of the Landau criterion is defined as

$$v_c = \left.\frac{E(p)}{p}\right|_{\min} \,. \tag{4.4}$$

Before introducing more concepts of superfluid transport and clarifications beyond the two-fluid model, i.e. the macroscopic wavefunction, vortices, phase-slips etc. the superfluidity discussed here is put in context with our experimental system.

4.1.1 *Unitary Fermi Gas*

The experiments presented here will be focused on the region of the BEC-BCS crossover around the Feshbach resonance. This region of crossover is described by the unitary Fermi gas [65]. In this region the s-wave scattering length a of the atom interaction diverges as can be seen in Fig. 4.1(b) and the properties of the system can be quantified by a single dimensionless parameter $1/k_F a$. Around the broad resonance the strongly interacting Fermi gas shows a universal behavior. As a consequence of the universality the equation of state does not depend on microscopic properties of the system but only on T/T_F and $1/k_F a$. In the limit of $1/k_F a \ll -1$ the unitary Fermi gas connects to the BCS superfluid limit, while at $1/k_F a \gg 1$ it connects to the BEC of molecules, see Fig. 4.1(a).

Superfluidity in the unitary Fermi gas is achieved via pairing of spin-half fermions to Cooper pairs which then can form a macroscopic wavefunction, similarly to the BCS limit. Notably, the pair-size here is on the order of the particle spacing which makes the unitary gas highly correlated and difficult to treat theoretically. The critical temperature for the superfluid to normal transition of the unitary Fermi gas is a universal value, given by $T_c/T_F \approx 0.167$ [66, 109] in the homogeneous gas. In a harmonic trap the critical

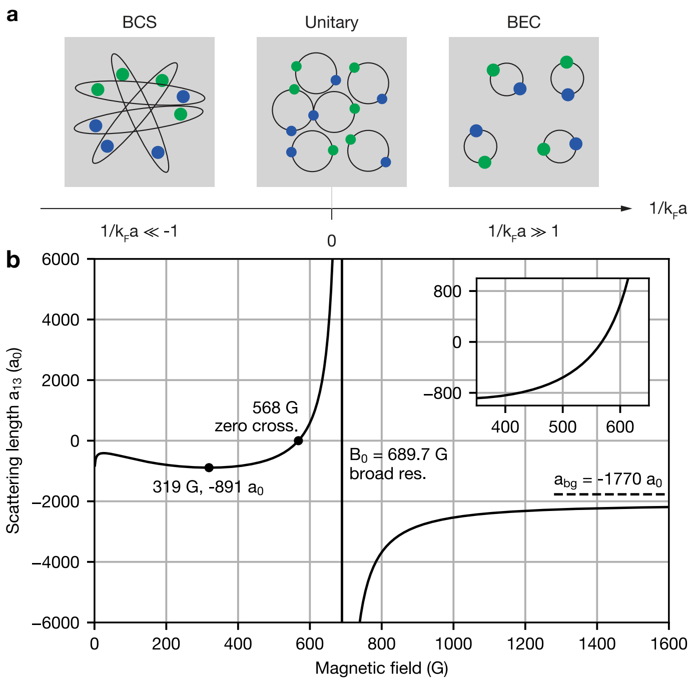

Figure 4.1: BEC-BCS crossover and Feshbach resonance in ^{6}Li. (a) Illustration of the particle density and the pair-size across the BEC-BCS crossover. S-wave scattering length as a function of magnetic field (b) for the $|1\rangle - |3\rangle$ mixture of ^{6}Li. The unitary Fermi gas is located around the resonance, where the scattering length diverges $B_0 = 689.7\,\mathrm{G}$. The BCS limit can be found for $B > B_0$ while the BEC limit is located between B_0 and the zero crossing of the scattering length at $B = 568\,\mathrm{G}$. Weak attractive and repulsive interactions $a_{13} = \pm 800 a_0$ can be explored around this zero crossing. Adapted from Ref. [71].

temperature is $T_c/T_F \approx 0.21$ [110] where T_F is the Fermi energy in the trap. Equivalently, the critical entropy in the trap is larger $S_c \approx 1.6Nk_B$ than the homogeneous value $S_c \approx 0.7Nk_B$. The universal gap of the unitary superfluid is given by $\Delta \approx 0.44E_F$ [111] where E_F is the Fermi energy.

4.1.2 Superfluidity – Microscopic

The discussion of superfluidity can be refined by introducing a more microscopic description in terms of a wavefunction and pairing between fermions. Even for small attractive interactions two fermions can form a bound state, i.e. a Cooper pair, which is stabilized by the Pauli blocking. This results in the whole gas changing its phase which is called Cooper instability [112] since the gas is instable in the presence of pairing [16]. The wavefunction of the newly formed state, i.e. the BCS wavefunction, is then given by

$$|\psi\rangle = \prod_k (u_k + v_k c^\dagger_{k\uparrow} c^\dagger_{-k\downarrow}) \, |0\rangle \; , \tag{4.5}$$

with $u_k = \sqrt{N_p}\phi_k u_k$ and $|u_k|^2 + |v_k|^2 = 1$. The parameter v_k^2 gives the probability of occupation of the pair state $(\mathbf{k}, -\mathbf{k})$ while u_k^2 the occupation of the corresponding hole state. The wavefunction describes a product of two fermions pairing in a single momentum state $(\mathbf{k}, \uparrow, -\mathbf{k}, \downarrow)$. The previously mentioned superfluid gap Δ is then the energy of the bound-state defined as $\Delta = \frac{V_0}{\Omega} \sum_k \langle c_{k\uparrow} c_{-k\uparrow} \rangle$, i.e. the energy necessary to break a pair.

The superfluid is forming due to the presence of off-diagonal long-range order in the system, quantified by

$$\langle \psi^\dagger_\uparrow(\mathbf{r}_2 + \mathbf{r}) \psi^\dagger_\downarrow(\mathbf{r}_1 + \mathbf{r}) \psi_\uparrow(\mathbf{r}_1) \psi_\uparrow(\mathbf{r}_2) \rangle \; , \tag{4.6}$$

which has to be finite at long distances $r \to \infty$. Here the long-range order refers to Cooper pairs being in the condensate. The order parameter can then be defined via the expectation value of finding such pairs in the condensate

$$\Delta(\mathbf{R}) \sim \langle \psi^\dagger_{k\uparrow} \psi^\dagger_{-k\downarrow} \rangle \; , \tag{4.7}$$

with the center of mass coordinate $\mathbf{R} = (\mathbf{r}_1 + \mathbf{r}_2)/2$. An order-parameter in general quantifies when a phase is ordered, it is non-zero in the phase and zero outside the phase, for example the magnetization in the case of a ferromagnet. For superfluids the order-parameter is often used synonymously with the gap though they are only equal in the BCS limit [113]. The phase of the order parameter ϕ will be later important since it provides the potential for a superfluid velocity.

At a finite temperature the superfluid state will have excitations introduced which modify its bare gap Δ_0 such that it becomes zero at the transition temperature T_c/T. Importantly, the excitations of a fermionic superfluid can be of single particle or collective origin. The single particle excitation is related to the breaking of a Cooper pair and the related creation of quasiparticles above the gap. These excitations require a minimal energy given by the gap Δ which implies that single fermions cannot enter the superfluid, i.e. there is a phase-separation between paired and spin-polarized fermions [114]. This phenomenon also has significant influence on transport between spin-imbalanced gases [67]. There is no phase separation between normal and superfluid constituents of the gas. The second type of excitations are collective excitations which are gapless, massless density oscillations, i.e. Goldstone modes. Notably, these excitations have a linear dispersion relation and can therefore carry entropy even at temperatures below the pairing gap [113], though only diffusively. These collective excitations are often called the second sound of the gas [22, 24, 28]. Finally, the second type of collective excitations present in superfluids, i.e. the Higgs mode, is a gapped massive collective excitations [115] which can decay into other excitations. The energy dependence of the collective excitations are different in superconductors and superfluids due to the Anderson-Higgs mechanism [116]. In superconductors the Goldstone mode is shifted up in energy by the so-called plasmon frequency.

4.2 CONCEPTS IN SUPERFLUID TRANSPORT

In this section the previously introduced properties of superfluidity are used to introduce concepts like the excess current, weak links etc. which are important for the following discussions in this thesis.

Superfluid Current – Current-Phase Relation

The macroscopic wavefunction of the superfluid has a phase ϕ which encompasses its spatial dependence. Thus, the current density in a superfluid is given by

$$\mathbf{j}_s = \frac{i\hbar}{2m}(\Psi\nabla\Psi^\dagger - \Psi^\dagger\nabla\Psi) = \frac{\hbar}{2m}n_s\nabla\phi\,, \tag{4.8}$$

where n_s is the superfluid fraction and ϕ is the phase of the order-parameter. The current can flow dissipationless since it is characterized by the equilibrium wavefunction Ψ [41]. The current-phase relation shows that superfluid transport can be driven by a phase bias which is not possible in a normal Fermi liquid. This relation is the underlying reason for transport phenomena like the Josephson effect.

Critical Current

The superfluid current as previously introduced, is related to the phase gradient of the superfluid $\nabla\phi$ and the superfluid density n_s. The superfluid velocity can then be related to the phase gradient via $j_s = n_s v_s$ and $\mathbf{v}_s = \frac{\hbar}{2m}\nabla\phi$. The critical current I_c, or pair-breaking current, is then given by the current at which superfluidity can no longer be maintained. This can be understood from a free energy argument where with increasing velocity of the pairs v_s their density n_s decreases which will lead to breakdown of superfluidity [117, 118]. An alternative picture is that the quasi-particle energies get shifted by the superfluid velocity such that above the critical velocity v_c excitations can form without energy cost [7]

$$v_c = \frac{\Delta}{\hbar k_F}\,. \tag{4.9}$$

Coherence Length

The presence of the phase in the superfluid order-parameter also gives rise to a new length-scale in the system. The coherence length of the superfluid $\xi \sim \hbar v_F/\Delta$ is the length scale over which the phase is allowed to vary, while

Parameter		Value
Critical temperature uniform	T_c/T_F	$\simeq 0.167$
Critical temperature harmonically trapped	T_c/T_F	$\simeq 0.21$
Superfluid gap	Δ	$\simeq 0.44E_F$
Healing/coherence length	ξ	$\simeq 0.6/k_F$
Pair coherence length	ξ_{pair}	$\simeq 1/k_F$

Table 4.1: Properties of the unitary superfluid at zero temperature [65].

for changes of the phase over shorter ranges superfluidity will break down. This coherence length is often called healing length of the superfluid. Importantly in transport configurations the healing length is also an indicator of the validity of a hydrodynamic treatment of transport [113]. Whenever a junction is wider than the healing length the hydrodynamic picture is expected to hold. The reason being that the wavefunction cannot be squeezed smaller than the coherence length in order to fit through a narrow constriction.

Weak Links

There has been a tremendous amount of theory work on weak links [8, 119] over the last 50 years. The general and very broad definition of a weak link is that the critical current inside the link is much smaller than the critical current of the two terminals connected by the link

$$I_{c,link} \ll I_{c,bulk} \,. \tag{4.10}$$

Importantly, the weak-link is distinct from a junction which provides a tunnel coupling between two reservoirs. The weak link separates two superfluid reservoirs with a macroscopic wavefunction that have equal wavefunction amplitudes but distinct phases. The link will only act as a perturbation to the wavefunctions allowing them to become phase coherent. This kind of structure can show up in many different systems. The prototypical example is a superconducting-normal-superconducting (SNS) interface where the wavefunctions of the superfluid penetrate the normal region and overlap partially such that their interference leads to a phase equilibration. Another example is a Dayem bridge [120], which has uniform critical current density j_c but a much smaller total current $I_{c,link} \ll I_{c,bulk}$ in the weak link which can be achieved by a constriction with size on the order of the coherence length ξ [118].

4.3 JOSEPHSON EFFECT

The Josephson effect is one of the fundamental processes in superfluid transport. Though first predicted for tunnel junctions [106] it has been also extensively studied in weak links [8]. The underlying mechanism is the macroscopic nature of superfluidity which encompasses a superfluid phase which can drive a current. The phase of the order-parameter implies a 2π periodicity of the supercurrent and the supercurrent can only flow whenever there is a phase gradient across the link, i.e. $I_s(n\pi) = 0$. Since the current is also

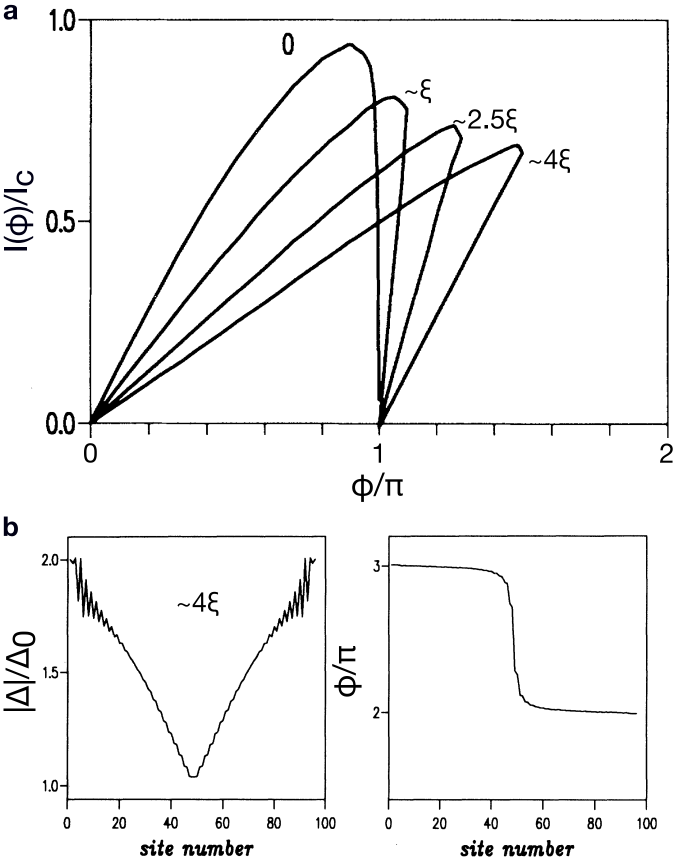

Figure 4.2: Current-phase relation of a long weak-link. (a) displays the current-phase relation $I(\phi)$ for a weak link of different lengths $l = 0 \ldots 4\xi$ at a transparency of $\alpha = 1$. For lengths $l > \xi$ the current-phase relation becomes multivalued, indicating a second solution to the phase relaxation via phase-slip centers. (b) Order parameter and its phase as a function of space at finite temperature $T = T_c/2$ for the phase-slip solution. The order-parameter has a node at the phase-slip center, where the phase drops by 2π. The small oscillations are at $\lambda_F/2$ due to the particles phase coherence. Figure adapted from Ref. [121].

symmetric around $\phi = 0$ [8], a phase difference ϕ across a weak link gives a sinusoidal relationship between the current and phase

$$I_s = I_c \sin\phi\,, \tag{4.11}$$

where I_c is the critical current. In addition, the phase between the reservoirs is related to their voltage difference via

$$\dot{\phi} = \frac{1}{\hbar}\Delta\mu\,. \tag{4.12}$$

Depending on whether a voltage is applied to the junction or not the supercurrent is either constant (DC) or oscillates (AC). In most situations the current-phase characteristic of the DC Josephson effect can have shapes beyond the simple sine [119]. Notably, a pure phase bias will not drive any other current than a supercurrent and there will be no voltage drop at the junction [8].

4.3.1 Multivalued Current-Phase Relation

Here, we are interested in the DC Josephson effect and the change of the current-phase relation for varying junction lengths. The limit of multivalued current-phase relations is of particular interest because it illustrates a way of introducing dissipation into superfluid transport. Where dissipation is related to the flow not being a pure supercurrent anymore, i.e. there is resistive behavior. Figure 4.2(a) shows the current-phase relation of a weak link for different lengths l, in multiples of the coherence length ξ. Whenever the length of the junction becomes larger than ξ there exist two current solutions at each phase value, i.e. the current-phase relation becomes multivalued. To understand how the I-ϕ relation can become multivalued the case of a one-dimensional junction of length l can be considered. In the limit where $l < \xi$ the phase between the two superfluids can only vary linearly in the link, i.e. the normal DC Josephson effect. In the second limit where $l > \xi$, a second solution is possible where the phase is relaxed non-adiabatically via a phase slip [8, 122, 123], shown in Fig. 4.2(b). This phase-slip solution is present for $\phi > \pi$ and is concurrent with a node of the order-parameter in the link. The dependence on the coherence length originates from the fact that below the coherence length variations of the order-parameter are not possible, thus phase-slips can only enter the weak link whenever it is longer than the coherence length.

4.4 SUPERFLUID TRANSPORT WITH A VOLTAGE BIAS

In our experiment instead of a phase bias a voltage bias is applied, in the form of a chemical potential bias $\delta\mu$. This bias configuration is quite different to the previously discussed phase bias since it can drive the system out-of-equilibrium, mainly due to the excitations experiencing a bias [7, 118]. Depending on the normal resistance of the junction a normal current is able to flow and interact with the supercurrent. The voltage bias at the weak link will induce a time dependence of the superfluid phase given by

$$\dot{\phi} = \frac{1}{\hbar}\Delta\mu\,. \tag{4.13}$$

This results in an oscillation of the current at a frequency f [8]

$$f = \frac{1}{h}\delta\mu\,, \tag{4.14}$$

disregarding possible impedance's (for example a capacitance) of the weak link the phase-difference is then increasing linearly in time at the frequency $\omega = 2\pi f$ via

$$\phi = \omega t + \text{const.}\,. \tag{4.15}$$

Thus, the supercurrent I_s is given by

$$I_s = I_c \sin(\omega t)\,, \tag{4.16}$$

which means the time-averaged supercurrent $\bar{I}_s$ is zero for $\bar{V} \neq 0$. As previously mentioned, in the AC Josephson regime a voltage bias can also drive normal currents. The junctions are therefore often treated as a resistively- or capacitively-shunted junction [7, 8, 118].

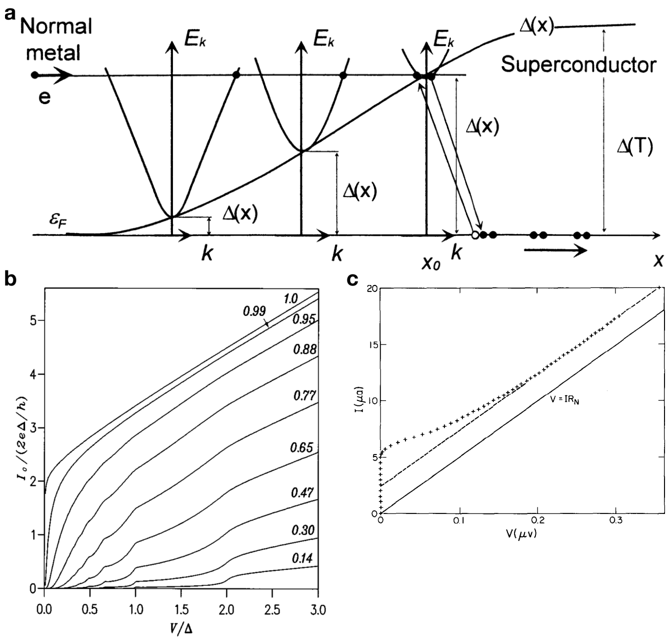

Figure 4.3: Andreev reflection process and current-voltage characteristics for Andreev reflections and phase-slips. (a) Spatial evolution of the dispersion relation when a quasi-particle from a normal reservoir is impinging on a superfluid reservoir, adapted from Ref. [118]. The particle and the reflected hole are at the same energy, thus allowing no heat current. (b) Current-voltage characteristic of a superconducting quantum point contact for varying transparencies α, adapted from Ref. [124]. In the limit of high transparency $\alpha \to 1$ there is an excess current $I_{\text{exc}} > 0$, while for small transparencies $\alpha \to 0$ a subgap structure becomes visible. (c) Current-voltage characteristic of the phase-slip process, the phase-slip center carries an excess current of about $I_{\text{exc}} = I_c/2$ (dashed line), adapted from Ref. [125].

Current-Voltage Characteristic

In the current-voltage characteristic of a weak-link two regimes can be distinguished by the magnitude of the voltage with respect to the gap. In the limit where the applied voltage is larger than twice the gap 2Δ the current can be transported by normal currents [7, 8] above the gap and the current-bias characteristic becomes linear $\bar{V} \approx \bar{I}R_N$. Notably, this limit can still have supercurrent contributions in terms of oscillations which is why it is called resistive and not normal regime [8]. The second regime, i.e. where the voltage bias is smaller than the gap is discussed later. In the subgap regime the current evolves from a supercurrent to a normal current.

Excess Current

In order to quantify the properties of a junction it is useful to define the so-called excess current [126]. The previously discussed transport above the gap at large voltages displays a linear current-voltage relationship, displaced with respect to zero by the excess current. The excess current is therefore defined as

$$I_{exc}(V) = I_s(V) - I_n(V)\,, \tag{4.17}$$

where the excess current is the extra current due to the supercurrent. Generally the excess current can be found via extrapolation of the normal current to $V = 0$. In the example of an SNS weak link the current bias characteristic is given by [127]

$$I = V/R_N + \frac{8\Delta}{3R_N}\tanh\left(\frac{V}{2k_BT}\right)\,, \tag{4.18}$$

for $\Delta \ll k_BT$. The excess current in this case is thus given by a nonlinear current as a function of the bias, characterized by a hyperbolic tangent.

Andreev Reflection Process

Figure 4.3(a) illustrates the Andreev reflection process of a normal particle impinging on a normal-superfluid (NS) interface [7, 42, 118]. The Andreev reflection process is responsible for transport in an NS interface where normal particles can approach the interface below the superfluid gap. In this subgap limit transport can still take place via the Andreev reflection process.

In the interface region the order-parameter of the superfluid is considered to increase on the length scale of the superfluid healing length. The normal particle, entering the interface where the gap is small becomes part of the quasi-particle branch of the superfluid filling an appropriate k state. It will then progress further in space, accompanied by an increase of the gap and a decrease of its momentum k getting close to k_F. At the point where the momentum k is equal to k_F the normal particle finds a partner to pair with in order to enter the superfluid condensate. Since the normal particle cannot enter the condensate it has to change it's state and a hole gets reflected.

Multiple Andreev Reflections

The subgap current-bias characteristic of an SNS junction (but also for S-Insulator-S or S-S'-S junctions) is obtained assuming multiple Andreev reflection processes at each interface [127]. Here, the particle emitted from the left superfluid is accelerated by the voltage difference and gets Andreev reflected at the second interface as a hole, again accelerating by the voltage difference. The particle pairs with a partner and enters the superfluid on the right. This process repeats until the particle energy in the normal region reaches the quasi-particle branch above the gap, i.e. until $N\Delta\mu = 2\Delta$. The full Andreev process then transports $2N + 1$ particles from left to right. Importantly, any scattering of the particles/holes inside the normal region will quickly lead to a suppression of the Andreev process since the process has to be repeated N times [124], as can be seen in Fig. 4.3(b). The scattering is quantified by the transparency $\alpha = [0, 1]$ which can be found to affect the current via α^N [124], where N is the number of reflections. Assuming the Andreev process as the underlying microscopic origin of the nonlinearity in our experiment it is found that the transparency of the quantum-point-contact is very close to unity [38].

Importantly, the particle-hole symmetry at the Andreev reflection [42, 128] imposes that there is no heat current between superfluid and normal region, i.e. no entropy is transported by the Andreev process.

Phase Slips

One of the main mechanism responsible for resistivity in narrow superconducting junctions are phase-slips. They can occur in the limit of large currents above the critical current, where the phase of the order parameter spontaneously relaxes. Thus, the supercurrent must be converted to a normal current leading to a resistive behavior [7, 108, 129], see Fig. 4.3. In a voltage biased junction the phase increases linear in time which will accelerate the supercurrent continuously until it reaches the critical current I_c. At this point the supercurrent breaks down spontaneously [125], concurrent with the order-parameter dropping to zero. Subsequently, the superfluid can “heal”, i.e. recondense, within a distance of the healing length and the dynamics will repeat. The name phase-slip originates from the concurrent relaxation of the phase gradient and the order-parameter. This phase-slip process is one fundamental dissipation process in Josephson junctions [7, 129]. In the current-voltage characteristic the phase-slips are responsible for steps and carry a time-averaged supercurrent $\sim I_c/2$ [129]. Interestingly, this reduction of the time-averaged supercurrent seems like a differential resistance dV/dI [127], though in real-time it corresponds to an interruption of the supercurrent. A simple theoretical model [7, 129] suggests that the local steady-state supercurrent in the phase-slip is half the critical current, while the other half is a normal current.

For completeness, a second type of phase-slips exist which are thermally activated described by LAMH theory [7, 130–132]. Here, no external voltage is necessary to accelerate the superfluid, but any supercurrent I_s will modify the free-energy barrier towards a phase-slip such that thermally excited pair breaking excitations, i.e. phase-slips become more likely [133].

4.5 SUPERFLUID TRANSPORT IN FERMIONIC QUANTUM GAS JUNCTIONS

Though superconductors have been extensively studied in condensed matter systems [8, 119, 133] and superfluid transport has been the focus of research for liquid helium [134] quantum gas experiments are comparatively early in their studies of superfluidity. Here, a terse overview over the two-terminal experiments transport experiments employing fermionic superfluids is given.

The measurement of the speed of sound [19, 135] are some of the first experiments employing transport to measure excitations which in principle also can be present in a two-terminal configuration [136]. Particularly interesting for us is the role of Goldstone modes, i.e. the second sound, in the fermionic superfluid [22] which is the gapless excitation mechanism able to carry entropy. In the measurements of the second sound [22] the gas was excited via a parametric evolution and subsequently the first and second-sound was measured via the density profile of the cloud. Notably, the second-sound velocity depends on the superfluid fraction n_s/n_n suggesting that in a two-terminal geometry a direct propagation of second-sound through a junction requires a finite superfluid density at any point in the junction. Interestingly, there are theory calculations [136] which suggest that the second-sound can contribute to entropy transport in a weak link junction via a direct tunneling process where a pair from the condensate tunnels at equal energy and subsequently couples to a Goldstone mode and vice-versa.

The second type of experiments closest to our realization of a transport experiment are the observations of the Josephson effect [33, 34, 137] through a tunneling junction. The major difference to our experiment are the properties of the tunnel junction and the resulting magnitude of normal and supercurrent in the junction. While our results presented here are obtained in a highly transparent, voltage-biased junction the Josephson oscillations have been observed in a voltage-biased regime where the normal current is almost completely suppressed by the resistance of the tunnel junction. In terms of the geometry, observing a Josephson effect in the voltage-bias regime requires a small transparency such that the superfluid oscillations are not shunted away from a large dissipative current [124]. In our experiment the transparency is close to its maximal value [38] such that we do not expect to measure large Josephson oscillations. Interestingly, in the low-transparency regime investigated via Josephson oscillation [138] the phase slips are believed to be the dominant dissipation mechanism competing with the coherent oscillations.

In our experiment the transport between strongly interacting reservoirs, superfluid in equilibrium, in the 2D [37], 1D [38] and temperature biased [69, 87] regime has been studied. As previously mentioned the voltage bias and the strong normal currents lead to drastically different effects due to the competition between superfluid and normal transport and the resulting intrinsically non-equilibrium behavior [7, 118]. It is found that in our experiments the junction can be treated as a weak link, in the 2D limit [37], due to the length of the junction with respect to the superfluid healing length. Interestingly, with the quantum point contact a non-linear current-bias characteristic is measured, corresponding to a non-zero excess current, an indicator of superfluid transport [126, 127]. The corresponding theory calculations suggest that Andreev reflections [38, 42, 124] are the microscopic processes responsible for the non-linear current bias characteristic (see Fig. 4.3(b)).

4.6 CONCLUSION AND OUTLOOK

In Part III the concepts introduced here are used to characterize our observations It is already interesting to note that a non-linear current-voltage characteristic is closely related to superfluidity due to the implied connection between large DC Josephson currents at zero voltage-bias and the resistive/Ohmic currents at large voltages, above the gap [127]. This conceptual behavior is quantified by the excess current which, if non-zero, is then an indicator of superfluidity. We also find that having a nonlinear current-voltage characteristic is not enough to determine the underlying microscopic process in play, as can be seen when comparing Fig. 4.3(b) and (c). Interestingly observing zero excess current does not imply that there are no superfluid transport processes at play, e.g. in the dirty superconducting QPC [124].

In the context of entropy transport between superfluids we see that on the one hand the superfluid itself cannot carry entropy while on the other hand there are gapless excitations carrying entropy and dissipation phenomena in the voltage biased superfluid transport such as phase-slips which lead to dissipation and normal currents inside a superfluid junction [133]. The question though remains whether the typically observed steps in the I-V characteristic [7] in conjunction with phase slips would also be observable in our system. There are still open questions on how entropy is propagating between or through finite temperature superfluids [139] and what role the channel connecting the superfluids or the boundary between the normal and superfluid phase play. The questions remain mainly because in condensed matter systems at low energies phonons can mask the entropy transport [140], charge effects can induce unwanted currents [43] and the heat current often have to be inferred [141]. Quantum gases thus provide a straight-forward platform to study entropy transport between superfluids due to the direct extraction of the entropy and the lack of phonons and charge.

Part I

EXPERIMENTAL SETUP AND TECHNICAL UPGRADES

5

TECHNICAL DETAILS OF THE EXPERIMENT

CHAPTER CONTENTS

In this chapter an overview of the experimental apparatus including parts of the ultra-high vacuum system, the magnetic coils and the optical setup is provided. The technical improvements implemented during this thesis are described in Ch. 6.

The optical part of the experiment has been upgraded several times over the years, whereas the vacuum system and coil setup remains unchanged. Therefore, for a detailed description of the vacuum system, the magnetic field coils configuration and the current stabilization system the thesis of B. Zimmerman is recommended [73]. Moreover, the thesis of T. Müller [79] provides a comprehensive discussion of the microscope and the high resolution imaging system. Finally, the optical setup above the microscope, generating the constriction potentials and allowing for spatial light modulation has been rebuilt recently, which is presented in the thesis of M. Lebrat [36].

5.1 ULTRA HIGH VACUUM SYSTEM

The ultra-high vacuum system providing the conditions for experiments with ultracold atoms over extended periods of times is made up out of four different sections, as displayed in Fig. 5.1. The oven (right in Fig. 5.1) and main chamber (center of Fig. 5.1) are separated by a gate valve and the main chamber is separated by a gate valve from the Zeeman slower window (left in Fig. 5.1). In the following the properties of the vacuum system and the magnetic field coils of parts of the apparatus are discussed.

Oven Chamber

The oven chamber (rightmost part of Fig. 5.1) is a large volume chamber, pumped by an ion-getter pump (*GammaVacuum 20S DI*) and a titanium sublimation element (*GammaVacuum TSP 3 filaments*). The oven was replaced and refilled in September 2020 and is connected via a DN16CF flange to the chamber. The vertical bellow visible in Fig. 5.1, connected to the top of the oven was removed. We find that it had no influence on the oven chamber pressure being below $< 5 \times 10^{-10}$ mbar. The pressure gauge for the oven chamber is mounted opposite of the ion-pump before the connection to the angle valve used for the initial pumping. The recirculating atomic reflux-wick oven [142, 143] is heated to $\sim 440\,^\circ\mathrm{C}$ which evaporates the lithium and creates a beam of atoms which is shaped within the oven by a conical outlet

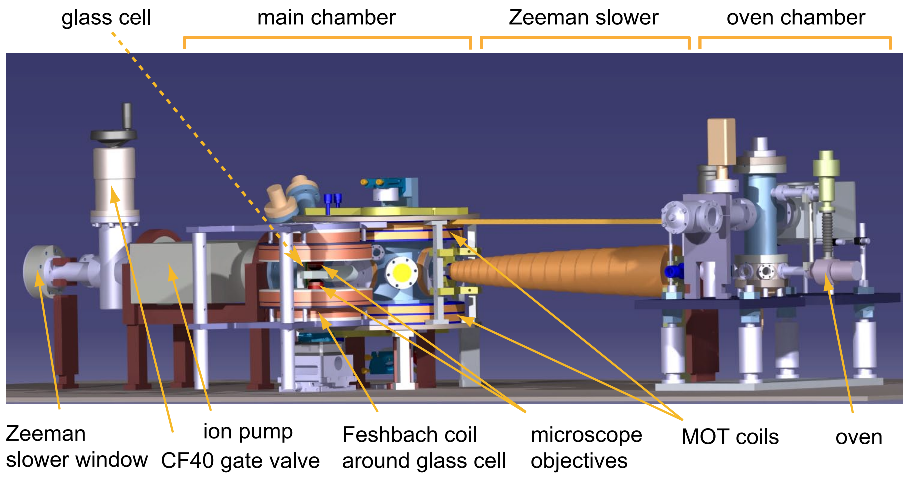

Figure 5.1: Ultra-high vacuum system including the magnetic field coils. From right to left, in the reflux oven ^{6}Li is heated to $\sim 440\,°\mathrm{C}$ resulting in a hot atomic-beam, collimated by two apertures in the oven chamber. The Zeeman slower creates a magnetic gradient along the propagation direction allowing us to slow the beam with a counter-propagating, red-detuned beam. The Zeeman slower ends in the main chamber where three pairs of retroreflected beams make up the MOT. The main chamber is followed by the main ion pump and a gate valve connecting the Zeeman slower beam entrance viewport. The glass cell has an octagonal shape and is mounted to the main chamber via a glass tube. Taken from Ref. [79].

region (outlet angle 23°). In the oven chamber two apertures are used to reduce contamination of the Zeeman slower by transversally propagating atoms, while a mechanical shutter can be used to block the atom beam.

Zeeman Slower

The oven chamber and the Zeeman slower are connected with a DN16CF flange followed by a gate valve (*VAT DN16CF all metal*) which allows varying the pressure independently in the main vacuum and the oven chamber. In addition, the Zeeman slower includes a differential pumping tube section (inner radius 1.5 mm, length 14.5 cm) at its oven chamber side, providing a pressure differential of 10^{-4} between the chambers. The Zeeman slower coils provide a square-root shaped magnetic field, decreasing towards the MOT chamber from initially $\sim 929\,\mathrm{G}$, connecting smoothly to the MOT fields, when operated with a single power supply at 50 V and 8 A. The Zeeman slower coils are not connected directly to the vacuum system but are mounted on a spool carrier, which is water cooled.

Zeeman Slower Window

The atomic beam, if not captured by the MOT, passes through the main chamber and is deposited on the slower beam entrance viewport which is at the leftmost side of the apparatus shown in Fig. 5.1. The entrance viewport is a DN63CF sapphire viewport which is particularly resistant to corrosion from lithium. Nevertheless, over the years, a white coating has formed which reduces its transmission. The viewport can be replaced by closing a CF40 gate valve separating it from the main chamber, see left side of Fig. 5.1.

Main Chamber

The magnetic field of the Zeeman slower was taken into account for the MOT field coils, such that the atoms are decelerated towards the MOT position. In the main chamber three pairs of CF40 viewports are used to create three pairs of MOT beams by retro-reflecting the three incoming beams using a quarter waveplate, mirror combination. Two additional pairs of DN16CF viewports, mounted at 45° with the horizontal plane, allow imaging of the MOT. The octagonal glass cell is mounted via a glass tube to a DN40CF flange, opposite to the glass cell a DN63CF viewport allows optical access for the transport dipole trap. In line with the Zeeman slower, the main chambers' ion pump (*GammaVacuum 100L DI Inline*) is mounted with a DN100CF flange. The pressure gauge and a titanium sublimation pump are mounted in the connection between ion pump and main chamber. The pressure gauge is no longer operational, while the ion pump shows too large currents due to leakage. We find that the vacuum lifetime of the atomic cloud is beyond the duration of the experimental cycle ($\tau = 9\,\mathrm{s}$ in main chamber, $\tau = 44\,\mathrm{s}$ in glass-cell). The main chamber is surrounded by three different type of magnetic field coils, displayed in Fig. 5.2. The MOT fields are created by two pairs of large, water-cooled coils in anti-Helmholtz configuration, producing a quadrupole field with a gradient of $6.75\,\mathrm{G/cm}$ in x- and y-direction and $-13.5\,\mathrm{G/cm}$ in vertical direction when operated at $30\,\mathrm{A}$.

Glass Cell

The glass cell (middle of Fig. 5.1) has an octagonal shape, made by contacting 10 pieces of fused silica plates. The cell is anti-reflection coated for three different wavelengths, i.e. 671 nm, 532 nm, 761 nm, on its upper, lower and front outside surfaces. The thickness of the glass is 4.000(5) mm which was taken into account when the microscope was designed. In order to reduce reflections and etaloning, the cell is rotated by 3° around the vertical axis and imperfect mounting led to a rotation of 1° around the experimental x-axis (atomic beam propagation direction).

5.2 RESONATOR DIPOLE TRAP

The mirror holders of the resonator dipole trap are placed on a baseplate, mounted via a DN200CF flange to the main chamber. On the baseplate the holders are located next to the lower entrance viewport of the MOT and the Feshbach coils (FB_1, see Fig. 5.2). The mirrors are mounted in a metal cage, in front of a planar 45° mirror connecting the resonator optically to the outside via DN16CF viewports on the bottom of the main chamber. The resonator consists of a planar M_1 ($R_1 = \infty$) and a curved mirror M_2 ($R_2 = 150\,\mathrm{mm}$), simplifying the resonator alignment. The distance between the mirrors $L = 14.975\,\mathrm{cm}$ was measured via the mode spacing of different transversal modes which is slightly below the upper stability limit of this configuration. The incoupling waist on the planar mirror is $w_0 = 45\,\mu\mathrm{m}$ which gives a trap diameter of $2w_{L/2} = 1.1\,\mathrm{mm}$ at the MOT position, in the center of the optical cavity. Originally, the planar mirror was moveable by a ring piezo which has become unusable during the baking of the chamber. This makes the locking intrinsically difficult since the cavity is no longer locked to a laser but the other way around, which puts additional demands on the laser, i.e. it has to be tuneable over a full free spectral range

$\nu_{\text{FSR}} = 1\,\text{GHz}$. The new locking scheme of the resonator trap, providing a continuous lock is described in Sec. 6.2.

Resonator Feshbach Coils

The resonator dipole trap, in its center, is surrounded by a coil pair (see FB_1 in Fig. 5.2) in Helmholtz configuration providing a strong, homogeneous magnetic field which we use to improve the evaporation efficiency in the resonator dipole trap via interactions. Each coil is made up of 99 windings in 4 layers of a rectangular hollow core copper wire ($4 \times 4\,\text{mm}^2$). The coils are water-cooled via their hollow core wires and generate a magnetic field strength of $B = 3.5\,\text{G/A}$, nominally operated at $300\,\text{G}$. The current is controlled by a homebuilt PI loop [73] in conjunction with a current transducer.

5.3 MICROSCOPE AND MAGNETIC FIELD COILS

In this section we aim to provide a summary of the optical setup of the microscope as well as the magnetic coil configurations surrounding the glass cell.

Magnetic Field Coils around the Glass Cell

The glass cell is encompassed by 6 coil pairs which allow us to tune gradients in all three directions in addition to the large Feshbach field which also produces a field curvature, leading to magnetic trapping in the horizontal plane. The coil assembly is shown in Fig. 5.2 on the right-hand side. The coils are mounted on a homebuilt aluminium frame which is decoupled from the vacuum system and from the microscope.

Closest to the glass cell the Helmholtz HH and the Feshbach FB_2 coils are mounted. The parameters of the Feshbach field coils are summarized in Tab. 5.1. The Feshbach coil has an L-shaped cross-section which is placed such that the Helmholtz coil is wound on the Feshbach coil completing the L to a rectangular cross-section, while having an outer diameter of $\text{OD}_{\text{HH}} = 238\,\text{mm}$. The field curvature is imposed by mounting the Feshbach coils slightly away from the Helmholtz configuration. The Helmholtz coils are mounted in Helmholtz configuration, thus creating a homogeneous field at the atom position with $B/I = 5.42\,\text{G/A}$. Generating the large Feshbach fields, i.e. $300 \ldots 1000\,\text{G}$, requires large currents of up to $110\,\text{A}$. The currents are generated by a high current power supply (*EA PA-PS-9080-300*) which can supply up to $I_{\text{max}} = 300\,\text{A}$ at $U_{\text{max}} = 80\,\text{V}$ which is far above our requirements. The supply is operated in constant voltage mode and connected to an additional current regulation system which includes an insulated gate bipolar transistor (IGBT) in series with the coils which allows us to vary the total resistance to control the current supplied to the coil. The current is measured inductively with a low noise current transducer (*LEM IT-200s*) and the feedback signal is generated by a homebuilt PI loop. The regulation system includes several interlock mechanisms, triggering a switch-off of the power supply, whenever the dissipated power surpasses a threshold. The water-cooling ($\sim 0.5\,\text{l/min}$ per coil) allows us to operate the Feshbach coils at $\sim 32\,°\text{C}$ for a current of $79\,\text{A}$ for $8\,\text{s}$ of a $25\,\text{s}$ total cycle time. During this thesis a new current regulation system based on Ref. [144] was built, which is described in Sec. 7.1, but not yet implemented. In addition, a new cooling-water distribution and chiller (*Van der Heijden 210-WW-B400*,

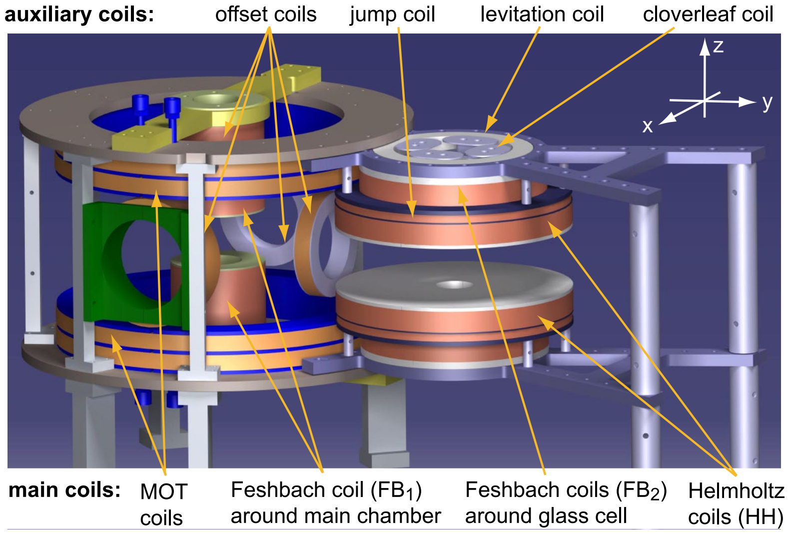

Figure 5.2: Coil configuration around the MOT chamber and the glass cell. The main chamber on the left is surrounded by two water-cooled MOT coils in anti-Helmholtz configuration. In addition, five additional offset coils (in vertical direction wound around the Feshbach coils) allow us to tune the position of the MOT position. For the first optical evaporation in the resonator a Feshbach coil pair (FB$_1$) is mounted in the inlets of the top and bottom flange. On the right, the coils around the glass cell are shown. The Feshbach coils (FB$_2$) create a magnetic confinement in horizontal and strong field in vertical direction. The four clover-leaf coil pairs are used to generate magnetic gradients in the horizontal plane. The jump and levitation coils produce gradients in the vertical direction and are used to levitate the cloud and aid optical evaporation, respectively. The coils in Helmholtz (HH) configuration are not used. Taken from Ref. [79].

FB_2 parameters	Value	
Windings	N	146
Diameters	ID, OD	44 mm, 188 mm
Height	l	57 mm
Coil distance	d	68 mm
Hollow core wire	$L_{out} \times L_{out}, R_{in}$	$4 \times 4\,\mathrm{mm}^2$, 1.25 mm
Magnetic field	B/I	8.7310(8) G/A
Field curvature	$B''_{x,y}/I$, B''_z/I	$0.4145\,\mathrm{G/cm^2/A}$, $0.829\,\mathrm{G/cm^2/A}$
Resistance	R	$0.084\,\Omega$
Inductance	L	980 µH
LR cutoff frequency	f_c	13.6 Hz

Table 5.1: Feshbach coil parameters. The main Feshbach coil has an L-shaped cross-section, with an inner aperture made for the microscope objective. The coil can generate fields up to 1000 G, whereas higher currents lead to too large temperatures. The magnetic fields are regulated with a PI circuit based on a transduced based current measurement. The generated field is given by the sum of a homogeneous B and curved B'' part resulting in a quadratic confinement. The resistance and inductance (here stated per coil) limit the response of the coil while also suppressing high frequency current noise.

temperature stability $\Delta T < 0.05\,\mathrm{K}$) will improve the temperature stability for future experiments.

The large inductance of the Feshbach coil implies that it cannot be used to quickly switch fields which is why an additional Jump coil is placed on top of the Helmholtz coil which can be used to manipulate magnetic fields quickly, see Fig. 5.2. Currently, the coil is operated in anti-Helmholtz configuration to create gradients in vertical direction, aiding the optical evaporation with a tilt [78]. The coil system is completed by a levitation coil pair which is used to compensate gravitation and four pairs of coils in clover-leaf configuration which generate gradients in the horizontal plane at the atom position, i.e. $B'(x, y, z = 0) \neq 0$. The clover-leaf coils, generating gradients in the transport y-direction are operated by a low-noise, four-quadrant power supply (*Toellner TOE 7621-60*, $I_{max} = \pm 5.3\,\mathrm{A}$, $U_{max} = \pm 60\,\mathrm{V}$) which allows fast switching and modulation of the currents, even with an inductive load.

Microscope and High Resolution Imaging System

The microscope setup is displayed in Fig. 5.3(a). The microscope objectives are mounted above and below the glass cell in a tube held by the upper-breadboard and the table, respectively. The microscope assembly is mounted separately from the vacuum system and the coil assembly. The objectives are custom designed lens assemblies (*Special Optics*), optimized for operation with the glass-cell, providing diffraction limited performance at a numerical aperture of $NA = 0.53$. The microscope parameters are summarized in Tab. 5.2.

The tube holding the microscope is made of a glass-ceramic (*MACOR*), reducing interaction with the magnetic fields, and is threaded into the microscope holder. The thread allows vertical, coarse position shifts (750 µm per revolution) to align the focus position. In daily operation all alignments of the microscope can be done with the piezo XYZ-translation stage (*Piezosys-*

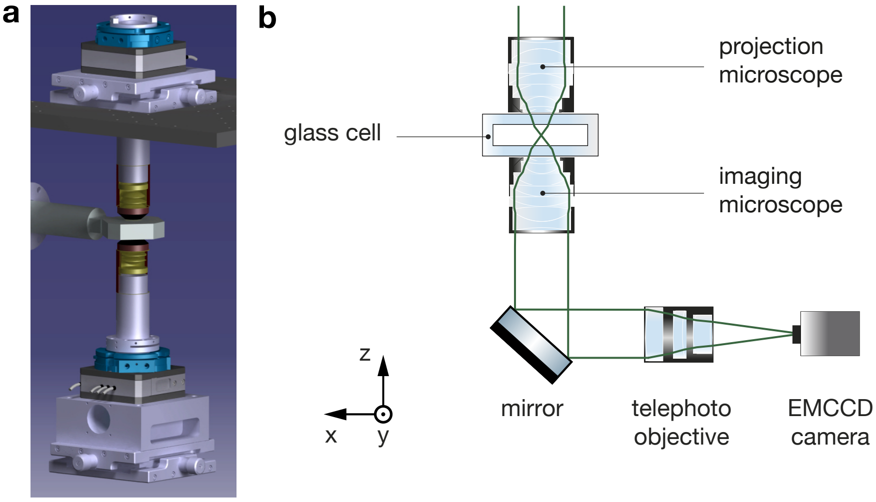

Figure 5.3: Microscope mechanical and optical setup. (a) The microscope optics are mounted in a glass-ceramic which is held by a goniometer allowing adjustments of tip and tilt. The goniometer is placed in a three-axis, closed-loop, piezo translation stage which is mounted in a mechanical XY translation stage. This setup for both upper and lower microscope, allows fine and coarse alignment along five axes. (b) The upper microscope is used for projecting optical potentials and as an input for resonant light. The lower microscope is used for imaging, paired with a custom telephoto objective allowing diffraction limited operation at 532 nm, 770 nm and 671 nm. The telephoto objective images the atom plane onto an EMCCD camera with a magnification of 54 and a diffraction limit of 770 nm at 671 nm. Adapted from Ref. [79] and Ref. [71].

tem Jena Tritor 102 SG EXT), providing 100 µm travel. The stage is operated in closed-loop mode where the feedback is provided by a homebuilt PI-loop based on an FPGA (*NI Compact RIO* with *9264*, *9205*, *9401*). The bandwidth of the piezo response < 300 Hz only allows to compensate slow drifts of the microscope, while fast vibrations due to acoustic noise, cannot be compensated. Nowadays, operating the experiment over extended periods of time we find that we require less frequent re-alignments once the experiment has thermalized. The thermalization can be observed with a temperature sensor mounted on the microscope. During this thesis the climate control of the room was upgraded which reduced temperature fluctuations of the air to < 0.2 K which is one of the reasons for the stability of the microscope. The position drift of the strain-gauge inside the piezo translation stage is 2 µm/K which means that a drift of 1.75 K would move a diffraction limited imaging system out of focus.

The lower microscope objective is accompanied by a specifically designed telephoto objective (*Special Optics*) shown in Fig. 5.3(b). The telephoto objective images the atom-plane onto an EMCCD camera (*Andor Ixon 887*) with a magnification of 54 and a diffraction limited resolution of $\Delta r_{\mathrm{Rayleigh}} = 770\,\mathrm{nm}$. The magnification is theoretically given by the ratio of focal lengths $M = f_{\mathrm{tele}}/f_M = 54.2$ and was experimentally measured to be $M = 54.0(2)$ using a hole pattern on a precision test target [79]. The effective pixel size in the atom plane is $296 \times 296\,\mathrm{nm}^2$ which gives a total frame size of $\mathrm{ROV} = 150 \times 150\,\mu\mathrm{m}^2$. The pixel size is about half the diffraction limit which was chosen to sample the point-spread-function (PSF) of a fluorescing, single atom. For absorption imaging the pixels are binned 2×2 in order to increase the signal without losing resolution. The high resolution

Microscope parameters		Value
Focal length	f_M	18 mm
Numerical aperture	NA	0.53
Clear aperture	D	18 mm
Operating wavelengths	λ_M	532 nm, 671 nm, 770 nm
Telephoto focal length	f_{tele}	975 mm
Magnification	M	54.0(2)
Resolution at 671 nm	$\Delta r_{\text{Rayleigh}}, \Delta r_{\text{FWHM}}$	770 nm, 660 nm
Chromatic shift	$\Delta f(\lambda_M)$	$<$ 500 nm
Depth of field	DOF	3.5 µm
Field of view	FOV	100 µm × 100 µm
Region of view	ROV	150 µm × 150 µm
Effective pixel size	x_{px}	296 nm × 296 nm

Table 5.2: Microscope and high resolution imaging system parameters.

also means the depth of field (DOF = 3.5 µm) of the imaging system is small, such that the lower microscope (see Fig. 5.3(b)) has to be aligned vertically to the atom plane.

Besides the high-resolution imaging system, a second imaging path, split with a polarizing beam splitter before the telephoto objective, is used to characterize the optical potentials projected on the atoms. The secondary imaging system has a magnification of $M = 250\,\text{mm}/18\,\text{mm} = 13.9$ with an effective pixel size of $250 \times 250\,\text{nm}^2$. The secondary camera is a USB camera (*Flir Chameleon2*) which allows a simple read-out and is mainly utilized for our wavefront correction algorithm [62] and subsequent beam characterization.

5.3.1 *Auxiliary Imaging Paths*

Here, the imaging paths in the main chamber of the experiment are described, whereas a detailed description of the new spin-resolved absorption imaging system can be found in Sec. 6.3, while the details of the high-resolution imaging are found in Sec. 5.3. In order to characterize the experiment during all steps of the experimental sequence, we have multiple imaging systems for imaging the MOT and resonator dipole trap in the main chamber and the final atom cloud in the glass cell.

Main Chamber Imaging System

The main chamber has two imaging paths, one for fluorescence imaging of the MOT and another for absorption imaging shown in Fig. 5.4. The fluorescence imaging of the MOT is always operational and provides an indication of the atom number in the MOT, though it is not calibrated. Nevertheless, the fluorescence counts correlated with the final atom number helps to troubleshoot issues with the MOT and allows to disentangle them from problems that may arise at a later stage in the experiment.

The absorption imaging system on the other hand has to be configured to be operational. For the imaging light the fiber of the x-absorption imaging in the glass-cell has to be moved to the y-absorption path and mirror is placed

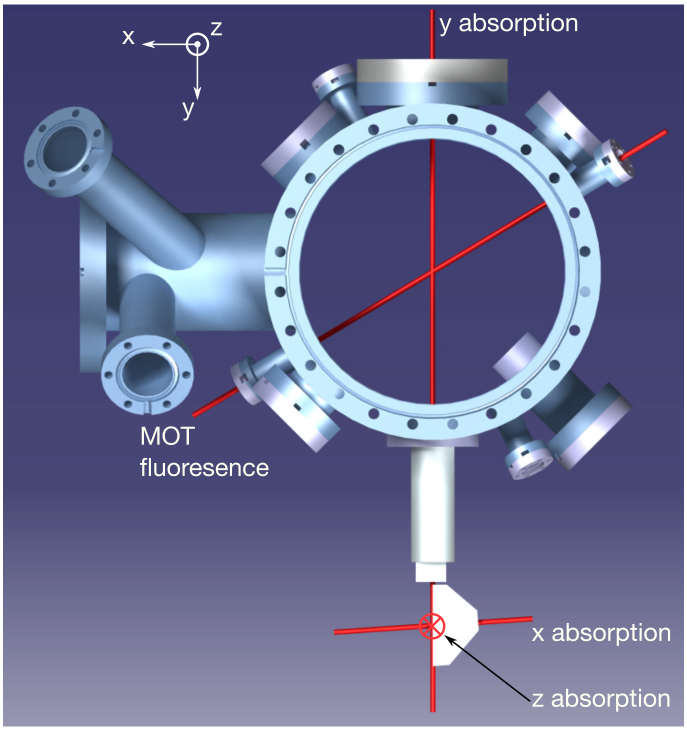

Figure 5.4: Imaging paths in main chamber and glass cell. In the main chamber two imaging systems, y-absorption and MOT fluorescence, intersecting at the center are in use. The fluorescence imaging is used to non-invasively characterize the compressed MOT during the experimental cycle, while the absorption imaging system is only used when problems within the main chamber arise. The atomic cloud in the glass cell can be absorption imaged from two directions, x and z. The low resolution imaging system in x-direction is used to measure atom numbers and temperatures precisely and is detailed in Sec. 6.3. The high resolution vertical imaging system is used to determine the local density of the cloud and is presented in Sec. 5.3. Adapted from Ref. [73].

on a magnetic mount such that the light propagates along the path of the final, optical dipole trap. Since this path is also used to stabilize the power of the dipole trap another flip-mirror has to be flipped such that the light can reach the camera (*PointGrey FireWire Camera*). The imaging system has a calibrated magnification of $M = 0.6$ which results in an effective pixel size of 12.4 µm on the atoms. The effective saturation intensity is not calibrated which means the ideal scattering cross-section is used to measure the atom number which overestimates the real value. In order to image with a defined quantization axis the main chamber Feshbach coils are used to image at $B = 300\,\mathrm{G}$. The main chamber imaging path can be used to image the compressed MOT, the atoms in the resonator and the atoms in the transport dipole trap. The MOT itself is difficult to image due to its large optical density absorbing the light almost completely.

5.4 TWO-TERMINAL TRANSPORT GEOMETRY

In this section the optical dipole traps used for transporting the atoms from main chamber to the glass-cell and the hybrid-trap used for the subsequent transport experiments are introduced. Secondly, the lightsheet trap is described which generates a two-dimensional (2D) constriction between two three-dimensional (3D) reservoirs. Finally, we detail the lithographic technique, used to imprint the one-dimensional wire onto the 2D lightsheet. A more detailed description of the transport geometry can be found in the theses of S. Krinner [70] and D. Stadler [145].

Transport Dipole Trap

In order to transport the atoms from the resonator trap to the glass-cell a tightly focused Gaussian beam is moved by 267.5 mm via a lens on an air bearing translation stage. The light for the dipole trap is generated by a low-noise seed laser at 1064 nm (*Coherent Prometheus*) which is amplified by a fiber amplifier (*NuFern NuAMP 10W*) and power stabilized with a PI loop at 3.5 W for the optical transport. The beam waist on the atoms is $w_x, w_z = 22(1)\,\mu\mathrm{m}$ which results in a trap depth of $V_0 = 0.28\,\mathrm{mK}$. In order to compensate position fluctuations due to the long lever-arm of the beam and the movement, the beam position in the glass-cell and in the main chamber are stabilized using a position sensitive device (*Thorlabs PSD*) in conjunction with a piezo operated tip/tilt mirror. We find that without this stabilization the atom-number fluctuations are increasing.

Hybrid Optical-Magnetic Trap

The transport dipole trap is not stable enough in position for the transport experiments and is thus loaded into a counter-propagating dipole trap which is position stable due to its short lever arm. This is the main dipole trap, generated by the same laser shifted in frequency via an AOM. On the atoms the beam has a larger waist $w_x, w_z = 70\,\mu\mathrm{m}$ and is nominally operated with at a power of 0.8 W, before evaporation. The focused Gaussian beam creates a trapping potential in its transversal direction approximated by

$$V_{\mathrm{Dipole}} = \frac{1}{2} m_{6\mathrm{Li}} \omega_x^2 x^2 + \frac{1}{2} m_{6\mathrm{Li}} \omega_z^2 z^2 \,, \tag{5.1}$$

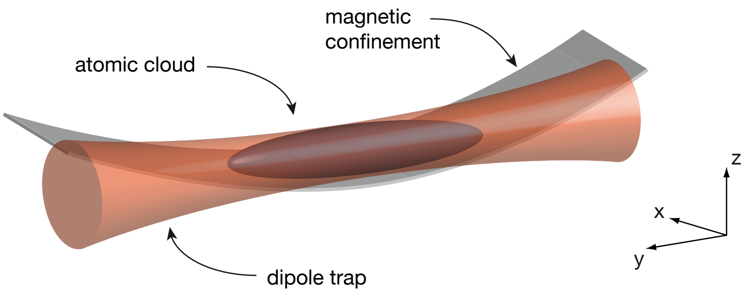

Figure 5.5: Hybrid optical and magnetic trap. The optical confinement is provided by a focused Gaussian beam at 1064 nm with a waist of $w_x, w_z = 70\,\mu m$. In addition, the magnetic field curvature provided by the Feshbach coils generates a weak longitudinal magnetic confinement for the atoms. The sum of both traps results in a cigar-shaped atomic cloud. Taken from Ref. [71].

where $\omega_{x,z}$ are the trap frequencies obtained from the trap depth V_0 via

$$\omega_{x,z} = \sqrt{2V_0/m_{6Li}w_{x,z}^2}\,. \tag{5.2}$$

In principle the focused Gaussian beam also provides confinement along its direction of propagation but for this large waist trap the confinement is quite small, i.e. $\omega_z = 1.6\,\mathrm{Hz}$ at $0.8\,\mathrm{W}$. Figure 5.5 shows the magnetic confinement provided by the Feshbach coils which we use to longitudinally confine the cloud. The magnetic field curvature provides a harmonic confinement potential proportional to the magnetic moment of the atoms $\mu(B)$

$$V_{mag} = -\frac{1}{2}\mu(B)B''y^2 = \frac{1}{2}m_{6Li}\omega_y^2 y^2\,, \tag{5.3}$$

where the magnetic field curvature is given by $B''/I = 0.4145\,\mathrm{G}/(\mathrm{cm}^2\mathrm{A})$ and $\mu(B)$ is a function of the hyperfine state in which the atoms are prepared. The trapping frequencies in our system are given by $\nu_y \approx \sqrt{B}\cdot 1.15\,\mathrm{Hz}/\sqrt{G}$. The combination of both traps provides harmonic confinement in all three spatial directions, generating a cigar-shaped atomic cloud, as shown in Fig. 5.5.

Lightsheet Beam

Figure 5.6 shows the lightsheet beam transversally (in x-direction) intersecting the hybrid trap. The resulting trap geometry is a cloud of two half-harmonic reservoirs separated by a 2D region. The lightsheet beam is a TEM_{01}-like beam generated from a Gaussian beam passing through a binary $0-\pi$ phase-plate. The light, coming from a 532 nm laser (*Coherent Verdi V10*), is sent through a fiber with end-cap in order to withstand the required laser powers. The fiber collimator is specifically designed (*SuK Fiber Collimator*) to produce an elliptically shaped beam with a $1:3$ aspect ratio. The long axis of the beam is orthogonal to the phase plate such that one half of the beam picks up a phase of π. The light is subsequently focused on the atoms using an $f = 250\,\mathrm{mm}$ achromatic lens. The phase shift of π leads to a nodal line in the focal plane, while the aspect ratio of $y:z = 1:3$ is

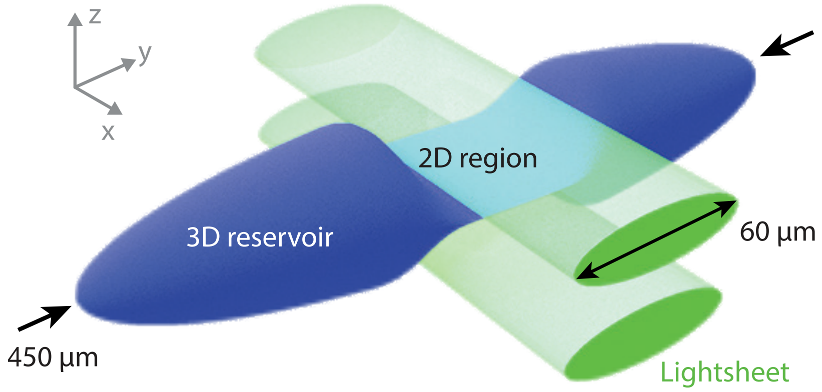

Figure 5.6: Vertical confinement using a TEM$_{01}$ beam. The lightsheet beam is intersecting the cigar shaped cloud transversally, creating a vertically squeezed 2D region of length $2w_y = 60\,\mu\text{m}$. The maximal confinement in vertical direction is $\sim 10\,\text{kHz}$ for 1 W of light at 532 nm, limited by the damage threshold of the optical fiber used. The 2D region is much smaller than the overall size of the cloud, thereby reducing its impact on the overall thermodynamics of the large 3D reservoirs. The Rayleigh range of the lightsheet beam $z_R = 500\,\mu\text{m}$ is much bigger than the cloud, thus providing the same confinement along the full width. Adapted from Ref. [79] and Ref. [71].

transformed to a ratio of 3 : 1 on the atoms. The resulting intensity profile is given by

$$\frac{2P}{\pi w_y w_z} \operatorname{erfi}\left(\frac{z}{w_z}\right) \exp\left(-\frac{2z^2}{w_z^2}\right) \exp\left(-\frac{2y^2}{w_y^2}\right), \tag{5.4}$$

where the vertical waist is $w_z = 9.5(2)\,\mu\text{m}$ and the horizontal waist is $w_y = 30(1)\,\mu\text{m}$.

This repulsive potential creates a vertical squeezing of the cloud which, for the beams peak intensity, is quasi-two-dimensional, i.e. $\nu_z = 10\,\text{kHz} > k_B T/h$. The peak intensity at 0.9 W, which is the maximal power we can send through the fiber, is around $46\,\mu\text{K} \approx 13\,E_R$, where E_R is the recoil energy. The power of the lightsheet beam is stabilized with a PI loop after the glass-cell which requires careful alignment and attention to the polarization of the light. Since there is no polarizing beam splitter after the fiber the power stabilization cannot be polarization dependent. In order to align the lightsheet on the atoms, a motorized mirror is used (*NewFocus Picomotor*) which allows for precise alignment with respect to the cloud. In addition, a USB camera is installed in the beam path after the glass-cell which images the beam during the experimental cycle and determines the beams' position and waist which is logged in a database and visualized in *Grafana*. Since the optical setup for the generation of the lightsheet beam is quite compact and mounted from below to the upper breadboard, which holds the microscope. The common-mode movement of microscope and lightsheet makes realignment of the lightsheet beam position rarely necessary.

Wire

The transversal confinement in x-direction is also provided by a TEM$_{01}$ like beam at 532 nm, though this beam is generated using a lithographic

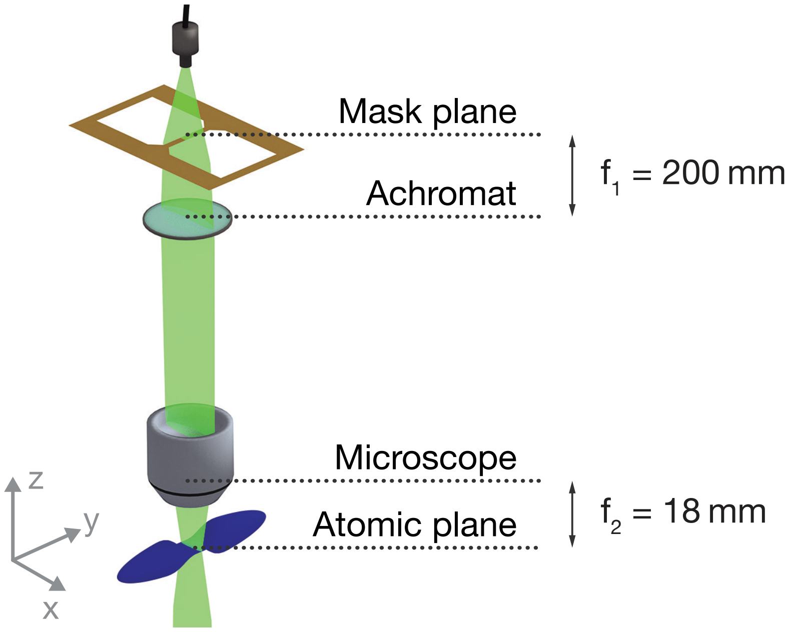

Figure 5.7: Lithographic creation of the wire confinement. The transversal wire confinement is created by imaging the masked region of a lithographic mask onto the atoms using a 11.1 demagnification. The resulting beam resembles a TEM_{01} mode with a 1.5 µm wide dark region in its center which allows a path for transport. The narrowness of the feature allows for strong confinements, i.e. $\nu_x = 15\,\text{kHz}$, at a moderate power of ~ 75 mW. The length of the wire can be tuned from $2w_y = 6\,\mu\text{m}$ up to 20 µm by changing the waist of the beam before the microscope using a cylindrical lens. Additional features on the lithographic mask add versatility to the experiment. Adapted from Ref. [71].

mask shown in Fig. 5.7. The lithographic mask provides several, different geometries which can be projected on the atoms, increasing the versatility of the experiment. For the experiments presented here, a chromium covered rectangular mask produces a shadow which is imaged onto the atom cloud. The mask is illuminated by an elliptical beam, the aspect ratio of which can be tuned via a cylindrical lens. The mask is imaged using an ($f_1 = 200\,\text{mm}$) achromatic lens together with the microscope ($f_M = 18\,\text{mm}$) such that the dark region in the atom plane has a width of $w_{x,\text{Dark}} = 1.5\,\mu\text{m}$. The small waist of the dark region makes it fairly easy to create a strongly confined 1D region, where confinement frequencies of up to 15 kHz are practical. Adjusting the aspect ratio of the elliptical beam allows us to tune the waist of the beam in y-direction, thereby tuning the length of the wire from $w_y = 3\,\mu\text{m}$ to 10 µm. The peak potential is typically about $5\,\mu\text{K} \approx 1.5\,E_R$ and in transversal direction the wire beam has a waist of $w_x = 78\,\mu\text{m}$ which blocks atoms from flowing around the wire region.

The wire power is stabilized using a photodiode. The position of the wire in the horizontal plane is aligned via the microscope position, but the transport does not depend strongly on this alignment. The more sensitive position is the focus of the wire. Since the wires dark notch is close to the diffraction limit, it quickly disappears when the upper microscope is out of focus. Therefore, the transport experiments depend strongly on the position of the wire focus which has to be aligned at least once per day, even when running the experiment continuously. Before the continuous operation of the experiment the focus position was optimized every other hour.

Wall

The transport experiments need a well-defined beginning and end which is achieved with a wall beam. The wall beam is an elliptical beam at 532 nm which is slightly larger than the wire beam in transport direction $w_y = 8.6\,\mu\text{m}$ and of similar size in the transversal direction $w_x = 54\,\mu\text{m}$. For a typical wall power of 100 mW the peak potential is $8.5\,\mu\text{K} \approx 2.5\,E_R$ which blocks even the hottest atoms.

Gate

The previously discussed lightsheet and wire beams confine the cloud and in turn reduce the local density due to the increased zero point energy, i.e. $h(\nu_x + \nu_z)/2$. This means, that in practice there is no transport whenever only the repulsive constriction beams are operated such that the wire is a 1D constriction. The depletion of atoms is compensated by imposing an attractive gate beam on the cloud around the wire. The beam is provided by a 767 nm laser which is made up of a homebuilt tapered amplifier seeded by a homebuilt diode laser. The gate beam is a symmetric Gaussian beam with a typical waist of $w_{x,y} = 30\,\mu\text{m}$, though this waist can be adjusted via the fiber coupler of the beam from 25 µm to 45 µm. Typically, the gate beam can be operated up to a depth of 2.5 µK, as long as the lightsheet prevents atoms from leaving the trap via the beam. The gate beam is power stabilized using a photodiode and a PI loop which allows the precise tuning of the gate potential, necessary for transport experiments. The beams position can be modified using a motorized mirror (*NewFocus Picomotor*), utilized for daily alignments. In addition, fast position shifts are possible via a piezo driven tip/tilt mirror. This allows shifting the beam into one of the reservoirs before transport, e.g. for parametric heating of the cloud [87].

5.5 SPATIAL LIGHT MODULATION

Spatial light modulation has been used extensively in the experiment to create diffraction limited beams which are used to locally manipulate [61, 63, 101, 146, 147]. The concept of spatial light modulation refers to the spatial engineering of a light beams' wavefront which is transformed into a real-space pattern with a lens. Fourier-optics imposes that the complex amplitude of the light-field in the back focal plane of a lens is Fourier transformed into a complex amplitude in its focal plane. In the experiment, a digital micro mirror device (DMD) is used to devise the amplitude and phase of light. The application of the DMD in our experiment has been detailed in the semester theses of S. De Léséleuc [148], J. Mohan [149], in the master thesis of F. Rabec [150] and in the PhD thesis of M. Lebrat [36].

Here, we are going to detail the DMD setup build during this thesis which is used with near-resonant light at 671 nm while the previously built DMD setup was used to create repulsive potentials at 532 nm. Figure 5.8(a) shows a schematic of the optical setup used to project the light onto the atoms. The DMD (*Vialux V7000*) is an array of micrometer-sized mirrors $13.6 \times 13.6\,\mu\text{m}$ which have two tilt position settings at $\Theta = \pm 12°$ which is referred to as ON and OFF. The mirrors are operated by individual CMOS circuits, allowing fast switching speeds 22.7 kHz only limited by the mechanical ringing

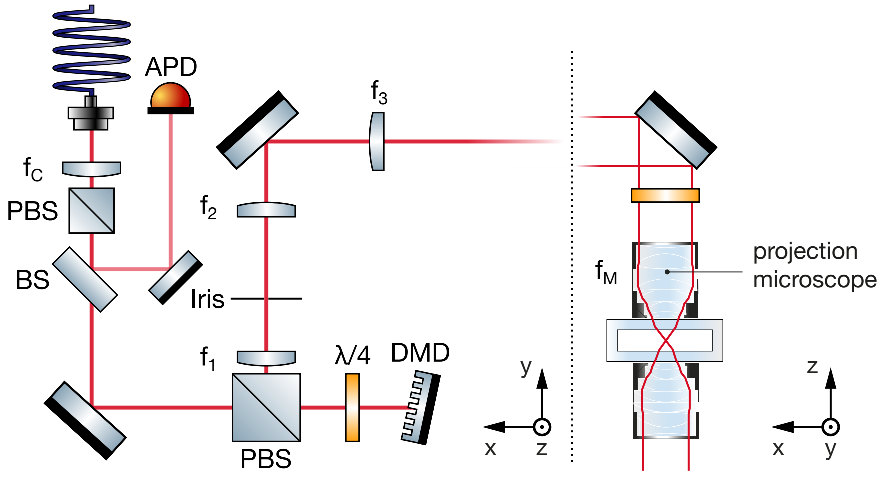

Figure 5.8: Optical setup for spatial light modulation using a DMD. The beam after the fiber is polarization cleaned using a polarizing beam splitter (PBS) and amplitude stabilized with an avalanche photodiode (APD). The waist of the beam is adjusted such that it fills the DMD area from where the light field is retro-reflected, due to the Littrow configuration, and separated from the incoming light with a quarter waveplate and a PBS. The telescope f_1, f_3 is used in Fourier configuration (f_2 is not present in the Fourier configuration) to adjust the beam waist such that it fills the microscopes clear aperture. Then the microscope is effectively in a $2-f$ configuration, with the DMD in the back focal plane and the atoms in the focal plane. Thus, the complex amplitude of the light field in the atom plane is a Fourier transform of the complex amplitude of the field on the DMD. Whenever the DMD is supposed to be imaged on the atoms, i.e. the imaging configuration, the lens f_2 is used to shrink the DMD mirrors in real-space by a demagnification of 50. Then the effective pixel size is $270 \times 270\,\mathrm{nm}^2$ on the atoms, allowing to grayscale an image with the DMD.

of the mirrors structure. The array of mirrors at an angle effectively acts as a blazed grating with $\theta_B = 12°$ when illuminated with light, creating a diffraction pattern with maxima at θ_m. The blazing condition imposes that the incident angle θ_i and diffraction angle are related, in order to maximize diffraction and specular reflection, via $\theta_i + \theta_m = 2\theta_B$. In order to keep the optical setup compact we chose to operate the DMD in the Littrow configuration, i.e. the incident angle θ_i and a diffraction order θ_m are equal, which is the case for the sixth diffraction order.

In the experiment a quarter waveplate and a polarizing beam splitter are used to separate the incoming light and outgoing diffraction order as shown in Fig. 5.8(a). The lenses following the DMD are chosen with the following restrictions:

- The optical setup needs to be convertible from imaging to Fourier configuration.
- The effective DMD mirror size on the atoms should be below the diffraction limit to allow non-binary amplitude modulation.
- The effective size of the DMD should cover the field of view of the microscope (see Tab. 5.2).
- The DMD beam before the microscope should fill its clear aperture CA = 18 mm to create diffraction limited features.
- The transmission through the microscope is above 50 %.

- Optical elements can only affect the DMD's optical path.

These restrictions can be fulfilled with this lens configuration where the second lens f_2 is used to switch between imaging and Fourier configuration.

	671 nm path	532 nm path
f_1	150 mm	200 mm
f_2	−50 mm	80 mm
f_3	300 mm	400 mm
f_M	18 mm	18 mm

The imaging configuration is used to image the DMD's mirrors onto the atoms with a demagnification of $M = 50$ which results in an effective pixel size of 270×270 nm, smaller than the diffraction limit. In turn, ~ 9 pixels are within a diffraction limited region. This enables "gray-scaling" an image by switching $0 - 9$ pixels on the DMD per diffraction limited spot on the atoms.

The Fourier configuration is achieved by having only three lenses f_1, f_3 and f_M after the DMD. In this configuration the DMD is effectively in the back focal plane of the microscope such that the wavefront in the DMD plane is Fourier transformed onto the atom plane. In order to actively modulate the wavefront, an additional grating is superimposed on the DMD by switching of half the mirrors at a certain period, called "supergrating". Distorting this supergrating by shifting it will modify the local phase of the light, while changing its width will modify the lights' amplitude. Thus, both amplitude and phase can be modified which is used to correct aberrations and project arbitrary potentials. The lens arrangement in the 671 nm path in the Fourier configuration (no f_2) leads to a magnification of $M = 2$ of the beam emanating from the DMD $2w_{\mathrm{DMD}} = 9.8$ mm (DMD area $14 \times 10.5\,\mathrm{mm}^2$) resulting in a beam diameter of $2w_M = 19.6$ mm in front of the microscope. We use an iris in the focal plane of the first lens f_1 to crop out the orders of the DMD diffraction which are not used for the spatial light modulation. Importantly, in Fourier configuration the DMD efficiency is low $< 3\,\%$ due to the limited diffraction efficiency, the amplitude modulation and the imposed supergrating. The initial alignment of the DMD setup is described in Ref. [71].

Due to the low power requirements when operating close to the atomic resonance with small beams the power on the DMD is often very low, i.e. the saturation parameter per power $\tilde{s} = I/I_{\mathrm{sat}}P$ at a waist of 1 µm is $\tilde{s} \approx 25\,\mathrm{nW}^{-1}$. For this reason an avalanche photo diode (APD, *Thorlabs APD*) is used to stabilize the power of the beam. In addition, it is often still necessary to place an optical attenuator in the path after the DMD to reach adequate intensities on the atoms.

Aberration Correction

Recently, the DMD has been operated exclusively in the Fourier configuration which allows us to correct aberrations due to the optical elements. In order to detect aberrations we use a technique similar to a Hartmann-Shack sensor, pioneered in Ref. [62]. The mirrors on the DMD are set to their OFF position, except a small circular aperture (e.g. $r_{\mathrm{HS}} = 20$ px) including the supergrating. This aperture probes a small region of the overall wavefront where the aberrations can be linearized to tilts of the wavefront. In the atom plane the tilts in the wavefront lead to position shifts of the focus position.

Moving the aperture over the DMD array the tilt of each individual section of the wavefront can be extracted which allows us to reconstruct its phase. The phase mismatch in the wavefront is compensated by locally shifting the supergrating and the process is iterated until we reach wavefront aberrations $< \lambda/10$.

Digital Holographic Amplitude and Phase Modulation

The amplitude in the atom plane is shaped by using a holographic technique which relies on amplitude and phase modulation in the DMD plane. For the applications in this thesis both amplitude and phase were modulated to shape a single Gaussian beam, while in principle more complex patterns can be created with pure phase modulation [149]. The technique in use here is called Lee-Hologram [151] which relies on a binary hologram.

The light field in the DMD plane $f(x, y)$ is related via a Fourier transform to the light field in the atom plane assuming a $2-f$ system

$$g(x,y) = e_l F\left(\frac{x}{M\lambda f_M}, \frac{y}{M\lambda f_M}\right), \tag{5.5}$$

where e_l is a pure phase factor, $F(\mathbf{k})$ is the Fourier transform of $f(\mathbf{r})$ and M is the magnification of the telescope preceding the microscope. The field on the DMD is given by the incident field $f_i(\mathbf{r})$ multiplied by the DMD transfer function $h(\mathbf{r})$. The transfer function is then specified by

$$A(\mathbf{r}) = |f(\mathbf{r})|/|g(\mathbf{r})|, \tag{5.6}$$

$$\phi(\mathbf{r}) = \arg\left[f(\mathbf{r})\right]/\arg\left[g(\mathbf{r})\right], \tag{5.7}$$

though only $A(\mathbf{r})$ can be affected directly on the DMD. The phase is modulated via the supergrating which modifies the local phase by shifts of the grating. The binarized transfer function $h_b(x_i, y_i)$ is then calculated from the target phase $\phi(\mathbf{r})$ and amplitude $A(\mathbf{r})$ using

$$h_b(x_i,y_i) = \Theta\left(\cos\left(\phi(x_i,y_i) + \frac{2\pi}{q_x\delta x}x_i + \frac{2\pi}{q_y\delta x}y_i\right) - \cos(\pi w(x_i,y_i))\right), \tag{5.8}$$

with Θ being the Heaviside function, the pixel size δx, the discretized pixel position x_i, y_i and the supergrating pitch specified by q_x, q_y. The parameter $w((r))$ specifies the filling fraction $[0, 1/2]$ of the supergrating – also called supergrating width – which can be used to modulate the amplitude, given

$$w(\mathbf{r}) = \frac{1}{m}\sin^{-1}\left(\frac{A(\mathbf{r})}{\max\left[A(\mathbf{r})\right]}\right), \tag{5.9}$$

where w changes the local diffraction efficiency which is proportional to the local amplitude. The target amplitude is normalized such that the minimal and maximal value correspond to $w = 0$ and 0.5 respectively. The field in the atom plane is then given by

$$g(x,y) = \mathcal{F}\left[h_b f_i\right]\left(\frac{x}{\lambda M f_M}, \frac{y}{\lambda M f_M}\right). \tag{5.10}$$

This holographic technique allows us to correct aberrations in our optical system which we use to obtain spot waists of ~ 1 µm for a DMD pixel area of 400 × 400 which was used in Ch. 8. With the second, 532 nm DMD path waists of 0.74 µm were achieved in the past [71].

6

TECHNICAL UPGRADES OF THE EXPERIMENTAL APPARATUS

CHAPTER CONTENTS

Over the years some parts of the experiment have become unstable and cumbersome to operate. Mainly the power limitations of the MOT laser caused by a degrading tapered amplifier and the lacking stability of the resonator lock were the two most time-consuming technical deficiencies. In addition, new ideas regarding spin-resolved absorption imaging and improvements in the understanding of atom-light interactions dictated more improvements. In this chapter the implemented technical upgrades of the apparatus are described. The upgrades focused on the one hand on the overall stability via a new resonator lock, a new MOT laser which alleviate power limitation and continuous data-logging to simplify troubleshooting. On the other hand new experimental techniques were implemented which allow spin-resolved absorption imaging as well as three-level atom light interactions.

In Sec. 6.1 the MOT laser based on a frequency doubled Raman fiber amplifier and its power distribution is described. Then Sec. 6.2 details the new optical setup and Field-Programmable-Gate-Array (FPGA) based Pound-Drever-Hall (PDH) lock of the resonator dipole trap. In the following Sec. 6.3 the spin-resolved absorption imaging is outlined while in Sec. 6.4 the laser setup used to address a three-level system is presented. Finally, in Sec. 6.5 a terse summary of the data-logging is given.

6.1 UPGRADE OF THE MOT LASER

In this section the new laser setup for the magento-optical-trap (MOT) and Zeeman slower is described. The degradation of the previous setup based on a tapered amplifier (*homebuilt*) for the Zeeman slower and a combined external cavity diode laser (ECDL) - tapered amplifier (*Toptica TA100*) for the MOT demanded a new laser setup. The old setup is described in detail in Ref. [79] and Ref. [73].

One of the main challenges for ultracold ^{6}Li experiments is the unavailability of proven and powerful laser sources. The proven solutions, i.e. tapered amplifiers, only provide $\sim 500\,\mathrm{mW}$ while other solutions [152] are unstable. We decided to use a combination of a new technology, called Raman fiber amplification [153] (RFA) combined with a proven technology in second harmonic generation [154] (SHG) using periodically poled lithium niobate [155] (PPLN) crystals. This approach provides high laser powers at 1342 nm which are doubled to produce 3.5 W of output power at 671 nm, though we found operating at this high power leads to laser power degradation of the RFA. Nevertheless, operating at lower powers allows a stable operation without degradation. The second harmonic generation was realized within the semester thesis of F. Rabec [156].

6.1.1 Raman Fiber Amplifier

The Raman fiber amplifier (RFA) is a commercially available (*MPBC RFA-1342-8W*) laser amplifier seeded by a narrow-linewidth ECDL source (*Toptica DLpro*) $\gamma = 10\,\mathrm{kHz}$.

Raman fiber amplification is harnessing the normally unwanted nonlinear process called stimulated Raman scattering [157] (SRS) where high optical powers inside a fiber lead to forward and backward photon scattering. The Raman process originates from vibrational states of molecules in the fiber which can be populated via a Raman process involving a virtual excited state and an emission in a red-detuned sideband. In optical silica fibers the SRS effect is known for a long time [158] and there have been extensive developments to use this effect for, intrinsically broadband, amplifiers for telecommunication applications [159–161]. Figure 6.1 shows the typical spectrum of the spontaneous Raman scattering inside a single-mode silica fiber, taken from Ref. [162]. The fiber is pumped at $\lambda_p = 526\,\mathrm{nm}$, while the resulting spectrum has frequency components at $\sim 25\,\mathrm{nm}$ from the pump wavelength. The Raman gain g is calculated from

$$\frac{P_{out}}{P_{in}} = \exp\left(g I_{p,0} L\right) , \tag{6.1}$$

where P_{out}, P_{in} are the signal input and output power, $I_{p,0}$ is the effective input pump intensity and L is the length of the fiber.

For the Raman fiber amplifier used in our experiment, the broadband amplification of the Raman process is used to amplify the seed laser at 1342 nm via the stimulated Raman process pumped at 1064 nm. This allows us to generate up to 9.5 W at 1342 nm from a 40 mW seed, i.e. a gain of $\sim$ 23dB. To achieve this output power the laser is pumped with 25 W of light at 1064 nm which most likely led to the observed degradation. The RFA had to be repaired once by the supplier due to an increase of back-reflection inside the fiber and concurrent decrease of output power. The supplier expected the wavelength multiplexer, used for combining and splitting the pump and seed light to be the reason for the degradation. After the repair the laser was fitted with a water cooling module which is supposed to increase its lifetime. Up until now – 8 months after the repair – we did not experience a degradation, though we operate the laser at about $\sim 4\,\mathrm{W}$ of output power. This power is enough for the MOT laser setup due to the high efficiency of the SHG setup.

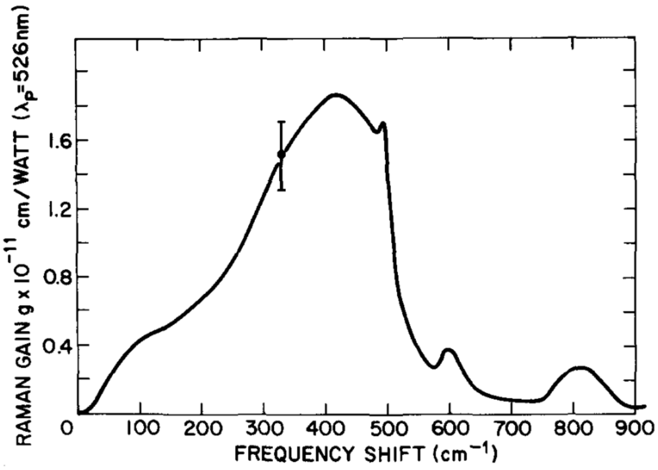

Figure 6.1: Typical Raman gain spectrum of an optical fiber. The Raman gain is displayed as function of the frequency shift from the pump wavelength $\lambda_p = 526\,\text{nm}$. The gain spectrum is broadband, having frequency components up to 552 nm. Taken from Ref. [162].

6.1.2 Second Harmonic Generation using Cascaded PPLNs

In order to generate light at the MOT frequency, the amplified signal at 1342 nm is doubled in frequency to 671 nm using two cascaded periodically poled lithium niobate crystals (PPLN) in quasi-phase matching (QPM) condition. Figure 6.2 schematically shows the process of second harmonic generation, which is based on the interaction between strong electromagnetic fields and the crystals' internal electric dipoles resulting in a nonlinear relation between polarization density P and electric field

$$P = \epsilon_0 \chi E + \chi^{(2)} E^2 + 4\chi^3 E^3 + \dots , \tag{6.2}$$

where $\chi^{(2)} = 2d$ and $\chi^{(3)}$ describe the strength of second-order and third-order nonlinear interaction, respectively. In case of second harmonic generation (SHG), given an electric field $E = [A(w)e^{iwt} + A^*(w)e^{-iwt}]$, the nonlinear polarization density is given by

$$P_{SHG}(t) = d\,A(w)A^*(w) + \text{Re}\left[d\,A^2(w)e^{i2wt}\right] , \tag{6.3}$$

where $A(w)$ is the complex electric field amplitude. The resulting polarization has a zero frequency component $P(0) = d\,A(w)A^*(w)$ as well as a $2w$ component $P(2w) = dA^2(w)$ which is the field we are interested in. In addition to the frequency matching condition given by $2w_1 = w_2$ there has to be a matching of wavevectors of the incoming and outgoing fields. Assuming incoming plane waves, the complex field amplitude is given by $A_1(w) = a_1 e^{-i\mathbf{k}_1\mathbf{r}}$ and the outgoing waves have to fulfill the phase matching condition

$$2\mathbf{k}_w = \mathbf{k}_{2w} . \tag{6.4}$$

The frequency- and phase-matching condition in conjunction provide a sustained interaction between light and medium in time and space. In a nondispersive media and for co-propagating waves the phase matching condition $2nw_1/c = nw_2/c$ is satisfied as long as the frequencies are matched

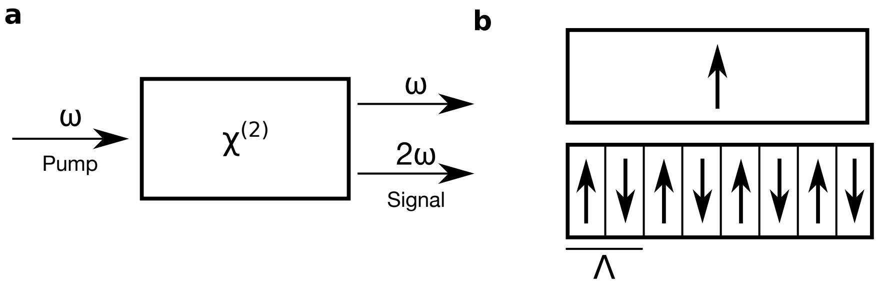

Figure 6.2: Second harmonic generation in a bulk crystal and in a periodically poled crystal. (a) The light at the input of the nonlinear material is called pump. The nonlinear process provides an upconversion of the incoming lights frequency to twice its value. The outgoing signal is at twice the frequency of the pump. The pump is still present at the output, due to the imperfect conversion efficiency. (b) In a bulk crystal (upper square) the nonlinear coefficient **d** has a constant direction in space, providing a decreasing SHG efficiency in space due to the dispersion in the crystal leading to a loss of the phase-matching condition. The distance over which the nonlinear process decoheres is given by the coherence length L_c. This decoherence in the bulk can be rectified by periodically alternating the direction of **d**, where the period is a multiple of L_c. The periodic poling leads to a new quasi-phase-matching condition which can be met tuning the temperature of the crystal.

$2w_1 = w_2$. In reality all media are dispersive the two conditions are independent

$$\begin{aligned} 2w_1 &= w_2\,, \\ 2n_w w_1/c &= n_{2w} w_2/c\,. \end{aligned} \tag{6.5}$$

Figure 6.2(b) shows a periodically poled crystal which we use to fulfill these conditions by inverting the nonlinear coefficient $n(z)$ after a period Λ. In a medium with position dependent nonlinear coefficient $d(\mathbf{r}) = d_0 e^{-i\mathbf{G}\mathbf{r}}$, here assumed to vary harmonically, the phase-matching is given by

$$2\mathbf{k}_w + \mathbf{G} = \mathbf{k}_{2w}\,. \tag{6.6}$$

Creating the harmonic position dependence is in practice not possible, but varying the nonlinear coefficient rectangularly with period Λ provides a Fourier series of harmonic function, one of which can be used to phase match the waves. The Fourier series is given by $d(z) = \sum_{m=-\infty}^{\infty} d_m e^{-i2\pi m z/\Lambda}$. The resulting phase-matching condition is

$$2w_1 n_w + m2\pi c/\Lambda = w_2 n_{2w}\,, \tag{6.7}$$

where the grating period $\Lambda = mL_c$ matches a multiple of the coherence length L_c of the SHG process. Here, the coherence length L_c is the length over which the nonlinear process stays efficient, i.e. $L_c = 2\pi/\Delta k$ where Δk is the phase mismatch of the waves. The quasi-phase matching is eventually achieved by tuning the refractive index of the media $n_i(T)$ via the temperature such that the condition in Eq. 6.7 is fulfilled.

The progress in fabrication of periodically poled crystals, in particular lithium niobate, via their ferroelectric properties allows us to use an easy to handle crystal to achieve high SHG efficiencies [163, 164] without the need of an enhancement cavity. In our SHG setup periodically poled, 5% MgO doped lithium niobate is used (*Covesion MgO:PPLN 40mm*), due to its higher damage threshold [165] compared to undoped PPLN. PPLN itself is advantageous for our application since it has a large nonlinear coefficient

$d_{333} = 25\,\mathrm{pm/V}$ [166] (crystal axis is aligned by manufacturer to extraordinary axis).

The previously discussed concepts of second harmonic generation were assuming plane waves and were valid in the undepleted pump approximation. In reality Gaussian beams are impinging on the crystal which will lead to diffraction inside the crystal. In essence, this means that there is an optimum waist in the crystal, between having a diffraction limited focus which would maximize intensity in a spot and having a collimated beam with constant waist along the direction of propagation. Boyd and Kleinman have solved the wave equations for SHG using Gaussian beams [154, 167] while assuming an undepleted pump. These results allow us to calculate the optimal waist and determine the waist position inside the crystal. The first finding is that the optimal waist position is always in the center of the crystal, i.e. the Gaussian beam has to be focused into the crystal. The second finding is that the length of the crystal is related to the optimal Rayleigh range z_R of the beam

$$L = 5.68 z_R \,, \tag{6.8}$$

which is known as the Boyd-Kleinman formula [167]. The optimal waist for our setup is $w_0 = 37.6\,\mu\mathrm{m}$. Importantly, the phase-mismatch $\Delta k = 2k_w - k_{2w}$ in the case of Gaussian beams is not optimal at $\Delta k = 0$ due to dephasing introduced by the Gouy phase. The quasi-phase matching condition for Gaussian beams is given by

$$2(n_w - n_{2w})w - 2\pi c/\Lambda = 3.2c/L \,. \tag{6.9}$$

The dispersion of the crystal varies with temperature which allow us to achieve the phase-matching condition. The temperature dependence of the refractive index is given by the Sellmeier equation [168, 169]

$$\begin{aligned} n^2(f(T),\lambda) &= a_1 + b_1 f + \frac{a_2 + b_2 f}{\lambda^2 - (a_3 + b_3 f)^2} + \frac{a_4 + b_4 f}{\lambda^2 - a_5^2} - a_6\lambda^2 \,, \qquad (6.10) \\ f(T) &= (T - 24.5)(T + 570.82) \,, \end{aligned}$$

where the wavelength λ is in units of μm and the temperature T in °C. The Sellmeier coefficients for MgO:PPLN can be found in Ref. [170]. For the crystal in use the poling period $\Lambda = 13.6\,\mu\mathrm{m}$ gives a phase-matching temperature of $T = 41.84\,°\mathrm{C}$.

Finally, to find the theoretical maximum of the SHGs conversion efficiency and the optimal length of the crystal for the maximal pump power, i.e. $P_{1342} = 9.5\,\mathrm{W}$ we have to include the pump depletion, leading to a saturation of the output. This turns out to be highly complicated when using Gaussian beams, which is why we use the analytic solutions for monochromatic plane waves [171]. For zero second harmonic input the conversion efficiency is given by

$$\eta = V_b^2 \mathrm{sn}^2\left(\frac{\Gamma L}{V_b}\middle| V_b^4\right) \,, \tag{6.11}$$

where sn is a Jacobi elliptic function. This formula simplifies in the case of perfect phase matching, i.e. $V_b = 1$, to

$$\eta = \tanh^2(\Gamma L) \,, \tag{6.12}$$

$$\Gamma = \sqrt{\eta_{\mathrm{norm}} I_w} \,, \tag{6.13}$$

$$\eta_{\mathrm{norm}} = \frac{8\pi^2 d_{\mathrm{eff}}^2}{n_w^2 n_{2w} c \epsilon_0 \lambda_w^2} \,. \tag{6.14}$$

Importantly, the conversion efficiency implies that having multiple crystals will lead to an enhanced conversion efficiency compared to having a single crystal of equal length. This stems from the fact that with two cascaded crystals a higher intensity in each crystal, due to the optimal waist condition from Boyd-Kleinman, will lead to a larger conversion efficiency. Here, we cascade two crystals which comes with an additional condition on the phase between the crystals [172]. The dispersion in air and in optical elements will lead to a phase mismatch between the signal E_{2w} and the pump E_w in the second crystal. The phase mismatch can be compensated via the distance between the crystals where the optimal phase difference is given by

$$\phi_{2w} - 2\phi_w = \pi/2 + m2\pi \,. \tag{6.15}$$

In addition, we avoid achromatic aberrations and dispersion in optical media by using two parabolic mirrors to collimate and refocus the beams into the second crystal.

6.1.3 Optical Setup for Second Harmonic Generation

Here, we discuss the optical setup used for second harmonic generation (SHG) with two cascaded PPLNs and the new power distribution used for the magneto optical trap (MOT) and the Zeeman slower.

Second Harmonic Generation with Cascaded PPLNs

Figure 6.3(a) shows the optical setup used for frequency doubling 1342 nm to the lithium MOT frequency, around 671 nm. Learning from the previous MOT setups we tried to keep the optical paths as short as possible which is not visualized in the schematic representation in Fig. 6.3. After amplification by the Raman fiber amplifier (RFA) the light passes through a half-wave plate in a precision rotation mount which allows to precisely adjust the polarization to the extraordinary axis of the crystal, optimizing the non-linear conversion efficiency. Following the mirror, the light is focused into the crystal using a lens ($f = 100\,\text{mm}$) mounted on a XY translation stage. The PPLN crystal is mounted in an oven (*Covesion Oven 40mm*) which is placed on a precision XYZ translation stage (*Thorlabs MBT616D/M*) in order to align the poling-aperture ($0.5 \times 0.5\,\text{mm}^2$) to the beam and the focus of the beam to the center of the crystal. A high precision $\sigma_T \lesssim 2\,\text{mK}$ temperature controller (*Meerstetter TEC-1091*) stabilizes the ovens' temperatures using a PT100 resistance temperature detector (RTD). The output of the first crystal is collimated, wavelength independently by a 90° off-axis parabolic mirror (*Thorlabs MPD129-P01*, $f = 50.8\,\text{mm}$) and is refocused by an equivalent mirror into the second crystal. The optimal distance between the two crystals was previously determined to be ~ 20.4 cm with an optical delay line. The second crystal is again mounted in an oven which is placed on a XYZ translation stage. The output of the second PPLN is passing a dichroic mirror splitting signal and pump light. The signal is collimated using a lens while the pump is discarded in a beam dump.

Alignment of the Doubling Crystals

The main conclusion of using the SHG setup based on PPLNs is that the optical setup is insensitive to alignment. During the manufacturers repair of the RFA the system was non-operational for ~ 2 months and did not require

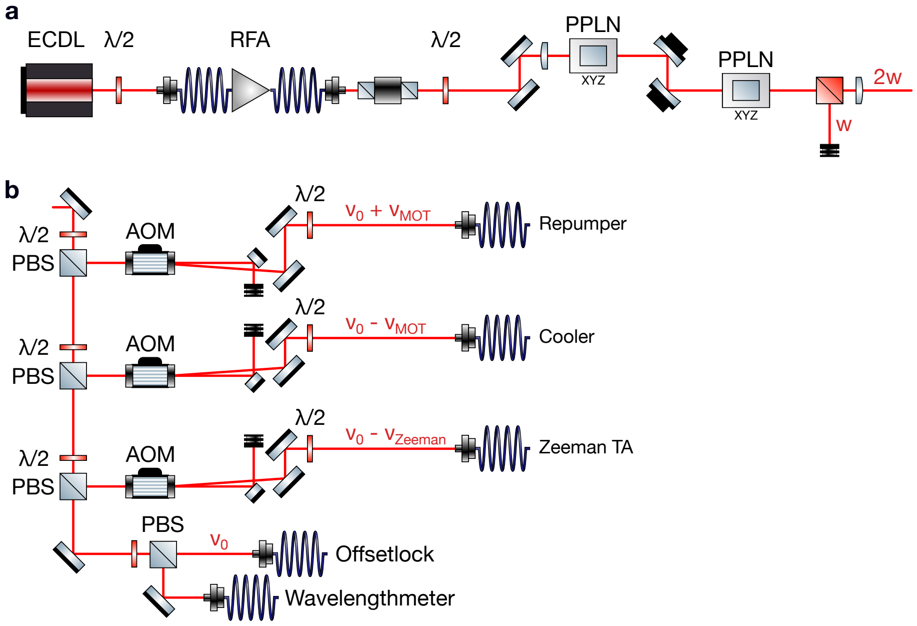

Figure 6.3: Optical setup for SHG and MOT power distribution. (a) The external cavity diode laser (ECDL) is seeding the Raman fiber amplifier (RFA) which produces up to 9.5 W of light at 1342 nm. The cascaded PPLNs are injected using two mirrors followed by a focusing lens on a translation stage, focusing the pump light to the optimal waist 37.6 µm in the center of the first PPLN crystal. The emitted signal and pump are collimated and refocused using two 90° off-axis-parabolic mirrors into the second PPLN. Afterwards, the signal and pump are separated using a dichroic mirror and the signal is collimated with a lens. (b) The MOT laser light created by the SHG is split into three different arms for cooler, repumper and Zeeman slower. The remaining light is sent to the offset lock photodiode and to the wavelength-meter. In the current configuration – operating the RFA at low powers – the Zeeman slower light is seeding a tapered amplifier (*Toptica BoostTA*) the output of which is then sent to the atoms.

realignment after the RFA's return. This insensitivity stems from the large aperture of the PPLN chips ($0.5 \times 0.5\,\mathrm{mm}^2$) with respect to the beam waist ($w_0 = 37.6\,\mu\mathrm{m}$) in the center of the crystal and at its interface ($w_\mathrm{I} = 113\,\mu\mathrm{m}$). Nonetheless, the initial alignment requires precision translation stages to find the aperture without tilting the crystal and the correct focus position inside the crystal. We found that during the initial alignment the second crystal was more sensitive to the alignment than the first one. This could be a result of the signal in addition to the pump at the input.

The major tuning knob for the efficiency of the SHG in the cascaded PPLNs is the temperature of the crystals. For a single crystal we find experimentally a temperature bandwidth of 1.55 °C, which was predicted to be 1.5 °C by theory. In case of a single crystal with twice the length this bandwidth would half, which indicates the challenge in finding the optimal temperatures of two crystals. In the light frequency domain we find a single crystal bandwidth of $\sim 25\,\mathrm{GHz}$ which is decreasing the same way for longer crystals. The interesting observation we made when optimizing the temperature of the two crystals is the necessity to '''walk" (equivalently to beam walking for fiber alignment) the temperature setpoint's to find a global optimum. The reason being that whenever the first crystal is at its individual peak efficiency the pump is depleted at its output leaving less pump intensity for the second crystal. Therefore, for each setpoint of the first crystals' temperature the second crystals' temperature has to be tuned to find a local optimum, which allows us to approach the global optimum via a gradient ascent. This large temperature dependence also meant that we needed a high quality temperature controller allowing us to stabilize in the 10 mK regime.

Temperature Controller

Here, the homemade integration of a commercially available temperature controller is introduced which allows us to stabilize adequate setups up to $\sigma_\mathrm{T} = 2\,\mathrm{mK}$ stability. The controller is a *Meerstetter TEC-1091* original equipment manufacturer (OEM) device which is originally designed to control Peltier elements. For us, the footprint of the device $65\,\mathrm{mm} \times 38\,\mathrm{mm}$ combined with its large cooling power 42 W and good software made it the best choice for our application. The manufacturer specified temperature precision and stability to be at least 0.01 K which we are able to surpass.

For the operation of the TEC-1091 we designed a printed circuit board (PCB) which allows us to make use of the full flexibility of the device. The temperature measurement on the system side can be performed in either 2-Wire configuration which allows a simultaneous 2-Wire measurement on the heat sink side or in 4-Wire configuration which negates the heat-sink measurement option. We also integrated a connector to the fan control of the TEC-1091 which allows us to use a speed controlled fan on the heat sink side if necessary. Finally, the optionally available display is integrated into the front panel of the PCB in addition to a rotary encoder and a USB port which allows controlling the temperature and accessing the software, respectively.

The software is useful due to the access to every possible setting of the controller, including the PI parameters, resistance-temperature look up tables, display settings etc. In addition, the manufacturer provides an automatic tuning algorithm for the PID parameters which works well, allowing us to achieve the high precision without having to tune any PID parameter by hand.

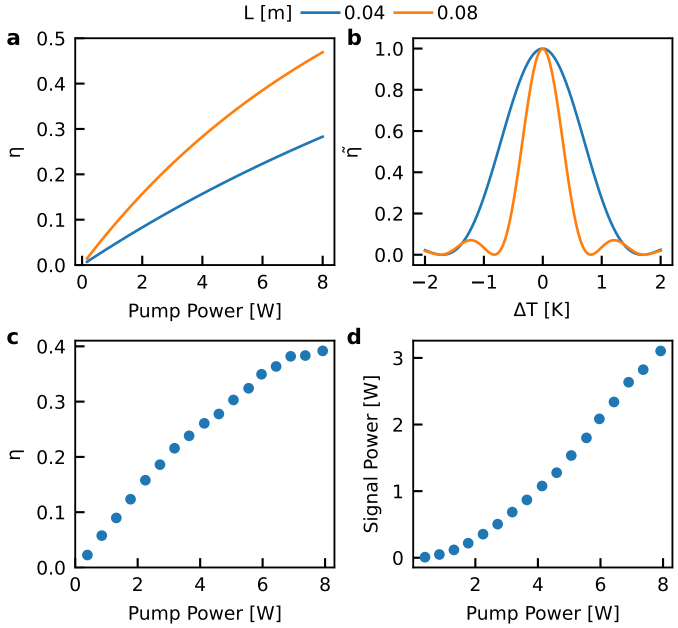

Figure 6.4: SHG efficiency and output power. The theoretical nonlinear conversion efficiency (a) as a function of the pump power shows a saturation behavior at high powers due to the pump depletion, see Eq. 6.12. The comparison between crystals of different lengths shows that the longer crystal has a larger efficiency but also smaller quasi-phase-matching temperature width (b). The measured nonlinear conversion efficiency η (c) is displayed as a function of the pump power at 1342 nm. The maximal efficiency we reached was 39 % at an input power of 8 W. The disparity between theory and experiment comes from thermal gradients within the crystal, the photorefractive effect [173] and the dispersion in air. (d) The output power at 671 nm is displayed for varying pump powers. At the highest pump power we can produce 3.1 W of light at the MOT frequency.

RFA and SHG Performance

In this section the performance of the Raman fiber amplifier, the SHG setup as well as the new MOT power distribution is discussed.

The Raman fiber amplifier in its repaired version, i.e. with a water cooling circuit, can produce up to 9.5 W of light at 1342 nm. Due to the previously described degradation, most likely due to a defect wavelength demultiplexer, we operate it at much lower powers of around 4 W. The RFA has two modes of operation, a constant power and a constant current mode. We operate in the constant current mode since we found that the constant power mode leads to an unforeseen switch-off behavior whenever the reflection photodiode inside the laser receives too much power. This photodiode triggers an interlock mechanism whenever the Raman scattering leads to spontaneous back-reflections which can hurt the seed laser. Since the reflection is correlated with the gain of the laser, we operate at a constant gain, i.e. constant current, to achieve a stable operation. In terms of frequency stability and linewidth, the ECDL-RFA combination outperforms our former setup, operating at 671 nm. The ECDL seed has a native linewidth of 10 kHz over 100 ms which is more than an order of magnitude better than an ECDL at 671 nm. In addition, the mode-hop free tuning range is ~ 40 GHz which allows for stable operation without re-locking during the day-to-day operation. Finally, the fiber amplifier naturally provides a high quality, Gaussian beam at its output which is hardly altered by the SHG, thus allowing for high fiber coupling efficiencies and no need for beam shaping.

Figure 6.4 displays the performance of the cascaded PPLN SHG in terms of efficiency and output power. The efficiency is initially increasing linearly before reaching the pump depletion regime, where a saturation behavior sets in, following the predicted behavior, see Eq. 6.12. The theoretically achievable efficiency is $\eta = 0.47$ for a crystal with length $L = 80\,\mathrm{mm}$, which assumes perfect phase matching between two cascaded crystals. The temperature bandwidth of the quasi-phase-matching is 1.5 K for the short crystal and 0.75 K for the long crystal. The measured nonlinear conversion efficiency (see Fig. 6.4(c)) follows the theoretically expected behavior. We find its peak value $\eta = 0.39$ to be below the theoretically expected value which has several reasons. The dispersion in air is not perfectly compensated and thermal inhomogeneity within the crystal [174] lead to a reduced conversion efficiency. In addition, the photorefractive effect [173] leads to a modification of the refractive index via the excitation of electrons, leading to an increased absorption and reduction of conversion efficiency. The measured output power at 671 nm shows that we can reach up to $P = 3.1\,\mathrm{W}$ which is four times bigger than the available power in our previous, tapered amplifier based, MOT setup. In addition, the mode of the light is good, which allows us to inject $> 70\,\%$ of light into an optical fiber. Finally, the high efficiency allows us to operate at much lower pump powers and still achieve adequate MOT beam intensities, thus reducing the RFAs degradation in the long term.

6.1.4 MOT Power Distribution and Frequency Lock

Following the separation of wavelength' after the SHG, the MOT light is collimated to a waist of $w_0 = 1\,\mathrm{mm}$ and split, using polarizing beam splitters, into the different MOT beam paths. Figure 6.3(b) shows the optical setup for the repumper, cooler and Zeeman slower beams, the path to the offset-lock [175] and the path to the wavelength-meter (WLM, *HighFinesse WS8-2*).

The main change from the previous frequency locking scheme is that the Zeeman slower light is now coming from the frequency shifted MOT laser and not directly from the Reference laser. The old locking scheme is described in detail in Ref. [73]. The new MOT frequency lock is shown in Fig. 6.5(a) where the ECDL at 1342 nm is used for feedback which does reduce the PI-loops' bandwidth due to the long fiber inside the RFA. We do not see any negative effects of this reduced bandwidth, mainly due to the stable and narrow laser diodes in the infrared regime. The frequencies for the MOT beams and the Zeeman slower are all created using AOMs driven by radio frequencies. This also allows us to stabilize the beam powers after the fiber on the experimental table using an analog PI loop (*NewFocus LB1005*).

The optical setup for this purpose is shown in Fig. 6.3(b). Care has been taken that all beam paths are short and efficiencies of AOMs $> 80\,\%$ and fiber couplings $> 70\,\%$ are high. Besides the MOT beams, the light is sent to the wavelength-meter which allows quick troubleshooting of the laser frequency. The AOM's and the fiber-couplers are placed in kinetic mirror mounts, allowing us to reduce the amount of mirrors needed for beam walking. The MOT laser is shifted by half the hyper-fine-structure splitting $\nu_{=}\mathrm{MOT} = +228\,\mathrm{MHz}/2$ to the blue such that it is red-detuned by

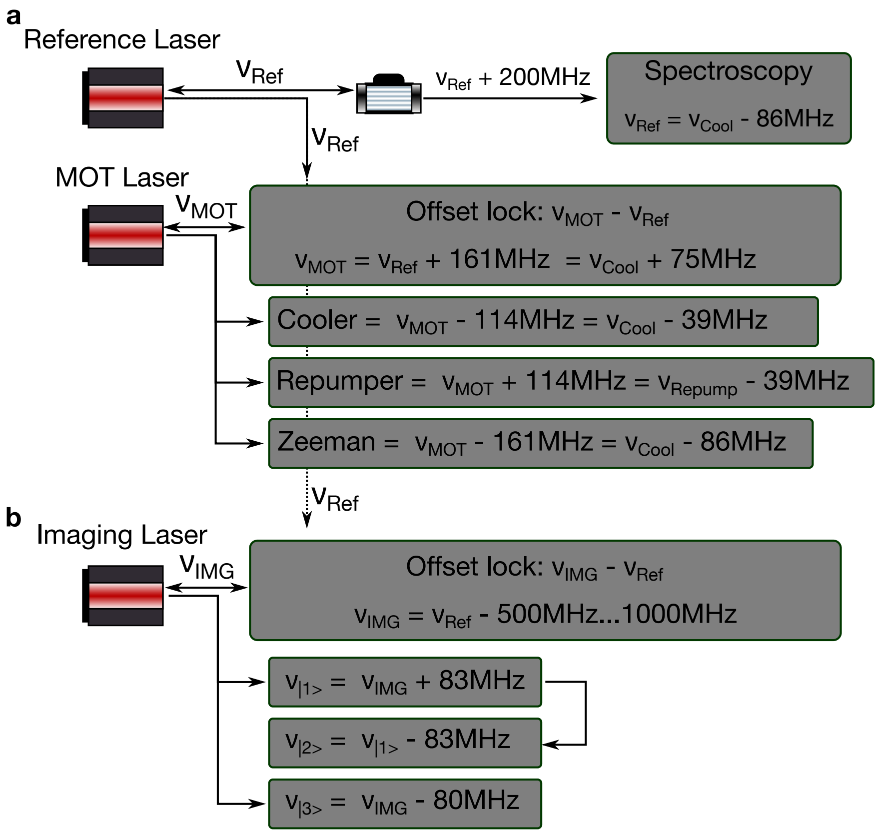

Figure 6.5: MOT and imaging laser offset lock. The reference laser is frequency locked with a 200 MHz offset to the crossover line between the cooler and repumper transition using frequency modulation, Doppler-free absorption spectroscopy. The MOT laser (a) is then locked to the reference laser using the beat-note between the two lasers which is frequency shifted by 161 MHz via a radio frequency mixer. The MOT beams, i.e. cooler and repumper, are then created by shifting the MOT light symmetrically, using an AOM, by ± 114 MHz such that both beams are red-detuned by -39 MHz from their respective transition. During the compression of the MOT to the compressed-MOT these detunings are linearly ramped via the offset lock frequency. The Zeeman slower beam is shifted by -161 MHz with an AOM which red-detunes it by -86 MHz from the cool-transition. (b) The imaging laser is offset-locked in the same way the MOT lasers is, but with a bigger and more tunable offset of $500 \ldots 1000$ MHz. The imaging light for the three lowest hyperfine states $|1\rangle$, $|2\rangle$, $|3\rangle$ is created using AOM's shifting the imaging frequency to the respective transitions.

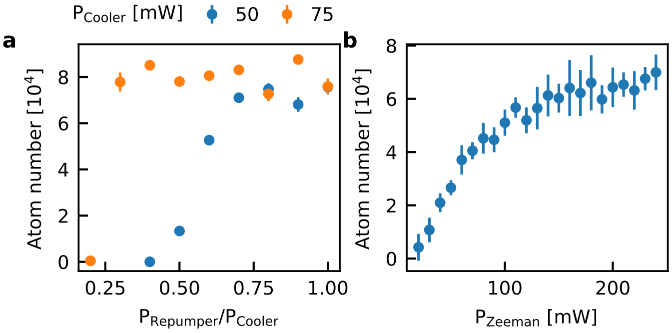

Figure 6.6: MOT and Zeeman slower power. (a) The final atom number saturates for both a lower cooler beam power (blue circles) and for a high cooler beam power (orange circles). In the limit of lower power the repumper beam power has to be increased to achieve the maximal atom number. This shows that in lithium both the cooling and repumping transition are of similar importance for the laser cooling and the beams can be used to compensate each-others power and still achieve the same laser cooling performance. (b) The Zeeman slower performance in terms of final atom number shows no clear saturation behavior at large Zeeman slower beam powers. This behavior is likely related to the lithium coating on the entrance window of the Zeeman slower beam, reducing its intensity on the atoms.

$-39\,\text{MHz}$ of the repumping transition $2^2S_{1/2}, F = 1/2 \rightarrow 2^2P_{3/2}, F = 3/2$, which creates the repumper beam. For the cooler beam, the MOT laser is shifted in the opposite direction $-114\,\text{MHz}$ by an AOM such that it is red-detuned ($-39\,\text{MHz} = -6.5\Gamma$) from the cooling transition $2^2S_{1/2}, F = 3/2 \rightarrow 2^2P_{3/2}, F = 5/2$. This detuning is reduced during the compression of the MOT to the compressed-MOT to about $3\,\text{MHz}$. The Zeeman slower beam is shifted by $-161\,\text{MHz}$ which detunes the beam $-86\,\text{MHz}$ from the cooling transition. We find that the addition of a repumping beam to the Zeeman slower increases the loading by about 20 %, but do not use it in the experiment.

In case of the moderate MOT laser power, i.e. 1.7 W, we are saturating the repumper beams power-lock photodiodes on the experimental side ($P_{\text{Repumper}} = 100\,\text{mW}$). Figure 6.6(a) shows that increasing the MOT power to these values does not increase the atoms number in the experiment, operating both cooler and repumper beams at a similar power $P_{\text{Cooler,Repumper}} > 50\,\text{mW}$ gives the maximal atom numbers. This indicates that the experiment is not limited by the MOT loading but by the following evaporation and transfer steps. The Zeeman slower on the other hand is power limited, mostly due to the coating on the Zeeman slower beam entrance UHV-viewport from the continuous atomic beam, which reduces its transmission.

6.2 UPGRADE OF THE RESONATOR DIPOLE TRAP

In this section we discuss the newly implemented optical setup of our first evaporation stage within an optical resonator and the electronics used for the stable PID loop configuration. The resonator dipole trap is the first evaporation stage in the experiment following the laser cooling in the MOT. It is therefore required to have a large volume and trap depth such that the rather hot $T_{\text{cMOT}} \approx 500\,\mu\text{K}$ and not-so dense $w_{\text{CMOT}} \approx 1\,\text{mm}$ Lithium cloud can be captured after the compressed MOT. For this reason a large waist, high power dipole trap was built using an in-vacuum optical resonator, pro-

Resonator parameters	Values	
Length	L	0.149 75 m
Mirror Radius of Curvature	R1 / R2	150 mm / ∞
Mirror Reflection	R	99.98(5) %
Mirror Transmission	T	150 ppm
Loss Parameter	α_s	721 ppm
Finesse	$\mathcal{F}$	10200
Linewidth	$\Delta\nu$	98 kHz
Free Spectral Range	ν_{FSR}	1 GHz
Intensity Enhancement	S	1580

Table 6.1: Cavity parameters of the in-vacuum resonator dipole trap. From the measured finesse $\mathcal{F}$ and the assumed the mirror reflection R, the loss parameter α_s and the intensity enhancement S were calculated. The finesse $\mathcal{F}$ was measured from a cavity-ring-down measurement. Linewidth and free spectral range are determined from the cavity spectrum. Table adapted from Ref. [73].

viding optical enhancement of the light intensity ×1500 and is therefore operated with a large waist $w_{\perp,L/2} = 550\,\mu\text{m}$. The cavity parameters of the optical resonator in-vacuum are given in Tab. 6.1. The finesse $\mathcal{F}$ measurement and the derivation of the other parameters is described in detail in Ref. [73].

The shortcomings of the old optical resonator and its electronics are

- **Long, unstable optical beam path.** The light from the original laser (*Coherent Mephisto 2W*) was sent in free space $L_{path} \approx 2\,\text{m}$ through many optical elements before being coupled into the optical cavity.
- **Low power.** The laser beam power in front of the resonator was limited to ~ 700 mW.
- **Single pass AOM.** The AOM used for amplitude stabilization and fast laser frequency feedback was in single pass configuration. Thereby, the frequency feedback affects the spatial resonator coupling via the AOM deflection angle.
- **High frequency EOM.** The resonance frequency of the EOM $f_c = 228\,\text{MHz}$ was too large for the linewidth of the resonator $\Delta\nu = 98\,\text{kHz}$ therefore not allowing an optimal sideband modulation depth.
- **Frequency Lockbox.** The frequency lockbox was analog and modified to be able to lock the resonator. There was no possibility for a relock feature.
- **Fast frequency lock.** The fast frequency lock was only adjusted via a P-gain, thereby not providing a proper lock.

All these shortcomings together meant that the experiment could not be run without an operator in the lab, since the resonator had to be re-locked several times per day.

Implementing several optical as well as electronic upgrades to the resonator setup, which will be discussed in the following, allowed us to overcome the main limitations of the setup. In the current, upgraded state, the system can operate without supervision 24/7 and only rarely needs realignment to achieve its maximal loading efficiencies.

6.2.1 Improved Optical Setup

The improved optical setup is shown in Fig. 6.7 and includes three fiber connected parts used for (a) laser amplification and frequency sideband generation, (b) amplitude stabilization and fast frequency feedback. Figure 6.7(c) shows the resonator in-coupling setup, the PDH photodiode and the transmission photodiode.

Starting from the seed laser (*Coherent Mephisto 2W*), which is operating at a wavelength of 1064nm and with a power of about $1\,\mathrm{W}$, most of the light is discarded into a beam dump using a polarizing beam splitter (PBS), before injecting a Ytterbium doped fiber amplifier (YDFA, *Nufern PM-1064 10W*) which can provide up to $10W$ of output power.

The output light is sent through a wedged electro-optic modulator (EOM) phase modulating the light at $\nu_{\mathrm{EOM}} = 5\,\mathrm{MHz}$, thus providing frequency sidebands for the Pound-Drever-Hall (PDH) lock [176, 177]. The wedge in the EOM crystal is of particular importance here since it allows us to reduce offset drifts in the lock signal originating from residual amplitude modulation at the sideband frequency tremendously [178, 179]. Residual amplitude modulation stems from etaloning and the imperfect alignment between the polarization of the light and the modulation axis, i.e. the crystals' principal axis. The alignment will drift over time leading to a drift of the zero baseline of the PDH lock signal, thereby degrading the performance. The EOM crystal is birefringent, i.e. $n_\perp \neq n_\parallel$, thus adding a wedge along one of the crystals' principal axis will deflect the light polarized along this axis at a different angle compared to the light which is not polarized along this axis. Thus, the wedge spatially separates the incoming signal into two components of pure polarization. The resulting amplitude modulation can be easily compensated with an AOM. In addition to the wedge, we use a Peltier element, i.e. a thermoelectric cooler (TEC), to stabilize the temperature of the crystal to $\Delta T \approx 2\,\mathrm{mK}$, thus reducing drifts in temperature which can affect the aforementioned alignment and the crystals' refractive index. In principle, we could have an additional feedback on the DC-port of the EOM which would allow us to further reduce drifts of the modulation depth via an offset voltage [178].

The phase modulated light is sent through a fiber to a double pass AOM setup operating at $\nu_{\mathrm{AOM}} = 200\,\mathrm{MHz}$ (*Gooch'n'Housego 200MHz*). This double pass setup in cat-eye configuration [180] allows us to control the amplitude of the light using the cavity transmission and fast frequency feedback for the cavity lock without changing the cavity alignment. For the frequency modulation a homebuilt AOM driver is used based on a voltage controlled oscillator (*MiniCircuits ROS-244+*) with a modulation bandwidth of $\Delta\nu = 50\,\mathrm{MHz}$, thus allowing a very fast frequency lock to the resonator.

The light after the double pass AOM is sent through a final fiber to the optical setup used for the cavity injection. The beam is collimated after the fiber, deflected by three kinematic mirrors, followed by the resonator coupling lens mounted in an XYZ translation stage. The waist of the beam is focused on the first cavity mirror and the angles are adjusted using the two mirrors for optimal coupling efficiency. The sidebands, reflected off the first resonator mirror are sent to a homebuilt photodiode, placed after one of the coupling mirrors. The leakage light through the mirror is enough for the PDH lock. The transmission of the resonator goes partly to another homebuilt photodiode which is used for the amplitude stabilization and the

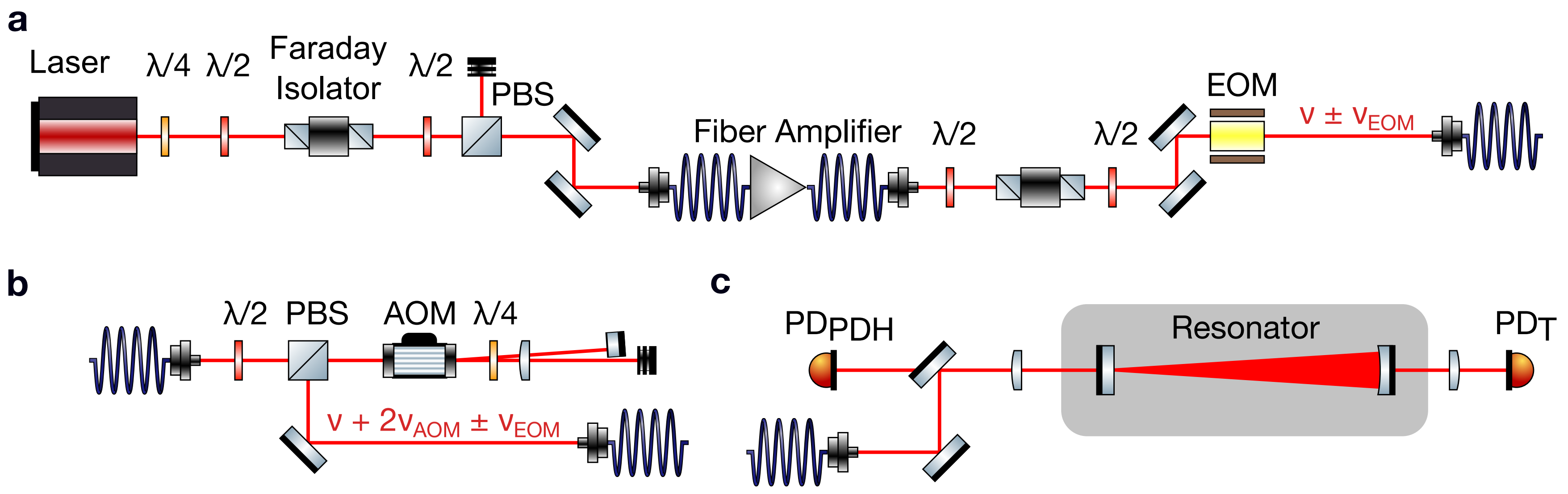

Figure 6.7: Optical setup resonator trap. The optical setup used for frequency stabilizing the laser to the resonator and amplitude stabilizing the resonator transmission is shown. It is split into three fiber connected parts, here (a)-(c). (a) The 1064 nm seed laser (*Coherent Mephisto 2W*) is coupled into a fiber amplifier (*NuFern SFA-PM1064-10W-0*) providing sufficient power for the dipole trap. The output of the fiber amplifier is sent through a wedged electro-optic modulator (*Qubig PM7-SWIR-5MHz*) to create sidebands for the Pound-Drever-Hall locking scheme. (b) For amplitude stabilization and evaporation the beam is sent through a double pass AOM (*Gooch'n'Housego 200MHz*), thus also allowing fast frequency feedback. (c) For the optimal resonator coupling the beam is sent to the cavity with the minimal amount of optics after the fiber. The reflection from the resonator is collected with a homebuilt photodiode via the leakage of a mirror, the transmission is measured with a homebuilt photodiode after the resonator.

evaporative cooling, most of the transmitted light is discarded in a beam dump.

Optical Lattice Cancellation

One of the major drawbacks of using this kind of optical resonator as a dipole trap is the intrinsic standing wave lattice formed by the retroreflected light. We tried to get rid of this lattice by adding frequency sidebands at the free spectral range of the resonator [74]. Optical cavities are resonant, whenever a wave fits into them with knots at the mirrors, the distance in frequency of such waves is given by the free spectral range (FSR). Sidebands, generated at $\pm\nu_{\mathrm{FSR}}$ are $q+1$ and $q-1$ orders of transmission through the cavity. This means that in the center of the cavity, the sidebands and the carrier are perfectly out of phase leading to a flat intensity profile.

The free spectral range of our resonator is around $\nu_{\mathrm{FSR}} \approx 1\,\mathrm{GHz}$ making it technically difficult to achieve the required modulation depth $\alpha = 1.2$ [74]. We managed to achieve this modulation depth by using a double pass EOM (*Qubig PM9-NIR*) reducing the RF power requirements by $-6\,\mathrm{dB}$.

Nevertheless, we did not manage to see a loading or cooling improvement with the lattice cancellation. The most probable reason being that our resonator is asymmetric. Hence, the atoms in the center will experience an acceleration towards the flat, incoupling mirror whenever the intensity profile is flat.

6.2.2 Upgraded Electronic Setup

The main improvement for the frequency lock of the resonator is the use of a digital, FPGA based proportional-integral (PI) controller, i.e. the RedPitaya STEMLab 125-14, in conjunction with a computer based re-lock mechanism.

Figure 6.8(a) schematically shows the electronics generating a stable error signal. The EOM is driven by the EOM driver (*Qubig QDR200-HD*) with $\nu_{\mathrm{EOM}} = 5\,\mathrm{MHz}$. The EOM driver has an integrated RF heterodyne mixer which demodulates the reflection signal of the optical cavity from the PDH photodiode. The error signal is encoded in the sideband $\pm\nu_{\mathrm{EOM}}$ amplitude, encoding the phase of the reflected carrier. Demodulating the PDH photodiode signal at the EOM drive frequency ν_{EOM} with a phase of $\pi/2$ gives the low frequency error signal V_{err} at the mixer output. In addition, the driver provides an internal EOM-resonance locking scheme which optimizes the EOM drive frequency to be resonant with the EOMs' LC-circuit. This allows us to operate at a more stable error-signal slope, i.e. feedback gain. The error signal V_{err} is sent through an analog divider (*Analog Devices AD734*) before going to the digital PI lock box. The analog dividers inputs are adjusted such that the output stays constant when the laser power is reduced during evaporation

$$V_{\mathrm{out}} = 10\left(\frac{Z_2 - V_{\mathrm{in}}}{V_{\mathrm{set}} - X_2}\right), \tag{6.16}$$

where V_{set} is the voltage set-point for the resonator transmission and Z_2, X_2 are adjustable voltages. The analog divider has a large enough bandwidth (GBP $= 200\,\mathrm{MHz}$) to not reduce the overall bandwidth of the frequency feedback loop. The digital PI lock is generated using a RedPitaya *STEMlab 125-14* which is an FPGA with two fast inputs $\sim 50\,\mathrm{MHz}$ and two fast outputs $\sim 50\,\mathrm{MHz}$ as well as additional, slower analog input/output's (IOs). At

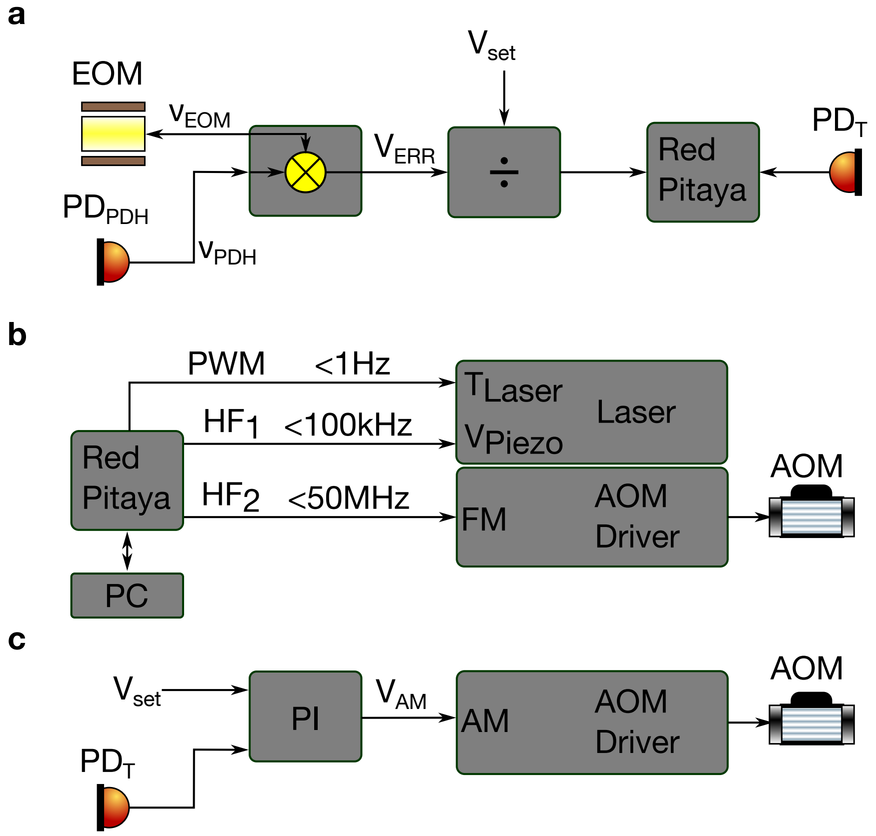

Figure 6.8: Electronics setup for resonator frequency locking and amplitude stabilization. (a) The schematic electronics setup used to create the error signal for the PDH frequency lock of the laser to the optical resonator. The EOM driver (DR, *Qubig QDR200-HD*) is creating the signal (LO) for the laser sidebands and demodulates the reflection signal (RF) of the cavity coming from the PDH photodiode using an integrated RF heterodyne (HD) module. The error signal (IF) is sent to an analog divider and from there to the RedPitaya FPGA (*STEMLab 125-14*) which is used for the frequency feedback. The RedPitaya also receives the transmission signal of the resonator. (b) The frequency lock scheme, includes three PI loops in different frequency and tuning range regimes. Slow feedback (< 1 Hz) is provided via pulse-width-modulation (PWM) to the temperature set-point of the laser. Fast feedback (< 100 kHz) from one of the high frequency outputs of the RedPitaya is going to the piezo inside the laser. Ultra-fast feedback (< 50 MHz) is achieved via frequency modulation of the double pass AOM. (c) Amplitude stabilization is realized with an analog PI lockbox (*New Focus LB1005*), provided a set-point from the experimental control. The PI lockbox subsequently controls the amplitude of the double pass AOM drive frequency.

one of the fast inputs of the RedPitaya an additional voltage divider limits the input voltage to the maximal range of $V_{pp} = 2\,\mathrm{V}$. The second input of the RedPitaya is connected to the transmission photodiode of the resonator, the signal of which is used for the re-lock scheme.

Figure 6.8(b) shows the frequency feedback scheme provided by the RedPitaya, allowing us to have frequency feedback in a range from 0 to $< 50\,\mathrm{MHz}$ with large tuning ranges. Once the error signal is digitized inside the RedPitaya, the vast toolbox of digital signal processing, provided here by the PyRPL software package [181] can be used. The use of digital filters enable us to easily split the feedback loops into different bands of the frequency spectrum.

- **Laser temperature feedback.** The temperature of the laser which has the largest frequency tuning coefficient $\sim 3\,\mathrm{GHz/K}$ and tuning range $\sim 30\,\mathrm{GHz}$ is at the same time responding the slowest $< 1\,\mathrm{Hz}$. Thus, we use one of the pulse-width-modulation (PWM) outputs of the RedPitaya which after external low-pass filtering provides a good DC signal. The error signal provided to the PI loop for the temperature stabilization is digitally low-pass filtered such that the feedback does not interfere with the other PI loops.

- **Laser piezo feedback.** The voltage applied to the piezo inside the laser provides intermediate frequency feedback both in terms of bandwidth $< 100\,\mathrm{kHz}$ and frequency tuning coefficient $\sim 1\,\mathrm{MHz/V}$. One of the fast outputs of the RedPitaya is connected to a high voltage amplifier $G = 18\,\mathrm{V/V}$ with a limited bandwidth $< 30\,\mathrm{kHz}$. Again the error signal is digitally filtered to prevent crosstalk between the feedback loops.

- **AOM frequency feedback.** Frequency modulation of the double pass AOM provides the fastest possible frequency feedback. In principle the voltage controlled oscillator allows us to modulate with $50\,\mathrm{MHz}$ with a tuning coefficient of $6\,\mathrm{MHz/V}$, though the overall tuning range is limited by the double pass AOM alignment.

This combination of feedback loops provides a good lock on the main resonance of the resonator, though mechanical stress, temperature fluctuations and laser mode jumps can bring the laser out of lock. For that reason we implemented a re-lock algorithm running on the host computer of the RedPitaya which, in our experience, always finds the locking point again. Once the laser is out of lock the software starts sweeping the piezo voltage to find the cavity resonance. Once a resonance is found the peak transmission is compared to the expected value and if it is too low, i.e. the laser is locked to a higher order resonator mode, the sweep is continued. In the case where no resonance is found within the piezo tuning range, which is smaller than the free spectral range, a new, slow sweep is started on the temperature set-point of the laser. Its large tuning range, beyond the free spectral range, allows us to find a cavity resonance and lock the laser to it.

The amplitude stabilization displayed schematically in Fig. 6.8(c) is based on a standard, analog PI loop. The amplitude set-point V_{set} is subtracted from the resonator transmission signal, provided by the transmission photodiode, generating the error signal. The control signal is sent to a voltage variable attenuator (VVA) inside the AOM driver which reduces the RF output power of the double pass AOM driver thereby changing the laser power in the first order of the AOM diffraction. The bandwidth of this feedback is limited by the VVA to $\sim 100\,\mathrm{kHz}$.

6.2.3 Further Improvements

Though we already achieved a 24/7 unsupervised operational state of the resonator trap there are possible improvements to increase the overall atom number, temperature and stability of the system.

- **Amplitude noise.** One major improvement would be to apply the experiences we made in the frequency lock to the amplitude stabilization. It is possible to use two photodiodes operating with different bandwidths to increase the dynamic range and the signal-to-noise of the system. The first, slow photodiode ($< 10\,\text{Hz}$) would have lower noise and a larger dynamic range in this frequency range. The second, fast photodiode would provide the means to remove any high frequency noise on the amplitude, thereby reducing noise related atom losses in the trap. In combination, this setup reduces the overall noise and allows us to evaporate to a lower laser power, possibly increasing the atom number and reducing their temperature.

- **PDH error signal.** In the current setup, the slope of the frequency feedback error signal is kept constant using an analog divider. We find that in the current setup, the open-loop division leads to an imperfect stabilization of the feedback gain. Alternatively, it is possible to use an AOM before the PDH photodiode to actively stabilize the amplitude of the reflection signal on the photodiode, thereby generating a constant feedback gain.

6.3 SPIN-RESOLVED ABSORPTION IMAGING

In this section, we discuss the upgrade of the low-resolution, horizontal absorption imaging system. The new imaging system allows multi-spin imaging in a single experimental run at high magnetic fields without the need for a Stern-Gerlach pulse [182] or phase-contrast imaging [183]. The spins are imaged in multiple imaging shots, in quick succession using a high-speed shift of the cameras' pixels. A more detailed description of the new imaging system can be found in Ref. [80].

This technique is the simplest applicable form of spin resolved imaging for lithium due to the constraints given by the low mass of the atoms and the magnetic fields we have to operate at in order to apply our thermometry. Both, the mass and the large homogeneous fields, make techniques like Stern-Gerlach pulses difficult to implement due to the short time of flight, while phase-contrast techniques require tedious calibrations to obtain trustworthy atom numbers.

In the following sections we are going to introduce the optical setup used to generate the imaging light and set its frequency as well as the readout and calibration methods.

6.3.1 Optical Setup for Spin-Resolved Imaging

Figure 6.9(a) shows the optical setup before the imaging fiber used to generate short pulses of resonant light at two different frequencies in quick succession. The optimal absorption imaging condition for lithium [81] imposes short illumination times, i.e. $\lesssim 3\,\mu\text{s}$, which means AOMs are necessary to switch the imaging light of the respective transition. Since the response of the homebuilt imaging laser is too slow, shifting the offset lock for the imaging pulses is not feasible. The frequency of the imaging laser ν_0 is locked to the reference laser with an offset lock (see Fig. 6.5(b)) which allows an adjustable detuning from the D_2 line, allowing us to image at variable magnetic fields. The light from the laser is passing the first AOM which introduces a frequency shift of $\nu_1 = +80\,\mathrm{MHz}$ into resonance with the state $|1\rangle$ imaging transition (σ_- polarized, $|1\rangle \to |2^2P_{3/2}, F = 1/2, m_J = -3/2, m_I = 1\rangle$). The zeroth order, is picked of with a D-shaped mirror and passes AOM3 which shifts ν_0 by $\nu_3 = -83\,\mathrm{MHz}$ into resonance with the state $|3\rangle$ imaging transition (σ_- polarized, $|3\rangle \to |2^2P_{3/2}, F = 1/2, m_J = -3/2, m_I = -1\rangle$). The two beams are combined with a 50/50 beam splitter (BS) in front of the imaging fiber. In case the states $|1\rangle$ and $|2\rangle$ are supposed to be imaged, a flip mirror allows to shift the imaging light for state $|3\rangle$, using AOM$_2$, by $\nu_2 = -83\,\mathrm{MHz} = -\nu_3$ back to the imaging transition of state $|2\rangle$ (σ_- polarized, $|2\rangle \to |2^2P_{3/2}, F = 1/2, m_J = -3/2, m_I = 0\rangle$). The small frequency offsets, introduced by the AOM frequencies not exactly matching the transition frequencies, are compensated by small shifts of the imaging lasers offset frequency for each individual imaging pulse.

The optical imaging system used to image the atomic cloud is shown in Fig. 6.9(b). The cloud is illuminated by a collimated, linearly polarized beam in the horizontal, x-direction. The cloud is imaged using two telescopes in $4-f$ configuration with a total magnification of 3. The first telescope $f_1 = 100\,\mathrm{mm}$, $f_2 = 150\,\mathrm{mm}$ creates an image of the cloud in its image plane, where a razor knife edge is placed. The knife edge is imaged by the second telescope $f_3 = 200\,\mathrm{mm}$, $f_4 = 100\,\mathrm{mm}$ onto the CCD chip of the camera. The knife edge creates a shadow on the CCD, only allowing a reduced, cropped region of the imaging light to propagate. The dark, masked region of the CCD is subsequently used to store the images of the atomic clouds during the imaging process (see Fig. 6.9). A narrow linefilter in front of the camera is used to block stray-light and leakage from the lightsheet beam propagating along the same axis.

The image acquisition process is outlined in Fig. 6.9(c). The camera (*Andor iKon 934-M*) is a high quantum efficiency (92.6 %), low read-out noise CCD camera which has a vertical shift mode allowing us to take many individual pictures in a defined horizontal region, each being shifted downwards after acquisition, thus allowing very fast frame rates. The vertical shift time of a single row is 2.25 µs which means in the case of our imaging setup, i.e. 100 rows per image, the frame rate is given by $(t_{\mathrm{exposure}} + t_{\mathrm{shift}})^{-1} = (52\,\mu\mathrm{s} + 225\,\mu\mathrm{s})^{-1} \approx 3800\,\mathrm{FPS}$. Since the free expansion of the cloud between images would lead to a substantial difference between the clouds, we image both spin-states in-situ. In the experiment this means the spin-state which is imaged first will still be in the image of the second spin-state as a background. For this reason a longer, resonant imaging pulse is introduced after the images of the clouds which resonantly accelerates the remaining atoms out of the frame. This procedure is happening before the bright-images. The resulting image sequence is given in Tab. 6.2. Each imaging pulse has a total length of $t_{\mathrm{exposure}} = 52\,\mu\mathrm{s}$ though the atoms are only illuminated during the illumination time $t_{\mathrm{illumination}} = 2\,\mu\mathrm{s}$. During the junk image pulses the remaining atoms are illuminated for $t_{\mathrm{junk}} = 10\,\mu\mathrm{s}$. After the two atomic clouds are imaged, two more reference images with light are taken, the bright images. The image sequence is ended with a final picture without light, the dark picture. The bright and dark pictures are used to get rid of shot-to-shot imaging intensity fluctuations as well as to remove the background. In our experiment the bright pictures are used for a commonly

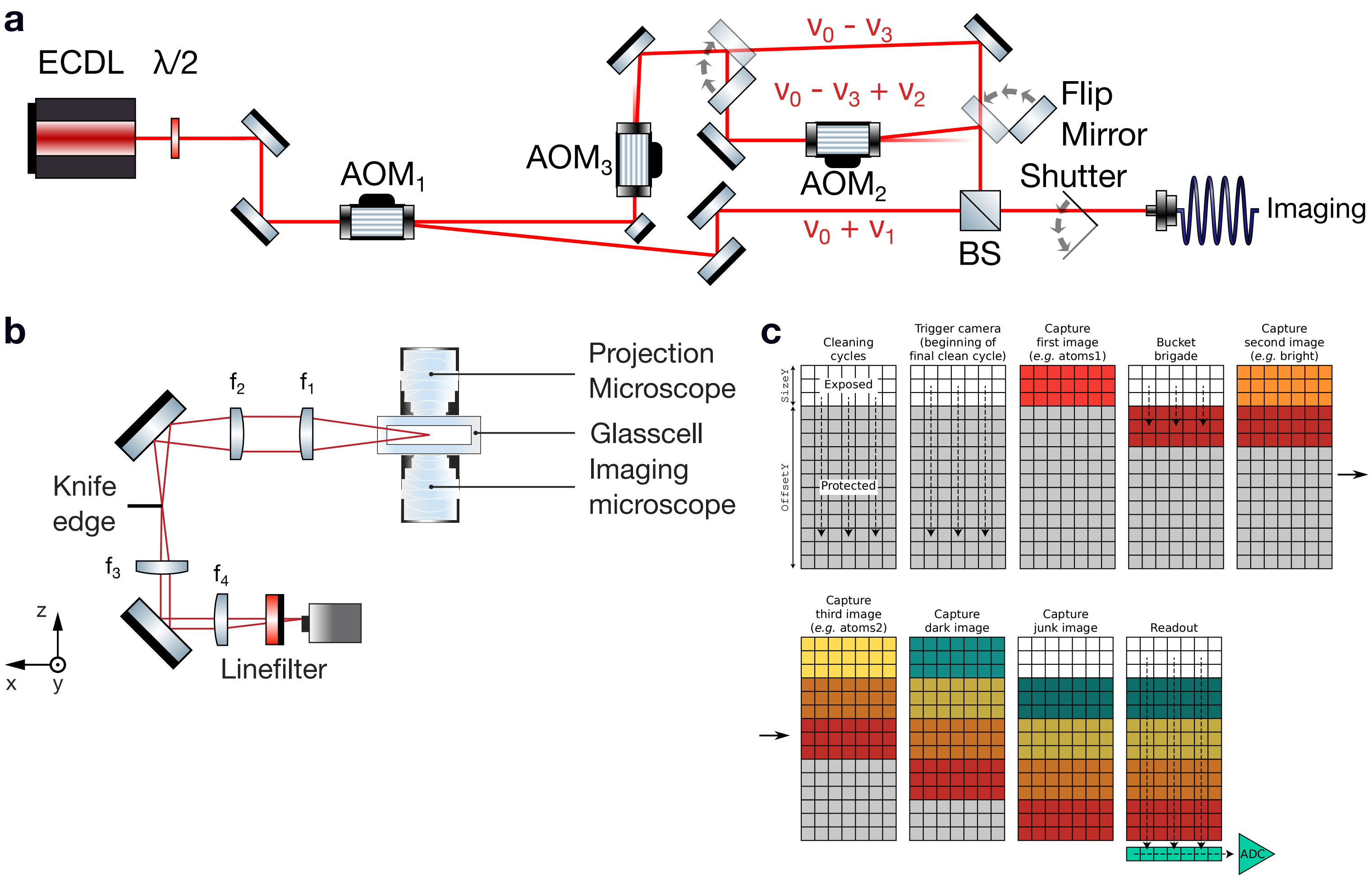

Figure 6.9: Optical setup of the spin resolved imaging system. (a) The optical setup before the fiber allows us to image two different spins at a time. The laser frequency is shifted by AOM$_1$ to the state $|1\rangle$ transition and with AOM$_3$ to the state $|3\rangle$ transition. In order to image state $|1\rangle$, $|2\rangle$ a flip mirror can be used to shift the AOM$_3$ back to the state $|2\rangle$ transition with AOM$_2$. The imaging system (b) is a $4-f$ configuration with a magnification of 3. The knife edge masks a region of the CCD chip of the camera, such that images can be stored in the dark region during the imaging process. (c) The imaging process starts, after cleaning, with the first atom picture which is followed by a fast shift to the masked region. This process is repeated until all required images are taken and only then the whole CCD is slowly read out, reducing the read noise. (c) is adapted from Ref. [80].

Image	Atom_1	Atom_2	Junk_1	Junk_2	Bright_1	Bright_2	Dark
Frequency	$\nu_0 + \nu_1$	$\nu_0 - \nu_3$	$\nu_0 + \nu_1$	$\nu_0 - \nu_3$	$\nu_0 + \nu_1$	$\nu_0 - \nu_3$	–
Illumination time	2 µs	2 µs	10 µs	10 µs	2 µs	2 µs	0

Table 6.2: Image sequence for spin resolved imaging. The image sequence contains 7 images, each taking 100 rows of pixels on the CCD. For the atom and junk images the imaging beam frequency is kept fixed, while the illumination time is changed. The duration of each image, i.e. the exposure time, is constant $t_{\text{exposure}} = 52\,\mu\text{s}$. Between each image its pixel rows, containing the image information, are shifted, which takes $t_{\text{shift}} = 225\,\mu\text{s}$.

used fringe removal algorithm [83], which allows to calculate an optimal bright picture from a linear combination of reference bright pictures and a section of the atom picture. Once the image acquisition has finished, each individual pixel is read-out with a 16 bit ADC which has a read noise which is smaller than the photon shot noise [80].

6.3.2 *Magnification Calibration*

In order to obtain correct atom numbers and second moment values from the picture of the cloud, a well calibrated imaging system is necessary. Signal-to-noise considerations impose an optimal imaging intensity $I/I_{\text{sat}} = 2$ [81] which implies that we operate in the high intensity absorption imaging limit. The absorption cross-section, which depends on polarization and the atomic structure, is calibrated using the technique from Ref. [82]. We rely on this calibration to obtain the correct optical density of the cloud.

The second important calibration is the magnification which we rely on to obtain the correct size of the cloud which enters the thermometry of the cloud. Here we can make use of a unique trick given the projection microscope and the wall beam. The wall beam separates the cloud in two half harmonic reservoirs and its center can be easily determined using the horizontal imaging system. The wall beam can be moved by translating the projection microscope using its closed-loop-piezo translation stage. In addition, the translation can be independently measured using our second, vertical imaging system through the microscope. Assuming the magnification 54 of the microscope imaging system is correct (has been calibrated with a test target), the movement of the wall beam in y-direction can be measured with both the vertical and horizontal imaging system. The ratio of the measurements will give the ratio of magnifications of two imaging systems. The resulting magnification for the horizontal imaging system is $M = 3.025(34)$ which is equivalent to the value expected from theory.

6.4 LASER SETUP FOR A PHASE-STABLE LAMBDA SYSTEM

Light matter interaction with a three-level system, as discussed in Sec. 3.3 requires two, phase-locked beams at distinct frequencies. Here we generate two beams from the same laser with a frequency offset of up to 2 GHz using custom AOMs (*Intraaction 475MHz AOM*). Even though, creating the beams from a single laser and sending them through the same fiber leads to mostly common-mode phase fluctuations we implement a phase-lock to compensate fluctuations stemming from the different AOM paths. In the

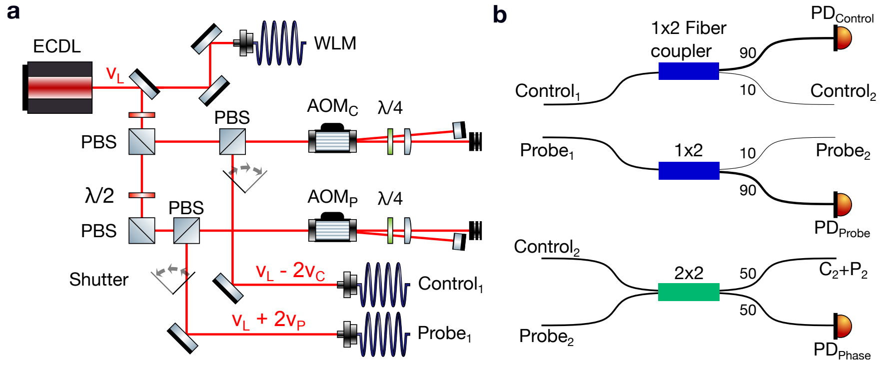

Figure 6.10: Optical setup for control and probe beam of the lambda system. (a) The near-resonant laser is locked using a wavelength-meter (WLM) to an arbitrary frequency. The light is split into two AOM paths, for the probe and control beam, respectively. The probe beam AOM (AOM$_P$) shifts the laser by $+2\nu_P = 850\ldots1050\,\text{MHz}$, while the control beam AOM (AOM$_C$) shifts the laser by $-2\nu_C = 850\ldots1050\,\text{MHz}$. The double path setup is in cat-eye configuration and needs only minor realignment to achieve the full frequency bandwidth of the AOM with adequate AOM efficiency. Each beam can be switched using a shutter in the path, before the fiber. The beams are not combined before the fiber, but using a fiber coupler system (b). The first fiber couplers split the respective beam with a 90/10 ratio, where the 90 % arm is sent to a photodiode for amplitude stabilization. The second, fiber-to-fiber connected, fiber coupler is combining the probe and control beam with a 50/50 ratio. The first output goes to the experimental table, while the second output goes to a high-speed photodiode which is used for the phase-lock of the two beams.

future the setup can easily be extended to two fibers and a phase lock on the experimental side.

The near-resonant laser, an external cavity diode laser (*Toptica DLPro*), is locked using a wavelength-meter (*HighFinesse WS8-2*) which allows free tuning of the frequency ν_L independent of an offset-lock bandwidth. The wavelength meter has an accuracy of 2 MHz and a minimal detectable deviation of 200 kHz with a detection bandwidth of 500 Hz. This allows us to impose a stable frequency of the near-resonant laser, compensating thermal drifts, but fast sweeps or linewidth narrowing are certainly not possible. The measured standard deviation of the frequency of the laser indicates a frequency deviation of $\sim 1\,\text{MHz}$. The accuracy of the wavelength-meter is retained over extended periods of time via calibration to the reference laser, which is spectroscopy-locked. Since the control and probe beam are frequency shifted from the same laser, these frequency fluctuations are common-mode and thus do not contribute to the two-photon detuning $\Delta = \nu_C - \nu_P$.

The laser is split using polarizing beam splitters into the two AOM paths for the control and probe beam, as sketched in Fig. 6.10(a). Each path is made up of a double path AOM setup in cat-eye configuration. The AOMs' center frequency is 475 MHz and the 3dB bandwidth is 100 MHz, whereas the peak efficiency is around 62 %. The AOMs are driven with a commercially available RF signal generator (*Rigol DSG815*) followed by a homebuilt RF amplitude and RF switch configuration, allowing amplitude modulation, RF switching and phase/frequency modulation via the external modulation port of the signal generator. The RF signal generators are both supplied with an external 10 MHz reference clock which is also provided to a third, demodulation source (*Windfreak SynthNV*) used for the demodulation of the control-probe beam beat note. In double pass configuration we reach a maximal efficiency of 45 % at the AOMs' center frequency with a 3 dB bandwidth of about ±8 MHz (FWHM = 16 MHz). This means that in order to change the two-photon detuning by more than 64 MHz the AOMs have to be realigned. The diffraction orders of the AOMs are chosen such that the control beam AOM shifts the laser frequency by $-2\nu_C$ while the probe beam AOM shifts it by $+2\nu_P$. The resulting frequency difference between the two beams is $2\nu_P + 2\nu_C$.

Figure 6.10(b) shows the fiber coupler system used for amplitude and phase stabilization of the two beams. The main challenge arising from the co-propagating beams is the loss of amplitude information after the optical fiber connecting the laser and the experiment. Nevertheless, amplitude fluctuations due to free-space to fiber coupling drifts can be compensated. We use two polarization maintaining 1×2 fiber couplers (*Thorlabs PN670R2A1*) with a 90/10 power ratio between the two outputs. Here, the large output of the coupler is sent to a DC coupled photodiode, allowing amplitude stabilization and closed-loop amplitude modulation using a PI loop. The two smaller outputs, i.e. Probe_2 and Control_2, are fiber-to-fiber coupled to a polarization maintaining 50/50 fiber coupler/splitter (*Thorlabs PN670R5A1*) which provides one output which is again fiber-to-fiber coupled to the transfer fiber, which connects to the experiment. The second output of the 50/50 splitter is sent to a high frequency, AC-coupled, phase-lock photodiode (*Thorlabs DET025AFC/M*) which provides the beat-note of the two lasers at $\nu_{\text{beat}} = 2\nu_P + 2\nu_C$. The beat-note is demodulated in an RF mixer using the bare RF frequency from the demodulation source which provides the DC-signal which is proportional to the phase difference between the two beams. This error signal is sent to the frequency modulation port of one of the two AOM RF signal generators, providing a PI loop via the time integration coming from $\phi = \nu t$. The integrator gain of the PI loop can be varied via the frequency modulation depth, while the proportional gain can be varied via a variable attenuator on the error-signal.

6.5 IMPROVEMENTS IN DATA LOGGING

In this section we are going to detail the minor improvements implemented in the experiment, mostly related to the monitoring of the apparatus, aiding the troubleshooting and the subsequent improvements. The main contribution to the improvements is the increase in data logging, supported by new hardware and software solutions. The different methods of data taking can be separated into recordings which are triggered by the experiment, i.e. synchronous recording, and those which happen continuously, independent of the experiment cycle, i.e. asynchronous recording.

6.5.1 *Synchronous Data Recording*

For synchronous recording of the experiments' status in terms of power of laser beams and magnetic fields, we use PC oscilloscopes (*Picotech Picoscope 4824A*) with 8 channels operated using a Python script. The script is software triggered via an Ethernet protocol which initializes the Picoscope at the beginning of each experimental cycle. A hardware trigger is used to start the recording which is subsequently saved on the computer. Another software script is waiting for data to be written to the computer, analyzes and displays the recordings. The displayed traces of the laser powers and magnetic fields allow quick troubleshooting whenever for example the PI lock fails or a shutter is manually switches off. In addition, the mean value of the traces in defined time windows are sent to a database (*InfluxDB*, hosted by the IT department of the department) which is visualized on a website using Grafana. This allows long term tracking of laser powers and magnetic fields as well as helps to understand and troubleshoot the experimental cycle in real time.

Moreover, we use several CCD cameras (*Flir Chameleon2*) similarly to record the position and power of some laser beams critical to our transport setup. The computer runs a Python script configuring the camera which is software triggered with every new experimental cycle, then a hardware trigger on the camera is used to trigger the exposure at a certain point during the experiment. The software is then processing the picture, i.e. fitting a Gaussian or a TEM_{01} profile, to the recorded beam and the parameters are stored. The stored parameters are then sent to our database which is visualized in Grafana. This procedure allows us to observer the thermalization of the experiment and estimate the timescales at which realignments of the different beams are necessary. Furthermore, the variable exposure time allows us to take pictures of extremely low power optical beams and estimate their total power. In the case of the near-resonant beams estimate their total power.

Asynchronous Data Recording

Asynchronous recording is mostly used to track temperatures as well as laser powers which do not vary during the experiment to detect degradation. For this purpose a commercially available data-acquisition unit is used (*Keysight DAQ34970A*) which has three slots for multiplexer modules with 20 channels each (*Keysight 34901A*). The unit itself is in its essence a 6½ digit ($\sim 21\,\mathrm{bit}$), digital multi-meter (DMM) which is connected to the different channels using relays switches. This configuration allows the device to measure temperatures via RTDs or thermocouples, voltages, currents and resistances with high accuracy. The channels are continuously scanned at a rate of up to $\sim 60\,\mathrm{ch/s}$ (scanning speed depends on accuracy) and the measurement results are saved on the device. The system operates as a server and can be queried via ethernet using Python. The recordings are regularly queried from a computer transferred to the InfluxDB database and visualized in Grafana. This system allows us to track the temperature of our magnetic field coils, the laser powers, the temperature of our lithium oven, the temperature of our lab, the pressure in our UHV chamber etc. all using one device. In Grafana, it is easy to create "alarms" which will trigger an email to the specified recipients in case of a failure in our lab. In addition, the DAQ device has four digital outputs which can be configured to be triggered whenever a certain measurement is beyond a defined threshold. This feature is part of our interlock system which triggers a switch-off of our coils whenever they get too hot.

7

FUTURE IMPROVEMENTS OF THE EXPERIMENT

CHAPTER CONTENTS

This chapter provides an overview over the technical projects we realized together with different semester or master students during this thesis, their future implementation in the experiment and the improvements they would provide. The main improvement ideas can be categorized as follows:

- **Magnetic field stability** Operating at stable magnetic fields would allow us to achieve narrower magnetic transitions between the high- and low-field seeking states, which could lead to interesting physics when coupling the states coherently. See Sec. 3.3 for the theory proposals.

- **Cleaning cavity** The design of a high transmission optical cleaning cavity was envisioned to provide a new, lock-free imaging path in conjunction with high efficiency, serrodyne phase modulation. Even though this might not be necessary, the stable and cheap cavity is also useful for cleaning the wide, spontaneous background of a diode laser or tapered amplifier.

- 20 bit **digital to analog converter** The low noise, high resolution digital-to-analog converter will simplify applications which require high dynamic range, like our current, analog magnetic field stabilization or the frequency selection in a piezo driven optical cavity with large free spectral range.

- **Fast stereo-camera imaging** Reading out cameras with ~ 400 FPS and closed loop feedback on a beams position or even angle was achieved with a dual camera system operated by an FPGA board which provided feedback on piezo driven mirrors.

- **Low cost mirror motor** We designed a low cost ~ 125 CHF/axis mirror motor which can operate most available kinematic mirror mounts with $< 0.08°$ closed-loop resolution.

- **Top-hat lightsheet** For future transport experiments larger constriction areas are necessary to allow for more complex potentials. This requires a homogeneous 2D confinement over longer length scales. This confinement can be achieved with a top-hat shaped beam, superimposed with a TEM_{01} like beam which can be achieved with a custom designed phase-plate (*HoloOr*).

7.1 MAGNETIC FIELD STABILIZATION

The realization of a new magnetic field stabilization presented here is based on a design in Ref. [144]. The new stabilization system was realized together with B. van Ommen during his master thesis [105].

Reaching a narrow linewidth in a two-photon transition between the lowest and fifth-lowest hyperfine state $|1\rangle - |5\rangle$, requires low magnetic field noise. For this transition the ground-state energy splitting strongly varies with the magnetic field $d\nu_{15}/dB = 2.78\,\text{MHz/G}$ (for the common-mode states $|1\rangle - |3\rangle$ the energy splitting is $d\nu_{13}/dB = 6\,\text{kHz/G}$). In the current setup we measure an RMS noise of $B_{rms} = 10\,\text{ppm}$ which would mean RMS fluctuations of the atomic two-photon detuning of $\sim 2\,\text{kHz}$ at $B = 690\,\text{G}$. A more extensive noise analysis, including the noise-spectral-density of the magnetic field can be found in Ref. [105], though the obtained linewidth is similar. This means if we want to resolve narrow spectral features with such a transition, e.g. the superfluid gap Δ, we would like to reduce the magnetic field RMS noise below 1 ppm which we achieved in a test setup. Importantly, the magnetic field noise was measured in terms of a current noise to which the magnetic field is related linearly. This means that external noise sources, like stray fields, were not accounted for and cannot be compensated by the realized system. Finally, the new system not only provides a closed-loop stabilization of the current but also a feedforward compensation of 50 Hz noise and its higher harmonics.

Feedback and Feedforward Current Stabilization

The electrical circuit used to stabilize the current running through the coil is shown in Fig. 7.1(a) (red line). The current supply is providing a current I_0 to the high current circuit, which has two paths, one running through the current sensor, i.e. the current transducer, and the coil and another path parallel to the feedback (shunt) transistor. The shunt transistor is resistively varying the feedback current I_{FB} split from the coil circuit, thereby controlling the primary current I_p. In addition, an in-loop feedforward shunt, after the current sensor allows compensating 50 Hz-noise independently of the feedback. The feedforward shunt varies the shunted feedforward current I_{FF}, thereby affecting the coil current I_{coil} but, due to its location after the current sensor, not the stabilized current.

Feedback Circuit

Figure 7.1(a) shows the schematics of the feedback system, where the analog signal chain is made up of the following parts

1. The current transducer (*LEM IN500-S*, meas. range $-800\ldots800\,\text{A}$, accuracy 10 ppm, RMS noise 3.5 ppm in $0-100\,\text{kHz}$) is inductively measuring the current running to the coils. The wire, connecting to the coils is wound 4 times around the transducer to cover our operating range, i.e. $30\ldots110\,\text{A}$.
2. The secondary current $I_s = \frac{4}{750} I_p$ is measured at the output of the transducer with a measurement resistor network. The network con-

sists of six high precision, low thermal drift 25 Ω resistors in parallel. This configuration reduces the power each resistor dissipates individually, thereby minimizing thermal drifts.

3. An instrumentation amplifier made up of three low-noise OPAMPS (*ADA4004*) is used to measure the voltage drop over the resistors, eliminating common-mode noise.
4. Two stages of set-point subtraction are used to realize high precision and a large proportional gain. The error signal is given by $V_{\mathrm{err}} = 200V_1 + V_2 - 202V_{\mathrm{signal}}$ where V_{signal} is the signal and V_1, V_2 are the voltage set-points provided by two different digital-to-analog (DAC) converters (*Analog Devices AD5541A*). The first DAC provides a coarse set-point while the second DAC allows an additional fine adjustment with in total ~ 22 bit.
5. The first analog notch filter removes the intrinsic excitation frequency of the current transducer at 15.625 kHz. The second notch filter acts as an active low-pass filter determining the bandwidth of the feedback loop, i.e. $f_{3\mathrm{dB}} = 10\,\mathrm{kHz}$. The filters are followed by a phase compensator which allows to adjust the feedback circuit to the phase lag generated by the inductance of the coil and the capacitance of the current source.
6. The integrator is realized by two poles in the transfer function, i.e. two integrators. This allows more freedom for adjustment of the integrators transfer function.
7. The output voltage of the integrator is connected to the shunt transistor varying its resistance, thereby varying the primary current I_p via the shunt current $I_p = I_0 - I_{FB}$

Feedforward Circuit

In order to provide a feedforward on the 50 Hz power line coupling into the coil current, the feedforward has to be synchronized to the line. For this purpose a transformer is used which transforms the line down to ~ $5\,V_{\mathrm{RMS}}$ which is rectified with a flip-flop gate. The rectified line provides a trigger to the microcontroller at the line frequency. The contributions of higher harmonics to an optimal feedforward signal has to be determined experimentally.

Digital Circuit

The digital side of the feedback system is sketched with yellow lines in Fig. 7.1(a). The lab control computer is sending the currents set-point to a microcontroller (*Teensy 4.1*) via ethernet and receives the measured current and the error-signal. The microcontroller is connected, via an isolated SPI interface, to the digital-to-analog converters used for setting the current and to an analog-to-digital converter (*Analog Devices AD7177*, noise free bits 24.6 at 5 Hz sampling) reading the current. The current supply is also connected to the lab computer and its current output is chosen to be slightly above the set-point such that the feedback transistor is able to shunt some current. Since the digital-to-analog converters are the main contributors to the error budget of the overall system, several precautions were taken to improve

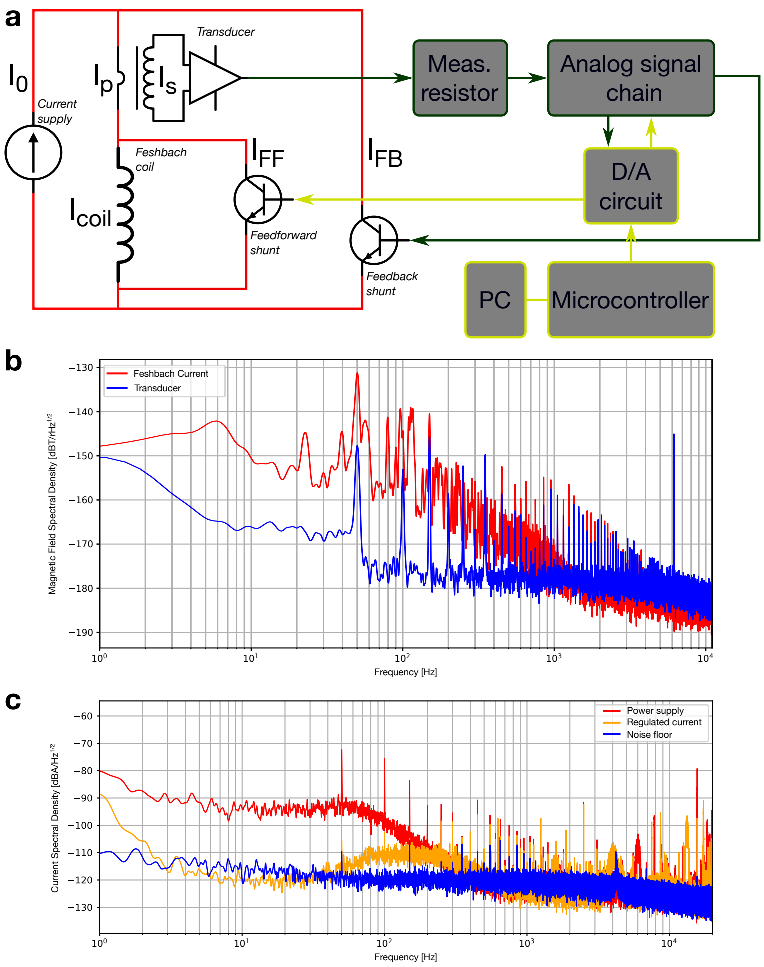

Figure 7.1: Magnetic field stabilization feedback system and noise measurements. The current feedback circuit (a) includes two parallel circuits in line with the power supply, each including a shunting transistor parallel to the Feshbach coil. The first circuit shunts the current I_{FB} thereby providing feedback on the current measured by the transduced. The second circuit shunts current within the loop around the coil to compensate 50 Hz noise with a feedforward synchronized to the phase of the power line. (b) Measured magnetic field noise of the Feshbach coils in the experiment as a function of frequency. The total RMS noise is 10 ppm. (c) Noise improvement observed in a test setup with the new regulation scheme, the final total RMS noise was 0.96 ppm. (b)-(c) Adapted from Ref. [105].

their noise and stability. Firstly, four ultra-stable voltage references are used in parallel (*Analog Devices LTC6655LNB-5*, voltage drift 1 ppm/K, RMS noise 0.21 ppm in $0-1$ kHz) such that their RMS noise is reduced by a factor of two. Experimentally we find that the RMS noise of the voltage references is 0.17 ppm while the peak-to-peak ripple is 0.8 ppm which likely stems from an imperfect thermalization. These voltage references feed the DAC which acts as precision voltage divider, thereby relying on a stable, low-noise reference. The outputs of the DACs are low-pass filtered with a 2.2 Hz passive filter which reduces the possible set-point changes, but eliminates noise. Importantly, we do not require stable magnetic field ramps, but a constant magnetic field with low noise. The DAC used for the feedforward circuit is filtered by two low-pass filters at 161 Hz and 4.1 kHz which smooth its output wavefront which has its main frequency components at multiples of 50 Hz. The feedforward DAC is connected via a buffering OPAMP directly to the feedforward shunt transistor.

Current Shunt

The two current shunt circuits shown in Fig. 7.1 are made up by a bipolar transistor (*TIP-29A*) which is operated by the feedback or feedforward signal, respectively. The transistors base current is varied via the signals which are current-buffered with an additional bipolar transistor (*BC846*). The base current range is adjusted with a voltage divider on the voltage feedback signal and the phase lag of the transistor at high frequencies is compensated with a filter.

System Performance

The noise in the experiments Feshbach coil setup was measured with an auxiliary current transducer (*LEM IN-500S*), where we find that most of the current noise is present below 1 kHz as shown in Fig. 7.1(b) (red line). The RMS noise in the measurement window of $1-1000$ Hz is determined to be 10.2 ppm at 79 A. The frequency behavior of the noise can be expected, since the coils form a very good LR low-pass circuit with a cutoff frequency of $f_{3\,\mathrm{dB}} \approx 13\,\mathrm{Hz}$. Taking this measurement into account we adjusted the bandwidth $f_{3\,\mathrm{dB}} = 10\,\mathrm{kHz}$ of the feedback circuit.

The feedback systems performance was determined in a test setup, separated from the experiment, with a commercial current supply (*Delta Elektronika SM 18-50*) and a coil test setup, similar to the experiment. The current noise spectral density with and without regulation is shown in Fig. 7.1(c). The noise is reduced by 20 dB in the range of $3-100$ Hz by the feedback, while above 300 Hz the regulation seems to have less of an effect. In the measurement window of up to 1 kHz the RMS noise of the current source 5.6 ppm at 50 A is reduced to 0.96 ppm which would be an order of magnitude better than the current noise value in the experiment.

Implementation

To implement the current stabilization system in the experiment a few changes have to be made to the analog feedback system:

- The gain of the differential amplifier has to be changed to match the required tuning range of the experiment.
- The phase compensator circuit has to be adapted to the output capacitance of the current supply and the inductance of the coils.

- The integrator filter has to be optimized to optimally compensate the current noise.

- The feedforward circuit needs to be adjusted using the spectral response of the atoms.

7.2 HIGH TRANSMISSION CLEANING CAVITY

Narrow line filters in the optical frequency range are hard to come by, the best grating based filters provide spectral bandwidths of $\sim 50\,\mathrm{GHz}$ with reflection efficiencies of 90 %. Here, we designed a simple but stable filtering cavity with a high transmission of 76 % and a narrow linewidth of 28 MHz, which is frequency locked to the laser. In addition, we use serrodyne [184] phase modulation of light with a fiber EOM to shift a laser by up to 1 GHz with a sideband efficiency of $27-50\,\%$, surpassing sinusoidal modulation which is limited to sideband modulation depths of 33 %. Assembly and testing of the cavity was completed within the semester thesis of B. van Ommen [185].

Cavity Design

The filtering cavity has been designed with the following constraints

- **High transmission.** This requires mirrors with very low losses and intermediate reflectivity since the overall cavity transmission depends on losses per roundtrip as well as the total number of round trips.

- **Broadband coating.** In order to have a broad blocking window the cavity mirrors need to have a rather broad reflection coating.

- **Large free spectral range.** Since transmission is possible at every multiple of the free spectral range.

- **High stability.** Though the cavity will be locked to the laser, long term drifts can move the cavity out of the locking range.

- **Fast frequency lock.** The cavity should be able to follow fast changes of the laser frequency.

The final mechanical design of the cavity and its holder is shown in Fig. 7.2. The base of the cavity is placed on four optics posts, insulated with a vibration damping material. The upper part of the base, where the cavity-cage system is mounted, is separated with a Peltier element from the heavy baseplate. The Peltier element allows us to stabilize the cavity temperature while the heavy baseplate reduces vibrations and provides a heat-sink with large thermal mass. The cavity-cage system is made from stainless steel while the cage rods are made from Invar which has a very low thermal expansion coefficient. For frequency tuning of the cavity, a ring piezo (*Noliac NAC2123*) is glued to each mirror holder where in turn the cavity mirror is glued to. The mirrors are precision polished fused silica substrates (*Laseroptik*, D12.7 × 6.35 mm, $R = 99.7\,\%$ at 671 nm). Once the cavity is assembled an additional housing made from plexiglass and acoustic foam is placed around the cavity. The housing increases the thermal stability and insulates the cavity from acoustic noise.

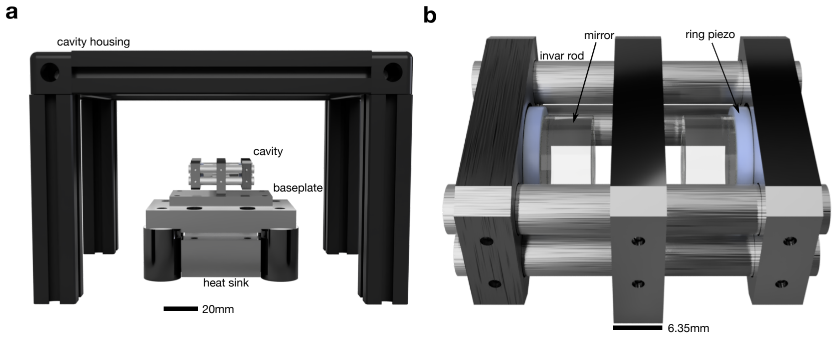

Figure 7.2: High transmission filter cavity system. The rendering (a) includes the cavity, the baseplate and the housing. The cavity is held by Invar rods, reducing thermal fluctuations of the cavity length. Furthermore, the baseplate is temperature stabilized with a Peltier element. The housing provides thermal and acoustic insulation. The cavity mirrors (b) are mounted in 0.58 cm distance to provide a wide free spectral range. Reflectivities and the surface qualities of the mirrors are chosen such that a high cavity transmission 76 % can be obtained. Ring piezo's glued to the mirrors provide means to lock the cavity to the frequency of a laser.

Resonator parameters		Values
Length	L	0.58(1) cm
Mirror Radius of Curvature	R1, R2	200 mm
Mirror Reflection	R	99.7 %
Loss Parameter	α_s	720 ppm
Finesse	$\mathcal{F}$	931
Linewidth	$\Delta\nu$	27.6(3) MHz
Free Spectral Range	ν_{FSR}	25.7(6) GHz
Overall Transmission	T_{cavity}	76 %
Transmission Contrast	T_{min}/T_{max}	110 dB

Table 7.1: Filter cavity parameters.

Cavity Characterization

The cavity parameters are summarized in Tab. 7.1. To extract the cavities free spectral range, the cavity is purposefully miss-aligned such that higher transverse modes can be coupled into the resonator. The EOM used for the PDH lock is modulated at 95.3 MHz with a large modulation depth such that each transverse mode has two sidebands spaced by twice the EOM frequency. Scanning the piezo over a large range allows us to sample many of the cavity resonances and thereby reconstruct the frequency-to-voltage conversion of the cavity $df/dV = 741\,\mathrm{MHz/V}$. Subsequently, the distance between the lowest transverse mode can be measured which is the free spectral range. In addition, the frequency-to-voltage ratio is used to determine the linewidth of the cavity. The ratio of free spectral range and linewidth gives the finesse of the cavity.

Cavity Frequency-lock

As previously discussed, we require the filter cavity to have a fast frequency lock to the laser, such that ramps of the laser frequency can be followed.

To achieve a fast and reliable lock, an FPGA based lock system (*RedPitaya 125-14*) is used. The error signal is generated with the PDH technique [186] where the demodulated signal is sent to the RedPitaya. The flexible digital notch-filter configurations in the PyRPL interface [181] are used to cancel the mechanical resonances of the cavity which are present mostly in the window of $14-25\,\mathrm{kHz}$. The feedback signal is generated using the PI loop module of PyRPL which allows us to feedback on the frequency with two different PI loops, operating in different frequency windows. The first PI loop generates a fast frequency feedback which is attenuated by $20\,\mathrm{dB}$ at its output and sent to one of the piezos. The second PI loop has a low bandwidth and its feedback signal is amplified $\times 20$ with a high voltage piezo amplifier (*Falco Systems WMA-100*) to compensate slow drifts of the cavity. The final lock provides a locking range of $\pm 600\,\mathrm{MHz}$ for the fast feedback and does not need re-locking when operating the filter-cavity continuously.

Serrodyne Modulation

One of the intended applications of the cleaning cavity was to replace our imaging laser. Imaging requires a singular, stable frequency which can be produced via a high frequency sideband of the MOT laser. The sideband amplitude in sinusoidal phase modulation is given via the Jacobi-Angler transform by

$$\begin{aligned} E_{\mathrm{phase}} = & E_0 \exp\left(i w_L t + i A \sin\left(w_{\mathrm{phase}} t\right)\right) = \\ & E_0 e^{i w_L T}\left[J_0(A) + 2\sum_{n=1}^{\infty} i^n J_n(A) \cos\left(n w_{\mathrm{phase}} t\right)\right], \end{aligned} \tag{7.1}$$

where $J_n(A)$ are nth Bessel functions of the first kind, A is the phase modulation depth and w_{phase} is the phase modulation frequency. The intensity in the carrier is then given by $I_0 = J_0^2(A) I$ and in the first sideband $I_1 = J_1^2(A) I$, where I is the total intensity. The sinusoidal modulation is therefore limited to a maximal intensity of $\approx 0.34 I$ in the first sideband.

Serrodyne modulation [184, 187, 188] can overcome this limit via the relation between frequency and time in terms of a Fourier transform. Similar to Fourier optics where a tilt in the wavefront leads to a shift in the focus position here, a "tilt" in time domain will shift the frequency in one direction. The sinusoidal modulation can be interpreted as a normal grating in the light domain while now we are interested in a blazed grating, i.e. a sawtooth like modulation by $\phi(t) = m\nu_{\mathrm{serr}} \cdot t \bmod 2\pi m$. The frequency shift is then given by ν_{serr} which is the lowest frequency, i.e. the lowest order, in the waveform. In practice, the sawtooth signal is generated by a nonlinear RF element (nonlinear transmission line (NLTL)) which has an amplitude dependent propagation speed, therefore shaping a sawtooth out of a sine. The main challenge in serrodyne modulation is the fall-time of the sawtooth which limits the modulation efficiency. Generally the frequency shift is limited by the bandwidth of the overall system via $\nu_{\max} \approx f_c/35$ [187]. Notably, whenever more sophisticated frequency spectra are necessary, phase-retrieval algorithms, e.g. the Gerchberg-Saxton algorithm, can be used to optimize the required spectra [189].

In our system, a NLTL (*Marki Microwave NLTL-6796*) with $f_c < 50\,\mathrm{GHz}$ is used which means that our setup is limited by the fiber EOM (*Jenoptik PM660*, $f_c \approx 7\,\mathrm{GHz}$) used for the phase modulation and not the RF electronics. Experimentally, we find a non-monotonous modulation efficiency, due to the low frequency cutoff of the NLTL. The efficiency was measured with the filter cavity locked to the sideband of interest. In the window of $350 - 950$ MHz the efficiency is above $\sim 34\,\%$ with a peak of $47\,\%$ at around 600 MHz. For higher frequencies the efficiency drops linearly to $22\,\%$ at 1200 MHz which is the highest frequency shift we measured. Thus, we find that the serrodyne modulation could be useful for modulation frequencies up to 950 MHz, likely limited by the fiber EOM. For higher frequencies sinusoidal phase modulations outperform the serrodyne modulation in our system.

Conclusion

In summary, we have designed and built a high transmission optical filter cavity which provides a narrow filter with high suppression around 671 nm. The cavity lock is stable and fast which allows quick shifting of the laser frequency. In addition, we tested serrodyne modulation with subsequent filtering and found that we can reach adequate efficiencies in a frequency shift window up to 950 MHz. Using such a laser system for absorption imaging is limited by the damage threshold of 20 mW and insertion efficiency of $25\,\%$ of the fiber EOM which would result in imaging powers of ~ 1.75 mW before the AOM and final fiber coupling. This low power makes it thus not sustainable in a real experiment. Nevertheless, the filter cavities design and the built cavity can be used for background filtering of tapered amplifiers or ECDLs in our experiment, which are important for off-resonant spectroscopy.

7.3 LOW-COST MIRROR MOTOR

The need for remote and automated operation of a highly complicated, temperature dependent quantum gas experiment is apparent. Whenever the enclosure of an optical table is opened, the temperature changes, leading to drifts of the optical apparatus. There are sensitive alignments of mirrors which cannot be achieved by hand, e.g. the alignment of the lightsheet beam on the atoms. Therefore, we are interested in a low cost mirror motor which can operate any commercially available kinematic mirror mount with high precision. The choice of servo and some design choices are inspired by Markus Greiner (*private communication*). The mirror motor system has been characterized within the semester thesis of L. Peters [190].

Figure 7.3 shows renderings of the operational mirror motor which is used to operate a kinematic mirror mount (*Thorlabs Polaris*). The servo motor (*Feetech STS3032*) is mounted in a servo motor holder which is sliding on a precision machined 6 mm steel shaft via a linear ball bearing. The linear ball bearing is press fit in the servo motor holder while the shaft is held with a set screw in the shaft connector. The shaft connector can be glued or screwed to the mirror. The servo and the mirror adjustment screw are connected via a cylindrical mirror connector which is adapted to the specific adjustment knob of the mirror.

The servo motor has a closed-loop drive which provides 12 bit position precision and a step mode which allows closed-loop movement by more than 360°. The communication with the motor is handled by a microcontroller (*Teensy 4.1*) which is communicating via a serial protocol with the servo allowing up to 1 MBPS (megabit per second). Each servo motor has an identifier which allows communication with many parallel servos. For

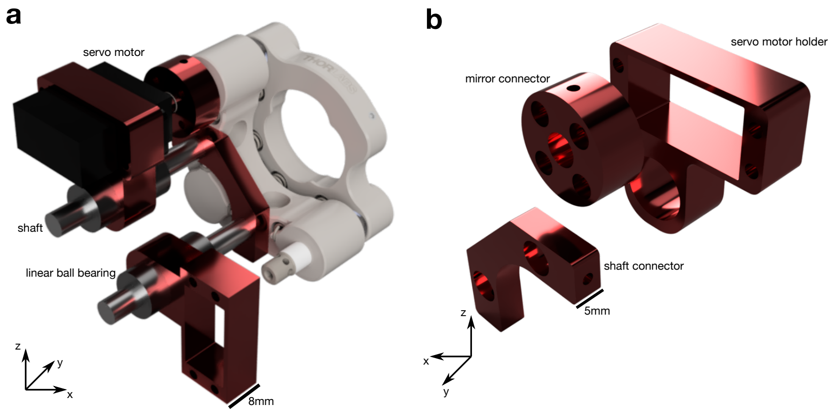

Figure 7.3: Rendering of the mirror motor system. (a)-(b) Rendering of a kinematic mirror mount (*Thorlabs Polaris 1"*) operated with two mirror motors. The servo motors are held by an aluminum holder (red) which is moving with a linear ball bearing on a precision machined shaft. The shaft is connected to a shaft holder which holds the motors of each axis and provides a rotational fix point. The adjustment screw of the kinematic mirror mount and the servo motor are connected with a shaft connector which is adaptable to the different commercially available adjustment knobs. The parts in red are machined in-house while the rest is commercially available.

the initial testing a simple break-out board, connecting servo and microcontroller was used. The software was set up such that position settings can be set from the computer communicating via USB with the microcontroller.

Mirror Motor Performance

The servo-motor can rotate the mirror adjustment screw by a minimal angle of $0.088°$ which corresponds to a screw movement of $d_x \approx 62\,\mathrm{nm}$ for a screw with 100 thread-per-inch. The tilt angle of an optical beam impinging on the mirror is then $2\alpha = 2d_x/L_m \approx 4.9\,\mu\mathrm{rad}$, where $L_m = 2.54\,\mathrm{cm}$ is the kinematic mirror mounts' length. Experimentally we measure the minimal displacement by moving the servo in several steps which is recorded with a camera at a distance of 31.5 cm from the mirror. A fit with to the beam profile gives the central position which is used to calculate the minimal angular displacement $\alpha = 5.9(8)\,\mu\mathrm{rad}$. The second important measurement is repeatability which is determined by moving the motor from its initial position by a certain step-size and back, subsequently comparing the position. We find that for rotations up to 180° the repeatability is below our measurement sensitivity $\alpha_{\mathrm{meas}} = 0.5\,\mu\mathrm{rad}$. In addition, we can record the hysteresis by recording the steps between the starting and final position, which shows that no hysteresis is visible. The measurements confirm the proper operation of the closed-loop position stabilization of the servo motor and show that for the current system the sensitivity is limited by the adjustment screw of the kinematic mirror mount.

Conclusion and Outlook

We designed, built and characterized a new, low-cost mirror motor which allows us to precisely adjust the position, most commercially available kinematic mirror mounts. We found that the servo motor is able to precisely determine its position with 12 bit accuracy which corresponds to a minimal angular displacement of 4.9 µrad on a 1" kinematic mirror mount. The total cost of the system is ∼ 200 CHF per kinematic mirror mount, including the electronics and the mechanical parts, but excluding the commercial kinematic mirror mount.

In future developments, we will implement ethernet communication between microcontroller and the host computer as well as a graphical user interface. Furthermore, the electronics will be upgraded to allow operation of many mirrors in parallel. In terms of sensitivity, the minimal angular displacement could be halved when using an adjustment screw with 200 threads-per-inch, which is commercially available.

7.4 HIGH-PRECISION DIGITAL-TO-ANALOG CONVERTER SYSTEM

Controlling a quantum gas experiment requires many analog and digital control signals which have well known timings and precise output values. In our experiment, computer based analog output cards are used (*National Instruments PCIe6738*) to send 16 bit analog signals to the different devices in the lab. This often requires long coaxial cables which can act as antennas to outside signals and cause crosstalk between different cables. Furthermore, they produce large ground loops between the computer and the devices, leading to even more pickup of noise and line interference.

In order to prevent this and to improve the precision and noise of the analog control signals in the experiment, a new digital-to-analog (DAC) converter board was designed, centered around a 20 bit DAC converter and all-digital communication up to the device which is to be controlled. The idea for such a board stems from Ref. [191]. Details of the PCB design and FPGA programming can be found in the semester and master theses of Z. Liu [192], L. and D. Pahl [193] and B. Dönmez [194].

The results shown in this section have been presented in the following publication:

> D. Pahl, L. Pahl, E. Mustafa, Z. Liu, P. Fabritius, J. Mohan, P. Clements, A. Akin and T. Esslinger
> *A low-noise and scalable FPGA-based analog signal generator for quantum gas experiments*
> *2021 IEEE International Conference on Quantum Computing and Engineering (QCE)*, 450-451 (2021)

7.4.1 *System Overview*

The three cornerstones of the systems' hardware are the high precision DAC, the all-digital communication and the ground separation. Figure 7.4(a) shows a schematic overview of the systems' hardware configuration. The control computer is calculating the voltage samples from the programmed functions and transmits them, including their timings to the FPGA board (*Digilent Zybo Z7-20*) via the network. The FPGA board is receiving the data with its processor and writes the samples to its working memory. The programmable logic section of the FPGA board is reading the samples via direct memory access (DMA) and creates a serial-peripheral-interface (SPI) signal from them. The SPI signal consists of three separate signals, i.e. a clock signal, a trigger signal and a data signal. The SPI signal is output at > 24 MHz via the PMOD connectors of the board and sent to the breakout board specifically designed for the system. The breakout board is used to translate the single ended SPI signals to low-voltage differential signals

(LVDS) which are more robust to noise and optimized for twisted wire ethernet cables. In addition, the breakout board receives the supply voltage for the DAC boards from a lab power supply. The standard ethernet cable consists of 4 twisted pairs which are used to transmit signal and power to the DAC boards. The supply voltage is chosen to be 24 V to reduce losses due to high currents.

On the DAC board, the digital signals are translated back to SPI signals which are required from the DAC chip (*Analog Devices AD5791*). The supply voltage is sent to a ground isolated DC/DC converter which has three outputs on the isolated side at ±15 V and 5 V. The SPI signals are transmitted via an SPI isolator to the isolated ground of the DAC board. The isolated ground section of the board houses linear regulators used to reduce the supply voltage noise stemming from the DC/DC conversion, the voltage reference (*Analog Devices LTC6655LNB*) and the DAC section including DAC chip and OPAMPs for buffering.

The placement of the DAC chip at the very end of the whole system and the small size of the DAC board allows placing the board close to the device which it controls. This minimizes the analog signal cable lengths which means the cable acting as an antenna only works for high frequencies and cross-talk is reduced due to spatial separation. The ground separation means that the device is providing a single ground reference for the DAC chip thereby not allowing a ground loop.

Figure 7.4(b) shows the new implementation of an experimental sequence. The experimental control software is already event-based, meaning a change of waveform is defined as a new event, but the hardware does not allow for changes of the sampling period between events. The adaptable sampling rate allows to greatly reduce the data-rate needed for operation and allows higher sampling rates wherever they are needed. In the current experimental control system the maximal accessible sampling rate is 100 kSPS due to our limited memory size. With the new DAC chip sampling rates of up to 1 MSPS are possible while the programmable logic allows us to reduce the sampling rate individually for each event in the sequence.

7.4.2 System Performance

The operational version of the DAC board is shown as a picture in Fig. 7.4(c) where two printed circuit boards (PCBs) have been stacked to reduce the total footprint. The upper PCB contains the ethernet connector, the ground separation and the digital translation from LVDS to SPI. On the isolated side there is an additional linear regulator providing 3.3 V to the rest of the board. The lower PCB contains linear regulators providing the positive and negative supply of the DAC and the OPAMPS as well as the additionally regulated supply of the voltage reference. The voltage reference is buffered by a four channel OPAMP allowing to change the output range of the DAC by all possible combinations of the values in $V_{\text{min}} = [-10, -5, 0]$ and a value $V_{\text{max}} = [0, 5, 10]$. The DAC chip is programmed by a 24 bit data string which contains some configuration settings and 20 bit of data. In principle, a DAC is a sophisticated voltage divider, using internal switches programmed by the data to divide the voltage from the voltage reference to obtain the desired output value. The output of the DAC is buffered by a low-noise OPAMP with a slightly larger output current ±40 mA which allows the DAC to drive small capacitive loads.

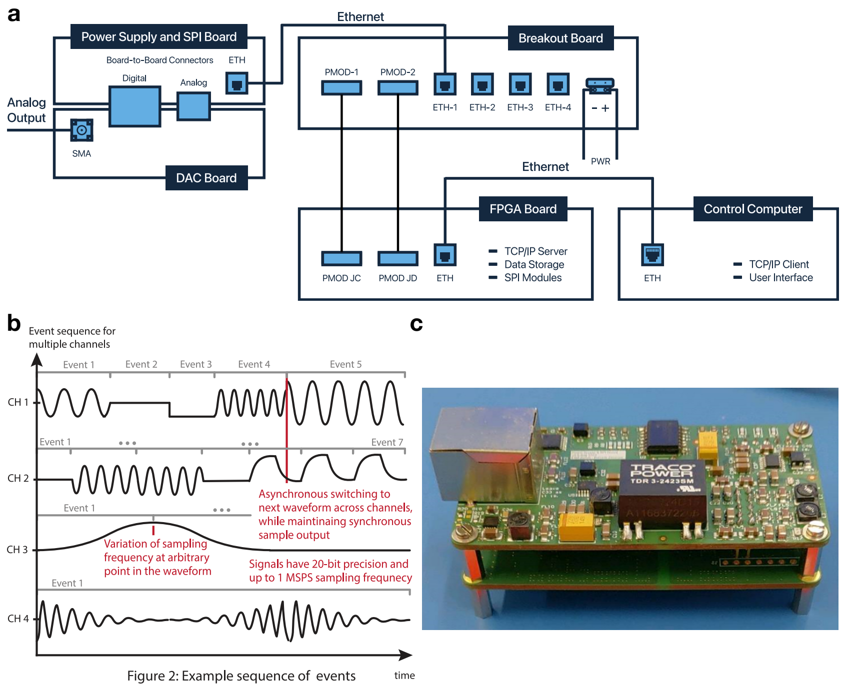

Figure 7.4: Low-noise digital to analog converter system. The architecture of the system is displayed where the computer controlling the experiment sends waveforms including metadata to the FPGA board. The FPGA board provides the correct timing and data via SPI signals to the break-out board which generates LVDS signals that can be transferred via ethernet cables. The DAC board includes a PCB for reception of the LVDS and ground-isolation and a second, stacked PCB for voltage regulation, the voltage reference and the DAC chip. (b) The event based waveform sequence includes variable sampling rates to reduce data requirements and asynchronous switching of the different channels. (c) Picture of a first operational version of the DAC board. (a) adapted from Ref. [194] and (b) adapted from Ref. [195].

In its current design the DAC board is operational and can output signals with varying sampling rate up to 1 MSPS for the previously mentioned output ranges. The full characterization of the board is still ongoing, specifically regarding noise and offset drifts.

7.4.3 Conclusion and Outlook

In summary, we have designed and built a new digital to analog conversion system which allows the high precision while rejecting common sources of noise and interference. The system allows event based sampling rates reducing memory consumption thus increasing the maximal possible sampling rate. The high accuracy and low noise should be particularly suited where precise analog setpoints with large dynamic range are necessary, like magnetic field stabilization and cavity frequency stabilization.

The project is not ready for the experiment yet, in order to be used in the experiment the following features have to be implemented:

- External clock synchronization to have stable timings between all devices.
- External, digital FPGA board trigger to synchronize starting times of the sequence.
- Housing for the DAC board to shield it from electromagnetic interference and reduce thermal drifts.
- Noise characterization and possible improvements of the DAC board

These improvements are currently implemented within the scope of a masters and a semester thesis. In the future, we are also planning to use the upper PCB of the design shown in Fig. 7.4(c) as a building block for other applications, like an ADC board or a low precision DAC board with several outputs.

7.5 STEREO-CAMERA READOUT AND FEEDBACK WITH AN FPGA

One major requirement for our experiment is stable positions of the beams making up the transport geometry, for details see Sec. 5.4. Besides passive stability, we also built a new beam position stabilization system which is able to provide feedback on position, angle, waist. From these quantities the focus position of any optical beam. The system is based on imaging the beam with two high-speed cameras at different positions along its direction of propagation. This allows the extraction of beam parameters from non-Gaussian beams via image processing and gives additional information on the full beam properties along its path. Commonly used feedback systems rely on quadrant photodiodes or position-sensitive devices which only provide positional information, while common beam profilers are slow and only use a single camera. The system has been programmed and characterized within the semester theses of E. Mustafa [196], G. Bisson [197], P. Anand and S. Marti.

The results shown in this section are accepted for publication:

> S. Marti, E. Mustafa, G. Bisson, P. Anand, P. Fabritius, T. Esslinger and A. Akin
> *FPGA-based real-time laser beam profiling and stabilization system for*

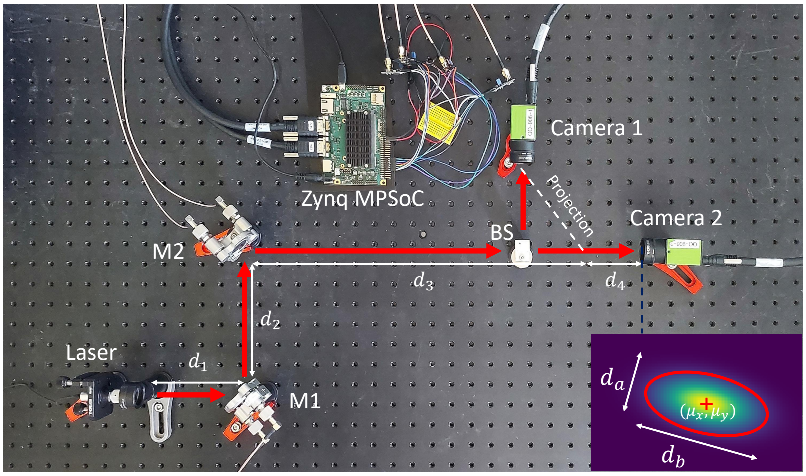

Figure 7.5: Optical setup for the stereo-camera system. The laser is diverted by two piezo mirrors onto a beam-splitter each followed by a camera. The cameras record pictures with a frame-rate of 43 FPS and the FPGA extracts the Gaussian beams moments' within 435 ns. The FPGA then calculates the error-signal of the beam position and the corresponding feedback signal within 383 ns including the data-transmission to the feedback DACs. The system in its current status allows feedback on beam positions and waists, but requires additional algorithms to provide beam-angle feedback.

quantum simulation applications
26th Euromicro Conference on Digital System Design (DSD'2023),
(2023)

7.5.1 System Overview

The central component of the apparatus is a dual camera read-out board (*Enclustra Mars EB1*) which is supplemented with an FPGA system on chip (SOC) (*Enclustra Mars XU3*). The cameras are two 5 MP CCD cameras (*JAI GO-5000-PMCL*) which are interfaced via a camera link connection and have a base frame rate of 107 FPS. Binning the pixels of the CCD or reducing the number of rows being read-out allows to increase the frame-rate. For example at a resolution of 640×1024 the frame rate would be ≈ 300 FPS.

Figure 7.5 shows the optical setup of the test-system. The beam is split with a beam splitter and imaged by the two cameras at different positions along the beam. Knowing the distance between the two cameras, it is possible to calculate the angle of the beam via its position-difference between the two cameras. In addition, from the measured waists, it is possible to extract the focus' position via the evolution of the beams' waist along the propagation direction $w(z) = w_0\sqrt{1 + (z/z_R)^2}$, where w_0 is the waist in the focus and z_R is the Rayleigh range. The subsequent feedback on position and angle is then provided by two piezo mirrors (*Thorlabs Polaris Piezo*), driven by four DAC directly from the FPGA SOC.

For the feedback, the cameras are read-out directly via the programmable logic which takes 21 ms for the data-transfer and 94 ns in latency on the programmable logic (PL). In the current system, the waist and position of a Gaussian beam are determined via its distribution on the pixels to simplify the image processing. This means that the PL calculates the two lowest moments $\langle x^n \rangle$ of the intensity distribution in two-dimensions x, y which give access to the mean and variance, i.e. position and waist, of the Gaussian. The correlation between the horizontal and vertical axis $\langle xy \rangle$ allows to determine the angle of the beam. This process takes 435 ns on the PL which is followed by the PI loop which receives its digital set-points from a computer. The PI loop and the following digital to analog conversion has a latency of 383 ns which means in total, the PL takes $\sim 1\,\mu\mathrm{s}$ for the complete feedback, excluding the camera limited frame rate.

The feedback loop is tested by imparting a deterministic disturbance with one of the piezo mirrors (M1 in Fig. 7.5) which is compensated with the second piezo mirror.

7.5.2 Conclusion and Outlook

The dual camera, FPGA feedback system can calculate beam position and waist including feedback in less than 1 μs allowing fast feedback on both quantities. The position of a beam was stabilized in both directions, using the system, though angle and waist feedback have not been implemented yet.

For future use of the system, the programmable logic has to be used in conjunction with the CPU in order to do more sophisticated calculations which allow the angle and waist feedback. In addition, a real fitting algorithm is planned to be implemented which should allow feedback on more subtle beam features, such as the width of the nodal line of a TEM_{01} beam. Finally, the fast read-out via camera link can be used for other applications, such as the position or intensity stabilization of many tweezers as well as the fast read-out of an EMCCD used for single atom detection.

Part II

QUANTUM TRANSPORT WITH NEAR-RESONANT LIGHT

8

SPIN-SELECTIVE AND DISSIPATIVE QUANTUM POINT CONTACT

CHAPTER CONTENTS

The content of this chapter closely follows our following publications:

M. Lebrat, S. Häusler, P. Fabritius, D. Husmann, L. Corman and T. Esslinger
Quantized Conductance through a Spin-Selective Atomic Quantum Point Contact
Physical Review Letters **123**, 193605 (2019)

L. Corman, P. Fabritius, S. Häusler, J. Mohan, L. Dogra, D. Husmann, M. Lebrat and T. Esslinger
Quantized Conductance through a Dissipative Atomic Quantum Point Contact
Physical Review A **100**, 053605 (2019)

8.1 MOTIVATION

We apply close-to-resonant light inside an atomic quantum point contact (QPC). Depending on the frequency the light either creates a spin-dependent potential which acts as a spin-filter or it will directly dissipate atoms locally from the previously closed system. This allows us to study the effect of an effective Zeeman potential inside a QPC on the transport properties and how weak interactions modify its effects. In addition, we observe the effect of dissipation on the quantization of transport through the QPC, and we introduce a theoretical model allowing *ab initio* calculations of either effects in the non-interacting regime.

The coupling between spin and particle transport has been studied extensively and is of both technological [198] and fundamental interest [199, 200]. Zeeman effects and spin-orbit coupling are considered to be the origin for effects like spin-polarized edge modes [201] and Majorana fermions [11]. In addition, spin-dependent effects can also be used to probe the properties of the bulk system such as spin-drag [202] and the pairing gap [111]. The ground-state nature and the well-controlled interaction in cold atom experiments provide an alternative system in which the particle degree of freedom can be coupled to the internal, i.e. spin, degree of freedom in analogy to a solid state platform. This allows the introduction of differential Stark shifts [203, 204] and spin-orbit coupling [54, 205]. The aspect of a local spin-dependent effect has not been studied in these systems yet, since aforementioned experimental realizations were focused on bulk effects. Applying the spin manipulation locally can give rise to new boundary effects at the interface between the spin-coupled and non-coupled system which is found in magnetic heterojunctions.

The atom-light interaction allowing us to introduce spin-dependent effects also introduces particle loss, i.e. dissipation. One of the signatures of our experiment is the quantized conductance which relies on the correlated transport [206] of fermions at low temperatures. Coupling this system to its environment via particle dissipation raises the question on how robust such signatures are. More generally, the open system poses questions on the robustness of quantum mechanics to interaction with the environment and on the competition between dissipation and coherence or interaction effects [56, 57]. The treatment of the open system is often done in the form of a Lindblad master equation [100] which implies a non-Hermitian evolution of the system, producing exotic phenomena related to exceptional points where eigenvectors collapse due to a critical dissipation strength [207, 208]. In the context of condensed matter system the interaction between transport and its environment has been studied extensively, though mostly in form of an incoherence electron scattering process [209–211] with particle number conservation. Our cold atom system, intrinsically nearly closed, thus provides an ideal ground to study the effect of stochastic particle loss has on quantized conductance. The effect of particle loss has been studied in cold gases via a myriad of techniques, including photoassociation of molecules [60] or molecular decay [58, 212], ionization of atoms with an electron beam [213] or a femtosecond laser [214] and scattering of photons from a near-resonant beam [215, 216].

We realize a spin-selective quantum point contact by projecting a near-resonant beam onto our 1D junction leading to a differential Stark shift for the hyperfine states, i.e. the pseudo spins. The effective Zeeman shift is large compared to the Fermi energy, the temperature and the bias allowing us to efficiently filter the transport according to the atomic spin. The inherent photon-scattering losses are minimized due to the local nature of the spin-filter which allows us to observe mean-field particle interaction effects affecting the effective strength of the Zeeman shift. The observed effects are theoretically modeled using a Landauer-Büttiker model. The dissipative effects are studied by tuning the frequency of the near-resonant beam to produce a purely dissipative atom-light interaction. The atom-light interaction is modeled via the atomic polarizability at high magnetic fields while the dissipation is described by a non-Hermitian contribution to the Landauer-Büttiker model. The density dependent loss is also used to measure the local density around the channel.

A non-interacting ultracold cloud of ^{6}Li is prepared in a two-terminal transport configuration, see Sec. 8.2 and Ch. 2. The transport theory used to model the spin-filter and the dissipation is presented in Sec. 8.3. The effect the spin-filter has on the transport is measured and discussed in Sec. 8.4 while the dissipation effects are described in Sec. 8.5. In addition, we present an application of dissipation as a local measure of the density in Sec. 8.5.2. Finally, we give a terse summary of the attempts at trying to apply the spin-filter in the strongly interacting regime in Sec. 9.2.

8.2 EXPERIMENTAL SETUP

The ultracold cloud of ^{6}Li is prepared in a balanced mixture of the lowest and third-lowest hyperfine state, here used as spin $|\downarrow\rangle$ and $|\uparrow\rangle$. The cloud is cooled to degeneracy where an atom number of $N = 1.1(1) \times 10^5$ per spin at a temperature of $T = 66(12)\,\mathrm{nK}$ is reached. The magnetic field is tuned to the zero-crossing of the Feshbach resonance at $B = 568\,\mathrm{G}$ where the gas is non-interacting. The quantum point contact (QPC) is created by two repulsive, intersecting TEM$_{01}$ like beams creating a transverse confinement of $\nu_x = 14.0(6)\,\mathrm{kHz}$ and $\nu_z = 9.03(5)\,\mathrm{kHz}$. The resulting reservoirs on the left and right of the QPC provide atoms for the transport at a mean chemical potential of $\mu_{\mathrm{res}} = (\mu_L + \mu_R)/2 = k_B \cdot 0.23\,\mu\mathrm{K}$. In the non-interacting regime the spin and particle-conductance are both equal and given by the conductance quantum $1/h$ per transport mode. The number of transport mode is controlled with an attractive Gaussian gate beam $w_g = 31.8(3)\,\mu\mathrm{m}$ (see Fig. 8.1(a)) which shifts the zero-point energy of the QPC w.r.t to the chemical potential. The local effective chemical potential is given by $V_g + \mu_{\mathrm{res}}$.

The near-resonant beam is projected through the high-resolution microscope using an aberration corrected wavefront which produces a Gaussian beam with a waist of $w_s = 2.0(1)\,\mu\mathrm{m}$, smaller than the QPC length $5.9\,\mu\mathrm{m}$ and the Fermi wavelength $\lambda_F = \sqrt{h/m\nu_z} = 2.7\,\mu\mathrm{m}$. The beam is σ_- polarized and centered on the QPC, while the position can be controlled using the digital micromirror device used for aberration correction. The frequency of the laser ν can be arbitrarily tuned due to the lock to a wavelength meter. For the spin-filter the frequency is tuned between the resonance frequency of the $|\downarrow\rangle$ and $|\uparrow\rangle$ transition to the $^2P_{3/2}$ manifold such that its absolute detuning is equal at $\delta_\uparrow = -\delta_\downarrow - 81.3\,\mathrm{MHz}$. This induces a repulsive potential for $|\uparrow\rangle$ and an attractive potential for $|\downarrow\rangle$ with equal magnitude $\pm V_s$. In the limit $I \ll I_{\mathrm{sat}}$ this magnitude is linear in the intensity, with $I_{\mathrm{sat}} = 25.4\,\mathrm{W/m^2}$. The typical power of the beam $P_s = 20(6)\,\mathrm{pW}$ corresponds to a peak intensity of $I_s = 3(1)\,\mathrm{W/m^2}$ which corresponds to $I/I_{\mathrm{sat}} = 0.13(4)$. In the case of equal detunings this produces an optical potential of $V_s = k_B \cdot 330(98)\,\mathrm{nK}$ and a scattering rate of $\Gamma_s = 3.1(9)\,\mathrm{kHz}$ while the loss rate per potential energy is given by $\Gamma_s/V_s = 9.4\,\mathrm{kHz}/(k_B\mu\mathrm{K})$. The spin-dependent potential can be viewed as an effective Zeeman shift $V_s = -\mu B_z$ due to a magnetic moment μ in an artificial magnetic field.

The resulting potential landscape can be modeled using the spin-independent zero point energy due to the x and z confinement, neglecting the gate beam

$$V_0(y) = \frac{1}{2} h\nu_z e^{-y^2/w_z^2} + \frac{1}{2} h\nu_x e^{-y^2/w_x^2}, \tag{8.1}$$

where $\nu_{x,z}$ are the confinement frequencies and $w_{x,z}$ are the waists along y. In addition, the spin-dependent potential $V_\alpha(y)$ is superimposed given by

$$V_\alpha(y) = \epsilon_\alpha V_s e^{-2y^2/w_s^2}, \tag{8.2}$$

with $\epsilon_\uparrow = +1$ and $\epsilon_\downarrow = -1$ while an imaginary potential describes the losses due to the photon scattering $\Gamma(y)$ via

$$iV_{\mathrm{loss}}(y) = -i\hbar \frac{\Gamma(y)}{2}, \tag{8.3}$$

where $\Gamma(y)$ is proportional to the intensity $I_s(y)$ of the near-resonant beam.

The atom density of the cloud are determined via an absorption image at the end of the experimental cycle. Fitting a 1D density profile to the cloud

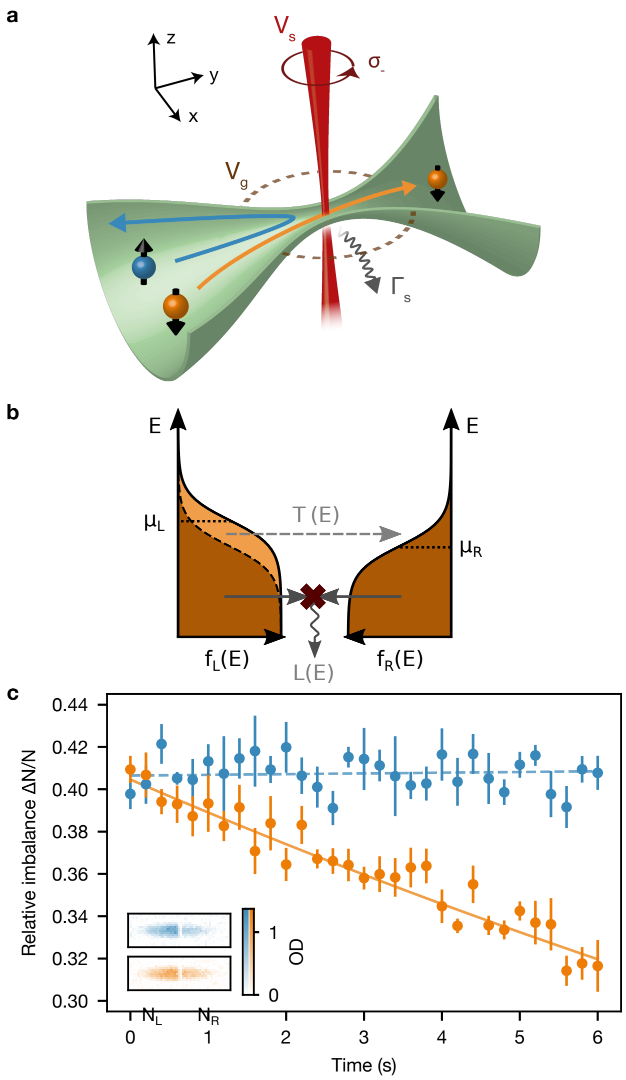

Figure 8.1: Quantum point contact with a spin-filter. (a) The QPC (green) is intersected at its center by a focused near-resonant beam (red) $w_s = 2.0(1)\,\mu\mathrm{m}$ imposing a spin-dependent potential $\pm V_s$, i.e. an effective Zeeman shift V_s. Atoms in the third-highest hyperfine state ($|\uparrow\rangle$, blue) are blocked while the lowest hyperfine state ($|\downarrow\rangle$, orange) can pass the beam. The spin-filter introduces additional losses via photon scattering determined by the rate Γ_s. The transport through the QPC is controlled by varying the attractive gate potential $-V_g$ which locally shifts the reservoir chemical potential μ_{res}. (b) The relative particle imbalance $\Delta N/N$ evolution as a function of time is measured at a chemical potential of $V_g + \mu_{\mathrm{res}} = k_B \cdot 0.61(2)\,\mu\mathrm{K}$ and near-resonant beam power $P_s = 20(6)\,\mathrm{pW}$. The particle current of atoms in state $|\uparrow\rangle$ is suppressed $I_\uparrow = -19(85)$ atoms/s while state $|\downarrow\rangle$ are unimpeded $I_\downarrow = 833(98)$ atoms/s, indicating fully spin-polarized transport. The error bars are standard errors of the mean over five measurements. Inset: Average cloud absorption picture after 6 s of transport time of five measurements.

then allows to extract the temperature, atom number and chemical potential of each reservoir via the equation of state, see also Sec. 2.2 for more details. Here, the spin resolution is obtained by repeating each experimental run twice and imaging the respective spin separately.

8.3 TRANSPORT MODEL OF THE DISSIPATIVE AND SPIN-SELECTIVE QPC

Transport in our QPC is well described by the Landauer-Büttiker formalism [6, 217, 218] which relates conductance to transmission. Here, this formalism is extended to the case of loss in the transport region. The loss is modeled as an imaginary potential. In addition, the time evolution is calculated by evaluating the Landauer-Büttiker formula at different points in time, where loss is present. The atomic physics background used to calculate the scattering rate and dipole potential due to the atom-light interaction at high magnetic fields is introduced in Ch. 3.

8.3.1 Landauer-Büttiker Model

The system in question is formally described by a Hamiltonian evolution $\hat{H}$ which is weakly coupled to the environment with no memory (Born-Markov approximation). The evolution of the full system is then described by a Lindblad master equation [39, 100]

$$\partial_t \hat{\rho} = -\frac{i}{\hbar}[\hat{H}_0, \hat{\rho}] - \sum_j \left(\frac{1}{2}\hat{L}_j^\dagger \hat{L}_j \hat{\rho} + \frac{1}{2}\hat{\rho}\hat{L}_j^\dagger \hat{L}_j - \hat{L}_j \hat{\rho} \hat{L}_j^\dagger \right) . \tag{8.4}$$

Here, the Lindblad operators $\hat{L}$ describe the loss process. It is possible to rewrite the master equation by neglecting the last term and including the first two terms of the sum in an effective Hamiltonian

$$\hat{H}_{\text{eff}} = \hat{H}_0 - i\frac{\hbar}{2}\sum_j \hat{L}_j^\dagger \hat{L}_j \,, \tag{8.5}$$

which can be further refined by inserting the loss mechanism of our system

$$\hat{H}_{\text{eff}} = \hat{H}_0 - i\frac{\hbar\Gamma}{2}\hat{\Psi}^\dagger(y)\hat{\Psi}(y) \,, \tag{8.6}$$

where $\hat{\Psi}(y)$ is the particle annihilation operator. This approximation neglects the fluctuations and the fermionic commutation relations introduced by the neglected term in Eq. 8.4 though it is the minimal way to describe non-Hermitian dynamics [207] via an imaginary potential. The neglected term becomes important when measurements at short timescales are required, where the stochastic nature of the loss process plays a role. In our system, the fluctuations timescales Γ^{-1} are short while the transport timescales are very long $\sim 4\,\text{s}$ such that we always measure a steady-state conductance.

Transmission, Reflection and Loss

The conductance between two reservoirs is described by the transmission function $\mathcal{T}(E)$ of the QPC at a given chemical potential, i.e. energy. The transmission describes the probability of a particle to be transmitted in its mode through the channel. The transmission of each individual mode can be calculated from its longitudinal potential, i.e. zero-point energy, where a particle is modeled as a plane wave. In the case of a complex-valued, spin-dependent potential $V_\sigma(y)$ as is here, the forward and backward scattering amplitudes for a single particle can still be calculated by solving the 1D Schrödinger equation using Numerov"s method. The total probability is no longer conserved since loss is included via the complex potential which is rectified by defining a loss probability $\mathcal{L}(E)$ such that

$$\mathcal{T}(E) + \mathcal{R}(E) + \mathcal{L}(E) = 1\,. \tag{8.7}$$

Landauer-Büttiker Formalism with Loss

The Landauer-Büttiker formalism can be derived from a consideration of left and right moving particles in a junction. Here we can start with the same consideration where the left and right movers are given by

$$\dot{N}^{\text{trans}}_{\rightarrow/\leftarrow} = \frac{1}{h}\int_{-\infty}^{+\infty} f_{L/R}(E)\mathcal{T}(E)\,dE. \tag{8.8}$$

In the 1D system this formula is independent of the fermionic velocity due to the 1D density of states [92]. The total atom number transported through the channel, per unit time, including the atoms below the Fermi energy, is given by

$$\begin{aligned}\dot{N}^{\text{trans}} &= \dot{N}^{\text{trans}}_{\rightarrow} + \dot{N}^{\text{trans}}_{\leftarrow} &(8.9)\\ &= \dot{N}^{\text{trans}}_{\rightarrow} - \dot{N}^{\text{trans}}_{\leftarrow} + 2\dot{N}^{\text{trans}}_{\leftarrow}. &(8.10)\end{aligned}$$

Figure 8.1(b) shows the different contributions to the total current. The measured current, orange shaded in Fig. 8.1(b), is given by the difference between left and right movers

$$\dot{N}^{\text{trans}}_{c=} I_N = \frac{1}{h}\int_{-\infty}^{+\infty} [f_L(E) - f_R(E)]\mathcal{T}(E)\,dE. \tag{8.11}$$

The subscript "c" is used to indicate the current "contributing" to the measured transport. The remaining atoms are transmitted below the transport window through the channel, see the brown shaded area in Fig. 8.1(b), and are described by the rate

$$\dot{N}^{\text{trans}}_{nc} = 2\dot{N}^{\text{trans}}_{\leftarrow}\,, \tag{8.12}$$

where "nc" stands for "non-contributing". The measured current I_N is then related to the conductance by Ohm's law

$$I_N = G\Delta\mu\,, \tag{8.13}$$

where in this context the chemical potential difference $\Delta\mu$ is small and thermoelectric effects are neglected.

8.3.2 Dynamic Transport Model – Cooling with Dissipation

The previously introduced model can be used to not only determine the conductance and current expected during transport but also as a function of time assuming equilibrated reservoirs. The loss-current depends on the total atom-number in the channel which is given by the sum of Fermi-Dirac distributions and the energy dependent loss $\mathcal{L}(E)$

$$
\begin{aligned}
-\frac{dN}{dt} &= \frac{1}{h}\int_{-\infty}^{+\infty}[f_L(E)+f_R(E)]\mathcal{L}(E)dE && (8.14)\\
&= \frac{1}{h}\int_{-\infty}^{+\infty}[f_L(E)-f_R(E)]\mathcal{L}(E)dE && (8.15)\\
&+\frac{2}{h}\int_{-\infty}^{+\infty}f_R(E)\mathcal{L}(E)dE. && (8.16)
\end{aligned}
$$

In analogy to the total number of transmitted particles the loss rate is also given by a loss from the net current I_N described by $\dot{N}_c^{loss}$ and a loss from below the transport window $\Delta\mu$ given by $\dot{N}_{nc}^{loss}$. The time evolution of particle number $N_{L,R}$ and internal energy $U_{L,R}$ in the reservoir is then calculated iteratively using Euler's method and the following steps. (i) converting extensive quantities $(N_{L,R}, U_{L,R})$ into intensive quantities $(\mu_{L,R}, T_{L,R})$ using the 3D equation of state of the non-interacting Fermi gas; (ii) reevaluating the Fermi-Dirac distributions in order to compute the derivatives of atom-number and internal energy via

$$
\begin{aligned}
\frac{dN_{L,R}}{dt} &= \frac{1}{h}\int_{-\infty}^{+\infty}f_{R,L}(E)\mathcal{T}(E)dE\\
&-\frac{1}{h}\int_{-\infty}^{+\infty}f_{L,R}(E)[\mathcal{T}(E)+\mathcal{L}(E)]dE && (8.17)\\
\frac{dU_{L,R}}{dt} &= \frac{1}{h}\int_{-\infty}^{+\infty}E\cdot f_{R,L}(E)\mathcal{T}(E)dE\\
&-\frac{1}{h}\int_{-\infty}^{+\infty}E\cdot f_{L,R}(E)[\mathcal{T}(E)+\mathcal{L}(E)]dE; && (8.18)
\end{aligned}
$$

and (iii) updating $(N_{L,R}, U_{L,R})$ after a small time-step.

One interesting application of the dissipation in the transport region is cooling the reservoirs via the energy dependent loss function $\mathcal{L}(E)$. Figure 8.2 shows the evolution of atom-number and temperature as a function of dissipation strength Γ for different gate potentials V_g. The cloud initially has $N_0 = 10^5$ atoms in each spin-state at a temperature of $T = 60\,\text{nK}$. The energy dependent transmission, loss and reflection is calculated for different loss rates Γ and subsequently the time evolution is calculated using the described method. Choosing a gate potential slightly below the onset of conductance (see Fig. 8.2(a)) will then lead to a cooling in the reservoirs, see Fig. 8.2(d). The cooling effect is similar to the tilting effect with a magnetic gradient [78], here the high onset only lets hot particles in the wing of the Fermi-Dirac distribution enter the transport region. The loss thus only affects the hot part of the cloud and thus cools the rest. The cooling effect calculated here is after an exposure time of 4 s. Though rather inefficient in this static scheme which is generally the case for cooling fermionic gases below degeneracy, the scheme could be improved by dynamically changing the wire confinement, thus decreasing the energy at which atoms can enter the channel.

8.4 SPIN FILTER IN AN ATOMIC QPC

The initial chemical potential bias is spin-independent such that only the channel produces a spin-dependent current. The typical atom-number imbalance is $\Delta N = 45(3)\cdot 10^3$ atoms for each spin state. The subsequent time

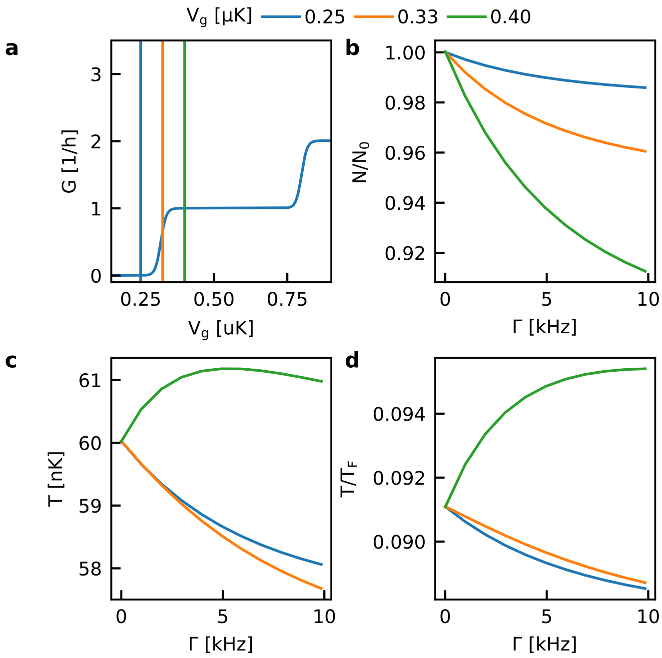

Figure 8.2: Theoretical cooling scheme with dissipation. The cloud is initially made up of $N_0 = 10^5$ atoms in each spin state at a temperature of $T = 60\,\text{nK}$. The transport geometry is equivalent to the one presented here. The evolution of atom-number (b) and temperature (a) is calculated given the introduced Euler method for different dissipation strength Γ and gate potentials V_g. The atom-number, temperature and Fermi temperature (d) indicated here are the final values after a time evolution for 4 s. When the gate potential V_g is chosen below or close to the onset of conductance (a) a cooling effect is visible (d) since only hot particles can enter the lossy transport region.

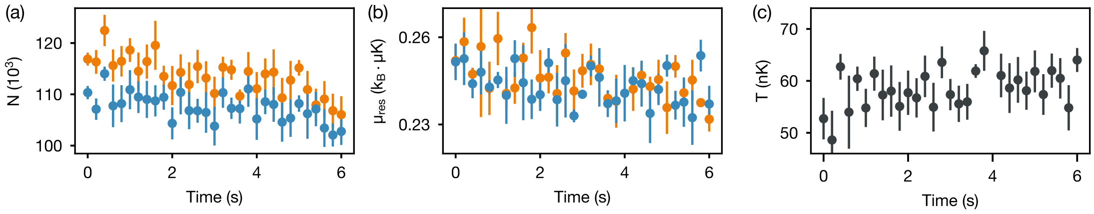

Figure 8.3: Reservoir evolution of atom-number, chemical potential and temperature. We find that within our preparation error the total atom number N (a) and chemical potential μ_{res} (b) hardly evolve. Concurrently the average temperature T is constant over 6 s.

evolution is measured and displayed in Fig. 8.2(c). For this measurement the interatomic scattering length was kept close to zero $a = 0(7)a_0$ where a_0 is the Bohr radius. The applied spin-filter has a strength of $P_s = 20(6)$ pW which corresponds to $I_s/I_{sat} = 0.13(4)$. The measured evolution of the particle imbalance is used to extract a particle current for each spin-state, which we find to be $I_\uparrow = -19(85)$ atoms/s and $I_\downarrow = 833(98)$ atoms/s. The system thus acts as a nearly ideal spin-filter equivalent to condensed matter realizations in spin-polarized tunnel junctions [219] or QPCs in strong magnetic fields [220], though the observed current polarization is similar to the best values obtained in magnetic heterostructures [221].

The concurrent losses due to the atom-light scattering with a peak value of $\Gamma_s = 3$ kHz affects the reservoir thermodynamics only weakly, see Fig. 8.3. The average chemical potential $\mu_{res} = (\mu_L + \mu_R)/2$ displayed in Fig. 8.3(b) reduces by $k_B \cdot 30$ nK, smaller than any other transport energy scale. Consistent with low atom-loss and chemical potential decrease the temperature shows no appreciable change. This behavior can be understood from the large atom-atom mean free path due to the zero-crossing of the Feshbach scattering length. Though every photon scattering event deposits at least $E_R = (h/\lambda)^2/2m = k_B \cdot 3.54\,\mu K$ of energy on a single atom, this atom likely leaves the system without depositing the kinetic energy in a scattering event. As long as the loss rate and total losses are small we thus expect the reservoirs to remain in a thermal state.

We can use this observation to faithfully measure the conductance of the channel using the Landauer-Büttiker formula. The spin-dependent transmission, i.e. conductance, can be probed by varying the local chemical potential $V_g + \mu_{res}$ relative to the spin-dependent QPC potential landscape. Here the scattering length was set to $a = 91(7)\,a_0$ and the conductance is repeatedly measured for different values of the local chemical potential, following the recipe in Sec. 2.4, i.e. calculating G from the atom number imbalance $\Delta N/N$ before and after 4 s of transport. The conductance G is found to exhibit a quantized plateau, the hallmark of single-mode quantized conductance as can be seen in Fig. 8.4(a). Without applying the spin-filter the conductance plateaus of the different spin states are overlapping though their height $G = 0.84(1)\,1/h$ is below the conductance quantum $1/h$ due to a residual temperature bias. The temperature bias is present due to the initial preparation and is neglected in the evaluation of the conductance.

Figure 8.4(b)-(c) display the conductance plateaus when the spin filter is applied and its intensity I_s is varied, thereby preventing spin $|\uparrow\rangle$ from being transported at a given chemical potential. The observed shift is given by the barrier $+V_s$ added to the zero-point energy of the QPC, see Fig. 8.4(e)-

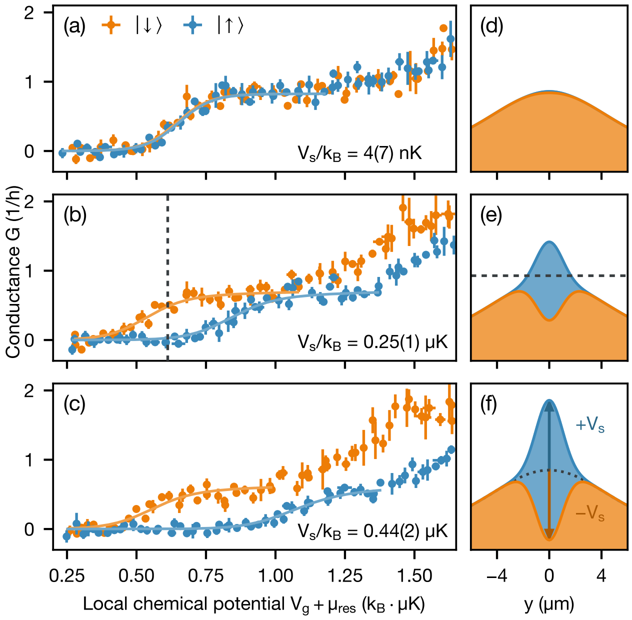

Figure 8.4: Spin-polarized quantized conductance. (a)-(c) Quantized conductance curves are obtained by measuring the conductance G as a function of the local chemical potential $V_g + \mu_{res}$ at a scattering length of $a = 91(7)\,a_0$ and without the spin-filtering beam. Introducing the spin-filter with $I_s = 0.13(4)\,I_{sat}$ (b) and $I_s = 0.17(5)\,I_{sat}$ (c) shifts the onset of conductance of the blocked state $|\uparrow\rangle$ (blue). Error-bars correspond to the standard error of the mean of three measurements. The Landauer model is fitted (solid line) to measure the spin-dependent potential which is found to be maximal at $V_s = k_B \cdot 0.44(2)\,\mu$K (c). (d)-(f) The quasi-1D potential landscape along the transport direction y indicates the spin-dependent potential. Grey dashed lines indicate the local chemical potential used for the measurements in Fig. 8.1 and Fig. 8.3.

(f). The corresponding opposite shift of the zero-point energy for $|\downarrow\rangle$ is found to be weaker due to the near-resonant beam being smaller than the QPC. We find that the maximal current polarization can be found for a chemical potential in the middle of the potential barrier (black dashed line in Fig. 8.4(e)) at $V_g + \mu_{res} = k_B \cdot 0.61(2)\,\mu K$ which is the local chemical potential chosen to measure the current polarization in Fig. 8.1(c). The conductance plateaus persists throughout the measured intensity range of up to $I_s/I_{sat} = 0.17(5)$ though the conductance value decreases to $G = 0.55(2)\,1/h$. The reason for the decrease of G in the plateau will be explained in Sec. 8.5.

We can extract the effective Zeeman shift V_s responsible for the shift of the conductance curves via a fit of the conductances (solid lines in Fig. 8.4(a)-(c)) using a numerical solution for the transmission and the Landauer model. The potential landscapes displayed in Fig. 8.4(d)-(f) are used in the simulation in addition to an imaginary potential $i\hbar\Gamma(y)/2$ modeling the photon scattering to calculate $\mathcal{T}(E)$, $\mathcal{R}(E)$ and $\mathcal{L}(E)$. The fit as a function of the peak intensity I_s gives a potential strength of $V_s/I_s = 103(17)\,k_B nK/(W/m^2)$ consistent with the theoretical expectation of $V_s/I_s = 98(3)\,k_B nK/(W/m^2)$. The maximally attainable shift we find is $V_s = k_B \cdot 0.44(2)\,\mu K$ which is around two times larger than the Fermi energy $E_F = h\nu_z/2 = k_B \cdot 0.22\,\mu K$.

8.4.1 *Weak Interactions*

Here we explore an interesting aspect of the spin-filter, namely how the interactions between spins compete with the potential V_s. For this purpose the broad Feshbach resonance of ^{6}Li is used which allows exploring the weakly attractive interactions $a = -800.0(7)\,a_0$ as well as weakly repulsive interactions $a = 800(16)\,a_0$. These interactions will renormalize the potential felt by the spins, thereby changing the shift of the conductance plateaus. In the interaction regime explored here a mean-field theory can be used to model the interaction effects. The quantized conductance curves measured at $\pm 800\,a_0$ and $I_s/I_{sat} = 0.13(4)$ are displayed in Fig. 8.5(a). The difference in effective potential shift $V_{s,\mathrm{eff}}$ is clearly visible and amounts to $k_B \cdot 0.1\,\mu K$. In addition, the height of the conductance plateau is further reduced due to additional losses in the interacting regime. The visible shift of conductance plateau separation is smaller in the attractive limit and larger in the repulsive regime which is confirmed by a fit with a step-function (logistic function) modeling the Landauer theory expectation. Figure 8.5(b) display the obtained effective separations $V_{s,\mathrm{eff}}$ as a function of intensity which confirms the effects of interactions.

The measurements are repeated for different intermediate interaction strength at fixed intensity, see Fig. 8.5(c). The effective separation is extracted for each interaction strength, displayed in Fig. 8.5(d). The dashed line in Fig. 8.5(d) is a theory curve calculated from a self-consistent Hartree mean-field theory. The mean-field model includes a new potential parameter $U = 2h\sqrt{\nu_x \nu_z}\,a$ which describes the extra potential that $|\downarrow\rangle$ adds to the potential felt by $|\uparrow\rangle$ when passing through the junction. The model describes the behavior of our system well, even though the effects of dissipation and density fluctuations have been neglected. This observation further supports the previously argued neglect of the fluctuation term in the Lindblad master equation. Here, similarly the density fluctuations are large but fast in the 1D QPC and the QPC is not in thermodynamic equilibrium. Nevertheless, the long measuring times provide an averaging mechanism which effectively averages out short-time fluctuations. The role of dissipation is likely more subtle since

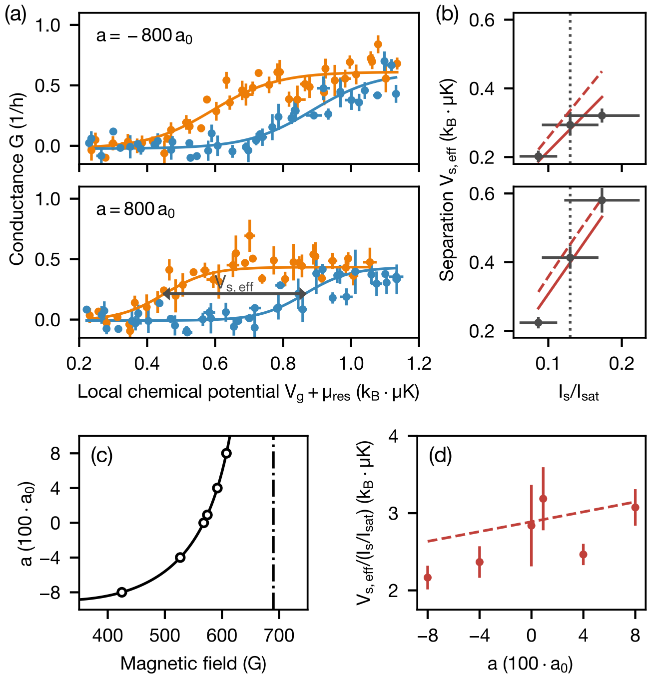

Figure 8.5: Mean-field interaction effects on the spin-dependent conductance shift. The conductance curves (a) are taken at $a = -800.0(7)\,a_0$ and $a = 800(16)\,a_0$, the maximal attainable weak interactions. The beam intensity is fixed at $I_s/I_{sat} = 0.13(4)$ and the detunings are equal for both spin-states. Fits with a logistic function (solid lines) determine the separation $V_{s,eff}$ in the interacting regime. The fitted separation (b), shown as a function of the saturation intensity factor, indicates the larger (smaller) shift for repulsive (attractive) interactions. (c) Values of the scattering length used for the measurements. (d) Ratio $V_{s,eff}/(I_s/I_{sat})$ displayed as a function of the scattering lengths explored here. The solid line is a Hartree mean-field theory prediction reproducing our observations.

they are supposed to play a substantial role in the interacting regime [57] since fluctuations and coherence are expected to be stronger in the 1D region [222].

8.5 DISSIPATION EFFECTS IN THE NON-INTERACTING QPC

In this section the effect of dissipation on the transport is quantified and used to benchmark the previously introduced model. In addition, a simple application of dissipation as a density dependent scanning microscope is introduced.

Loss Mechanisms

The previously introduced model, see Sec. 8.3, assumes a loss mechanism in terms of an imaginary potential which removes atoms from the channel without secondary effects, i.e. the atoms leave the trap immediately and forever. In reality the photon imparts a large kinetic energy on the atoms inside the channel. Since the channel is strongly confined which requires high optical potentials this imparted energy is not always enough to surpass the potential barriers and leave the trap. The highly energetic atoms thus can travel through the cloud and interact with them, depending on the interaction strength.

The movement of the atom between absorption and re-emission $\Gamma = 36.9\,\mu s^{-1}$ is small $< 1\,\text{nm}$. The potential barriers making up the QPC provide a peak potential barrier of $V_x = k_B \cdot 7\,\mu K$ and $V_z = k_B \cdot 48\,\mu K$ which is larger than the photon recoil $E_R = k_B \cdot 3.54\,\mu K$. The movement of the atom after the recoil can be modeled by the Lamb-Dicke parameter $\eta_z = \sqrt{E_R/h\nu_z} = 2.86(1)$, $\eta_x = \sqrt{E_R/h\nu_x} = 2.29(1)$ which describes the projection of the transverse momentum into a superposition of transverse QPC modes. The excited transverse mode the atoms get projected into on average is given by $n_{x,z} \simeq \eta^2_{x,z}$. Scattering probabilities between the atoms in the higher modes and atoms in the lower modes can be computed using Ref. [223]. We find that the probability of a collision happening between the atoms in different states is less than $0.4\,\%$ and can thus be neglected.

In the 3D reservoirs it is useful to consider the mean free path $\ell = 1/\bar{n}\sigma$, where σ is the scattering cross-section and $\bar{n}$ is the peak density, to estimate the secondary interactions of the highly energetic atoms. For an interaction strength of $a = 91\,a_0$ the mean free path is $\ell = 3.26(5)\,\text{mm}$ which is much larger than the reservoir size $0.25\,\text{mm}$. Furthermore, the potential depth in the reservoirs is $V_d = k_B \cdot 0.55\,\mu K$ which is smaller than the recoil energy meaning that the atoms will leave the reservoirs.

8.5.1 Transport with Losses

Figure 8.6 shows the atom-number imbalance $\Delta N/N$ and the total atom number N as a function of time, recorded for the conditions in Fig. 8.1(c). The numerical simulations shown in Fig. 8.6(c)-(d) reproduce the observation only using experimental parameters like initial atom-number, imbalance and temperature as well as the near-resonant beams intensity. This result shows that for weak intensities our approximations regarding the fluctuations in the Lindblad master equation are sound and on the long time-scales we can predict our experimental observations. Though we find theoretically that the reduction of transport for the blocked spin-state $|\uparrow\rangle$

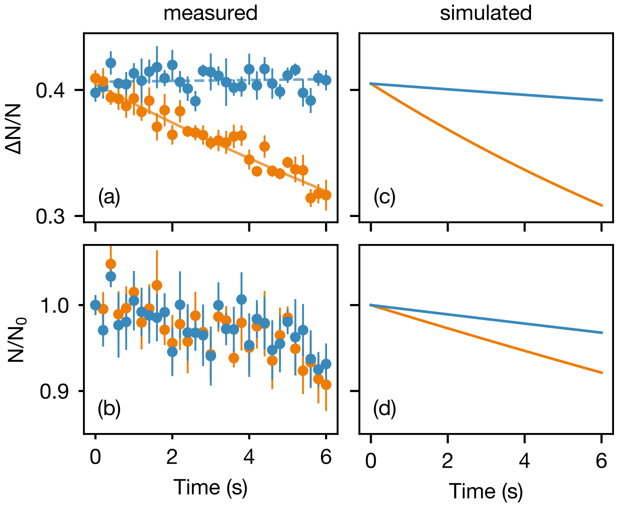

Figure 8.6: Measured and simulated particle and particle-imbalance evolution. The measured atom-number imbalance (a) and total atom-number (b) indicate the spin polarization of the current and the concurrent losses. The measurement were obtained for $V_g + \mu_{res} = k_B \cdot 0.61(2)\,\mu K$ and a near-resonant beam intensity of $I_s/I_{sat} = 0.13(4)$. The simulation results (c) calculated via the Euler integration previously introduced reproduce the transported atom-number and the atom-loss. The spin-dependence of the atom-loss observed in the theory is not found in the experiment due to the overall atom-number instability.

concurrently reduces its losses, we cannot observe this effect in the experiment.

We have previously seen that the particles which are effectively not transported, i.e. the "non-contributing" fraction, are affected by dissipation in the same way the particle current is. The majority amount of losses is thus from atoms not in the transport window, as can be seen in Fig. 8.1(b). This expectation is verified here by integrating the losses observed in the measurement in Fig. 8.4(b). The number of atoms contributing and not-contributing as well as transmitted and lost is given by

$$N_{c/nc}^{trans/lost} = \int_0^t \dot{N}_{c/nc}^{trans/lost} dt'' \tag{8.19}$$

The total atom number contributing to transport is then given by $N_c = N_c^{lost} + N_c^{trans}$ while the non-contributing atom number is $N_{nc} = N_{nc}^{lost} + N_{nc}^{trans}$. Figure 8.7(a) shows their value and their sum for $|\downarrow\rangle$. We find that 33 % of atoms present in the QPC region are lost, while only 21 % of atoms in the transport window are lost due to their higher momentum.

The conductance plateau in Fig. 8.7(c) shows that the lossy QPC still preserves the conductance plateau which can be fitted with our model given by

$$G_\sigma(x) = A G_\sigma^{th}(x - \mu_0, T, \bar{\delta}, V_s)\,, \tag{8.20}$$

where G_σ^{th} is the theoretically obtained conductance value via the Landauer-Büttiker formula. Temperature T and detuning $\bar{\delta}$ from the mean resonance frequency are fixed to the measured values. The chemical potential offset μ_0 and the scaling factor A accounting for the decrease of conductance below $1/h$ are fitted. The chemical potential offset is found to be $k_B \cdot 0.06(2)\,\mu K$ while the scaling parameter is $A = 0.78(3)$. The resulting spin-dependent

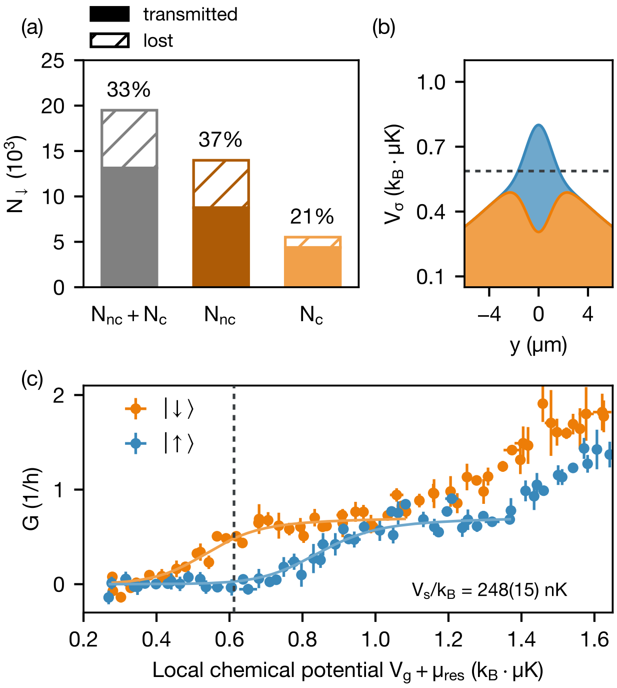

Figure 8.7: Conductance through a lossy QPC. The total atom-number contributions to transport and loss (a) indicate that more atoms are lost from below the transport window, i.e. N_{nc}, compared to the loss from the particle current N_c, due to the higher velocity of the latter. This explains the robustness of the conductance plateau to the losses. (b) The quasi-1D potential in transport direction indicate the spin-dependent shift of the onset of conductance due to the repulsive peak. The conductance curve (c) is fitted (solid lines) with the Landauer model $V_s = k_B \cdot 0.25(2)\,\mu K$ which agrees well with the *ab initio* calculated potential $k_B \cdot 0.29(11)\,\mu K$.

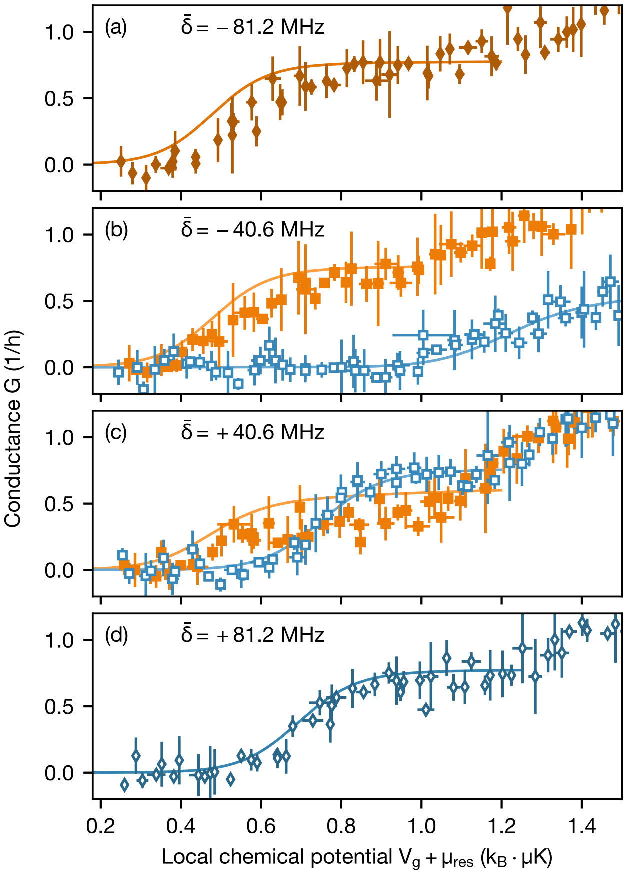

Figure 8.8: Landauer model validity for different dissipation strengths. The conductance G is measured at $a = 91(7)\,a_0$ for both spins $|\uparrow\rangle$ (blue, open symbols) and $|\downarrow\rangle$ (orange, closed symbols) as a function of local chemical potential for different detunings $\bar{\delta}$. The solid line shows a Landauer model prediction calculated solely using fit parameters from Fig. 8.7 and the varying detuning. We find that the model describes the data throughout the explored parameter regime.

potential value is $V_s = k_B \cdot 0.25(2)\,\mu K$ which is consistent with the theoretical value of $k_B \cdot 0.29(11)\,\mu K$. The loss probability calculated from the Landauer model is 21 % for the loss rate $\Gamma = 3\,kHz$ present here. This value is consistent with the plateau reduction from $G_0 = 0.84(1)\,1/h$ to $0.72(3)\,1/h$.

The loss rate is varied to determine the validity of our Landauer model for different dissipation strengths. For this purpose the detuning $\bar{\delta}$ is varied while the intensity of the near-resonant beam is kept fixed at $I_s/I_{sat} = 0.13(4)$. Figure 8.7 displays the resulting conductance curves when varying the detuning from $\bar{\delta} = -81.2\,MHz$, i.e. the resonance of state $|\uparrow\rangle$, to $\bar{\delta} = 81.2\,MHz$, i.e. the resonance of state $|\downarrow\rangle$. In the resonance condition of either state (see Fig. 8.8(a) and (d)) the atoms in that spin-state are completely lost within the transport time of 4 s. The remaining spin-state on the other hand still shows a plateau of quantized conductance. Shifting the detuning asymmetrically towards one of the spin-states (see Fig. 8.8(b)-(c)) leads not only to an increase of losses but also increases the optical potential which is particularly clear in the case of an additional repulsive shift in Fig. 8.8(b). Moving the frequency closer to the attracted state $|\downarrow\rangle$ as in Fig. 8.8(c) leads to both spins having a nearer onset of conductance, since the attractive shift is compensated by the QPC. Conversely, the conductance is clearly different in this limit due to the increased losses in the state closer in detuning. We find that our theory (solid lines in Fig. 8.8(a)-(d)) describes the conductance curves well, independent of the detuning. Notably, there are no additional fit parameters for the theory curves, only the detuning $\bar{\delta}$ is varied underscoring the validity of this model in a broad range of dissipation strengths.

8.5.2 Dissipative Scanning Microscope

Here, we use the dissipative beam as a density sensitive probe. The aberration correction provided by the DMD creating the beam also allows using aberrations, such as a tilt aberration, to move the beam in the atomic plane. This movement can be very small and thus allows resolutions on the submicron level [63].

The density is assumed to be two-dimensional and time independent which holds as long as density variations are small compared to the longitudinal extent of the beam, i.e. the Rayleigh range $z_R = 4.9(3)\,\mu\text{m}$ and the total loss is small. The integrated atom loss is then given by

$$N(0) - N(t) = \Delta t \int dx dy \Gamma(x,y) n_{2D}(x,y) dx dy \tag{8.21}$$

$$\text{with } \Gamma(x,y) = \Gamma_s e^{-2[(x-x_s)^2+(y-y_s)^2]/w_s^2}, \tag{8.22}$$

where Δt is the time over which the loss takes place. We find that the losses are given by a convolution of the intensity profile with the atomic density. Thus keeping the Gaussian waist w_s of the lossy beam small it is approximated by a delta function such that

$$n_{2D}(x_s, y_s) = \frac{2}{\pi w_s^2} \frac{N(0) - N(t)}{\Gamma_s \Delta t}. \tag{8.23}$$

The slight attractive shift from the near-resonant beam on the off-resonant spin state will decrease the local chemical potential.

Since this shift and the Gaussian waist is small we can repeatedly measure the density for different positions of the near-resonant beam to obtain a 2D map of the atomic density. Figure 8.8 shows such a map taken around the QPC, indicating the high density regions close to the channel and the reduced density inside the QPC. This technique is analogous to a scanning probe microscopy in condensed matter systems and provides an alternative to absorption imaging normally used in cold atom systems. Comparable techniques use a conservative potential [63] or an electron beam [213] to probe the local properties of a quantum gas. In comparison to absorption imaging the dissipative scanning gate technique has a higher resolution 0.3 µm which is only limited by the minimal displacement allowed by the DMD.

8.6 CONCLUSION AND OUTLOOK

Here we have shown how transport through a QPC can be engineered via near-resonant light to generate spin-polarized currents, demonstrating that the system is robust to single particle losses. The spin-filtering effects can be used to manipulate the spin conductance and to study interaction effects. We find that our transport measurements are sensitive to weak interaction effects occurring on the scale of the Fermi wavelength. The near-resonant

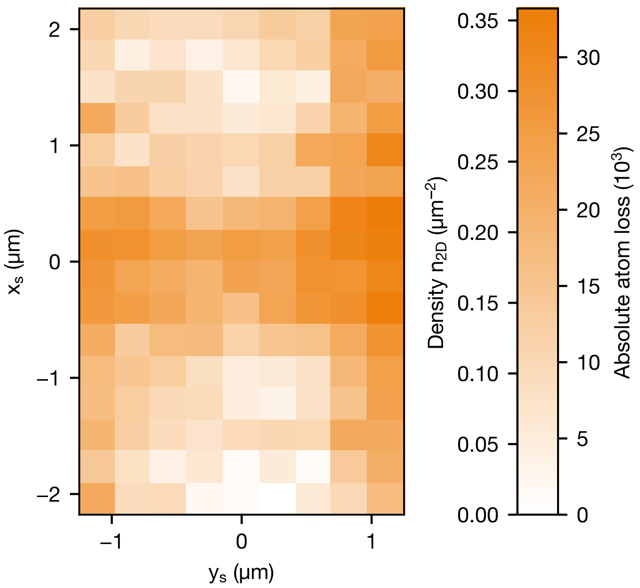

Figure 8.9: Dissipative scanning gate microscopy. The 2D map shows the total atom loss in state $|\downarrow\rangle$ after 4 s of integration time. The position is given by the position of the beam in the atom plane. The two-dimensional density n_{2D} can be obtained from this picture by deconvolving the Gaussian shape of the near-resonant beam with the measured density distribution. For this measurement a detuning of $\bar{\delta} = 40\,\text{MHz}$ and a beam waist of $w_s = 1.02(5)\,\mu\text{m}$. The beam intensity was $I_s = 24(8)\,\text{W/m}^2$ which produces a large photon scattering rate of $\Gamma_\downarrow = 90(30)\,\text{kHz}$.

beam implies a spin-dependent optical potential and scattering rate which both can be calculated from the atomic polarizability. We are able to model the energy dependent transmission and loss with an imaginary potential approach which, in conjunction with the Landauer-Büttiker formalism, reproduces the observed dispersive and dissipative effects on the conductance. In addition, integrating the model enables us to express the time evolution of particle number, particle imbalance and energy in the reservoirs. Finally, the dissipation can be used to locally remove atoms from the system which gives insight into the local density of the transport geometry.

In future experiments this scheme can be extended to more complex [61] spin-dependent structures and opens avenues to study the coupling between spin-, particle- and heat-transport [224], possibly in interacting systems. The increased understanding of the atom-light interactions at high magnetic laid the groundwork for studies of dissipation with strong interactions [101].

9

TOWARDS COHERENT MANIPULATION OF TRANSPORT WITH LIGHT

CHAPTER CONTENTS

Parts of the contents of this chapter are currently being prepared for publication.

9.1 MOTIVATION

The previously used spin-manipulation and dissipation scheme is particular interesting when the involved spins are strongly interacting. In the superfluid phase the effective Zeeman shift would compete with the gap which could lead to pair breaking effects in the channel. The role of coherence in the non-linear transport characteristics and its interplay with dissipation of the superfluid QPC is of equal interest and has been explored in our system [101]. Here, we would like to give an overview over the limitations that hindered the implementation of some schemes proposed in Ref. [147] and our new ideas using three-level atom-light interactions, where we already found that the electromagnetically induced transparency (EIT) can be used to mitigate dissipation. The three-level atom light interaction is the cornerstone of a plethora of possible directions of exploration such as narrow Raman spectroscopy to determine the local superfluid gap [111, 225], Raman coupling to induce spin-orbit coupling [54, 205] and subwavelength potentials [102, 226].

9.2 THE THINGS THAT DIDN'T WORK IN THE STRONGLY INTERACTING REGIME

Figure 9.1 shows the dipole potential and the photon scattering rate of the lowest and third-lowest hyperfine state, here called $|\downarrow\rangle$ and $|\uparrow\rangle$, respectively. The magnetic field is $B = 568\,\mathrm{G}$ and the intensity is chosen to be low with respect to the saturation intensity. We can identify three different ways of imposing a spin-dependent potential on the atoms.

The first shown in Fig. 9.1(a)-(b) is the one used in Ref. [146]. Here the differential Stark shift between the closed D2 transition at high magnetic fields is used to obtain a spin-dependent potential. The downside of this scheme is that the atoms will naturally decay back to their original state, but at a much higher kinetic energy $\sim E_R$. In the strongly interacting regime the mean free path in the reservoirs is no longer larger than the system size and thus this energy will be deposited via atom-atom interactions. We

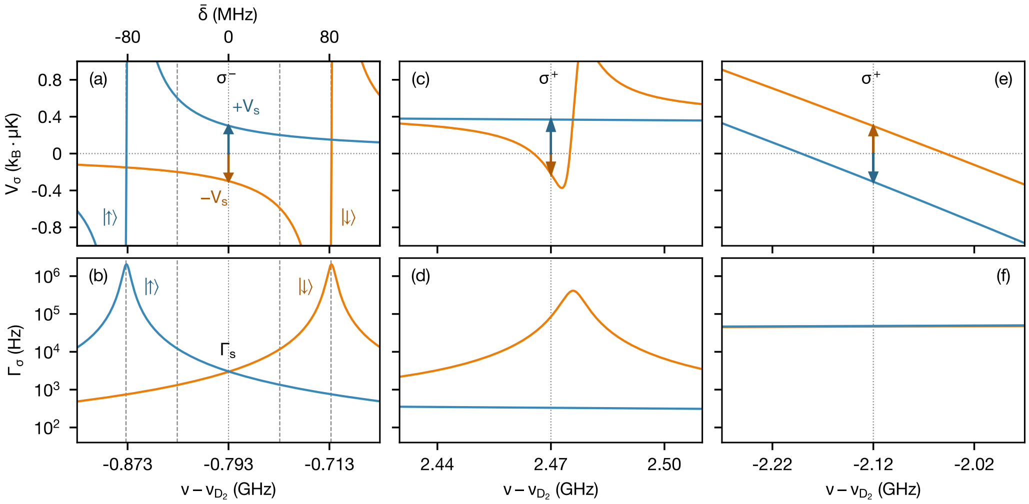

Figure 9.1: Scattering rates and dipole potentials creating spin-dependent potentials. The scattering rates and potentials are calculated using the formulas introduced in Ch. 3. The magnetic field is chosen to be $B = 568\,\mathrm{G}$ and the frequency is provided in terms of a detuning from the D2 line at zero magnetic field. The intensities are chosen such that the differential light shift is equivalent in the three panels $V_s = k_B \cdot 0.6\,\mu\mathrm{K}$. (a)-(b) Using σ_- polarized light and an intensity of $I = 3\,\mathrm{W/m^2}$ produces the spin-filter used in Ref. [146]. (c)-(d) With σ_+ light a spin-dependent potential can be obtained for a spin-dependent transition away from the D2 line, with $I = 136\,\mathrm{W/m^2}$. (e)-(f) At the zero-crossing between the D1 and D2 manifold σ_+ polarized light with $I = 1.2 \times 10^4\,\mathrm{W/m^2}$ can be used to create a spin-filter. Adapted from Ref. [147].

found that implementing a spin-filter with this scheme leads to a quick loss of all atoms in the system.

The second possible scheme is displayed in Fig. 9.1(c)-(d). The original misconception was that this transition $|1\rangle - |e17\rangle$ is "narrow" due to the small dipole-matrix element $d_{1,e17}$. The reality is that the excited state has a short lifetime $\tau = \Gamma^{-1} = 31.7\,\mu\mathrm{s}^{-1}$ which implies a broad transition, though the spontaneous scattering leads to optical pumping into a different groundstate $|5\rangle$. This optical pumping scheme is used in Ref. [101] to dissipate atoms. Figure 9.1(c)-(d) shows that the ratio of spin-dependent potential V_s to dissipation strength Γ_s is worse for this scheme compared to the previous which also makes this scheme not usable.

The final scheme relies on the zero-crossing of the dipole potentials of the hyperfine states between the D2 and D1 manifold, presented in Fig. 9.1(e)-(f). The zero-crossing will lead to a differential light-shift, though it requires much higher intensities due to the detuning from the resonances. We found that in the interacting regime this scheme is not usable due to a plethora of molecular transitions which lead to losses. Figure 9.2 shows a spectrum taken starting from the zero-crossing up to the beginning of the D1 manifold. It is possible to identify several molecular transitions, where the losses are in pairs of spins. Importantly, we find that increasing the power at the zero-crossing does not lead to the wanted spin-polarization but to losses which prevent us from using this scheme as well.

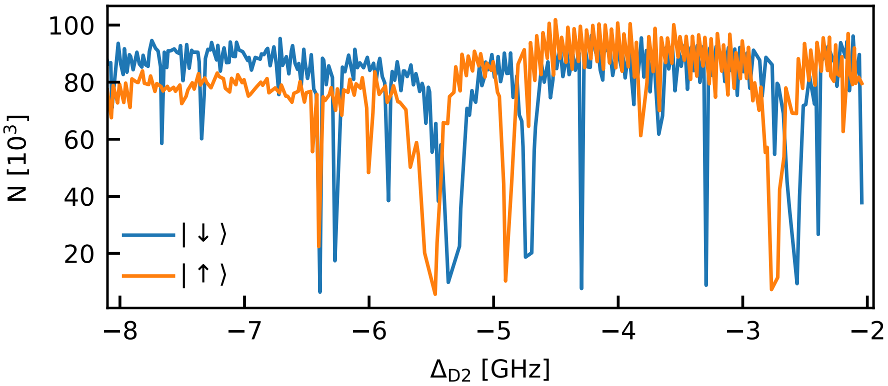

Figure 9.2: Spectrum between D1 and D2 manifold. The atom-number is shown as a function of the detuning from the D2 line at zero magnetic field for the spin states $|{\downarrow}\rangle$ (blue) and $|{\uparrow}\rangle$ (orange). The spectrum was taken for a unitary Fermi gas with a σ_+ polarized, highly-focused beam. The first line of the D1 manifold is located at about $\Delta_{D2} \approx -8.9\,\text{GHz}$ while the first line of the D2 manifold is at $\Delta_{D2} \approx -0.9\,\text{GHz}$.

9.3 RESTORING FAST TRANSPORT WITH ELECTROMAGNETICALLY INDUCED TRANSPARENCY

The previous section illustrated how difficult the use of near-resonant light in the strongly interacting Fermi gas is. Here we want to demonstrate that it is possible to create and harness three-level atom light interactions in this regime. To this end we employ the lambda-system $|1\rangle - |e17\rangle - |5\rangle$ introduced in Ch. 3 and displayed in Fig. 9.3(b). The lambda system is formed by two laser-beams driving the weak $|1\rangle - |e17\rangle$ and strong $|5\rangle - |e17\rangle$-transition called probe and control beam, respectively. Figure 9.3(a) shows a schematic of the optical setup, the probe and control beam are σ_+ polarized and co-propagating, intersecting the quantum point contact (QPC) at its center. The intensity of the beams can be controlled via their power and their waist $w_0 = 1.9\,\mu\text{m}$ is chosen to be smaller than the length of the QPC $6.8\,\mu\text{m}$. We use a digital micro-mirror device to correct the aberrations of the optical projection system such that there is no stray light in the reservoirs. The optical setup used to control the power and create the frequency offset between the beams is described in Sec. 6.4.

The ultracold gas of ^{6}Li atoms is prepared in a balanced mixture of the lowest and third-lowest hyperfine state, here called $|{\downarrow}\rangle$ and $|{\uparrow}\rangle$. The magnetic field is $B = 689.7\,\text{G}$ which corresponds to the Feshbach resonance of the spin mixture. After evaporation the total atom-number in the reservoirs is $N = 138(13) \times 10^3$ at a temperature of $T = 94(2)\,\text{nK}$ which corresponds to a degeneracy of $T/T_F = 0.29(1)$ which is above the superfluid transition. The transport geometry is imposed by intersecting two repulsive TEM_{01} like beams at the center of the cloud which confines the system in x and z direction. The confinement in x direction is provided by the wire beam with $\nu_x = 12.4(2)\,\text{kHz}$ and a Gaussian waist in transport direction of $w_{y,W} = 6.8\,\mu\text{m}$. In z direction the confinement is $\nu_z = 9.42(6)\,\text{kHz}$ with a waist of $w_{y,LS} = 30.2\,\mu\text{m}$ given by the lightsheet beam. The gate potential V_g is created by an attractive Gaussian beam with a waist of $w_g = 30\,\mu\text{m}$ shifting the zero-point energy of the QPC by $V_g = 2.2\,\mu\text{K}$. In order to observe transport a chemical potential bias is imposed via an atom-number imbalance which is recorded relaxing as a function of time. The atom-number and temperature of the clouds is measured via a spin-resolved absorption

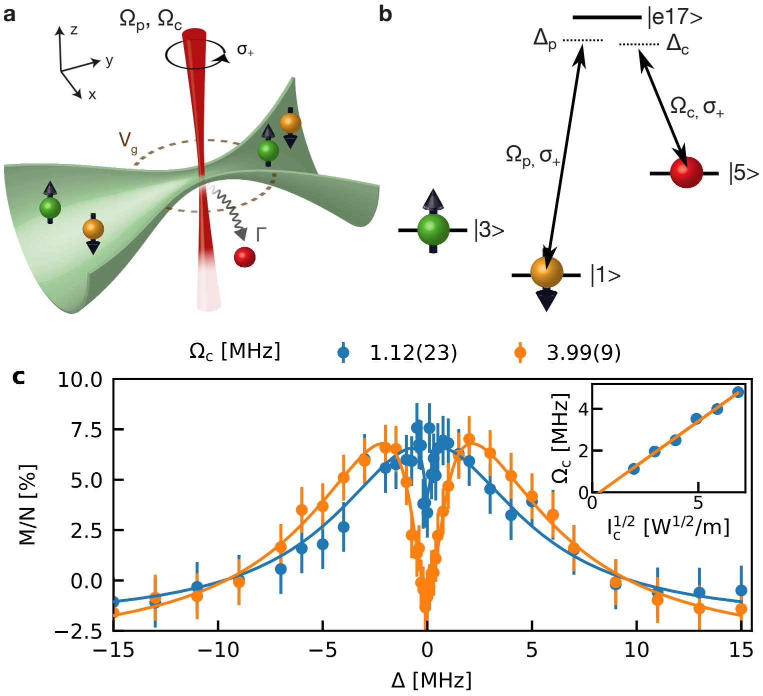

Figure 9.3: Electromagnetically induced transparency in a strongly interacting QPC. The co-propagating probe and control beam (a) are projected in the center of the quantum point contact (QPC). The legs of the lambda scheme (b) are formed by σ_+ polarized light where the two-photon resonance frequency is given by $\nu_{15} = 2014\,\text{MHz}$. The lambda scheme is made up by the three states $|1\rangle$, $|e17\rangle$ and $|5\rangle$. We find the EIT spectrum (c) by scanning the probe beam frequency and recording the relative magnetization M/N. At the EIT resonance $\delta = \Delta = 0$ the spin-dependent dissipation is suppressed which makes the magnetization a sensitive measure. The Rabi frequency of the control beam is calibrated by varying the control beam intensity and fitting the EIT spectrum to extract Ω_c. We find a linear relation between the Rabi frequency and the square-root of the intensity (inset of (c)) with a slope of $\Omega_c/\sqrt{I_c} = 0.80(7)\,\text{MHz}/\sqrt{\text{W/m}^2}$ which is consistent with the theoretical value $\Omega_c/\sqrt{I_c} = 0.82\,\text{MHz}/\sqrt{\text{W/m}^2}$ which assumes a uniform peak intensity.

image and our standard thermometry technique employing the second moment of the density distribution, see Ch. 2.

The control and probe beam stem from the same laser, thereby suppressing any frequency fluctuations which become common-mode. The light is frequency split using two acousto-optic modulators (AOMs) in double pass configuration to reach the necessary energy splitting between the two ground-states $\nu_1 - \nu_5 = 2014\,\mathrm{MHz}$. The detunings of the individual transitions are defined as $\Delta_1 = \nu_1 - \nu_p$ and $\Delta_5 = \nu_5 - \nu_c$, while the single photon detuning is given by $\Delta = \Delta_1$ and the two-photon detuning is $\delta = \Delta_1 - \Delta_5$. In a first experiment both beams are illuminating the channel for $2\,\mathrm{s}$ after which the atom-number in each spin-state is measured. This measurement is repeated for varying single photon detunings Δ and control Rabi frequencies Ω_c. Figure 9.3(c) shows the recorded spectrum which displays a dip in the resonance peak typical for EIT. The spectrum is measured via the relative magnetization $M/N = (N_\uparrow - N_\downarrow)/(N_\uparrow + N_\downarrow)$ since the probe laser is resonant with the $|\downarrow\rangle - |e17\rangle$ transition such that atom losses will occur spin-dependently. In addition, we find that molecular losses induced by the control beam are less pronounced by measuring the relative magnetization.

The theoretical model used underlying the absorption spectrum is obtained in a weak probe approximation $\Omega_p \ll \Omega_c$ of the three-level system, where the absorption is the imaginary part of the susceptibility $\chi^{(1)}$ given by [53]

$$\chi^{(1)} \sim \frac{4\delta\left(\Omega_c^2 - 4\delta\Delta\right) - 4\Gamma_{15}^2\Delta}{\left|\Omega_c^2 + (\Gamma_{15} + 2i\delta)(\Gamma_e + 2i\Delta)\right|^2} + \frac{i\left(2\Gamma_{15}\left(\Gamma_{15}\Gamma_e + \Omega_c^2\right) + 8\Gamma_e\delta^2\right)}{\left|\Omega_c^2 + (\Gamma_{15} + 2i\delta)(\Gamma_e + 2i\Delta)\right|^2}, \quad (9.1)$$

where Γ_e is the inverse lifetime of the excited state and Γ_{15} is the decoherence rate between the two ground-states, e.g. due to magnetic field noise. The splitting of the peaks in the EIT spectra is given by Ω and in the limit $\Omega_c > \Gamma_e$ [53] the spectrum becomes the Autler-Townes doublet [227]. We fit the spectra shown in Fig. 9.3(c) with the absorption function given by $\mathrm{Im}[\chi^{(1)}](\Delta)$ for varying control Rabi frequency in order to obtain a calibration of the Rabi frequencies on the atoms. We find that the calibrated control Rabi frequency follows the expected linear behavior as a function of the square-root of the intensity, see inset of Fig. 9.3(c). The calibration gives a Rabi frequency of $\Omega_c/\sqrt{I_c} = 0.80(7)\,\mathrm{MHz}/\sqrt{\mathrm{W/m^2}}$ is consistent with the theoretically expected value $\tilde{\Omega}_c = 0.82\,\mathrm{MHz}/\sqrt{\mathrm{W/m^2}}$. The probe Rabi frequency is related to the control Rabi frequency via their dipole-matrix elements $\Omega_p/\Omega_c = d_p/d_c\sqrt{I_p/I_c}$. In our system the intensities of control and probe field are equivalent such that the calibration of the control field is just multiplied by the factor $d_p/d_c \approx 0.054$ to obtain the probe Rabi frequency calibration $\Omega_p/\sqrt{I_p} = 43.2(4)\,\mathrm{kHz}/\sqrt{\mathrm{W/m^2}}$. This validates the weak probe approximation since $\Omega_p \ll \Omega_c$ and $\Omega_p \ll \Gamma_e$. We note that the height and perceived width of the EIT dip depends on the control Rabi frequency which stems from the dephasing Γ_{15} reducing the transparency [53], while the transparency is unchanged for $\Omega_c^2 \gg \Gamma_e\Gamma_{15}$. From the fit we find $\Gamma_e\Gamma_{15} = (2\pi)^2 4.6(5)\,\mathrm{MHz}$.

In a second experiment we apply EIT, i.e. $\delta = \Delta = 0$, during a transport experiment. The system is prepared with a chemical potential imbalance which is relaxed over $2\,\mathrm{s}$ as can be seen in Fig. 9.4(a). Without any near-resonant light present in the QPC (blue circles in Fig. 9.4(a)) the particle transport exhibits a non-linear current bias characteristic [38, 101]. The extracted particle current $I_N = -0.5\,\mathrm{d}\Delta N/\mathrm{d}t$ is displayed in Fig. 9.4(b) as a function of the chemical potential difference. We explore three different

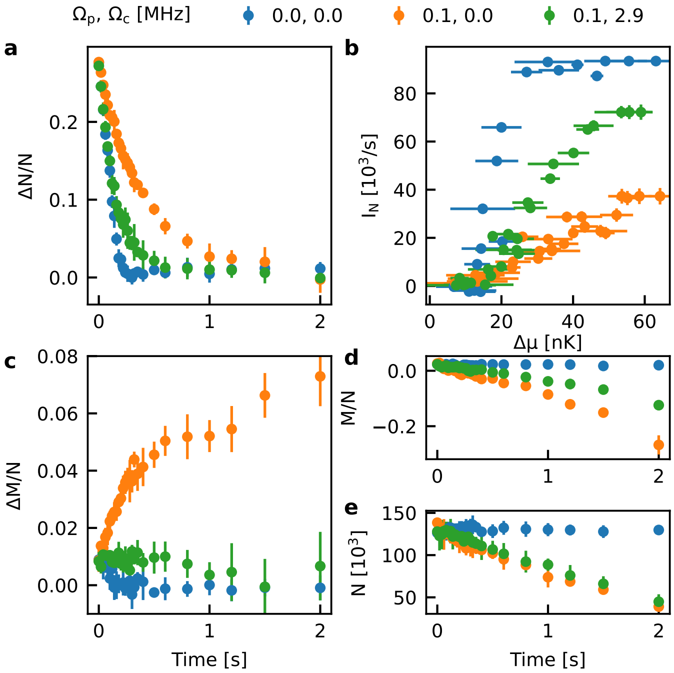

Figure 9.4: Restoring fast, non-linear current via EIT. The particle number imbalance is shown as a function of transport time for different configurations of the probe and control beam. Undisturbed (blue circles) particle-current $I_N = -0.5\, dN/dt$ (b) displays a non-linear current-bias characteristic. With only the probe beam present (orange circles) dissipation suppresses the non-linearity and the overall current. With both beams present (green circles) the initial current approaches its original value and displays a non-linear shoulder. The relative magnetization (c) indicates the same trend, where EIT leads to a suppression of dissipation and the evolution of the coupled system (green circles) approaches the non-coupled (blue circles). Atom number (e) and total magnetization (d) show that though many atoms are lost even in the EIT condition the current seems to be robust to those losses.

cases of either control or probe beam being on as well as both being present in the channel. The spin-dependent dissipation limit is reached when only the probe beam is present, leading to photon scattering of state $|\downarrow\rangle$ [101]. This dissipation reduces the particle current and makes the current-bias characteristic linear (green circles in Fig. 9.4(a)-(b)). In the case where only the control beam is on, no dissipation is observed since this beam is far detuned $\Delta_{1c} = 2014\,\mathrm{MHz}$ from the optical transitions of the transported spin-states. In the EIT condition, i.e. both probe beam and control beam are recovering the particle current almost back to its original value at large chemical potential imbalances. Around the "kink" in the nonlinear response the current becomes more linear but still shows a nonlinear shoulder in Fig. 9.4(b), implying that the sharp change of the current at low biases is more sensitive to the remaining dissipation.

In the same experiment we can extract the relative magnetization imbalance $\Delta M/N$, see Fig. 9.4(c) and the relative magnetization M/N Fig. 9.4(d) which provide insight into the spin-dependence of our scheme. We find that the spin-dependent dissipation provided by only having the probe beam present has the largest effect on the magnetization. In the EIT condition the magnetization-imbalance and total magnetization (Fig. 9.4(c)-(d)) both evolve differently than without dissipation confirming that the EIT does not fully suppress dissipative loss from the probe beam. The control beam seems to have no effect on the magnetization, likely due to its large detuning, but still creates an overall atom loss, see Fig. 9.4(e), which seems to have little effect on the particle current.

We further explore the effects of the three level system by varying the intensity of the probe and control laser. Figures 9.5(a)-(b) show the initial particle current and the change of magnetization $\dot{M}$ as a function of both intensities. We find that the contours in Figure 9.5(a) lie on a diagonal, indicating that for a given ratio of the two Rabi frequencies the particle current stays constant. In the limit of $\Omega_p \gg \Omega_c$ we find that the previously observed losses suppress the current, while in the other limit where $\Omega_p \ll \Omega_c$ the EIT condition is better fulfilled and the current survives. From the slope of the magnetization change shown in Figures 9.5(b) we find that the magnetization depends on the precise ratio between the Rabi frequencies, indicating again EIT. Without we would expect the spin-loss to purely depend on Ω_p and not on the ratio between the Rabi frequencies.

Another interesting feature we can extract from the data are the magnetization and particle-imbalance during a transport experiment as a function of the single photon detuning Δ. The QPC is illuminated by the probe and control beam with $\Omega_p = 0.12(1)\,\mathrm{kHz}$ and $\Omega_c = 2.9(2)\,\mathrm{MHz}$ and the control frequency ν_c is varied. Figure 9.5(c)-(d) shows the imbalances for different transport times $t = 0.12 \ldots 0.4\,\mathrm{s}$. The average of the spectra is shown in Fig. 9.5(d)-(e). Notably, the magnetization imbalance displays a symmetric spectrum while the particle imbalance has an asymmetric spectrum. We fit the symmetric spectrum with a Lorentzian line profile to determine its width, black line in Fig. 9.5(e). The linewidth is found to be $\Gamma_{\mathrm{fit}} = 2\pi \cdot 0.88(6)\,\mathrm{MHz}$ which is indicative of the response not being a single-photon effect where $\Gamma_e = 2\pi \cdot 5.87\,\mathrm{MHz}$. The asymmetric spectrum of the particle imbalance implies that particle transport is susceptible to off-resonant dispersive effects of the lambda system. The dark-state in which $|\downarrow\rangle$ is transported in the EIT condition is not only immune to photon scattering but also has zero energy, i.e. it does not see an optical potential due to either beam. Here we observe that detuning from the EIT condition will

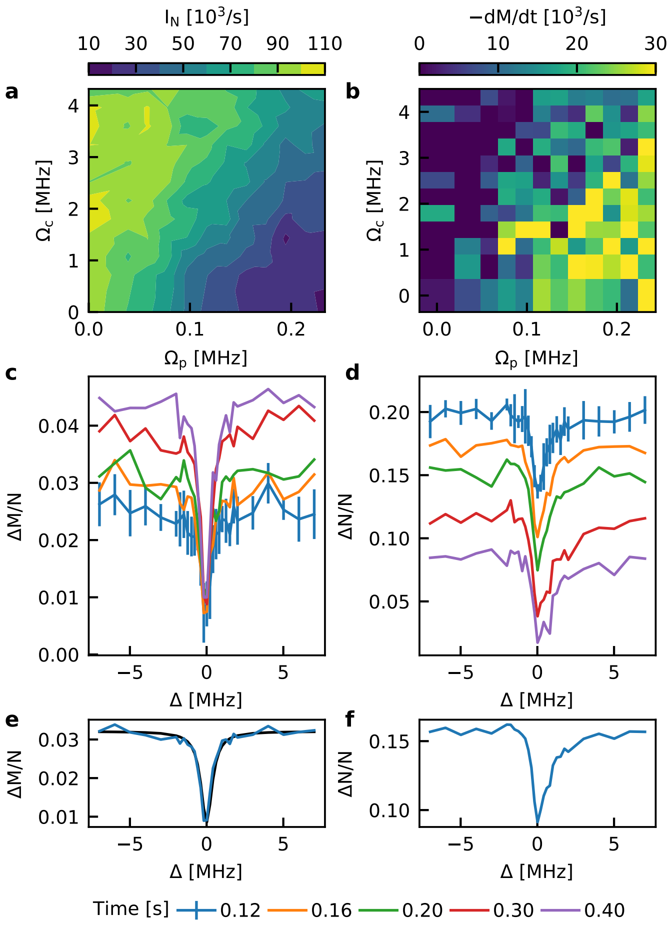

Figure 9.5: Effect of EIT on transport through a strongly interacting QPC. The initial particle current $I_N(0)$, i.e. the excess current I_{exc}, is extracted for varying control and probe Rabi frequencies at the EIT resonance $\delta = \Delta = 0$. The current is strongly suppressed when only a probe beam is present, dissipating state $|\downarrow\rangle$. The state can be rendered transparent when the control Rabi frequency is increased. We observe clear diagonal contour lines indicating the interplay between the probe and control transition. (b) The magnetization rate $\dot{M}$ displays a similar trend where the EIT condition is reached in the upper diagonal of the panel. The EIT spectra is extracted via transport (c)-(d) by recording the frequency dependent particle and magnetization imbalance after different transport times for fixed Rabi frequencies of $\Omega_p = 0.12(1)$ MHz and $\Omega_c = 2.9(2)$ MHz. The average spectra (e)-(f) are clearly different in that the magnetization-imbalance spectrum is symmetric while the particle-imbalance spectrum is asymmetric. We attribute the asymmetry of the transport spectrum to the dispersive effect of the three-level atom-light interaction.

introduce a potential. The transport is hindered for $\Delta < 0$ indicated by a larger particle imbalance, while for $\Delta > 0$ transport is faster. This is consistent with the dispersive response of the lambda-system, i.e. the real part of the susceptibility $\chi^{(1)}$.

In summary, we have shown that it is possible to create a three-level system in strongly interacting ^{6}Li via the combination of a weak and a strong transition. We find that EIT can be observed in this system and can be used to revive transport by suppressing dissipation at the two-photon resonance. Finally, transport is used as a sensitive measurement to observe the dispersive response of the three-level atom-light interaction. These observations are the starting point for future research on three-level atom-light interactions in strongly interacting ^{6}Li gases, some possible schemes will be presented in the following sections.

9.4 TOWARDS A SUBWAVELENGTH QUANTUM DOT

The idea to generate subwavelength potentials via a dark state in a lambda-scheme was proposed theoretically [102] and implemented experimentally [226]. The experimental realization was in the form of an optical lattice and allowed substantial lifetimes compared to the lifetime subject to photon-scattering. In our experiment, a realization of a subwavelength potential would allow a true tunneling barrier inside the QPC which enables the realization of a quantum dot within our transport geometry.

The subwavelength potential relies on non-adiabatic corrections to the dark-state energy in the limit where the population of the dark-state, i.e. the mixing angle α is changing quickly. In our experiment the dark state would be given by

$$|D\rangle = \cos\alpha\,|1\rangle - \sin\alpha\,|5\rangle \ , \tag{9.2}$$

with the mixing angle $\alpha = \arctan(\Omega_p/\Omega_c)$. The subwavelength potential acting on the atom in the dark state is then given by [102]

$$V_{DS}(y) = \frac{\hbar^2}{2m}\left(\frac{\partial\alpha(y)}{\partial y}\right) . \tag{9.3}$$

Technically, this scheme requires a spatially varying mixing angle $\alpha(y)$ which in the current beam configuration – co-propagating beams – is constant. Thus, this scheme would require a technical upgrade to impose the probe and control beam spatially separate on the transport channel. We aim to realize this using a deformable mirror to produce a single well-defined beam while the DMD will be used to spatially shape more complex patterns around this.

Figure 9.6 shows a possible scheme where a subwavelength potential is used to create a quantum-dot for spin $|{\downarrow}\rangle$. Two control beams with a waist of $w_c = 1\,\mu$m displaced by $7\,\mu$m are surrounding a probe beam with the same waist in their center, see Fig. 9.6(a). The atom, initially in state $|{\downarrow}\rangle$, propagating from left- to- right will see a STIRAP-like [228] counterintuitive pulse sequence which leads to a rotation, normally adiabatic [228], of the mixing angle α (blue line in Fig. 9.6(b)). The beams are resonant with the single-photon $\Delta = 0$ and the two-photon detuning $\delta = 0$ and have a peak Rabi frequency of $\Omega_p = 2\pi \cdot 3\,$MHz and $\Omega_c = 2\pi \cdot 6\,$MHz. The mixing angle was calculated via a numerical solution of the atom-light interaction of the lambda-system as a function of space, using *QuTip*. The resulting subwavelength potential V_{DS} is displayed in Fig. 9.6(b). The ultimate limit on the

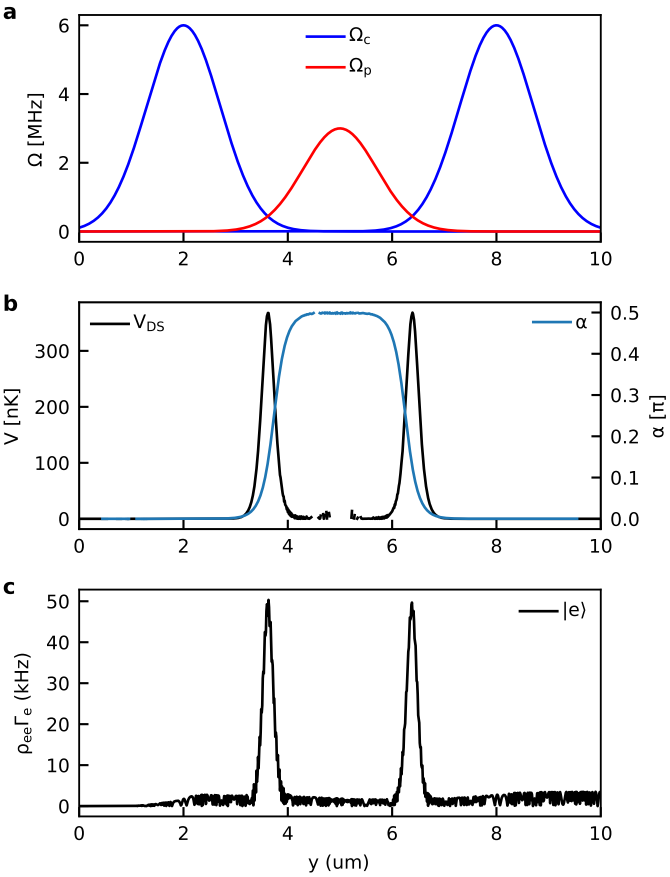

Figure 9.6: Scheme for a quantum dot created by subwavelength potentials. The probe and control beam (a) as a function of space lead to two subsequent STIRAP transitions of $|\downarrow\rangle$ to $|5\rangle$ and back. The fast change of the mixing angle of the dark-state leads to a subwavelength potential [102]. The atom-light interaction for an atom initially in $|\downarrow\rangle$ is simulated numerically as function of space. The detunings are chosen to be resonant in single-photon detuning $\Delta = 0$ and two-photon detuning $\delta = 0$. (b) The mixing angle (blue line) displays the expected behavior of the dark-state. The subwavelength potential is calculated using the formula from Ref. [102]. (c) The photon-scattering rate is estimated from the excited state population ρ_{ee}. The numerical simulation is numerically unstable when higher Rabi frequencies are used which lead to a lower excited state population, i.e. photon scattering rate.

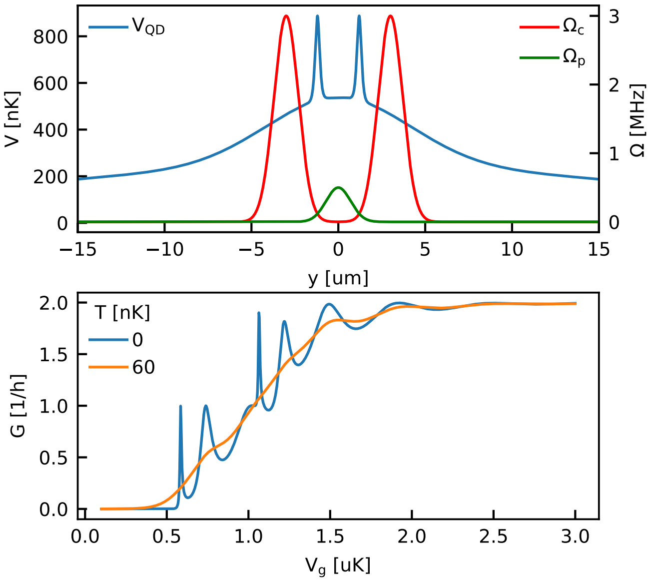

Figure 9.7: Conductance through a subwavelength quantum dot. (a) Transport potential landscape (blue line) for a quantum dot (QD) created by two subwavelength potentials. The control beam (red line) has two peaks around the probe beam (green line) leading to a quick change of the mixing angle α of the dark-state inducing the subwavelength potential [102]. (b) Conductance through the QD calculated from the potential landscape using the Landauer-Büttiker formalism. At zero temperature the resonant tunneling through the QD can be seen, while at finite temperature the signature is not as clear. Decreasing the length of the QD would lead to a bigger spacing of its energy levels which could allow to resolve them even at finite temperature.

width of the potential peaks is given by the magnitude of $\partial\alpha(y)/\partial y$ which depends on the waist of the beams, their relative position and their amplitude Ω. Here, we chose a moderate Rabi frequency to estimate the population of the excited state ρ_{ee} (see Fig. 9.6(c)) which becomes numerically unstable when large Rabi frequencies lead to smaller excited state population ρ_{ee}. The main challenge of the scheme is on the one hand the Rabi frequency which has to be large $\Omega_c^2 \gg \Gamma_e\Gamma_{15}$ [53] to suppress the bright state population and on the other hand the width of the beams. The calculated photon-scattering rate (see Fig. 9.6(c)) is as locally confined as the subwavelength potential which could introduce additional effects, i.e. the Zeno effect [222, 229], and might not limit the QD transmission significantly.

In addition to the potential we can also calculate its transmission and the conductance via the Landauer-Bütikker formalism. Figure 9.7 shows the total quantum dot potential including the transversal confinement of the wire and the lightsheet. We find that for zero-temperature the quantum dot (QD) energy levels are clearly resolved corresponding to the tunneling-peaks in the conductance. In the finite temperature limit the QD features are washed out, though optimizing the spacing of the beams could lead to a more optimal energy spectrum. Finally, implementing the scheme with strong interactions could lead to interesting spin-dependent effects due to the QD only being visible to state $|\downarrow\rangle$.

9.5 TOWARDS SPIN-ORBIT COUPLING IN A TRANSPORT EXPERIMENT

Spin-Orbit coupling as realized in cold-atom systems [54, 205] relies on the spin-dependent momentum kick an atom experiences when a two-photon Raman transition takes place, driven by angled probe and control beams [230]. In our experiment the lambda scheme would be formed by the $|1\rangle - |e1\rangle - |2\rangle$ three-level system, see Ch. 3 for details. The spin states in this system are $|\downarrow\rangle = |1\rangle$ and $|\uparrow\rangle = |2\rangle$. The probe beam is propagating in the $z - y$ plane with $\hat{k}_p = k_R(\hat{z} - \hat{y})/\sqrt{2}$ where $\hat{z}$, $\hat{y}$ are unit vectors. The control beam is at 90° angle such that $\hat{k}_c = k_R(\hat{z} + \hat{y})/\sqrt{2}$. In a Raman transition from $|\downarrow\rangle$ to $|\uparrow\rangle$ the atom would first absorb a photon from $\mathbf{k}_p$ and subsequently emit a photon into the control field with $\mathbf{k}_c$ such that the net momentum imparted on the atom is given by

$$\hat{q}_{\downarrow\rightarrow\uparrow} \sim \hat{k}_c - \hat{k}_p = +\hat{y}\,, \tag{9.4}$$

$$\hat{q}_{\uparrow\rightarrow\downarrow} \sim \hat{k}_p - \hat{k}_c = -\hat{y}\,. \tag{9.5}$$

$$\tag{9.6}$$

This means that depending on the spin of the atom it would experience a momentum kick in different directions. In the experiment this scheme could be implemented using the envisioned deformable mirror for one of the beams and the DMD for the other beam. The numerical aperture of the microscope would allow a beam angle of up to ~ 60° which would reduce the magnitude of the momentum kick, though this could be used to adjust the wave-vector to be close to the Fermi wave-vector. The effective momentum kick is given by

$$\hbar|q| = \hbar 2k_R \sin\left(\theta/2\right)\,, \tag{9.7}$$

where $\hbar k_R$ is the recoil momentum where $E_R/k_B = 3.5\,\mu\text{K}$. We can find the angle where the momentum kick is around the Fermi energy from

$$\theta = 2\arcsin\left(\frac{\lambda_L}{2\lambda_F}\right)\,. \tag{9.8}$$

In our experiment a usual Fermi wave vector $k_F = 2\pi/2\,\mu\text{m}$ would then give a beam angle of $\theta = 19°$.

In a first experiment we show that it is possible to introduce the required spin-rotation in the reservoir of the system. The reservoirs are prepared without transport geometry in a fully spin-polarized cloud with $N_\downarrow \approx 85 \times 10^3$ atoms. The probe and control beam are σ_- and π polarized and co-propagating in the vertical direction. The single photon detuning is set to $\Delta = \nu_{1,e2} - \nu_p = 355\,\text{MHz}$ while the two photon detuning is close to zero, i.e. we fulfill the two-photon condition off-resonantly. Figure 9.8 shows the magnetization $M/N = (N_\uparrow - N_\downarrow)/(N_\uparrow + N_\downarrow)$ and atom-number $N = (N_\uparrow + N_\downarrow)$ as a function of the single-photon detuning $\Delta_p = \Delta - 355\,\text{MHz}$. We observe a clear Raman resonance where the two-photon condition is fulfilled with limited atom-losses. The energy difference of the two spin states is found to be $\nu_{cp} = 76.009(6)\,\text{MHz}$ which is close to the theoretical value of $\nu_{12} = 76.029\,\text{MHz}$. The spectrum is fitted with a Lorentzian function which we use to extract the fidelity of the spin-rotation and the linewidth. We extract an efficiency of $90(2)\,\%$ and a full-width-half-max of $646(24)\,\text{Hz}$.

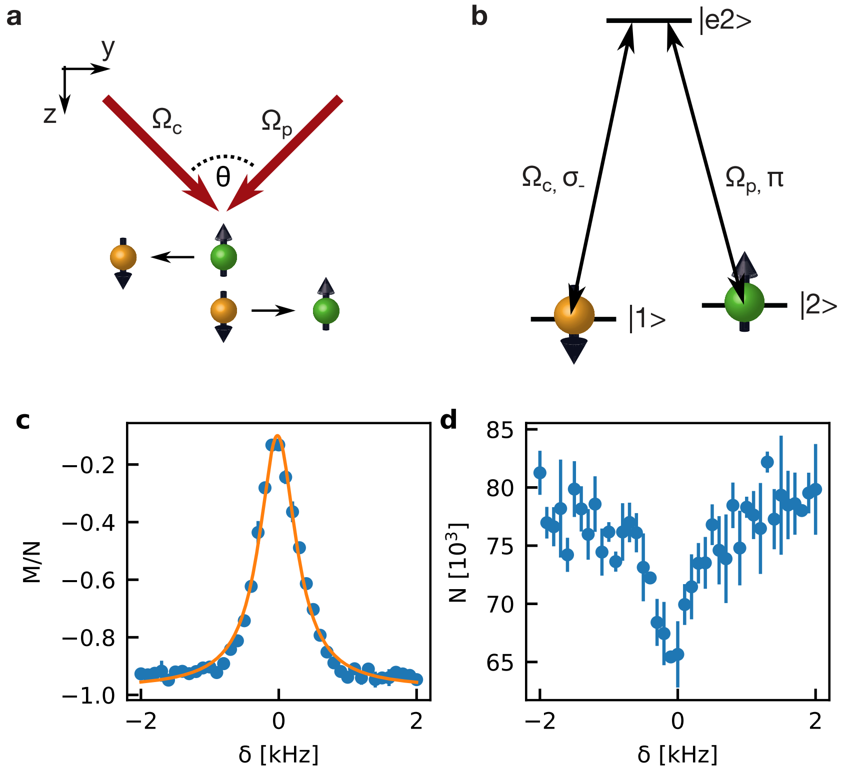

Figure 9.8: Spin-Orbit coupling scheme at high magnetic fields. (a) The spin-orbit coupling scheme uses probe and control laser at 90° angle [230] such that the direction of spin-rotation $\uparrow\rightarrow\downarrow$ ($\downarrow\rightarrow\uparrow$) determines the direction of the momentum kick $-\hat{y}$ ($+\hat{y}$). (b) The lambda system at high magnetic fields in ^{6}Li couples the lowest and second-lowest hyperfine state, called $|\downarrow\rangle$ and $|\uparrow\rangle$, respectively. The control beam couples the $|1\rangle - |e2\rangle$ transition while the probe mean drives $|2\rangle - |e2\rangle$, where $|e2\rangle$ is in the D1 manifold. (c) Measured relative magnetization as a function of the two-photon detuning ($\nu_p - \nu_c = 76.009(6)\,\mathrm{MHz}$) shows the narrow two-photon resonance and concurrent spin-rotation. The atom-number (d) displays limited losses due to the detuning from the single photon resonance $\Delta_p = 355\,\mathrm{MHz}$. We fit the spectrum and extract a linewidth of $\Gamma = 646(24)\,\mathrm{Hz}$ and rotation efficiency of $90(2)\,\%$.

9.6 CONCLUSION AND OUTLOOK

In summary, we have found that it is difficult to harness near-resonant light in a strongly interacting system, due to molecular losses and secondary loss events from particle collisions. We show experimentally that it is still possible to introduce three-level atom-light interaction at high magnetic fields and that we can observe EIT even with strong interactions. The transparency is used to restore the non-linear transport characteristic in the strongly interacting QPC. We find that transport is sensitive to the dissipative and the dispersive effects of EIT. This demonstrates that it is feasible to create lambda systems even at high magnetic fields where it is normally expected that the quantum number m_I is responsible for only having magnetic transitions between the hyperfine states. The lambda-system is the cornerstone for two more schemes we propose to use in a transport experiment. Firstly, the dark-state formed in the EIT condition can be used to create subwavelength potentials which we calculate numerically and propose to use for the creation of a quantum dot. The quantum dot transmission and conductance is calculated to demonstrate that the subwavelength potential allows to observe resonant tunneling features. Secondly, another lambda scheme is proposed to observe spin-orbit coupling in the strongly interacting system which can be used to affect spin transport inside the QPC. We find experimentally that the proposed lambda system can be used to drive Raman transitions between the lowest and second-lowest hyperfine states which are also states that do support strong interactions around their Feshbach resonance.

In the future the three-level atom light interaction can be used to study spin-orbit coupling in the QPC which combined with a pairing gap is the starting point for the creation of Majorana fermions [11]. The implementation of a quantum dot would allow us to study the Kondo effect [199] in quantum dots as well as effects of a spin-dependent quantum dot.

Part III

ENTROPY TRANSPORT BETWEEN SUPERFLUIDS

10

IRREVERSIBLE ENTROPY TRANSPORT BETWEEN TWO SUPERFLUIDS

CHAPTER CONTENTS

The results shown in this chapter have been or will be presented in the following publications:

> P. Fabritius, J. Mohan, M. Talebi, S. Wili, W. Zwerger, M.-Z. Huang and T. Esslinger
> *Irreversible Entropy Transport Enhanced by Fermionic Superfluidity*
> *ArXiv:2309.04359* (2023)
>
> S. Häusler, P. Fabritius, J. Mohan, M. Lebrat, L. Corman and T. Esslinger
> *Interaction-Assisted Reversal of Thermopower with Ultracold Atoms*
> *Physical Review X* **11**, 021034 (2021)

10.1 MOTIVATION

Superfluid flow is the underlying mechanism for many intriguing phenomena in condensed matter physics, liquid helium and cold atoms systems. The macroscopic nature of the superfluids wavefunction [41] is the reason for the observation of effects like the Josephson oscillations [8, 106] in superconductors, the superfluid fountain effect [134, 231] in liquid helium and persistent currents in cold atom rings [232]. Allowing a finite normal current in addition to the supercurrent considerably increases the complexity [7] of the transport process and leads to new, less understood situations [233].

The transport geometry created by our setup is an ideal system to study the fundamental properties of superfluid transport. Fermionic lithium allows us to reach low temperatures at strong attractive interactions which leads to a superfluid state [40, 111, 234]. Cold atom systems are naturally closed, well-understood and easy to manipulate permitting the direct measurement of entropy and configurable transport geometries decoupled from their environment. These systems have been used to study transport and equilibrium properties of the superfluid system extensively [16, 232, 235, 236]. In the two-terminal transport geometry both subgap superfluid transport [38, 101] through a quantum point contact and Josephson oscillations have been observed [33, 34]. The exploration of entropy transport in these systems up to now has been restricted to an intermediate temperature regime [69, 87] where the non-linear features of superfluid transport have not been observed.

Here, we impose a chemical potential bias, equivalent to a voltage bias in superconductors, or temperature bias between two superfluid reservoirs which is found to result in a non-linear particle current response, concurrent with a non-linear entropy current response. The overall entropy is simultaneously increasing indicating the irreversible nature of the observed transport process. The two different initial states prepared here correspond either to a pure entropy bias or to a combination of particle and entropy bias. For the initial state with a pure entropy bias the system is found to approach a non-equilibrium steady-state in the one-dimensional limit, while opening the channel does allow for relaxation of this state and generally decreases the transport timescales. Notably the transported entropy per particle is constant across the change of channel geometry and its value is far above the value for the superfluid in and around the channel. Implying that the observed current is not a supercurrent and that superfluidity itself increases the entropy transport via the non-linearity. The discrepancy between transported and local entropy per particle also implies that a hydrodynamic description of the transport within a two-fluid model is not possible, indicating that the observed behavior is a non-equilibrium effect. The observed current-bias characteristic is found to be described by a phenomenological model derived using the generalized gradient dynamics method [237] which is a generalization of Onsager's linear description of irreversible processes including non-linear, irreversible processes. Applying the phenomenological model we can extract the transport coefficients governing the transport which enables comparisons with microscopic theories.

At the writing of this thesis we are still working on determining the optimal thermometry technique used to extract entropy and atom-number. Anharmonicities from the dipole trap and fringes in the absorption imaging system lead to systematic differences between fitting the equation of state directly or applying the previously used second-moment method. The systematic differences mainly affect the overall degeneracy, i.e. the reservoir superfluidity, while qualitatively the observed transport measurements are consistent between all techniques. In the following the thermometry obtained from fitting the equation of state is used.

10.2 EXPERIMENTAL SETUP

The preparation and measurement process is equivalent for the data presented here and in the following Ch. 11. More details can be found in the technical section of this thesis (see Pt. I and Ch. 2). We prepare a cold cloud of ^{6}Li in the lowest and third lower hyperfine state in a hybrid optical-magnetic trap. We operate at a magnetic field of $B = 689.7\,\mathrm{G}$ which is the location of the Feshbach resonance for our mixture. After evaporative cooling we typically end up with total atom numbers of about $N = 342(36) \times 10^3$ atoms, temperatures of $T = 90(6)\,\mathrm{nK}$ and entropy per par-

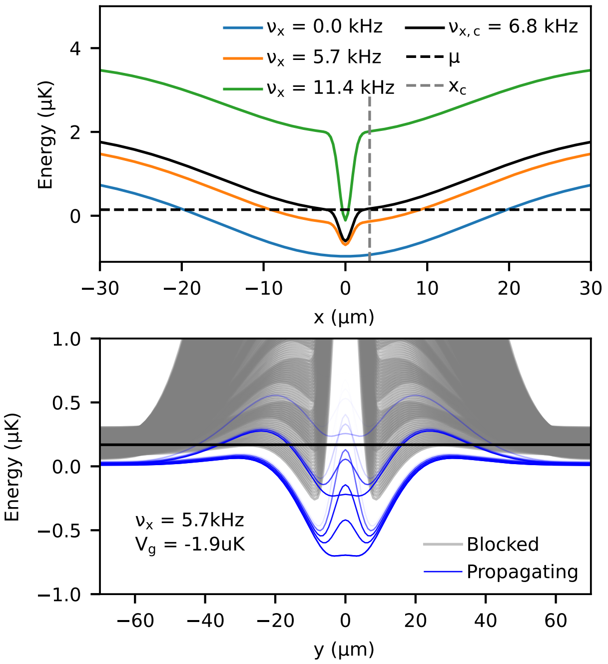

Figure 10.1: Potential landscape in transversal and in transport direction. The lowest transversal mode (a) as function of x is shown for different confinement frequencies used in the experiment at a fixed gate potential of $V_g = -2.2\,\mu\mathrm{K}$ and vertical confinement $\nu_z = 9.4\,\mathrm{kHz}$. When reducing the transversal confinement below $\nu_x \sim 6.8\,\mathrm{kHz}$ (black line) atoms can flow above the channel constriction. For lower confinements the system becomes quasi-2D where the confinement originates mainly from the trapping in z-direction. (b) shows the mode structure along the transport direction for modes which can be transmitted through the channel (blue lines) and modes which are blocked by the channel or by the reservoir connection (gray lines). The propagating modes shown here were calculated assuming a finite temperature $T = 90\,\mathrm{nK}$. The individual occupation of the propagating modes is indicated by their transparency. The modes in light blue would not be able to enter the channel at zero temperature.

ticle of $S/Nk_B = 1.49(10)$ below the superfluid transition $S_c/Nk_B = 1.69$ [40, 110]. The originally cigar shaped trap is separated into two half-harmonic traps by applying a repulsive, elliptical "wall" beam in transversal direction with a waist of $w_y = 8.6\,\mu\mathrm{m}$ in transport direction. This trap configuration is the end point of the experimental sequence, before the transport geometry is imposed. For the imaging of the atoms we take two in-situ absorption images of the atomic clouds in half-harmonic reservoirs for each spin, in quick succession (details in Sec. 6.3), such that in one experimental run both spin-states are imaged.

Transport Geometry

The transport configuration, i.e. the quasi-one-dimensional (1D) channel or quasi-two-dimensional (quasi-2D) constriction, is created by two TEM_{01}-like repulsive beams intersecting the cloud along the x- and z-direction. In the z-direction the cloud is compressed by a TEM_{01} beam with a longitudinal waist of $w_y = 30.2\,\mu\mathrm{m}$, a transversal waist of $w_z = 9.5\,\mu\mathrm{m}$ and a transversal confinement of $\nu_z = 9.42(6)\,\mathrm{kHz}$, this results in a quasi-2D ($h\nu_z/k_B T \approx 4$) region between the two reservoirs, independent of the confinement in x-direction. In the x-direction a second TEM$_{01}$-like beam is projected through the microscope with a waist of $w_y = 6.8\,\mu\text{m}$ in transport direction and a narrow notch in transversal direction $w_\text{notch} = 1.5\,\mu\text{m}$, allowing atoms to flow through. This wire beam creates a transverse confinement of up to $\nu_x = 12.4(2)\,\text{kHz}$ which is the experimental parameter varied throughout this chapter to change the transport geometry. Figure 10.1(a) shows the transversal confinement of the lowest mode along the x-direction, including the constriction beams and the gate beam. Details on how to calculate the energies of these modes can be found in Ch. 2. The gate beam is a Gaussian, attractive beam projected through the microscope onto the quasi-2D region around the channel. It has a waist of $w_{xy} = 31.1\,\mu\text{m}$ and a peak potential of $V_g = -2.2\,\mu\text{K}$. For strong confinements (green line in Fig. 10.1(a)) atoms have to pass through the notch of the x-confining beam since the chemical potential μ is far below the zero-point energy of the confining beams, therefore we call this regime the 1D regime. When the power of the channel beam is reduced its confinement and peak potential is decreasing such that below a confinement frequency of $\nu_x \approx 6\,8\text{kHz}$ atoms can pass the channel beam overhead, hence for lower confinements we call this the quasi-2D regime. Figure 10.1(b) displays the modes which can propagate through the channel (blue lines) and the modes which are blocked due to the potential landscape (gray lines) along the transport direction. We find that at a finite temperature of $T = 90\,\text{nK}$ the lowest modes can propagate, though with reduced occupation (transparency of the blue lines). Nevertheless, not all modes which have in principle a low enough energy in the center of our system ($y = 0$) are able to propagate from the reservoirs ($|y| \geqslant 60\,\mu\text{m}$) to the transport region [69].

Thermometry

In contrast to the previously used (see Sec. 2.2) thermometry method based on the second-moment of the clouds" column density we use a direct fit of the equation of state (EoS) here. The spin-resolved absorption imaging system (see Ch. 6) allows us to extract the in-situ column density $n_{i,m}(y,z)$ ($i = L, R$, $m =\uparrow,\downarrow$) for each spin and each reservoir. The raw images are taken $225\,\mu\text{s}$ apart and referenced to an optimal bright image [83]. The atom numbers are then obtained from integrating the column density in each direction for the two spin states and reservoirs, respectively.

The density distribution of each reservoir is fitted with the equation of state of a harmonically trapped unitary Fermi gas given by

$$n^\text{col}_{i\sigma}(y,z) = \lambda^{-3}_{Ti\sigma} \int_{-\infty}^{\infty} dx\, f_n \left[q_{i\sigma} - \left(\frac{x}{R_{xi\sigma}}\right)^2 - \left(\frac{y-y_0}{R_{yi\sigma}}\right)^2 - \left(\frac{z-z_{0\sigma}}{R_{zi\sigma}}\right)^2 \right], \tag{10.1}$$

where the temperature $T_{i,m}$ and the degeneracy $q_{i,m}$ are varied. The temperature determines both the thermal de Broglie wavelength via $\lambda_T = \sqrt{2\pi\hbar^2/mk_BT}$ and the clouds Gaussian thermal length $R^2_{j,i,m} = 2k_BT_{i.m}/m_{^6Li}(2\pi\nu_j)^2$. f_n is the density EoS of the unitary Fermi gas [40]. For this fit the central region of the cloud $\sim 60\,\mu\text{m}$ which includes the wall is excluded. The common center of the reservoirs y_0 is fixed from an independent fit to the dip in the density due to the wall beam, while the vertical cloud center z_0 is fitted for each spin-state as well as an angle of 0.45°. The advantage of this method compared to the thermometry via the second-moment is that it allows extraction of the degeneracy q_i independently of the calibrations of magnification and absorption cross-section.

Since the spin-resolved absorption imaging leads to a slight heating of the secondly imaged state we use only the thermometry of the firstly imaged state in the following. The atom-numbers in each spin-state are equal. The absorption cross-section of the imaging system is calibrated by matching the atom-number obtained via the cross-section to the atom-number calculated from the degeneracy and temperature obtained from the fit detailed here. The cross-section measured this way is 2.24 times smaller than the ideal value, similar to the value obtained by other groups [81, 238].

10.3 IRREVERSIBLE ENTROPY FLOW BETWEEN TWO SUPERFLUIDS

Superfluidity and its signatures have been studied in great detail in the equilibrium system [40, 65, 235] which we use here to gain a better understanding of our system in equilibrium. We can extract the trap-averaged entropy per particle $S/N = 1.49(10)k_B$ which is below the critical value of the normal to superfluid transition $S_c/N \approx 1.69k_B$ [40, 110]. Figure 10.2(a)-(b) shows the local degeneracy $T/T_F(\mathbf{r})$ for $T/T_F < 1$. These local quantities can be calculated from the 3D EoS of the homogeneous gas in the local density approximation. We find that in equilibrium the central region of the cloud where the channel is located is superfluid (blue contours in Fig. 10.2(a)-(b)). In case of a weak channel there are normal "sidemodes" entering the transport region as can be seen in Fig. 10.2(b). For the most degenerate regions in Fig. 10.2(a) we find a local entropy per particle of $s = 6.7(4) \times 10^{-4}k_B$ and degeneracy of $T/T_F = 0.026(2)$, resulting in a deeply superfluid gas around the channel with $\Delta/k_BT = 18(1)$, where Δ is the unitary superfluid gap.

Figure 10.2(c) shows the state-space $\Delta S, \Delta N$ and the entropy per particle S/Nk_B as a color contour in which we can almost arbitrarily prepare our system. For transport to occur we prepare an initial state in the state-space of extensive quantities ΔS and ΔN, resulting in thermodynamic biases in the intensive quantities $\Delta\mu$ and ΔT driving respective currents of the extensive properties I_N, I_S. Even though the initial state could in principle be arbitrary we restrict ourselves to small biases $|\Delta\mu/\Delta| < 0.5|$, $|k_B\Delta T/\Delta| < 0.2$, which in the non-interacting regime result in linear current-bias characteristics. The currents, driven by the imposed biases propagate the system through the state-space according to their initial states and respective equations of motion, given by

$$\begin{aligned} I_N(\Delta N, \Delta S) &= -\frac{1}{2}\frac{d\Delta N}{dt}, \\ I_S(\Delta N, \Delta S) &= -\frac{1}{2}\frac{d\Delta S}{dt}. \end{aligned} \tag{10.2}$$

In Fig. 10.2(c) some paths explored in our experiment are shown. The underlying entropy landscape – calculated from the EoS – shows that each path has a strictly positive entropy production rate $\dot{S} > 0$, meaning they are all irreversible. Experimentally we can verify that the overall system can be considered closed due to an absence of heating $\frac{dS/Nk_B}{dt} < 0.02\,s^{-1}$ (without transport) and particle loss $dN/dt = 0$. The observed increase of entropy in the closed system is possible to a buildup of entanglement entropy [39, 239–241]. Interestingly, depending on the initial conditions we can have strikingly different transport scenarios. In the case of an initial state, exhibiting a pure entropy imbalance (square in Fig. 10.2(c)) the sys-

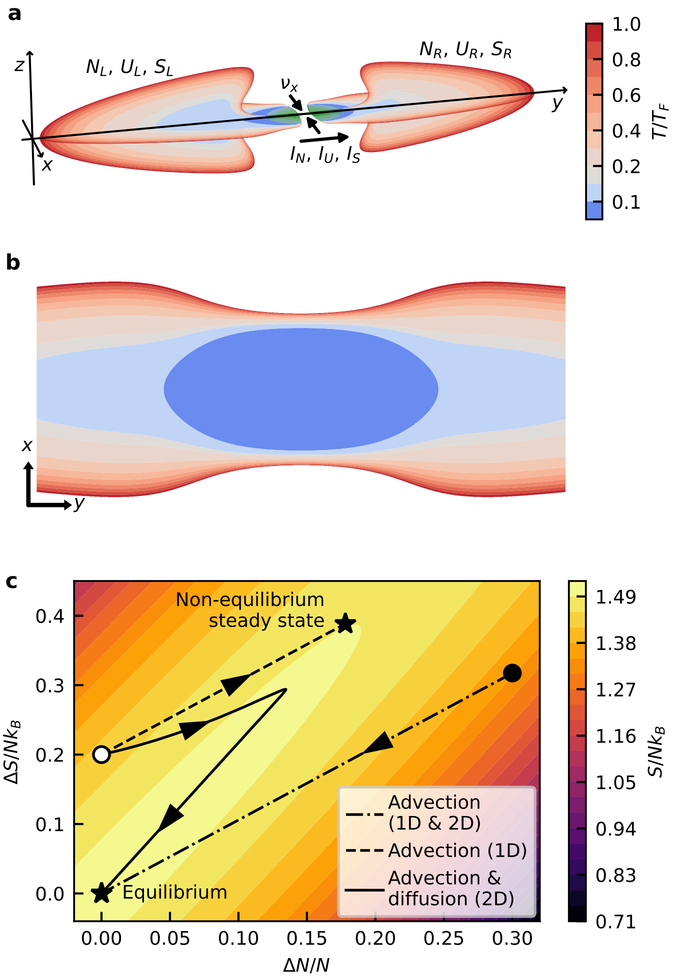

Figure 10.2: Irreversible transport of particles, energy, and entropy between superfluids. Local degeneracy $T/T_F(\mathbf{r})$ at equilibrium in the quasi-1D (a) and quasi-2D (b) channels. The blue contours $T/T_F < 0.167$ (the local normal to superfluid transition [40]) indicate the superfluid while red contours the normal regions $T/T_F > 0.167$. Away from equilibrium, differences in N_i, and S_i between the reservoirs ($i = L, R$) induce biases of the chemical potential and temperature that drive currents of the extensive quantities. The channel region (green) is not in equilibrium during transport, while the reservoirs remain in equilibrium, respectively. (c) Depending on the initial conditions (circle or square) and microscopically allowed processes, the reservoirs can exchange atoms, energy, and entropy advectively and diffusively, tracing out various paths through state space with the constraints that atom number and energy are conserved $dN/dt = dU/dt = 0$ and the entropy production is positive definite $dS/dt \geqslant 0$ until evolution halts at a steady state (stars) by reaching either a non-equilibrium steady state or equilibrium ($\Delta\mu = \Delta T = \Delta N = \Delta S = 0$) where the total entropy $S = S_L + S_R$ at fixed total particle number $N = N_L + N_R$ and energy $U = U_L + U_R$ has a global maximum.

tem can reach a non-equilibrium-steady-state (star in Fig. 10.2(c)) which, within our experimental time-scales, does not relax. A second possibility for this initial state is an initial build-up of entropy and particle imbalance due to advective transport $I_S \propto I_N$, followed by a relaxation via diffusive transport $I_S \neq 0$, $I_N = 0$. To be precise, the processes of advection and diffusion are present at all times during the evolution but the due to their different timescales and different thermodynamic forces it is possible to distinguish them. For the other case of an initial state, with a well-prepared entropy- and particle-imbalance (circle in Fig. 10.2(c)) only an advective relaxation takes place and reaches equilibrium independently on whether diffusion takes place or not. Notably, the initial conditions are not the only reason these processes take place, but the systems microscopic properties determine the exact evolution in the state-space.

10.3.1 Advective Transport

For the measurements presented in the following we repeatedly prepare the system with the same initial state and vary the time during which transport is possible, via the wall beam. For each transport time the measurement preparation and process is repeated $3-5$ times to obtain the respective statistic uncertainty. Due to the varying dimensionality in the transport configuration it is not possible to apply the three-dimensional (3D) EoS in this geometry. Thus, the transport beams are adiabatically ramped down, except the wall, and the cloud is imaged in a half-harmonic trap. In terms of thermometry the internal energy U_i and atom number N_i, for both reservoirs $i = L, R$, are obtained directly. The entropy $S_i(N_i, U_i)$ is a universal function of both and is used as an observable for the presented data. Due to the increase of entropy in the open reservoir system during transport the entropy current I_S is only an apparent current. Unequal heating in one of the reservoirs would appear as a current in our measurement, but also in the total entropy which means we can place a bound on such a current $I_S^{\text{cons}} \in [I_S - (1/2)dS/dt, I_S + (1/2)dS/dt]$ [101], where I_S is the measured current.

In the first measurement presented here an initial state with both entropy and particle imbalance is imposed $\Delta N(0), \Delta S(0) \neq 0$. The transport geometry, in particular transversal confinement ν_x and gate potential V_g, is chosen such that the imbalance relaxes to equilibrium within $0.5\,\text{s}$. Figure 10.3(a) shows the evolution of the particle imbalance for different transport geometries. For the strongest confinement $\nu_x = 12.3(1)\,\text{kHz}$ (red circles in Fig. 10.3) we observe a strong deviation from exponential decay indicated by the visible “kink” in the particle relaxation $\Delta N(t)$ close to equilibrium. Comparing this to the non-interacting quantum point contact (QPC) which displays an exponential relaxation due to its linear current-bias characteristic $I_N \propto \Delta\mu/h$, we not only find that the current $I_N = -(1/2)\ d\Delta N/dt$ we observe is much larger but also that the current-bias characteristic is nonlinear. This behavior has been already observed in our group on multiple occasions [38, 101] and has been modeled theoretically [242]. The surprising feature in the particle current I_N is its large sub-gap ($\Delta\mu < \Delta$ in equilibrium) magnitude and the resulting non-linearity. Both the enhancement of the current, far beyond the non-interacting value and the nonlinear (non-Ohmic) $I - \Delta\mu$ characteristic suggest that the system is superfluid. The nonlinear behavior persists when the 1D channel is opened (green points in Fig. 10.3) and it is still visible in the 2D regime (blue and orange points in Fig. 10.3).

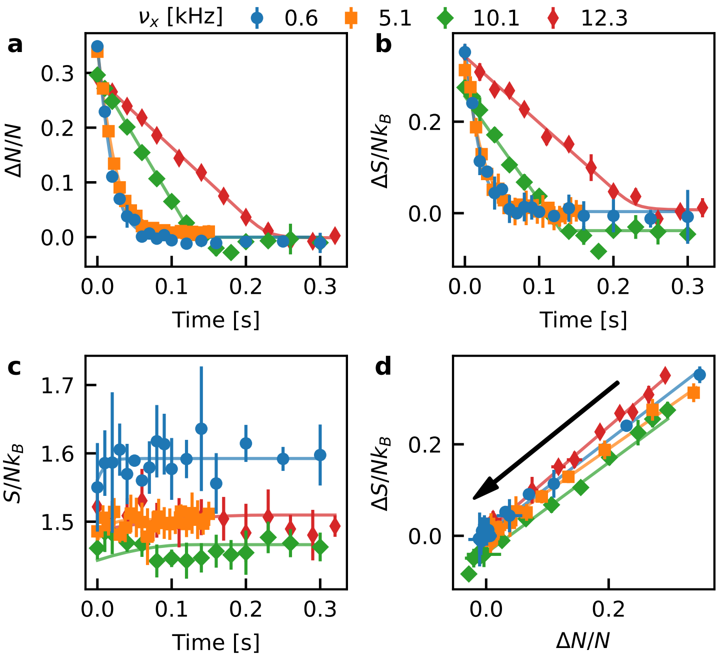

Figure 10.3: Observing the non-linear advective entropy transport. The particle (a) and entropy (b) imbalance evolution indicate a non-linear relaxation of the prepared initial state. Decreasing the transversal confinement the system relaxes faster, and the non-linearity becomes less sharp. The total entropy per particle (c) increases slightly compared to ΔS, indicating that entropy is indeed being transported. (d) The entropy imbalance plotted versus particle imbalance directly indicates a non-zero transported entropy per particle and reflects the direct proportionality which means the entropy is transported advectively. The solid lines are fits with a phenomenological model. The error bars correspond to the standard deviation of the mean of 3-5 measurements.

The current I_N is initially increasing due to the additional transport modes when opening the channel, though in the 2D regime this trend does not continue. We attribute this behavior to additional resistances in series with the 1D region of the channel. Firstly, the reservoir to 2D connection [69] (see Sec. 10.2), where not all modes coming from the reservoir can enter the quasi-2D region. Secondly, the resistance at the normal to superfluid interface [243]. In addition, we find that the kink of the non-linearity seemingly becomes less pronounced in the 2D limit. This can be explained by a larger linear contribution to the total current, e.g. due to normal modes entering the transport region (see Fig. 10.2(b)), and by the additional series resistances.

Figure 10.3(b) shows the entropy relaxation $\Delta S(t)$, strikingly resembling the particle relaxation $\Delta N(t)$ in Fig. 10.3(a). We can verify the resemblance by plotting the two imbalances against each other as can be seen in Fig. 10.3(d), showing that all paths are not only linear but also parallel to each other. The paths collapse on each other when accounting for the different initial states. The fact that the paths are linear shows a direct proportionality between particle and entropy current $I_S = s^* I_N$, with the proportionality constant being the advectively transported entropy per particle s^*. The fact that all paths collapse on one line shows that the transported entropy per particle s^* is almost independent of the transversal confinement ν_x. We can extract the transported entropy per particle from a linear fit $s^* = 1.03(2)\, k_B$. The value we find is surprisingly large for superfluid transport and close to the average entropy per particle in the reservoirs $S/N = 1.49(7)\, k_B$, while being much larger than the local equilibrium entropy per particle $s/k_B = 6.7(4) \times 10^{-4}$ in the channel region.

Breakdown of Hydrodynamics

Here, we want to show that our observation that the measured transported entropy per particle s^* is much larger than the local entropy per particle s is a result of the breakdown of hydrodynamics in the channel. The two-fluid model [76, 134, 244, 245] is a hydrodynamic description of superfluid flow, obeying the thermodynamic equation of state. One of the consequences of the model is that the fluid is made up of an ideal superfluid part which carries no entropy and a normal part which carries entropy. The fluid density is given by

$$\rho = \rho_s + \rho_n, \tag{10.3}$$

where ρ_s is the superfluid and ρ_n is the normal density of the fluid. In our system we find that the fact that the entropy current I_S is directly proportional to I_N violates the assumption of the system being close to a local equilibrium and thus hydrodynamics breaks down. The two-fluid model implies that the current in our system should be the sum of normal and superfluid currents

$$I_N = I_N^n + I_N^s, \tag{10.4}$$

where the entropy is only carried by the normal current $I_S = s_n^* I_N^n$. Inserting this into our observation that entropy and particle current are directly proportional we find

$$I_N^s = \left(\frac{s_n^*}{s^*} - 1 \right) I_N^n. \tag{10.5}$$

The normal current can be calculated from the integrated current density j_n over the cross-section of the channel which for a hydrodynamic current also determines the entropy current by weighting the current density j_n with the local, equilibrium entropy per particle

$$\begin{aligned} I_N^n &= \int dx\, dz\, j_n(x, y=0, z), \qquad (10.6) \\ I_S &= \int dx\, dz\, j_n(x, y=0, z) s(x, y=0, z), \end{aligned}$$

where we used $j_s = \bar{s} v_n = \bar{s}/n\, v_n n = j_n s$, with the entropy per volume $\bar{s}$. We can calculate the local entropy per particle s from the EoS of the homogeneous unitary Fermi gas [40] which is found to be tiny at the contacts to the wire $s = 6.7(4) \times 10^{-4} k_B$, due to the large degeneracy (see Fig. 10.2(a)-(b)). This vastly different local entropy s and transported entropy $s^* = 1.03(2)\, k_B$ leads to a logical contradiction when applying Eq. 10.5. The two-fluid model implies that our system would support two large, but opposite, currents $I_N^s \approx -I_N^n$ and their difference would be the current we observe in the experiment. This is in contradiction with the behavior of a time-averaged supercurrent in response to a chemical potential bias $\Delta\mu$. In the AC-Josephson limit the time average of the supercurrent vanishes, while in the limit of nonadiabatic phase slips the supercurrent and normal current flow in the same direction [246] (see also Ch. 4). Given a weak link, tunneling geometry the breakdown of hydrodynamics is expected [134] due to a rapidly varying superfluid order parameter over a short distance. The breakdown of hydrodynamics furthermore shows that the channel region is far from equilibrium. In addition, the observation $s \ll s^*$ implies that there is an irreversible conversion process from superfluid current in the contacts to normal currents in the channel and back to superfluid currents in the opposite contacts. It is interesting to note that a possible process must be independent of the transport geometry which seemingly has no influence on s^*. Finally, the observation that $s^* > 0$ shows that the observed entropy carrying, nonlinear current is indeed not a supercurrent. It is remarkable that the superfluidity in the contacts enhances I_N, leaving s^* seemingly unchanged, thus effectively increasing the entropy current I_S. Regarding the total entropy per particle, shown in Fig. 10.3(c) we find that the observed entropy current is flowing between the two reservoirs.

In order to verify these findings we have varied how the system is prepared. To that end the gate beam is switched on for varying times before the transport is started, for the data presented here the beam is ramped on over 10 ms followed by a wait-time of 5 ms before transport is started. Our observations stay unchanged for waiting times up to 0.5 s, longer than the overall relaxation time. In the case of waiting times of up to 3.5 s the relaxation becomes more exponential and s^* is reducing by $\sim 10\%$. In-situ imaging of the gate region around the channel indicates that the filling timescale of these local miniature reservoirs is on the order of several seconds. It is not yet clear how these regions affect transport, though our observations suggest that the non-equilibrium nature of the gas around the channel is important.

10.3.2 Diffusive and Advective Transport

The second type of initial states and resulting different paths in state-space ΔS, ΔN can be explored by applying a pure entropy imbalance $\Delta S(0) \neq$

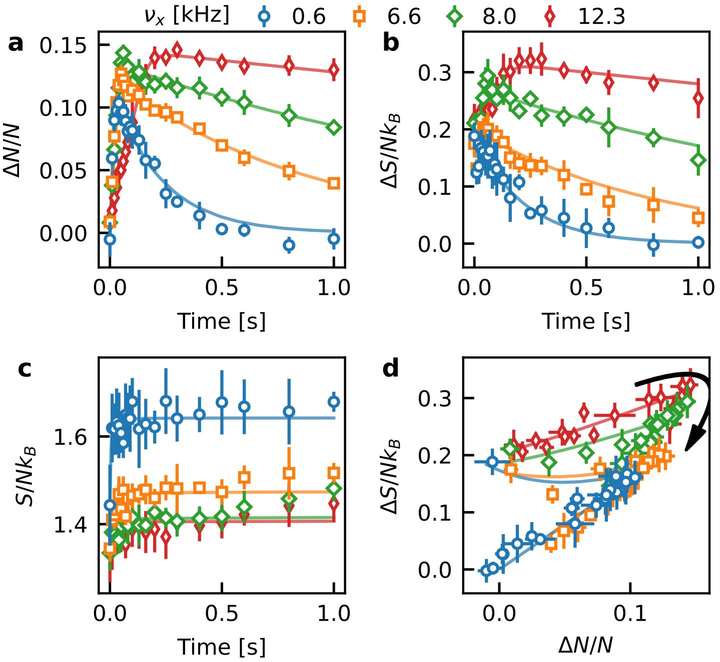

Figure 10.4: Simultaneous advective and diffusive entropy transport. (a)-(b) The particle and entropy imbalance evolution show the initial, fast advective response followed by a slow diffusive relaxation. Towards the quasi-1D limit (red diamonds) a non-equilibrium steady-state is reached, hardly evolving within our experimental timescales. The advective response is non-linear for strong confinement and becomes more linear in the quasi-2D regime (blue circles). Concurrently the timescales of advective and diffusive mode are enhanced. The net entropy (c) is initially increasing quickly, while the suppressed evolution in the 1D limit also limits the entropy growth. The entropy imbalance as a function of particle imbalance (d) illustrates the competition between diffusive and advective mode, determined by the transversal confinement. Error bars (data points) indicate the standard deviation (average) of $3-5$ repetitions.

0, $\Delta N(0) = 0$ (open circle in Fig. 10.2(c)). This initial condition corresponds to the configuration already explored in previous works on the thermoelectric effect [68, 69, 87], where an initial temperature imbalance ΔT results in a particle response $\Delta N(t)$. Figure 10.4 shows the result of the experiments performed in this work where a significantly smaller (factor 2) average temperature was prepared (for the new preparation method see Sec. 2.3) compared to previous works [69, 87]. For the strongest confinement $\nu_x = 12.3(1)\,\mathrm{kHz}$ (red diamonds in Fig. 10.4) the initial response of ΔN and ΔS is nonlinear and quickly reaches a state which hardly evolves within the maximal experimental transport time $t_{\mathrm{max}} = 1\,\mathrm{s}$. This limit of non-vanishing imbalances far from equilibrium is called a non-equilibrium steady-state which seems to be present in the 1D limit $h\nu_x/k_B T \gg 1$. The precise non-equilibrium steady-state approached by the system depends on the initial state and the path through state space, inherently related to the microscopic properties of the system. In previous works the steady-state has been observed [87] in the linear response regime and with larger average temperatures. Our measurements confirm that it persists even in the non-linear regime, where the currents responsible for reaching the non-equilibrium steady-state are ~ 6 times larger and non-Ohmic.

When reducing the transversal confinement ν_x the initial response becomes faster (green diamonds in Fig. 10.4(a)) while the non-equilibrium steady-state can relax back to equilibrium. While the initial response stays nonlinear, even in the 2D limit (orange squares in Fig. 10.4(a)), the secondary response is linear, manifesting itself in an exponential relaxation to equilibrium. The competition between the initial response and the secondary relaxation is visible for the dataset with the weakest confinement (blue squares in Fig. 10.4(c)) where the entropy response $\Delta S(t)$ shows almost pure exponential relaxation. Figure 10.4(d) further supports this picture of competition between two processes, where for both parts of the path in state space a linear proportionality is given. However, from the previous transport measurement (see Fig. 10.3) we know that the path in state-space of the advective dynamics are not changing with confinement, thus only the change of diffusive dynamics are responsible for the change of paths in state-space.

10.4 PHENOMENOLOGICAL MODEL OF THE NONLINEAR AND IRREVERSIBLE TRANSPORT PROCESS

In order to quantify our observations we can formulate a phenomenological model loosely inspired by the two-fluid model as a combination of linear and non-linear response to the applied biases. Previous models [38, 68, 69, 247], based on linear response are no longer applicable due to the observed nonlinear behavior. In this context linear response is described by a system of equations which describe the particle current I_N and the entropy current I_S as a linear function of the biases $\Delta\mu$ and ΔT

$$\begin{pmatrix} I_N \\ I_S \end{pmatrix} = G \begin{pmatrix} 1 & \alpha_c \\ \alpha_c & L + \alpha_c^2 \end{pmatrix} \begin{pmatrix} \Delta\mu \\ \Delta T \end{pmatrix}. \tag{10.7}$$

This system of equations obeys Onsager reciprocal relations [3, 248] which imply that the Peltier effect $I_S = \alpha_c \Delta\mu$ and the Seebeck effect $I_N = \alpha_c \Delta T$ are described by the same transport coefficient α_c (see also Sec. 2.4). The main point here is that Onsager"s theory describes coupled irreversible processes which we also observe in the nonlinear system, superfluid in equilibrium, since $I_S = s^* I_N$. Even though the Onsager reciprocal relations are only valid in linear response. In the following, we will introduce a formalism which generalizes Onsager"s theory to nonlinear irreversible processes, called generalized gradient dynamics [237].

10.4.1 *Generalized Gradient Dynamics*

The central framework of the formalism of generalized gradient dynamics [237] is to describe general irreversible processes via a gradient of the dissipation potential Ξ. Here, irreversibility and dissipation are almost equivalent, where dissipative processes refer to evolutions which produce entropy, while irreversible processes are constructed such that they are dissipative, and obey the Second law of Thermodynamics. The production of entropy is the main feature of the irreversible evolution which means in order to write equations for such an evolution it is necessary to have the entropy be expressed in terms of the complete state space of the system $S(\mathbf{x})$, where $\mathbf{x}$ is the vector describing the state space. The conjugate variables $\mathbf{x}^*$ are then derivatives of the entropy S with respect to $\mathbf{x}$

$$\mathbf{x}^* = \frac{dS}{d\mathbf{x}}. \tag{10.8}$$

Since the entropy is a potential driving the system towards equilibrium, the entropic conjugate variables $\mathbf{x}^*$ are the driving forces towards such equilibrium. The thermodynamic forces $\mathbf{X}$ in this framework can then be interpreted as linear functions of the entropic conjugate variables

$$\mathbf{X} = F(\mathbf{x}^*)\,, \tag{10.9}$$

where F is a linear operator. In turn, the currents $\mathbf{I}$ are defined as derivatives of the dissipation potential Ξ with respect to the forces $\mathbf{X}$

$$\mathbf{I} = \Xi_{\mathbf{X}}\,. \tag{10.10}$$

The challenge in finding an appropriate model which describes our observation is thus to find a dissipation potential Ξ which fulfills the requirements given by this framework based on the Second law of Thermodynamics and the process being irreversible. The formal requirements on the dissipation potential Ξ can then be written down in terms of the following criteria [237]

1. Positiveness $\Xi(\mathbf{x}) \geqslant 0$ and $\Xi(\mathbf{0}) = 0$. This condition ensures that there is no evolution in thermodynamic equilibrium.
2. Monotonicity of the derivatives $\mathbf{x} \cdot \partial\Xi/\partial\mathbf{x} \geqslant 0$. This condition ensures the Second Law of Thermodynamics $\dot{S} \geqslant 0$.
3. Convexity near the origin. This condition ensures the local stability of the thermodynamic equilibrium.
4. Degeneracy with respect to particle number $\partial N/\partial\mathbf{X} \cdot \partial\Xi/\partial\mathbf{x} = 0$. This condition ensures the conservation of particle number.
5. Degeneracy with respect to energy $\partial U/\partial\mathbf{X} \cdot \partial\Xi/\partial\mathbf{x} = 0$. This condition ensures the conservation of energy.
6. Evenness with respect to time reversal. This condition ensures that Ξ describes irreversible and not reversible dynamics.

In addition, the currents also fulfill the Onsager-Maxwell reciprocal relations which in this context are given by

$$\left(\frac{\partial I_1}{\partial X_2}\right)_{X_1} = \left(\frac{\partial I_2}{\partial X_1}\right)_{X_2}\,. \tag{10.11}$$

Entropy Production

One of the central ideas of the formalism we use here is that the entropy is a potential which drives the evolution towards equilibrium [237]. In our system the entropy S is a function of the state variables N, U, ΔN, ΔS. This means that independently of the initial and final point of the evolution the entropy production is given by

$$\begin{aligned}\delta S &= \int_0^\infty dt\,\dot{S}(t) = \int_0^\infty dt\,\frac{I_N(t)\Delta\mu(t) + I_S(t)\Delta T(t)}{T(t)}\\ &= \int_0^\infty dt\,\dot{\mathbf{X}}\cdot\mathbf{x} = \int_{\mathbf{X}_0}^{\mathbf{X}_\infty} d\mathbf{X}\cdot\frac{\partial\Xi}{\partial\mathbf{X}}\\ &= S(N,U,0,0) - S(N,U,\Delta N_0,\Delta S_0)\,.\end{aligned} \tag{10.12}$$

We find that the produced entropy is independent of the underlying microscopic processes and of the path of the system in state-space.

Derivation of the Phenomenological Model

In order to derive the dissipation potential we first start by formulating the thermodynamic forces and currents within our system. From previous works [69, 71, 87] we know that the total entropy production rate is given by

$$\frac{dS}{dt} = I_N \Delta\left(\frac{\mu}{T}\right) - I_U \Delta\left(\frac{1}{T}\right) = \frac{I_N \Delta\mu + I_S \Delta T}{T}\,, \tag{10.13}$$

where I_U is the internal energy current and $T = (T_L + T_R)/2$ is the average temperature. The vector of state space variables is then given by $\mathbf{x} = (N, U, \Delta N, \Delta S)$ and the vector of conjugate quantities is $\mathbf{x}^* = \partial S/\partial \mathbf{x} = (-\mu/T, 1/T, -\Delta\mu/2T, -\Delta T/2T)$. The conservation of atom number and energy in the closed system ensures that $\dot{N} = \dot{U} = 0$ and thus the state and conjugate vectors can be reduced to $\mathbf{x} = (\Delta N, \Delta S)$ and $\mathbf{x}^* = (-\Delta\mu/2T, -\Delta T/2T)$. We then find that the currents in our system can be obtained from the dissipation potential using Eq. 10.10

$$\begin{aligned} I_N &= T\frac{\partial \Xi}{\partial \Delta\mu}\,, \\ I_S &= T\frac{\partial \Xi}{\partial \Delta T}\,. \end{aligned} \tag{10.14}$$

In addition, Onsager reciprocity is fulfilled for a dissipation potential obeying Eq. 10.11 and thus in our case

$$\frac{\partial I_N}{\partial \Delta T} = \frac{\partial I_S}{\partial \Delta\mu}\,. \tag{10.15}$$

For the nonlinear model needed to correctly describe our data we can start by writing the linear model in terms of a dissipation potential

$$\Xi_n = \frac{G(\Delta\mu + \alpha_c \Delta T)^2}{2T} + \frac{G_T}{2}\left(\frac{\Delta T}{T}\right)^2\,, \tag{10.16}$$

with the conductance G, the Seebeck coefficient α_c and the thermal conductance G_T. This dissipation potential generates the currents

$$\begin{aligned} I_N &= G(\Delta\mu + \alpha_c \Delta T)\,, \\ I_S &= \alpha_c I_N + G_T \Delta T/T\,, \end{aligned} \tag{10.17}$$

where we can identify a linearly responding advective mode, driven by $(\Delta\mu + \alpha_c\Delta T)$, and a linearly responding diffusive mode, driven by ΔT. The nonlinear model is then derived by replacing the linear advective mode by a nonlinear advective mode, the functional form is inspired by results on the nonlinear response in a superfluid QPC [38, 122, 124, 249]. In Ref. [38, 101] the particle current was obtained from a numerical derivative and showed a sigmoid-like functional form. We found here that a hyperbolic tangent describes this behavior well. In addition, we know from our measurements in Fig. 10.3(d) that entropy and particle current are closely related via $I_S = s^* I_N$, the new model should fulfill this relation as well. We make the Ansatz

$$\Xi_s^a = \frac{\sigma I_{exc}}{T} \log\left[\cosh\left(\frac{\Delta\mu + s^*\Delta T}{\sigma}\right)\right]\,, \tag{10.18}$$

with the sharpness parameter σ, defining the sigmoid's step size. In analogy to the linear model, we find (see Sec. 10.4.3) that the minimal model which describes our observation is a sum of nonlinear advective and linear diffusive modes $\Xi = \Xi_s^a + \Xi_n^d$. This dissipation potential then generates the currents

$$\begin{aligned} I_N &= I_{exc} \tanh\left(\frac{\Delta\mu + \alpha_c \Delta T}{\sigma}\right), \\ I_S &= \alpha_c I_N + G_T \Delta T / T \,. \end{aligned} \tag{10.19}$$

This model fulfills Onsager's reciprocal relations as well as the previously stated requirements on a dissipation potential, thus imposing that the transport process is irreversible which in turn implies that α_c has to appear in both I_N and I_S.

Notably, the phenomenological model has two different modes of entropy transport. The advective mode is characterized by entropy transport via net particle transport, i.e. $I_S^a = \alpha_c I_N$. The diffusive mode transports entropy without net particle transport $I_S^d = G_T \Delta T / T$, i.e. Fourier's law. In previous works [87] it was already found that in the unitary Fermi gas at higher temperatures the two modes have quite distinct timescales. In the Fermi liquid regime the thermal and particle conductance are directly proportional due to the Wiedemann-Franz law, where the universal value relating the conductance's is the Lorenz number $L = G_T / TG = \pi^2 k_B^2 / 3$.

10.4.2 *Coefficients of the Phenomenological Model*

The previously derived phenomenological model has four transport coefficients, the excess current I_{exc}, the Seebeck coefficient α_c, the thermal conductance G_T and the step size σ, the values of which is defined by the underlying microscopic processes of the system. Implying the necessity to understand their effects on the evolution of the system in the state space of our system $\Delta S(t)$, $\Delta N(t)$. We solve the coupled differential equations obtained from Eq. 10.19 by inserting $I_N = -(1/2)\, d\Delta N / dt$ and $I_S = -(1/2)\, d\Delta S / dt$ and solving the resulting initial value problem. In order to express the biases in terms of the state-space variables we have used the reservoir response given by

$$\begin{pmatrix} \Delta\mu(t) \\ \Delta T(t) \end{pmatrix} = \frac{1}{\kappa \ell_r} \begin{pmatrix} \ell_r + \alpha_r^2 & -\alpha_r \\ -\alpha_r & 1 \end{pmatrix} \begin{pmatrix} \Delta N(t) \\ \Delta S(t) \end{pmatrix}, \tag{10.20}$$

with the dilatation coefficient $\alpha_r = -(\partial\mu/\partial T)_N$, the compressibility $\kappa = 1/4(\partial N/\partial\mu)_T$ and the reservoir Lorenz number $\ell_r = C_N / \bar{T}\kappa$.

Advective Response

In order to illustrate the behavior of the model we can analytically integrate Eq. 10.19 in the limit of no diffusive response $G_T \to 0$

$$\begin{aligned} I_N &= I_{exc} \tanh\left(\frac{\Delta\mu + \alpha_c \Delta T}{\sigma}\right), \\ I_S &= \alpha_c I_N \,. \end{aligned} \tag{10.21}$$

After integration we arrive at the solution of the differential equation

$$\begin{aligned} \Delta N(t) &= \frac{\kappa \ell_r \sigma \sinh^{-1}\left(\exp\left\{\frac{(\alpha^2 + l)(C_2 - 2 I_{exc} t)}{\kappa \ell_r \sigma}\right\}\right) - \alpha C_1}{\alpha^2 + \ell_r}, \\ \Delta S(t) &= \alpha_c \Delta N(t) + C_1, \end{aligned} \tag{10.22}$$

where C_1 and C_2 are the integration constants and the effective Seebeck coefficient α was introduced, where $\alpha = \alpha_c - \alpha_r$. Solving the initial value problem using the initial conditions $\Delta N(0) = \Delta N_0$ and $\Delta S(0) = \Delta S_0$ we find

$$\begin{aligned} \Delta N(t) =& -\alpha(\Delta S_0 - \alpha_c \Delta N_0)/(\alpha^2 + \ell_r) \\ &+ \frac{\kappa \ell_r \sigma \sinh^{-1}\left(e^{-\frac{2I_{exc}\left(\alpha^2+\ell_r\right)}{\kappa \ell_r \sigma}t} \sinh\left(\frac{\alpha(\Delta S_0 - \alpha_r \Delta N_0) + \Delta N_0 \ell_r}{\kappa \ell_r \sigma} \right)\right)}{\alpha^2 + \ell_r}, \end{aligned} \tag{10.23}$$

$$\Delta S(t) = \alpha_c \Delta N(t) + (\Delta S_0 - \alpha_c \Delta N_0).$$

From this functional form of the imbalances we can calculate the initial thermoelectric response of the system in the limit of an initially pure entropy imbalance (equivalently pure temperature imbalance) $\Delta S_0 \neq 0$, $\Delta N_0 = 0$

$$I_N(0) = -(1/2)\left.\frac{d\Delta N(t)}{dt}\right|_{t\to 0} = I_{exc} \tanh\left(\frac{\alpha \Delta S_0}{\kappa \ell_r \sigma}\right), \tag{10.24}$$

$$I_S(0) = -(1/2)\left.\frac{d\Delta S(t)}{dt}\right|_{t\to 0} = \alpha_c I_N(0).$$

Since the hyperbolic tangent is an odd function the direction of the response is determined by the sign of α and ΔS_0, similarly to the linear model [71]. In addition, we find that the excess current I_{exc} and the initial current $I_N(0)$ are closely related, and the latter is a good initial condition for a fit of the former.

Moreover, we can determine the peak response of the system in the limit $G_T = 0$ by taking the limit of infinite time

$$\Delta N(t \to \infty) = -\frac{\alpha(\Delta S_0 - \alpha_c \Delta N_0)}{\ell_r + \alpha^2}, \tag{10.25}$$

$$\Delta S(t \to \infty) = -\frac{(\ell_r - \alpha \alpha_r)(\Delta S_0 - \alpha_c \Delta N_0)}{\ell_r + \alpha^2}.$$

This confirms that the magnitude of α determines the peak of the thermoelectric particle response as well as its sign for the purely advective response, when initially a pure entropy imbalance is prepared $\Delta S \neq 0$, $\Delta N_0 = 0$. We find that ℓ_r is the most important coefficient of the reservoir response determining the peak response of the system, the other begin α_r.

Figure 10.5(a)-(b) shows the evolution in the limit of a purely advective response with an imperfectly prepared initial state. The evolution of particle and entropy imbalance is calculated for different values of the Seebeck coefficient α_c. In the case of no thermoelectric response, i.e. $\alpha = 0$, (green line in Fig. 10.5(a)-(b)) the particle imbalance ΔN reaches equilibrium while the entropy imbalance ΔS "overshoots" its equilibrium value. The reason for this behavior is an imperfectly prepared initial state, with an initial particle and temperature imbalance. Since there is no diffusive relaxation and the thermoelectric response is minimal, the advective mode $(\Delta\mu + \alpha_c \Delta T)$ relaxes, but the entropy imbalance is still non-zero due to a remaining temperature and chemical potential bias. Experimentally we observe this behavior in Fig. 10.3(b) where the final entropy imbalance is slightly negative, indicating a suppressed thermal conductance. In the second row of Fig. 10.5 the evolution with a diffusive mode and varying σ is shown. The linear diffusive mode can be quantified in terms of its characteristic timescale τ_T, which is given by

$$\tau_T = \frac{\ell_r \kappa}{2G_T/T}, \tag{10.26}$$

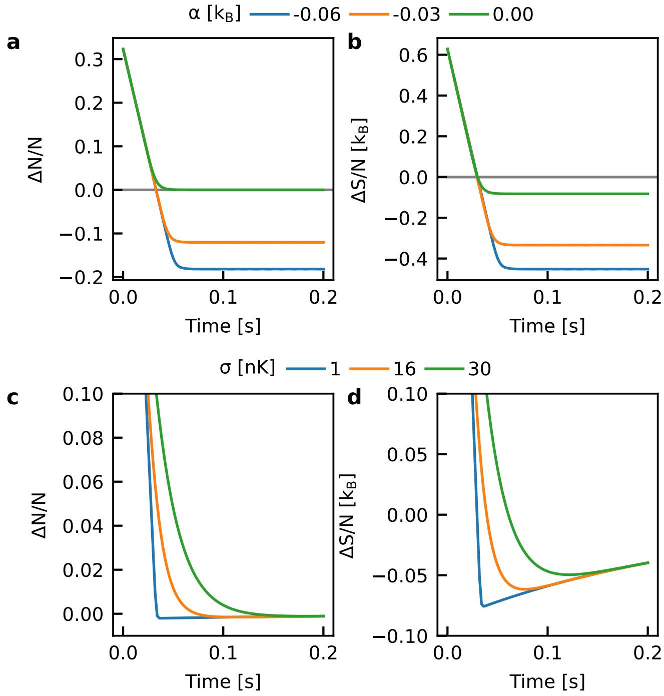

Figure 10.5: Advective evolution of the phenomenological model for different model coefficients. The panels display the relative particle and entropy imbalance as a function of time for different transport coefficients. The particle imbalance (a) and the entropy imbalance (b) are decreasing non-exponentially as a function of time indicating the non-linearity of the phenomenological model. The linear diffusive mode is suppressed $G_T \to 0$, while the nonlinear advective mode is quantified by $I_{exc} = 23\Delta/h$, where Δ is the superfluid gap, and $\sigma/k_B = 6\,\text{nK}$. When the Seebeck coefficient $\alpha_c = \alpha_r + \alpha$ is decreased both imbalances overshoot equilibrium, since less entropy per particle is transported. The effect of α on the initial slope of $\Delta S(t)$ is minute due to the change of α being small. (c)-(d) the diffusive mode is slow, but nonzero $\tau_T = 0.25\,\text{s}$, the thermoelectric response is small $\alpha \to 0$ while the excess current stays unchanged. Varying the non-linearity coefficient σ shows how increasing the coefficient brings the functional form closer to an exponential behavior indicative of linear response. The influence of σ on the slope of the particle response (see Fig. 10.5(c)) predicts some correlation between I_{exc} and σ for later fits.

in analogy to the particle conductance in the linear model, where $G = \kappa/2\tau_N$. Interestingly, when σ is increased the nonlinear advective response resembles a linearly responding mode

$$I_N|_{\sigma\to\infty} \approx I_{exc}(\Delta\mu + \alpha_c \Delta T)/\sigma\,. \tag{10.27}$$

In terms of microscopic interpretation of σ we can compare it to the superfluid quantum point contact [124] where a similar current-bias characteristic is observed. There the quantitative size of the non-linearity is interpreted as the number of allowed Andreev reflections m to overcome the superfluid gap, before the current is decreasing. Hence, the applied voltage eV (or equivalently chemical potential bias) is compared to Δ/m. In our system $\sigma = 6(2) \times 10^{-3}\Delta$ is quite small, meaning when comparing it to the superfluid gap Δ we find $m = \Delta/\sigma = 167(56)$. Thus, ~ 167 Andreev reflections would occur before the current I_N is appreciably reduced, though it is not clear whether this is the microscopic mechanism leading to our observations.

Diffusive and Advective Response

Whenever a linear diffusive mode is present in the model, i.e. $G_T \neq 0$, the system of differential equations could not be integrated analytically which means in the following the results will be from a numerical integration of Eq. 10.19, given a set of initial conditions ΔN_0, ΔS_0. Figure 10.6 shows the particle $\Delta N(t)$ and entropy $\Delta S(t)$ imbalance evolution for the second type of initial conditions explored in the experiment (see Fig. 10.4), where a pure entropy imbalance $\Delta N_0 = 0$, $\Delta S_0 \neq 0$ is prepared. The fixed transport coefficients of the model are equivalent to the ones in Fig. 10.5. When the excess current I_{exc} is varied (see Fig. 10.6(a)-(b)) the initial response is changing, similarly to Eq. 10.24, while in contrast to a purely advective response the competition between the two transport modes leads to a reduced peak response when the nonlinear advective mode becomes slower (I_{exc} decreases). Figure 10.6(c)-(d) display the purely nonlinear advective response for a varying thermoelectric response coefficient α. We have calculated the peak response value in Eq. 10.25 which showed that α determines the sign and the magnitude of the response which we find to be confirmed here by the numerical integration. Finally, the magnitude of the diffusive response is varied, displayed in Fig. 10.6(e)-(f), via its timescale τ_T (see Eq. 10.26) which quantifies the exponential relaxation of the mode. The exponential decay is shown in Fig. 10.6(e) (black dashed line), slightly offset from the numerically obtained evolution, indicating that the timescale τ_T used in the phenomenological model corresponds to the exponential timescale.

Competition between Diffusive and Advective Transport Modes

We have already discussed the competition between the two transport modes in our system in the distinct particle $\Delta N(t)$ and entropy $\Delta S(t)$ imbalance evolution. Here, we focus on the state space $\Delta S(t)$, $\Delta N(t)$ and the change in shape whenever the two modes are modified via one of the phenomenological model coefficients. Figure 10.7 shows the state-space evolution for varying excess current I_{exc} (a), effective Seebeck coefficient α (b), diffusive timescale τ_T (c) and nonlinear sharpness coefficient σ (d). For the different

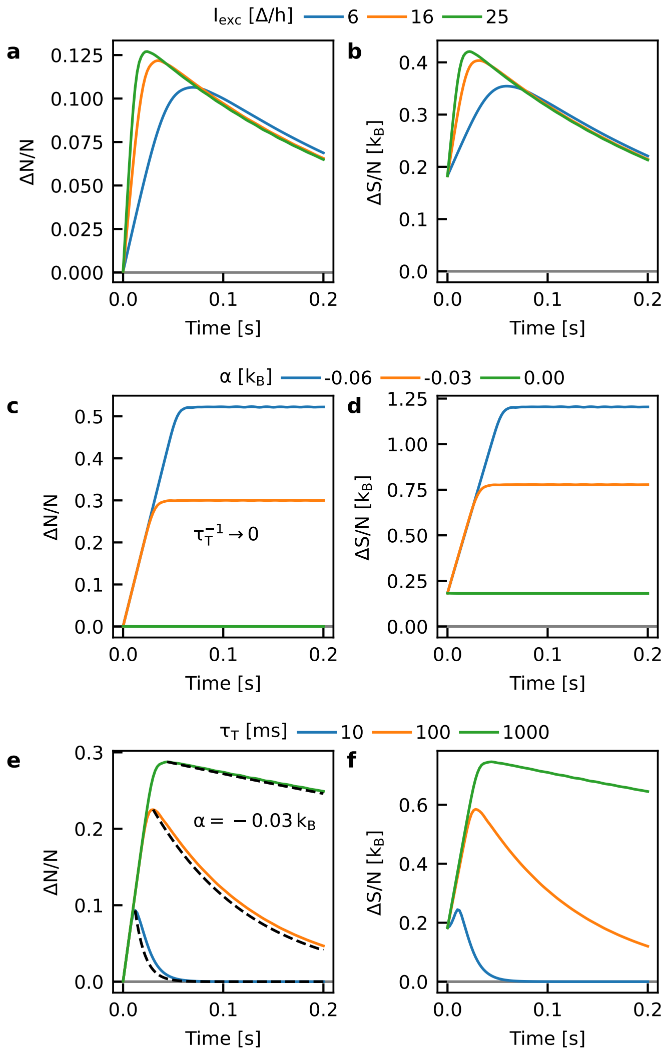

Figure 10.6: Diffusive and advective evolution of the phenomenological model. The left column of plots (a), (c), (e) display the particle imbalance evolution, while the right column (b), (d), (f) shows the entropy imbalance evolution. (a)-(b) display the systems” response for different values of the excess current I_{exc}. For decreasing excess current the initial response is becoming slower, the non-linearity gets less pronounced and the peak response decreases. The latter two effects appear due to the competition between the nonlinear advective and the linear diffusive response. The initial slope of the entropy relaxation hardly varies since the change of α is small. (c)-(d) The thermoelectric response coefficient α is varied for a purely advective evolution. There is no response for $\alpha = 0$ while increasing α leads to a larger peak response. In addition, the sign of α determines the direction of the response, thus confirming our findings from Eq. 10.24 and Eq. 10.25. (e)-(f) Effect of the linear diffusive mode on the transport process. The faster diffusive response leads to a suppression of the peak response and is followed by an exponential relaxation (black dashed line in (e)) of both imbalances. Both the α and G_T have little influence on the initial particle response.

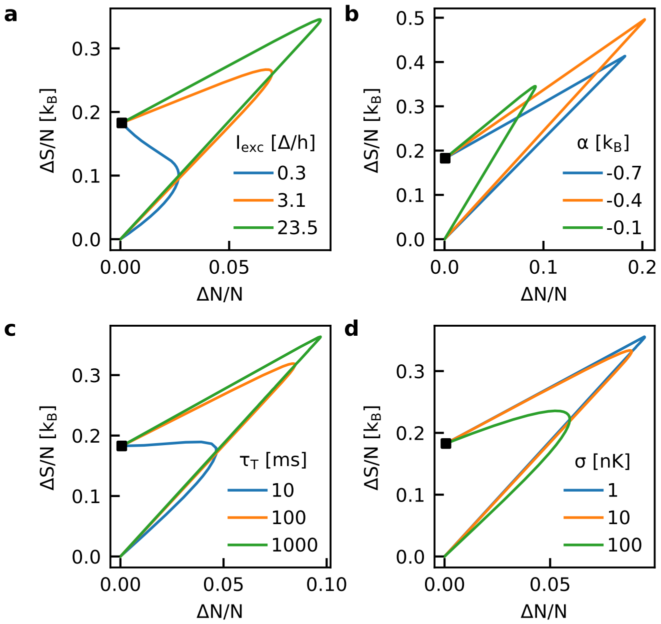

Figure 10.7: Competition between advective and diffusive modes in the state-space $\Delta S(t)$, $\Delta N(t)$. In state space the first slope up to the turning point quantifies the advective mode, while the second slope gives the diffusive mode. (a) Evolution in state-space for different values of the excess current I_{exc}. Decreasing I_{exc} changes the advective mode slope while the diffusive mode stays almost unchanged, up to the limit where the excess current is small (blue line). The thermoelectric response coefficient α (b) is varied which modifies both the first slope and the second slope, indicating the coupling of advective and diffusive response responsible for the relaxation of both particle and entropy imbalance. (c) Effect of the diffusive timescale τ_T on the state-space. The initial slope is decreased for a faster diffusive response due to the stronger competition between the modes, while the second slope stays unchanged. (d) The nonlinear sharpness coefficient has an effect similar to τ_T on the system. We find that making the advective mode less nonlinear, by increasing σ, effectively reduces its importance compared to the diffusive mode.

panels the following coefficients were chosen; $I_{exc} = 23.5\,\Delta/h$, $\alpha = -0.1\,k_B$, $\tau_T = 0.25\,s$ and $\sigma/k_B = 5\,nK$. We can calculate the ratios of imbalances via

$$\frac{I_S}{I_N} = \frac{d\Delta S(t)}{d\Delta N(t)} = \alpha_c + \frac{G_T \Delta T/T}{I_{exc}\tanh\left((\Delta\mu + \alpha_c \Delta T)/\sigma\right)}. \tag{10.28}$$

We find that the evolution in state-space is determined by the transported entropy per particle α_c and by the ratio between timescales of the diffusive and advective mode. The excess current I_{exc} is varied in Fig. 10.7(a), decreasing it leads to the diffusive evolution becoming more dominant and thus the equilibrium is approached on a more direct path (blue line in (a)). In Fig. 10.7(b) α is varied by changing α_c, thus affecting the initial as well as the final slope of the evolution in state-space. Importantly, α_c affects the competition between advective and diffusive mode, since diffusion itself cannot relax the particle imbalance but the diffusive relaxation of the temperature bias ΔT is accompanied by an advective response, thus relaxing ΔN. Reducing the timescale of diffusion τ_T (see Fig. 10.7(c)) makes the diffusion faster and thus again leads to a path in state-space which is more direct and less pointed indicating a seemingly more linear response. This can also be seen when the nonlinear sharpness coefficient σ is increased (see Fig. 10.7(d)) which reduces the overall scale of the advective response (the argument of the hyperbolic tangent), hence leading to a more rounded and direct path in state-space. Notably, we found that three of the model coefficients I_{exc}, τ_T and σ have a similar influence on the evolution thus already indicating the challenges of fitting this model to our data.

Entropy Response

Up to now only the evolution of the imbalances was discussed. Another important feature of the model is its dissipative and therefore irreversible nature implying the increase of entropy in order to reach equilibrium. The entropy production rate can be directly calculated from the particle and entropy current via

$$\frac{dS}{dt} = \frac{I_N \Delta\mu + I_S \Delta T}{T}. \tag{10.29}$$

This entropy production rate $\dot{S}$ can be integrated given an initial value and the result can be compared to the measured entropy. We use this in our fit to improve the estimation of the reservoir response coefficients.

10.4.3 Fitting Method

The complete phenomenological model is defined by the sum of the linear and nonlinear dissipation potentials $\Xi = \Xi_s + \Xi_n$ where Ξ_s is the superfluid, nonlinear transport model and Ξ_n is the normal, linear transport model.

Given the dissipation potentials in Eq. 10.18 and Eq. 10.16 as well as the equations of motion for the imbalances in Eq. 10.2 we find

$$\frac{d\Delta N(t)}{dt} = -2\left\{ I_{\mathrm{exc}} \tanh\left[\frac{\Delta\mu(t)+\alpha_c \Delta T(t)}{\sigma}\right] + G[\Delta\mu(t)+\alpha_c\Delta T(t)]\right\}, \tag{10.30}$$

$$\frac{d\Delta S(t)}{dt} = -2\{\alpha_c I_N[\Delta\mu(t),\Delta T(t)] + G_T \Delta T(t)/T\},$$

$$\begin{pmatrix}\Delta\mu(t)\\ \Delta T(t)\end{pmatrix} = \frac{1}{\kappa\ell_r}\begin{pmatrix}\ell_r+\alpha_r^2 & -\alpha_r\\ -\alpha_r & 1\end{pmatrix}\begin{pmatrix}\Delta N(t)\\ \Delta S(t)\end{pmatrix}.$$

The transport coefficients of the model are the linear particle conductance G, the transported entropy per particle α_c, the excess current I_{exc}, the linear thermal conductance G_T and the nonlinear sharpness σ. The reservoir response is quantified by the compressibility κ, the dilatation coefficient α_r and the reservoir Lorenz number ℓ_r.

Entropy Production

In order to integrate the entropy production rate $\dot{S}$ we calculate the total amount of entropy produced during the evolution which, subtracted from the final entropy, gives the initial value of the integration. We have previously seen that the entropy produced does not depend on the underlying evolution Eq. 10.12, which we can use to calculate δS. Given the linearized reservoir response and the relation between energy, particle and entropy imbalance $\Delta U \approx \mu\Delta N + T\Delta S$ we find

$$\delta S \approx \frac{\Delta N_0^2}{4T\kappa} + \frac{(\Delta S_0 - \alpha_r \Delta N_0)^2}{4T\ell_r\kappa}. \tag{10.31}$$

Subtracting $\delta S(t)$ from the equilibrium value of S we find

$$S(t) = S_{\mathrm{eq}} - \frac{\Delta N^2(t)}{4T\kappa} + \frac{[\Delta S(t) - \alpha_r\Delta N(t)]^2}{4T\ell_r\kappa}, \tag{10.32}$$

where $S_{eq}(\mu, T)$ is the equilibrium entropy.

Fit Procedure

The phenomenological model is fitted using a simultaneous least-squares fit of the relative particle imbalances $\Delta N_i/N_i$, the relative entropy imbalance $\Delta S_i/N_i k_B$ and the total entropy per particle $S_i/N_i k_B$ at different points in time t_i. The chi-squared statistic χ^2 to be minimized is given by

$$\begin{aligned}\chi^2 = \sum_i &\left(\frac{\Delta N_i/N_i - \Delta N(t_i)/N}{\sigma_{\Delta N/N}}\right)^2 \\ &+ \left(\frac{\Delta S_i/N_i k_B - \Delta S(t_i)/N k_B}{\sigma_{\Delta S/N k_B}}\right)^2 \\ &+ \left(\frac{S_i/N_i k_B - S(t_i)/N k_B}{\sigma_{S/N k_B}}\right)^2.\end{aligned} \tag{10.33}$$

The stability of the fit is improved by using the average uncertainty of the respective dataset as the weight of individual points $\sigma_x = \sum_i \sigma_{x,i}/n_{\mathrm{points}}$,

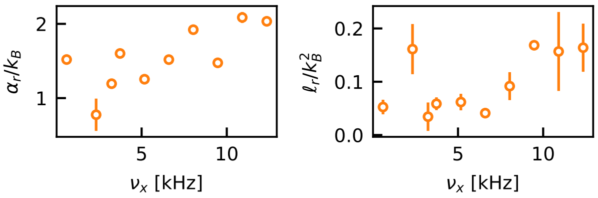

Figure 10.8: Fitted reservoir response coefficients for each configuration of the second experiment.

where $x = \Delta N/N$, $\Delta S/Nk_B$, S/Nk_B. This means that less weight is put on individual data points which can have underestimated uncertainties since the number of repetitions $3-5$ is restricted by the total time an experiment takes. The normalization by the total atom number, i.e. the usage of relative imbalances, improves our overall uncertainty since it reduces common-mode fluctuations due to atom number variations.

For all fits we neglect any linear particle conductance $G = 0$ as we have found that allowing G to vary underconstrains the fit, resulting in correlations with I_{exc}/σ. Another approach where G is estimated from the calculated number of modes $G = n_m/h$ increases χ^2 by $\sim 20\%$. In addition, the compressibility κ is fixed to its value during transport $\kappa = \kappa^{tr}(\mu^{tr}, T^{tr})$ calculated from the equation of state in the transport trap geometry.

For the fit of the first experiment (see Fig. 10.3) we fit I_{exc}, σ, α_c and ℓ_r. For the second experiment, (see Fig. 10.4) σ, α_c, $\Delta N(0)$, $\Delta S(0)$, G_T, α_r and ℓ_r are fitted, while I_{exc} is fixed to the initial current $I_N(0)$ (see Eq. 10.24). The initial current was obtained from a linear fit to the particle imbalance within the window $\Delta N/N \leqslant 0.07$. This method reduces correlation between fit parameters and produces reduced chi-squared $\chi^2_{red} \approx 1$ which indicates a good fit.

Fig. 10.3(b) and Fig. 10.4(b) show that the fitted entropy production underestimates the measured values. Fitting the final entropy value S_{eq} instead of calculating it from the average μ and T is increasing the final entropy by less than 2% while not affecting the other fit parameters.

Fit Results – Reservoir Response

Figure 10.8 shows the fitted values of the reservoir response coefficients used to fit the data in the second experiment. The first row of panels shows the bare values of α_r and ℓ_r, while the second row shows the fitted values relative to the values calculated from the equation of state. We find that α_r is fairly close to its value in the transport trap, while the fitted reservoir Lorenz number ℓ_r is much smaller than the calculated value ℓ_r^{tr}. It's important to note that the reason these reservoir response coefficients have to be fitted is the magnitude of the response in the second experiment. From previous calculations we know that the maximal advective response is given by $\Delta N_{max} = -\alpha\Delta S_0/(\ell_r + \alpha^2)$, in the case of a pure initial entropy imbalance. Since the transported entropy per particle is only slightly smaller than the dilatation coefficient, this means that ℓ_r had to be small to describe our data. We find that fitting these parameters has little effect on the transport coefficient I_{exc}, while α_c is correlated to α_r. In addition, the overall form of the model, i.e. the nonlinear response or irreversible nature, is not affected by the fit of the reservoir response which we have confirmed by the linear fits of $I_S = s^* I_N$ for the first experiment. Figure 10.9 shows a comparison

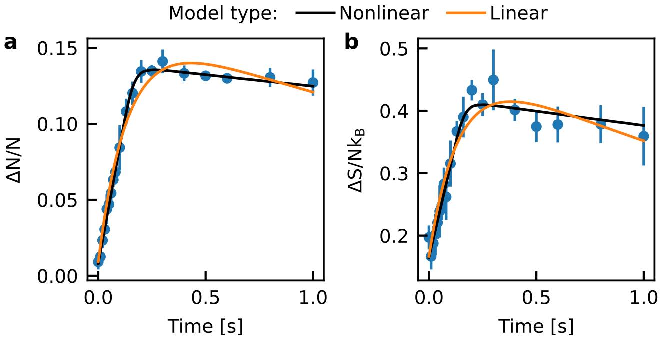

Figure 10.9: Comparison of the phenomenological nonlinear model with a linear model. The linear model is given by a biexponential function (orange line) and is fitted to the dataset with advective and diffusive response at the strongest confinement $\nu_x = 12.3\,\mathrm{kHz}$. The evolution given by the nonlinear phenomenological model (black line) is equivalent to the one shown in Fig. 10.4.

of a fit with the phenomenological model and a biexponential linear model previously used in [69, 87].

There are several possible explanations of the deviations between the measured and fitted reservoir response coefficients. The transport geometry is non-trivial, meaning there are transitions from normal to superfluid, changes of dimensionality 1D-2D and 2D-3D as well as possible series resistances. These interfaces can lead to thermodynamically distinct micro reservoirs within our overall system thus implying a local thermodynamic response which modifies the overall transport process.

Bootstrapping

Figure 10.10 displays a lower triangular matrix of plot panels where the circles correspond to the fitted values of the respective transport coefficient indicated in the rows and columns of the matrix where the fit parameters were obtained from repeated fitting of resampled data points of the second experiment with strong confinement $\nu_x = 10.9\,\mathrm{kHz}$. This so-called bootstrapping allows to generate the probability distribution of the fit parameters (histograms on diagonal of Fig. 10.10) and to obtain the correlations between fit parameters (scatter plots on lower triangle of Fig. 10.10). The fitted parameters in the bootstrapping process were the excess current I_{exc}, the dilatation coefficient $\alpha_{rs} = \alpha_r/\alpha_r^{tr}$, the nonlinear sharpness σ, the reservoir Lorenz number $\ell_{rs} = \ell_r/\ell_r^{tr}$, the thermoelectric response coefficient α and the diffusive timescale τ_T. For these fits α_{rs}, ℓ_{rs} and σ were varied globally for all datasets, while all available datasets were fitted simultaneously. The remaining coefficients were varied for each dataset individually. For 100 repetitions we find that all parameters are close to normally distributed, where the main deviations stem from the correlations between certain parameters. Firstly, the excess current I_{exc} is correlated with the sharpness coefficient σ which is expected from the functional form of the model where an increasing σ leads to a slower response (see Fig. 10.5(c) and Fig. 10.7(d)) due to the slope of the tanh changing. Secondly, the reservoir Lorenz number ℓ_r is correlated with the transported entropy per particle α_c which we can understand from Eq. 10.25 which implies that in order to match the maximal response of the system either $|\alpha|$ can be increased or ℓ_r can be reduced. All other sets of fitted coefficients of the phenomenological model are un-

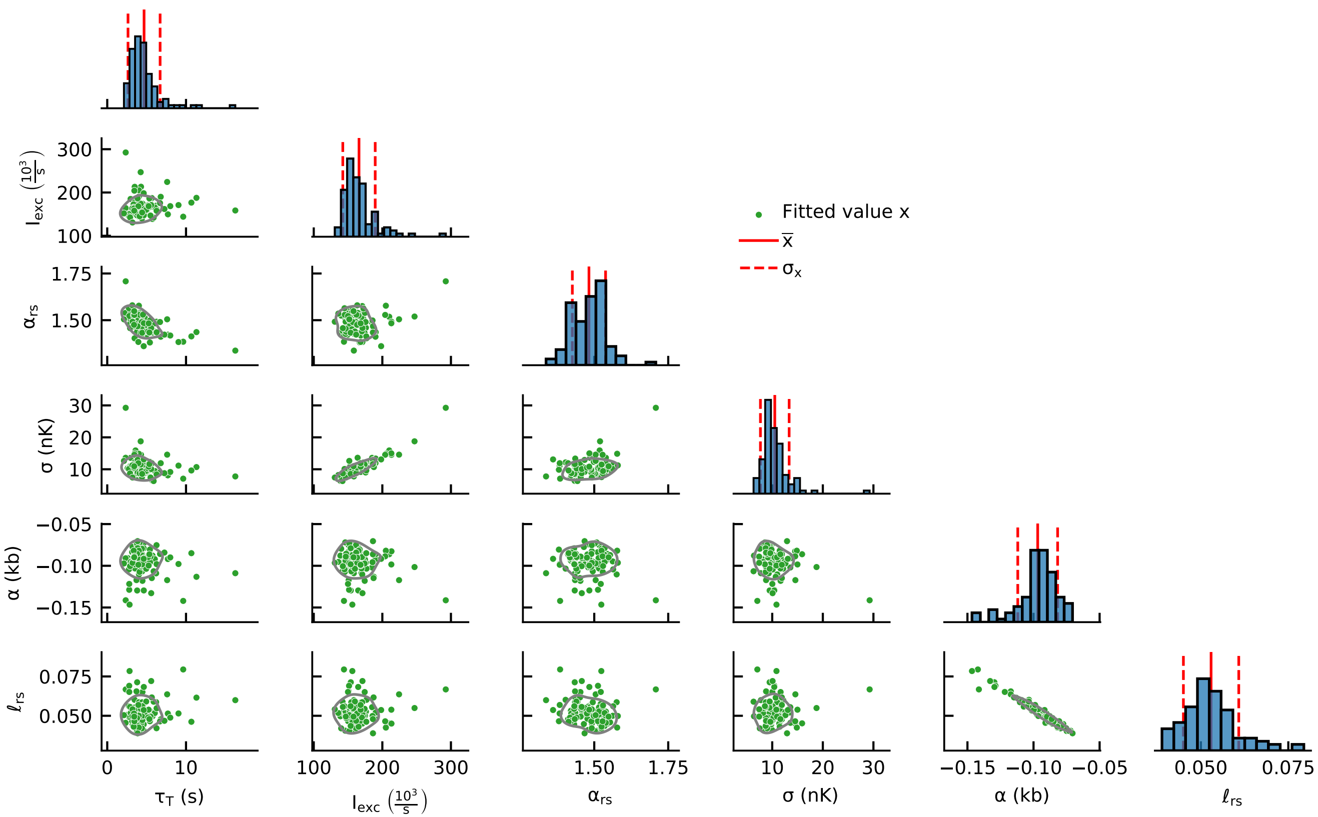

Figure 10.10: Bootstrapped fit parameters of the phenomenological model. For the displayed matrix of panels our datasets were resampled and subsequently fitted with 100 repetitions. The labels of the axis are indicated on the left and bottom of the matrix. The lower triangle of panels shows the fitted values (green circles) including an isoprobability distribution (gray line indicates 1σ interval). The diagonal shows the histogram of each individual fit parameter including its mean value (red line) and standard deviation (red dashed line).

correlated. In addition, we find that the fit is stable, i.e. all parameters have reasonable uncertainties, probability distributions and there are few outliers.

Paths in State Space

We have already found that the path of the evolution in state space depends on the competition between advective and diffusive response (see Fig. 10.7 and Eq. 10.28). This competition or coupling can be quantified using the slopes of the paths in state space. Inserting the reservoir response into Eq. 10.28 we find the path Π

$$\Pi = \frac{d\Delta S}{d\Delta N} = \alpha_c + \frac{2G_T(\alpha_r \Delta N - \Delta S)}{T\kappa\ell_r \, d\Delta N/dt}, \tag{10.34}$$

where the particle current I_N has been replaced by $I_N = -(1/2)\, d\Delta N/dt$. We observe (see Fig. 10.3(d) and Fig. 10.4(d)) that the path becomes linear in the limits where either of the entropy transport modes dominates, i.e. away from the turning point, such that $\Delta S(t) \approx \Pi(\Delta N(t) - \Delta N_0)$, where M is the slope in state space. Inserting this into the previous equation gives

$$M \approx \frac{2G_T \alpha_r \Delta N + T\kappa\ell_r \alpha_c \, d\Delta N/dt}{2G_T(\Delta N - \Delta N_0) + T\kappa\ell_r \, d\Delta N/dt}\,. \tag{10.35}$$

Firstly, when the advective mode is dominating transport the particle current is large meaning $d\Delta N/dt$ dominates in the previous equation which simplifies to

$$M_a = \alpha_c\,, \tag{10.36}$$

which is the slope we observe in Fig. 10.3(d). Secondly, whenever the advective mode has relaxed $(\Delta\mu + \alpha_c \Delta T) \to 0$ the diffusive mode will dominate the transport away from the turning point. In this limit we have already seen that the system is relaxing exponentially (see Fig. 10.6(e))

$$d\Delta N/dt = -\Delta N/\tau_T \tag{10.37}$$

due to the diffusion accompanying linear response of the nonlinear advective mode

$$I_{exc} \tanh\left(\frac{\Delta\mu + \alpha_c \Delta T}{\sigma}\right)\Bigg|_{\Delta\mu \to -\alpha_c \Delta T} = \frac{I_{exc}}{\sigma}(\Delta\mu + \alpha_c \Delta T) = \tilde{G}(\Delta\mu + \alpha_c \Delta T)\,. \tag{10.38}$$

Moreover, the system reaches equilibrium in this limit such that the formula for the slope can be simplified to $\Delta S(t) \approx M\Delta N(t)$, since $\Delta N_0 = \Delta N_{eq} = 0$. Inserting this into Eq. 10.35 we find the linear diffusive slope M_d

$$M_d \approx \frac{2G_T\tau_T\alpha_r - T\kappa\ell_r\alpha_c}{2G_T\tau_T - T\kappa\ell_r} \approx \alpha_r + \frac{\ell_r}{\alpha_r - \alpha_c}\left[1 - \frac{G_T/T\tilde{G}}{\ell_r + (\alpha_r - \alpha_c)^2}\right]. \tag{10.39}$$

Both M_a and M_d as well as τ_T can be extracted well from our data using linear as well as exponential fits in the right limits.

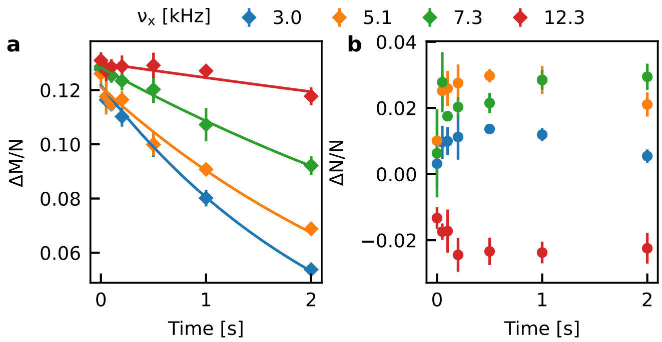

Figure 10.11: Spin transport in the unitary Fermi gas. (a) The relative magnetization imbalance is displayed as a function of time, indicating a slow, exponential relaxation. Decreasing the transversal confinement ν_x makes the spin-transport faster. (b) The relative particle imbalance indicates a bi-exponential behavior with a non-equilibrium steady-state in the quasi-1D limit (red circles). The solid line is a fit with an exponential decay function. Error-bars are standard deviations of the mean of 3 repetitions.

10.4.4 Spin Conductance

In superfluid transport, excitations are responsible for resistive behavior, one kind of excitations is a pair breaking process which creates a spin excitation. Pair breaking is the only possible excitation leading to a spin conductance in the superfluid transport experiment, since pairing leads to perfect spin-drag [67]. Thermal diffusion has a similar origin, where quasi particles can transport heat without net particle current, while the superfluid condensate does not carry any entropy. Importantly, the superfluid has collective excitations [23] which are gapless – in case of the Goldstone mode – and can carry entropy diffusively. It is thus interesting to compare the linear thermal conductance G_T to the linear spin conductance G_σ since they are somewhat related but due to the collective excitations not present in the spin-sector also distinct.

Figure 10.11(a) shows the relaxation of the magnetization imbalance $\Delta M = M_L - M_R$ for different confinement frequencies ν_x in a transport geometry equivalent to the ones used for the data in Fig. 10.3 and Fig. 10.4. The relaxation is exponential indicating a linear response $d\Delta M/dt = -\Delta M/\tau_\sigma$, with the timescale τ_σ. This timescale is extracted using an exponential fit (solid lines in Fig. 10.11). Similarly to the particle conductance G the spin conductance is related to its characteristic timescale via

$$G_\sigma = \frac{\chi}{4\tau_\sigma}, \tag{10.40}$$

where $\chi = \partial(N_\uparrow - N_\downarrow)/\partial(\mu_\uparrow - \mu_\downarrow)$ is the spin-susceptibility of the unitary Fermi gas, measured previously [27].

Interestingly, the evolution in state space $\Delta M(t)$, $\Delta N(t)$ (see Fig. 10.11(b)) follows a trend, similar to the evolution in previous experiments [69, 87] where the thermoelectric effect was studied in ΔN, ΔT state space, as well as in this work, where in the respective state space the evolution would look similarly. In the 1D limit of strong confinement ν_x (red points in Fig. 10.11(b)) we find that the initial magnetization imbalance ΔM_0 leads to a nonlinear-like increase of the particle imbalance, followed again, by a non-equilibrium steady-state. In the open channel (blue points in Fig. 10.11(b)) the particle imbalance first increases exponentially and subsequently relaxes

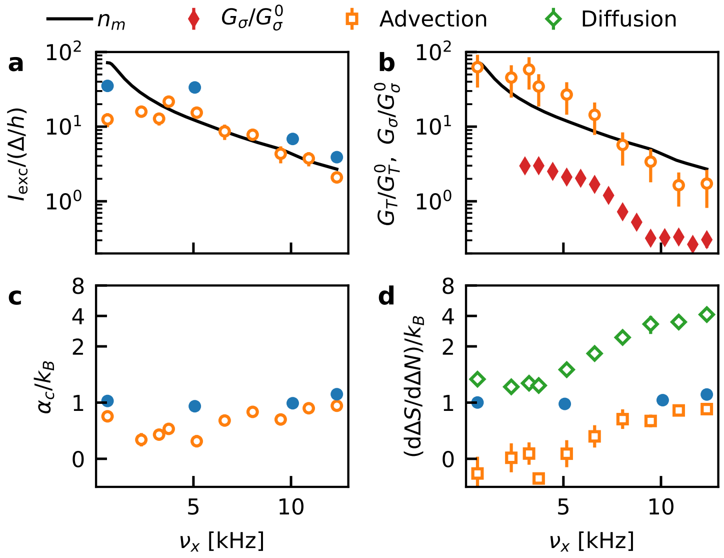

Figure 10.12: Transport coefficients of the linear and nonlinear transport modes across the 1D-2D crossover extracted from fits with the phenomenological model. The coefficients extracted from the first (second) experiment are plotted with filled (open) markers as function of transversal confinement. (a) The excess current normalized by the unitary superfluid gap and the number of modes n_m. (b) Normalized thermal conductance G_T/G^0_T and spin conductance G_σ/G^0_σ. The normalization factors are given by the non-interacting, single mode values $G^0_T = \pi^2 k_B^2 T/3h$, $G^0_\sigma = 1/h$. (c) Fitted Seebeck coefficient – transported entropy per particle – for both experiments. (d) Linear slopes of the paths in state-space for the limits of advective (□) and diffusive (◇) evolution.

exponentially again following a biexponential behavior also seen in previous works in the ΔN, ΔT state space [87].

10.5 COEFFICIENTS OF THE PHENOMENOLOGICAL MODEL

In this section the transport coefficients of the previously introduced fits with the phenomenological model are discussed and their implications for the microscopic processes in our system are described. Figure 10.12(a)-(c) displays the results of the fits with the phenomenological model as functions of the transversal confinement ν_x, while in Fig. 10.12(d) shows the fits of the slopes of the paths in state space as a function of ν_x.

Nonlinear Sharpness Coefficient σ

Regarding the sharpness of the nonlinear advective response we fit $\sigma = 8(1) \times 10^{-3}\Delta$ which indicates the significantly nonlinear nature of the advective response since it is far below the transport energy scales in our system. As previously introduced (see Ch. 4), the nearest interpretation of Δ/σ is the number of Andreev reflections processes within a superconducting SNS junction or superconducting QPC [122, 124, 250], i.e. the number of pairs transported during an Andreev process. The small uncertainty in σ and the possibility of fitting it globally for all datasets (see Fig. 10.10), shows that within the range of confinements we have explored experimentally, i.e. $\nu_x = 0.6\,\text{kHz}$ to $\nu_x = 12.4\,\text{kHz}$, the non-linearity of the advective mode is persistent according to the phenomenological model. This observation indicates the existence of a weak link type interface throughout the explored transport geometry.

Excess Current I_{exc}

Figure 10.12(a) shows the fitted value of the excess current I_{exc} which characterizes the nonlinear advective response, though it was originally introduced to characterize superconducting tunnel junctions [124, 126]. The excess current is normalized by Δ/h – the unitary superfluid gap in the channel region in equilibrium – and closely follows the number of transversal channel modes n_m (black line in Fig. 10.12(a)) which increases with decreasing ν_x. For weak confinements in the quasi-2D regime I_{exc} is saturating to a value below $n_m\Delta/h$, indicating the existence of additional series resistances in our system. The values of I_{exc} extracted from the first experiment in Fig. 10.3 are indicated as blue circles while the values from the second experiment in Fig. 10.4 are indicated as open orange circles. The systematic difference between the excess current extracted from either experiment is due to the fitting method, where for the second experiment the initial current $I_N(0)$ was used as a fixed coefficient of the phenomenological model. This initial current is a lower bound to the excess current (see Eq. 10.24) and in this case is likely suppressed compared to the real value of I_{exc} due to the linear diffusive mode (see Fig. 10.7(c)).

Thermal Conductance G_T *and Spin Conductance* G_σ

The linear diffusive mode is characterized by the thermal conductance G_T which is displayed as open orange circles in Fig. 10.12(b) normalized by its single mode non-interacting QPC value, i.e. $G_T^0 = \pi^2 k_B^2 T/3h$. For comparison, the spin conductance G_σ is shown in the same panel as red diamonds, similarly normalized by its single mode QPC value $G_\sigma^0 = 1/h$. The spin conductance is extracted from an experiment where a pure magnetization imbalance $\Delta M(0) \neq 0, \Delta N(0) = 0$ was prepared (see Sec. 10.4.4). We find that both the thermal and the spin conductance increase when the confinement is reduced below the quasi-1D limit $\nu_x \lesssim 7.8\,\mathrm{kHz}$ (see Fig. 10.1). In the quasi-1D limit the spin conductance G_σ is constant, around an order of magnitude below the value of a non-interacting QPC (black line in Fig. 10.12(b)). The thermal conductance, though following a similar trend, is consistently larger than G_σ and even approaches the non-interacting value in the 2D limit. In the low confinement limit both conductances saturate, again indicating additional series resistances discussed earlier. The difference between the two conductances is of particular interest since a tunneling of Goldstone modes [136] could contribute to the diffusive thermal conductance, thus reaching the non-interacting value. Notably, there are no gapless excitations in the spin sector, thus its transport cannot be enhanced by this kind of phonon tunneling. In the open channel less degenerate edge modes open (see Fig. 10.2(b)) which could allow quasi particles to traverse the channel thus enhancing both conductances. In the 1D limit the conductances are less distinct where the spin conductance is strongly suppressed below the non-interacting value, either due to the contacts [67] or the wire acting as filters with a large gap, thus preventing quasi particle excitations from entering the 1D channel. The thermal conductance is also suppressed below the non-interacting value, while the large error bar indicates a significant uncertainty, due to the difficulty for the fit to distinguish the advective and diffusive mode.

Advectively Transported Entropy per Particle α_c

Figure 10.12(c) shows the Seebeck coefficient α_c – or average advectively transported entropy per particle – which was extracted from the fits with the phenomenological model, from either the first (blue circles) or the second experiment (open orange circles). For comparison, the slope of the paths in state space is presented in Fig. 10.12(d), again extracted from the first (filled blue circles) and second (open symbols) experiment. We find that in the case of a purely nonlinear advective response the extracted parameters agree well, showing a remarkable insensitivity to the geometry of the system, in stark contrast to the previously discussed coefficients. In the case of a coupling between advective and diffusive response (open symbols) we find that α_c is again consistently above 0, the value one would expect for a supercurrent, but a trend with changing geometry is visible indicative of the difficulty for the fit to distinguish the two entropy transport modes. The trend of the advective mode slope (open green diamonds) and of the diffusive mode slope (open orange squares), illustrate the previously discussed competition, resembling the shape of an avoided crossing where the contribution of the respective mode is varied via the confinement ν_x. This hybridizing of the transport modes makes it inherently difficult to distinguish the diffusive fit coefficient G_T from the advective fit coefficient α_c, leading to a seemingly decreasing α_c for small ν_x. Notably, the seemingly exponential relaxation at small confinements in the first experiment (blue circle in Fig. 10.3(a)) is not indicative of a reduced non-linearity but can equally well be explained by an enhanced diffusive relaxation, given the enhancement of G_T obtained from the second experiment (open orange squares Fig. 10.12(b)).

10.6 ADVECTIVE TRANSPORT IN THE QUASI-3D REGIME - ENGINEERING α_c

In this section we like to put our current observations into context with our previous work where the transported entropy per particle α_c was varied [69]. We will mainly focus on the results in the strongly interacting regime, since an extensive discussion of the details is already provided in the thesis of S. Häusler [71]. Importantly, in we previously used the term advective entropy response which is the equivalent of the thermoelectric response in the state space ΔT, ΔN, where temperature can evolve via a net particle current, i.e. thermoelectrically, or without net particle current, i.e. diffusively.

Figure 10.13(a) shows the experimental configuration studied, where the 3D reservoirs are connected by a channel in the 2D-3D dimensional crossover ($k_B T/h\nu_z = 0.81$). Applying a variable – magnitude and sign – gate potential V_g in the channel allows us to tune the magnitude and sign of the thermoelectric response to an applied initial temperature imbalance $\Delta T_0 \neq 0$, $\Delta N_0 = 0$. In the non-interacting regime this change of sign can be understood from the change of particle-hole asymmetry, i.e. the energy dependent transmission, inside the channel when the gate potential is varied. In Fig. 10.13(b) the Fermi distribution on the hot (left panel) and cold (right panel) side of the channel as well as the mode structure $\Phi(E)$ (central

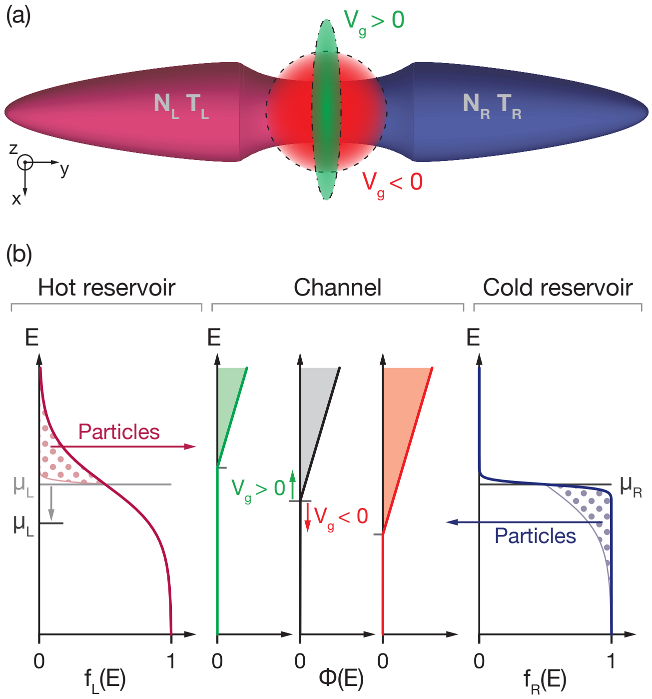

Figure 10.13: Concept and experimental setup. (a) Schematic view of a quasi-three-dimensional channel connected to a hot (red) and a cold (blue) reservoir of fermionic atoms. Their unequal temperatures T_L and T_R induce a net particle current that changes the initially equal atom numbers N_L and N_R over time. The thermoelectric response is tuned by a gate potential V_g inside the channel that is either attractive (red) or repulsive (green). (b) Roles of the reservoirs and channel in thermoelectric transport. The reservoirs inject particles into the channel according to their occupations described by the Fermi-Dirac distributions $f_L(E)$ and $f_R(E)$. As the hot (cold) side contains more particles at high (low) energies compared to the other side (dotted regions), two counter-propagating currents at different energies emerge (horizontal arrows). At equal atom numbers the chemical potential μ_L in the hot reservoir is lower than μ_R on the cold side introducing an asymmetry between them. A particle at energy E crosses the channel in one of the $\Phi(E)$ transverse modes. The energy dependence of their number (shaded regions) introduces an asymmetry in the channel. The gate potential energetically shifts the modes up ($V_g > 0$) or down ($V_g < 0$) allowing us to tune the response. The picture is valid for weak interactions as it also applies to Landau quasi-particles.

panel) of the channel are presented. Tuning the system from a heat engine to a heat pump, can be understood on this level from the shift in zero point energy E_0, where $\Phi(E > E_0) > 0$, shown in the central panel of Fig. 10.13(b). Firstly, when the zero-point energy is large (green line) only hot particle can be transmitted thus the entropy transported per particle is increased, α_c increases. Secondly, for a small zero-point energy (red line) both hot and cold particles can be transmitted through the channel, though the shift of overall chemical potential due to temperature $\alpha_r = -(\partial\mu/\partial T)|_N$ leads to a reservoir imposed imbalance in the opposite direction, i.e. low entropy particles are preferentially transported, such that α_c decreases.

In the following we will discuss the effects of interactions on this expected behavior in the non-interacting regime and the differences to our more recent measurements. For clarity, the previously discussed measurements will be called 1D-2D experiment while the measurements here are referred to as quasi-3D experiment.

10.6.1 Experimental Setup

The experiment is prepared in a balanced mixture of the lowest and second-lowest hyperfine state of fermionic ^{6}Li at a magnetic field of either $B = 528\,\mathrm{G}$, i.e. the non-interacting regime, or $B = 832\,\mathrm{G}$ which is the unitary regime. The originally cigar-shaped cloud is vertically confined at its center with a repulsive TEM_{01} beam propagating transversally. The resulting channel is a $w_y = 60.4\,\mu\mathrm{m}$ long region with a peak confinement of $\nu_z = 4.5\,\mathrm{kHz}$ ($k_B T/h\nu_z = 0.96(3)$) in its center. The transversal confinement in x-direction is given by the dipole trap and the gate beam with $\nu_x = 232(1)\,\mathrm{Hz}$. Evaporating into this geometry we end up with a total atom number of $N = 242(4) \times 10^3$, equilibrated between the two reservoirs $\Delta N_0 \approx 0$. The initial temperature bias is imposed by heating one of the reservoirs via amplitude modulation of an attractive beam inside the reservoirs. The wall beam, blocking the channel, is preventing equilibration before and after transport. The resulting temperature difference is on average $\Delta T = 90(7)\,\mathrm{nK}$ while the average temperature is $T = 174(2)\,\mathrm{nK}$. In order to tune the gate potential V_g either an attractive Gaussian beam or a repulsive elliptical beam is used (see Fig. 10.13(a)). The attractive gate has a waist of $w_{g,xy} = 33.9(1)\,\mu\mathrm{m}$, while the repulsive gate has a transversal waist of $w_{g,x} = 53.66(3)\,\mu\mathrm{m}$ and a waist of $w_{g,y} = 8.58(3)\,\mu\mathrm{m}$ in transport direction.

10.6.2 Measurements

Starting from the preparation of the initial state $\Delta T_0 \neq 0$, $\Delta N_0 = 0$ the transport channel is opened and the evolution of the imbalances is measured by repeated imaging of the cloud for different transport times. The imaging is done with the wall beam separating the clouds, such that the thermometry is performed on two half-harmonic reservoirs, see Sec. 2.2.

Thermoelectric Response in the Strongly Interacting Regime

Figure 10.13 shows the thermoelectric response of the strongly interacting Fermi gas in the quasi-3D geometry. The gate potential V_g is varied from strongly attractive $V_g = -1.06\,\mu\mathrm{K}$ to weakly repulsive $V_g = 0.37\,\mu\mathrm{K}$, resulting in a largely different thermoelectric response. In the weakly repulsive limit (red circles) the positive temperature imbalance $\Delta T = T_L - T_R$ leads to a positive initial particle current $I_N(0) = -(1/2)\,d\Delta N/dt|_0 > 0$ (see inset in Fig. 10.13) indicating that the particle current is from the hot to the cold reservoir. The absolute particle imbalance is increasing slowly due to the limited number of transport modes in this limit of large zero point energy. When decreasing the repulsive gate, the magnitude of thermoelectric response decreases, while the initial evolution becomes faster indicating a higher conductance. The turning point of the evolution is reached once the thermoelectric response has relaxed, which is followed by a diffusive relaxation of the remaining temperature imbalance. Similar to the particle conductance, determining the initial slope, increasing for smaller zero point energies, the thermal conductance G_T is also increasing as the repulsive gate becomes smaller. Even though the system does not reach equilibrium in the repulsive gate regime, the temperature imbalance is relaxing exponentially,

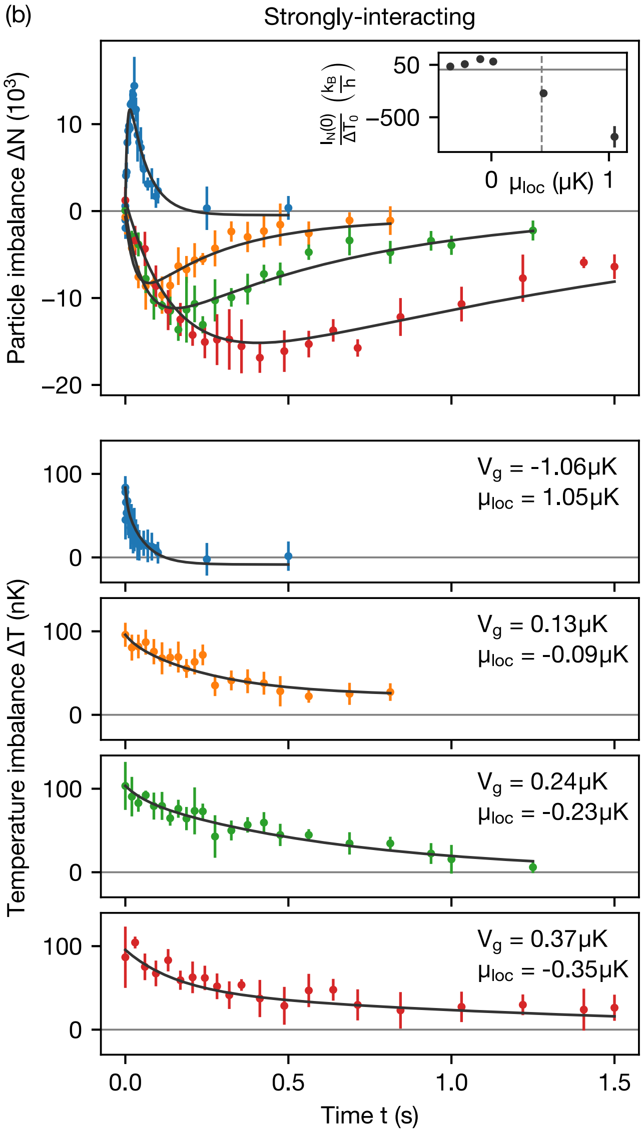

Figure 10.14: Tuning the thermoelectric response. Temporal evolution of the differences in atom number $\Delta N = N_L - N_R$ and temperature $\Delta T = T_L - T_R$ between the reservoirs of a strongly-interacting Fermi gas at different gate potentials V_g. Each data point represents a mean over ~ 5 repetitions and error bars show one standard deviation. Lines indicate fits with a phenomenological model involving the transport parameters conductance G, Seebeck coefficient α_c and Lorenz number L. For all estimations the conductance is fixed by a separate measurement (solid lines), except for the dashed line as it failed to converge otherwise. Insets: Initial particle current $I_N(0)$ normalized to the prepared temperature difference ΔT_0 versus local chemical potential μ_{loc} at the channel center. In the strongly-interacting regime the vertical dashed line shows the superfluid transition inside the channel while the reservoirs remain uncondensed.

indicating an overall linear response of the transport modes to the imposed biases. Finally, in the strongly attractive gate limit $V_g < 0$ (blue circles in Fig. 10.13) the particle response changes it sign $I_N(0) < 0$ which lets particles flow from the cold to the hot reservoir. Due to the increased number of modes the overall evolution is much faster, but still both the advective and the diffusive modes follow an exponential behavior, i.e. linear response.

Linear Phenomenological Model

The previously introduced linear model (Eq. 10.16) is used to describe the linear response of the system. From the model we can extract three transport coefficients, i.e. the conductance G, the Seebeck coefficient α_c and the Lorenz number L, which describe the evolution of the system. The linear model fulfills the Onsager reciprocal relations, hence imposing an irreversible evolution. The model in terms of entropy I_S and particle current I_N is given by

$$\begin{aligned} I_N &= G(\Delta\mu + \alpha_c \Delta T), \\ I_S &= \alpha_c I_N + G_T \Delta T/T. \end{aligned} \tag{10.41}$$

Given the equations of motion $I_N(t) = -(1/2)\, d\Delta N/dt$, $I_S(t) = -(1/2)\, d\Delta S/dt$ and the linearized reservoir response

$$\begin{pmatrix} \Delta\mu(t) \\ \Delta T(t) \end{pmatrix} = \frac{1}{\kappa \ell_r} \begin{pmatrix} \ell_r + \alpha_r^2 & -\alpha_r \\ -\alpha_r & 1 \end{pmatrix} \begin{pmatrix} \Delta N(t) \\ \Delta S(t) \end{pmatrix}, \tag{10.42}$$

we obtain the coupled differential equations for the particle and temperature imbalance evolution

$$\frac{d}{dt} \begin{pmatrix} \Delta N(t) \\ \Delta T(t) \end{pmatrix} = -\frac{2}{G\kappa} \begin{pmatrix} 1 & \kappa\alpha \\ \alpha/\ell_r\kappa & (L+\alpha^2)/\ell_r \end{pmatrix} \begin{pmatrix} \Delta N(t) \\ \Delta T(t) \end{pmatrix}, \tag{10.43}$$

with the thermoelectric response coefficient $\alpha = \alpha_c - \alpha_r$. In contrast to the full nonlinear phenomenological model these differential equations can be integrated analytically. Imposing the initial conditions $\Delta N(0) = \Delta N_0$, $\Delta T(0) = \Delta T_0$ we find [251] a biexponential function

$$\begin{aligned} \Delta N(t) &= \{e_+(t) + A e_-(t)\}\Delta N_0 + B e_-(t)\Delta T_0, \\ \Delta T(t) &= \{e_+(t) - A e_-(t)\}\Delta T_0 + C e_-(t)\Delta N_0, \end{aligned} \tag{10.44}$$

with $e_\pm(t) = (e^{-t/\tau_+} \pm e^{-t/\tau_-})/2$ and two exponential timescale $\tau_\pm$. The general coefficients A, B, C and the exponential timescales are functions of the transport coefficients and the reservoir response coefficients. The timescales are the determined by the overall timescale $\tau_0 = \kappa/2G$ scaled by the eigenvalues $\lambda_\pm$ of the transport matrix in Eq. 10.43, such that $\tau_\pm = \tau_0/\lambda_\pm$. The eigenvalues are found to be

$$\lambda_\pm = \frac{1}{2}\left(1 + \frac{L+\alpha^2}{l}\right) \pm \sqrt{\frac{1}{4}\left(1 + \frac{L+\alpha^2}{l}\right)^2 - \frac{L}{l}}. \tag{10.45}$$

The coefficients of the biexponential function in Eq. 10.44 are given by

$$A = \frac{1 - (L+\alpha^2)/l}{\lambda_+ - \lambda_-}, \tag{10.46}$$

$$B = \frac{2\kappa\alpha}{\lambda_+ - \lambda_-}, \tag{10.47}$$

$$C = \frac{2\alpha}{\kappa l(\lambda_+ - \lambda_-)}. \tag{10.48}$$

Fitting Method

The data presented in Fig. 10.13 and an equivalent dataset measured in the non-interacting regime are fitted using the proposed linear model, via the obtained biexponential function Eq. 10.44. The reservoir response coefficients α_r, ℓ_r and κ are calculated from the EoS of the unitary Fermi gas and fixed for the fit. In addition, the conductance G is fixed to a separately measured value, i.e. via pure particle transport. For the fit with the biexponential function, both the particle and temperature imbalance evolution are fitted at the same time via minimization of χ^2 given by

$$\chi^2 = \sum_i \left[\left(\frac{\Delta\tilde{N}(t_i) - \Delta\tilde{N}_i}{\sigma_N} \right)^2 + \left(\frac{\Delta\tilde{T}(t_i) - \Delta\tilde{T}_i}{\sigma_T} \right)^2 \right]. \tag{10.49}$$

The weighting of the residuals is done by the respective uncertainties σ_N and σ_T of the averaged points at each time t_i. The imbalances measured in the experiment $\Delta\tilde{N}_i$ and $\Delta\tilde{T}_i$ have offsets from equilibrium due to the imperfect preparation. The offset ΔN_{off} is either given by the relaxed, final values of the evolution, i.e. whenever the evolution has reached equilibrium, or if this is not the case by the initial value. The offset in temperature imbalance ΔT_{off} is fitted. The initial values ΔN_0 and ΔT_0 are fixed by the measured imbalances at $t_i = 0$. The remaining free, fit parameters are α, L and ΔT_{off}.

We compare the fit parameters from a least-squares minimization to the results obtained from a rank-order based method of minimization [252]. As the estimation of the parameters of an exponential model is generally challenging this comparison allows us to be confident in the least-squares method since the two approaches give comparable results. The fitted model is displayed in Fig. 10.13 (black lines) and shows that our fit works and that the model describes the data well.

10.6.3 Discussion and Comparison

Here we like to discuss the results of the fit, in particular the transported entropy per particle α_c and put it in context with our new measurements in the superfluid regime, see Fig. 10.12(c)-(d).

Table 10.1 contains the experimental parameters of the two different transport geometries and preparations. For the measurements in the first 1D-2D experiments, the reservoirs $q = \mu/k_B T = 2.9$ are above the critical degeneracy $q_c = 2.5$ and the contacts to the channel are deeply superfluid $T/T_F|_{loc} = 0.026$ in equilibrium. In the quasi-3D experiment [69] the reservoirs are less degenerate $q = 1.2$ and the contacts have a varying degeneracy, due to the change of V_g. For the strongest gate explored here the contacts are superfluid $T/T_F|loc = 0.06$ in equilibrium. The confinement in vertical direction is quite different, in the 1D-2D experiment the central region of the channel is always quasi-2D, while in the quasi-3D experiment the confinement ν_z is barely larger than the temperature $\nu_z/k_B T = 1.2$. The transversal confinement ν_x is varied in the 1D-2D experiment to study the 1D-2D crossover. In the quasi-3D experiment nu_x is constant and close to the smallest value of ν_x used for the 1D-2D experiments. Notably, the number of occupied transversal modes n_m is distinct in the two experiments. In the 1D-2D experiment the number of modes is always non-zero $n_m > 0$, even in the quasi-1D limit, while in the quasi-3D experiment there are no occupied modes (in the zero temperature limit) for the repulsive gates $V_g > 0.05\,\mu\text{K}$,

	Superfluid 1D-2D	**Strongly-interacting quasi-3D**
T	$90\,\mathrm{nK}$	$174\,\mathrm{nK}$
μ/k_BT	2.9	1.2
ν_z	$9.4\,\mathrm{kHz}$	$4.5\,\mathrm{kHz}$
ν_z/k_BT	4	1.2
ν_x	$0.6\ldots 12.4\,\mathrm{kHz}$	$0.23\,\mathrm{kHz}$
V_g	$-2.2\,\mu\mathrm{K}$	$-1.06\ldots 0.37\,\mu\mathrm{K}$
$T/T_F\|_{loc}$	0.026	$0.06\ldots 3$
$n_m\|_{T=0}$	$1\cdots\sim 60$	$0\cdots\gtrsim 100$

Table 10.1: Overview of the experimental parameters for the measurements in the 1D-2D crossover explored in Ch. 10 and in the quasi-3D limit in Ref. [69].

i.e. the transport modes are all thermally occupied. With a strong attractive gate there are many 100"s of modes occupied in the central region. In conclusion, the two experiments differ in that in the 1D-2D experiment the contacts are superfluid in equilibrium and at all times at least quasi two-dimensional, which is varied up to the quasi-1D limit, while in the quasi-3D experiment, the contacts" degeneracy is varied from non-degenerate to superfluid and the channel is always quasi-3D confined.

Advective Response

Figure 10.15(a)-(b) show the measured particle conductance G in the non-interacting (a) and strongly interacting regime (b). We find that G obtained in the non-interacting regime agrees well with the expectation from the calculated number of modes (black line in Fig. 10.15(a)). In the strongly interacting limit the conductance shows a similar behavior as a function of the local chemical potential, though each value of G is enhanced with a factor of $13(1)$ with respect to its non-interacting counterpart. There is no obvious increase in conductance when the equilibrium contacts transition from the normal to the superfluid regime (vertical orange line in Fig. 10.15(b)). This is in line with our observation that in these measurements there is no direct signature of superfluidity in this geometry [37]. Nevertheless, in this respect the different experiments agree in that the total particle current depends on the number of modes in the channel.

The Seebeck coefficient α_c is displayed in Fig. 10.15(c) as a function of the local chemical potential μ_{loc} in the center of the channel, assuming local equilibrium. The fitted values of α_c for the non-interacting measurements (blue circles) show a decrease with increasing chemical potential in agreement with the Landauer theory expectation (black line) up to $\mu_{loc} = 0$. For more degenerate contacts the Seebeck coefficient no longer follows the Landauer prediction, but it approaches the reservoir dilatation coefficient α_r, though never decreasing below it. The reason for the thermoelectric response to not change sign ($\alpha_c < \alpha_r$) in the non-interacting regime is not clear, though it might come from an insufficient characterization of the transport geometry which enters the Landauer model.

In the strongly interacting regime (orange circles in Fig. 10.15(c)) the transported entropy per particle α_c follows a similar trend as in the non-interacting case, i.e. it decreases for an increasing local degeneracy, approaching the reservoirs" entropy per particle. In contrast to the non-interacting

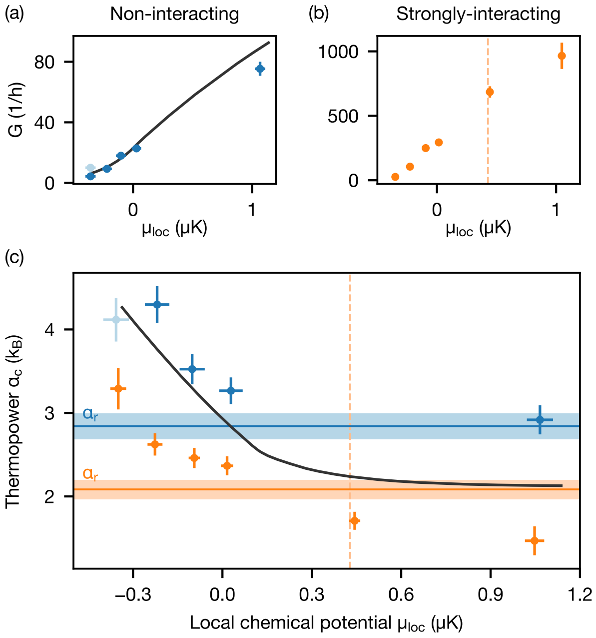

Figure 10.15: Controlling Seebeck coefficient with a gate potential. (ab) Conductance G versus local chemical potential μ_{loc} in the (a) non- and (b) strongly-interacting regimes. Separately measured values are indicated as dark points and the light blue one shows the fitted conductance corresponding to the dashed curve in Fig. 10.14. (c) Fitted Seebeck coefficient α_c without (blue points) and with strong (orange points) inter-particle interactions and the corresponding dilatation coefficients α_r of the reservoirs (horizontal lines). Shaded regions indicate one standard deviation to each side. Solid black lines show an *ab initio* prediction based on Landauer theory in the absence of interactions. The vertical dashed line locates the equilibrium superfluid transition inside the channel while the reservoirs remain uncondensed. No measurement was taken at $\mu_{\text{loc}} \sim 0.4\,\mu\text{K}$ in the non-interacting case.

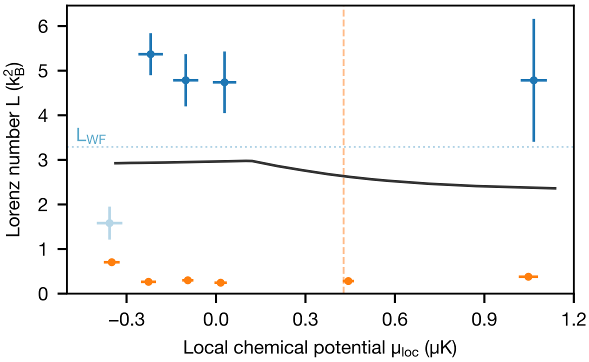

Figure 10.16: Lorenz number L versus local chemical potential μ_{loc} at the channel center. Fitted values in the non- and strongly-interacting regimes are shown as blue and orange points, respectively. The theoretical prediction based on Landauer theory is indicated by a solid black curve and the Wiedemann-Franz value $L_{WF} = \pi^2/3 \cdot k_B^2$ valid for degenerate Fermi liquids by a blue horizontal line. In the strongly-interacting case the vertical dashed line locates the superfluid transition inside the channel while the reservoirs remain uncondensed.

data, for strong interactions the thermoelectric response can change its sign and α_c reduces below α_r slightly below the equilibrium normal to superfluid transition (dashed orange line in Fig. 10.15(c)). Here, we find that in agreement with the observations in the superfluid 1D-2D crossover α_c is far above the local entropy per particle $s/k_B \approx 7 \times 10^{-3}$ for the largest degeneracy. Interestingly, the ability to vary α_c does not translate, though in both experiments the number of transport modes is drastically changed. Here, we like to address why the variation of α_c in Ref. [69] is not in contradiction to our observations in Fig. 10.12(c):

- The way we engineer the system to increase the transported entropy per particle, explicitly only letting hot particles transit the channel leads to a diverging α_c in the limit of large zero-point energy. This means that even in the limit of superfluid reservoirs the transported particles would not be a correct representation of the state of the gas in the reservoirs and the divergence of α_c would be expected to happen. Suggesting a linearly responding advective mode whenever $V_{ZPE} \gg \Delta$, since only normal particles contribute to transport.

- While in both experiments the number of modes n_m is varied over a large range, n_m in the superfluid 1D-2D experiments in Ch. 10 is never smaller than 1 meaning the regime of diverging α_c is not reached [87, 251].

- In both experiments, the limit of reservoir dominated response ($\alpha_c < \alpha_r$) is reached for large degeneracy and in both experiments in this limit α_c shows little variation as function of n_m.

Diffusive Response

The Lorenz number quantifying the diffusive mode in the linear response regime is shown in Fig. 10.16 for the non-interacting (blue circles) and strongly interacting (orange circles) measurements. The value of the Wiedemann-Franz law is within errorbars of the non-interacting values of L while in the strongly interacting limit the Lorenz number is an order of magnitude smaller than $L_{WF} = k_B^2\pi^2/3$. This violation of the Wiedemann-Franz law was already observed in [87] and in this case is confirmed in a distinct quasi-3D geometry. Importantly, the main reason for the violation in this limit is the interaction enhanced value of G. The thermal conductance G_T approaches its non-interacting value, in agreement with our previous measurements presented in Fig. 10.12(b). The Lorenz number itself does hardly vary with the change of local chemical potential since it is given by the ratio of particle and thermal conductance $L = G_T/TG$ which both vary with μ_{loc}. The constant Lorenz number shows that G and G_T vary equivalently with μ_{loc}.

10.7 CONCLUSION AND OUTLOOK

In summary, we have found that the entropy flow in our system between two connected fermionic superfluids is highly non-intuitive and to our knowledge cannot be explained with existing microscopic theories.

Firstly, we found that equilibrium superfluidity itself enhances the entropy transport. The particle current is directly proportional to the superfluid gap in the channel assuming equilibrium, while the entropy current is directly proportional to the particle current. Thus, the sharp increase of I_N with superfluidity in the reservoirs equivalently enhances I_S in our system. This observation is in contrast to commonly observed superfluid transport phenomena like Josephson or fountain effects, where the entropy free supercurrent transports particles. From the transport of entropy and the production of entropy we can conclude that the irreversible flow itself is not purely superfluid.

Secondly, the proportionality between entropy and particle current, i.e. the magnitude α_c of the advective transport mode, was found to be independent of the geometry of the system and much larger than the entropy per particle in the channel. This means that a hydrodynamic description of the superfluid transport in our system does not apply, independent of the geometry. The aforementioned breakdown of hydrodynamics in the channel confirms previous observations that our system is indeed a weak link [37, 38], where hydrodynamics is not expected to hold [134].

Thirdly, we derived a phenomenological model based on a non-linearly responding advective and a linearly responding diffusive entropy transport mode, supposing irreversible dynamics, in the framework of generalized gradient dynamics. The model fitted to our data reproduces our observations well, and we can deduce the transport coefficients determining the evolution of particle and entropy imbalance. The transport coefficients show that the timescales of advective and diffusive transport vary considerably with the geometry. The variation of timescales can also be deduced from the slope of the paths of the evolution in state-space which show the coupling of the two modes as function of confinement. Moreover, a comparison between spin conductance and thermal conductance shows that the extracted coefficients are consistent in the 1D limit, further strengthening the phenomenological model. In the quasi-2D limit the comparison shows that thermal diffusion is faster than spin transport indicating that gapless, massless Goldstone modes could contribute to the diffusion [136].

Finally, by comparing our previous results [69] on thermoelectric transport in a strongly-interacting quasi-3D geometry we found that also in that limit the transported entropy per particle is much bigger than the local entropy per particle. Indicating that also in this limit hydrodynamics fails to describe the evolution. We also find that the variation of the transported entropy per particle in these measurements is not in contradiction to our observations but can be attributed to the divergence of the Seebeck coefficient at large zero point energies where only thermally excited particles can enter the channel.

These observations can help to constrain microscopic theories of entropy transport in a superfluid unitary Fermi gas and also show the need for a more complete theoretical understanding of this conceptually simple system. Possible avenues of theoretical studies could be the role of topological excitations of the order parameter [253], i.e. phase slips in 1D and vortices in 2D, and their role in entropy transport [133, 246, 254, 255]. In addition, it is an open question in what way the strong correlations of the unitary Fermi gas influence these measurements and how particle-hole asymmetry which is often neglected in theory calculations [256], affect the thermoelectric properties of the system.

On the experimental side, a better understanding of the spectral response within the channel is necessary, which could be studied via local RF spectroscopy [111, 225] or using Raman spectroscopy [257, 258]. In addition, experiments with a modulated bias, either via a linear ramp [34] or via a sinusoidal modulation could lead to Shapiro steps [259, 260] which can help to disentangle the contributions of superfluid and normal transport in this system. Finally, a complete study of the entropy transport behavior throughout the BEC-BCS crossover is essential to understand the role of the unitary Fermi gas and the contribution of the distinct excitations [23] of the different pairing mechanisms to the transport.

11

DISSIPATION EFFECTS ON ENTROPY TRANSPORT BETWEEN SUPERFLUIDS

CHAPTER CONTENTS

The contents of this chapter being prepared for publication.

11.1 MOTIVATION

Coupling an initially closed system to its environment [39] via dissipation produces many intriguing phenomena, like the Zeno effect [222, 261] or dissipative phase transitions [60]. The interaction between dissipation and many-body states is particularly interesting since it involves the competition between coherent Hamiltonian evolution and incoherence dephasing or loss. To that end the irreversible entropy transport between two superfluids is an ideal platform to study these effects. The coupling between entropy and particle transport provides additional insights into the energy dependence of the transport due to the intrinsic dependence of advective entropy transport on the particle-hole asymmetry [42, 44]. The entropy transport in the limit of non-negligible contributions of normal currents to the superfluid transport (see Ch. 10) is particularly interesting due to its intrinsic non-equilibrium nature [7, 118]. Adding engineered dissipation to such systems can thus provide insights into their nature but also be used as a tool to modify their behavior [262].

Previous studies on engineered dissipation in BECs [59] have shown that dissipation with an electron beam can be used to suppress losses via the Zeno effect. While optically induced, spin-dependent particle loss in a transport configuration of two superfluids [101] has been found to be less destructive than expected. In the non-interacting limit of a QPC it has been shown that the dissipation can be described by a simple theoretical model which reproduces the transport properties of the system [147]. Finally, dissipation has also been used to drive dissipative phase transitions in a Bose-Hubbard system [60].

Here, the entropy transport between two unitary Fermi gases, superfluid in equilibrium, under the influence of dissipation in the form of spontaneous particle losses is studied. The dissipation is engineered by applying either an atomic transition [101], optically-pumping from a spin-state to an auxiliary state, or by a molecular transition [263]. We find subtle differences between the two different dissipation processes which could be related to their microscopic nature. In both cases it is found that dissipation reduces the excess current I_{exc}, which is the timescale of superfluid transport. The thermal conductance G_T – timescale of diffusive entropy transport – is increased by dissipation. In addition, the dissipation is surprisingly reducing the transported entropy per particle. Interestingly, the change of the Seebeck coefficient is minute while the observable effects on the transport dynamics are considerable. The previously derived non-linear phenomenological model is describing the observed evolution of particle and entropy imbalance and is used to extract the transport coefficients with a fit to the data. The extracted transport coefficients confirm the visible changes in the transport transients and show that the transported entropy is reducing due to dissipation independently of the transport geometry.

11.2 ENTROPY TRANSPORT WITH CONTROLLED DISSIPATION

The measurements presented in this section stem from the same experimental runs as in Ch. 10. We prepare a cold cloud of ^{6}Li in a balanced mixture of initially $N = 3.6(2) \cdot 10^5$ atoms in the lowest and third-lowest hyperfine states, here referred to as spins $\downarrow$ and $\uparrow$, respectively. The magnetic field is tuned to $B = 689.7\,\mathrm{G}$ which is the Feshbach resonance for this mixture. After evaporation the atoms have a temperature of $T = 92(2)\,\mathrm{nK}$ and Fermi temperature of $T_F = 457(7)\,\mathrm{nK}$. In these conditions the reservoirs are superfluid $S/Nk_B = s/k_B = 1.40(6)$ ($s_c = 1.69$ [40, 110]) in equilibrium before transport. The thermometry used is equivalent to the one previously used in Ch. 10 where we use the thermodynamic quantities of the lowest hyperfine state for our analysis, e.g. $\Delta N/N = \Delta N_1/N_1$ and $S/Nk_B = S_1/N_1k_B$. In addition to the constriction beams already described in Sec. 10.2 we project a tightly focused close-to-resonant beam into the channel in order to locally dissipate atoms, see Sec. 3.2.1 and Ref. [101] for details. The dissipation beam has a waist $w = 1.29(1)\,\mu\mathrm{m}$ smaller than the channel and the power can be tuned up to $P_{max} = 220(3)\,\mathrm{pW}$ or $I_{max} = 84(2)\,\mathrm{W/m^2}$.

In order to dissipate atoms spin-dependently $\hat{\Gamma} \propto \hat{c}_\downarrow$ we tune the beam's frequency to a weak resonance of $\downarrow$ which optically pumps atoms to the fifth-lowest hyperfine state $|5\rangle$ thus allowing to dissipate atoms without substantial subsequent heating due to the imparted recoil [101, 147]. For the spin-independent dissipation we tune the frequency to a molecular transition which optically associates pairs $\hat{\Gamma} \propto \hat{c}_\uparrow \hat{c}_\downarrow$ to an excited molecular state [263, 264], subsequently leaving the trap.

11.2.1 Measurements

The measurements presented here can be categorized into a set of two different experiments depending on the initial imbalances. We can prepare an almost arbitrary set of initial imbalances in the ΔN, ΔS state space. The prepared conditions are chosen such that on the one hand a clear diffusive response can be observed, meaning we prepare $\Delta N(0) = 0$, $\Delta S(0) \neq 0$ and on the other hand a purely advective response can be observed via preparing $\Delta N(0), \Delta S(0) \neq 0$. In the latter case the initial conditions are chosen such that the bias relaxes purely advectively (without diffusion) to equilibrium. In the following figures the open markers always indicate measurements obtained from an initially pure entropy imbalance. The filled markers indicate an initially mixed particle and entropy imbalance. Without dissipation the system is closed and explores the state space equivalently to Ch. 10. With dissipation the situation changes since effectively a third terminal is added allowing particle-flow out of the system (but not back) and heat flow into and out of the system. In our case the current into the third terminal cannot be quantified directly but the overall atom number loss and increase in entropy per particle can be measured. In the measurements presented here the strongest dissipation has been limited to values where the exponential lifetime of the system $\tau_{N,\max} = 0.612(4)\,\mathrm{s}$ is on the order of the longest transport times.

For the first experiment we prepare a nearly pure entropy imbalance and measure the resulting particle- and entropy-bias response as a function of time for the two different types of dissipation. Figure 11.1 shows the response for spin-dependent dissipation (open circles) in the left column and for molecular dissipation (open squares) in the right column. The two datasets are taken with a strongly confined channel $\nu_x = 10.9(2)\,\mathrm{kHz}$ resulting in a non-linear particle and entropy current response (blue, red points in Fig. 11.1(a)-(d)) without dissipation and the formation of a non-equilibrium steady-state, previously observed [87]. The total entropy and particle number displayed in Fig. 11.1(e)-(f) show that in the measurements without dissipation the atom number is conserved, and the entropy is strictly increasing ($\dot{S} > 0$). When imparting dissipation (orange, purple points in Fig. 11.1) we keep the intensity of the spin-dependent and molecular dissipation beam equivalent. We find an enhancement of the peak thermoelectric response in the case of spin-dependent dissipation as can be seen in Fig. 11.1(a). The peak particle bias is increasing beyond the value found without dissipation while the peak entropy bias stays close to the measurement without dissipation. This directly shows that the dissipation has decreased the transported entropy per particle. In addition, we find that the dissipation has a strong influence on the diffusive transport allowing the non-equilibrium steady-state to relax. This points to a suppression of the many-body effects inside the channel which were responsible for the reduced thermal diffusion. When increasing the dissipation further (green, brown points in Fig. 11.1) the peak response is below the non-dissipative value while the thermal conductance G_T is even larger, leading to a monotonic decrease of the entropy imbalance. Comparing the effect of spin-dependent and molecular loss on the transport we find that the increase in peak response due to dissipation is less pronounced (purple points) for molecular dissipation while at the same time the speed-up of the diffusive transport is also weaker (brown points). Generally it seems that the molecular and spin-dependent dissipation have a similar effect on the total atom loss, but the molecular dissipation has less effect on the transport dynamics. The spin-dependent loss, acting on $|\downarrow\rangle$ has been found [101] to produce a secondary loss rate of $|\downarrow\rangle$ which is $\sim 70\,\%$ of the original. Since we do not calculate the molecular association rate *ab-initio* the atom-number loss in state $|1\rangle$ will be used to compare the magnitude of the dissipation effects.

In the second experiment we probe the effect of spin-dependent dissipation in a less confined transport geometry $\nu_x \approx 5.1(1)\,\mathrm{kHz}$ and for both types of initial conditions also explored in Ch. 10 and partly in Ref. [101] (here with a weaker confinement). For the data in the left panels of Fig. 11.2 the initial bias is prepared such that the system relaxes purely via the advective mode. The right panels correspond to the situation where the initial advective response is followed by a diffusive relaxation. The measurements were performed at equal beam powers, such that the atom-light scattering rates is equivalent for the orange/purple circles and green/brown circles in Fig. 11.2. Figure 11.2(a), (c) show the evolution of the particle and entropy imbalance, where without dissipation the system reaches a state close to

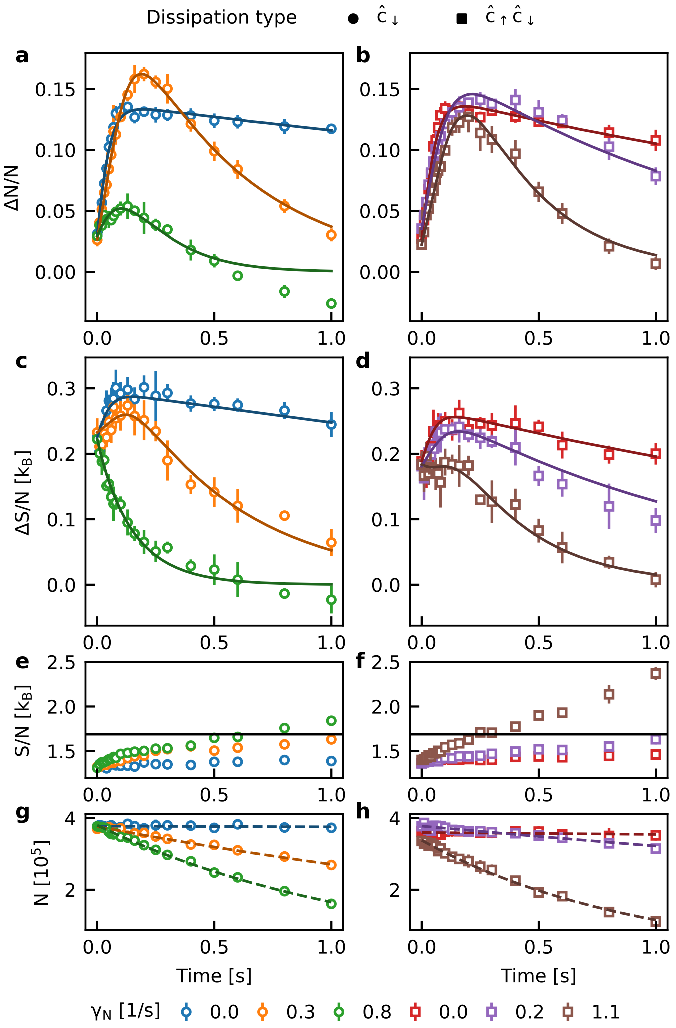

Figure 11.1: Effect of dissipation on the thermoelectric response. (a)-(b) The relative atom-number imbalance $\Delta N/N$ as a function of time displays that weak dissipation enhances the peak thermoelectric response while suppressing the non-linearity for strong dissipation strength. The left column shows the measurements (open circles) for spin-dependent dissipation, while the right column shows the data (open squares) for molecular dissipation. The relative entropy imbalance $\Delta S/Nk_B$ evolution (c)-(d) displays an increased thermal conductance G_T with dissipation. The solid lines are fits with the phenomenological model. The total entropy per particle (e)-(f) indicates that the dissipation is heating the system, the solid horizontal line is the superfluid transition. (g)-(h) Total atom number as a function of time, the dashed line is a fit with exponential decay constant γ_N. The errorbars represent the standard deviation of $3-5$ repetitions.

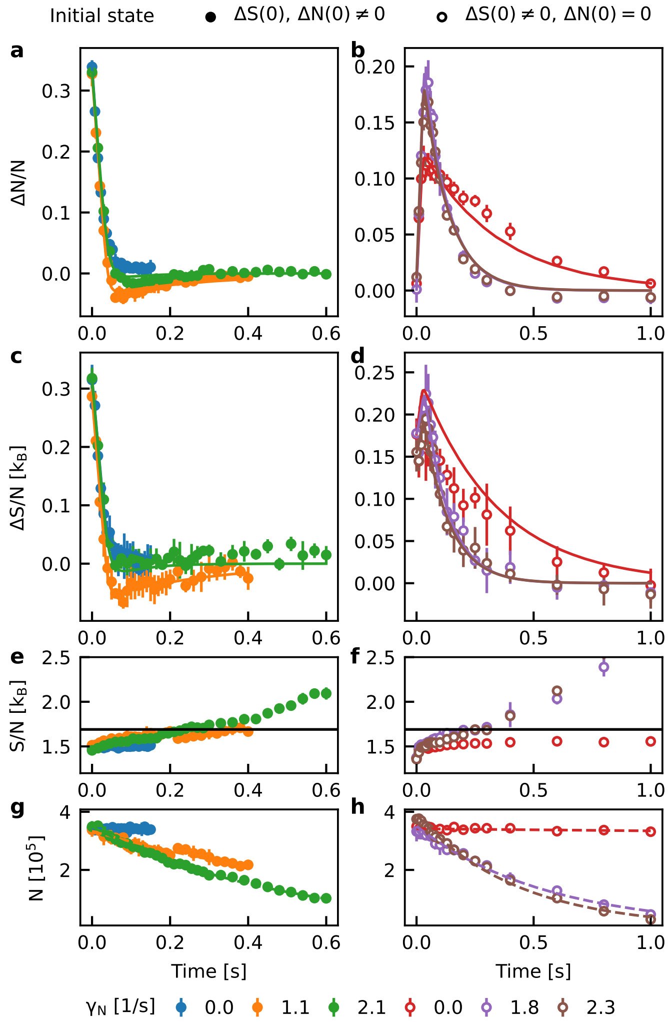

Figure 11.2: Effect of dissipation on the advective response at weak confinements. (a)-(d) Relative atom-number imbalance and entropy imbalance evolution with varying spin-dependent dissipation. The panels on the left (filled circles) correspond to an initial entropy and particle imbalance, the right panels (open circles) to an initial entropy imbalance. The dissipation leads to an advectively driven overshoot of the thermodynamic equilibrium followed by a diffusive relaxation. The solid line are fits with the phenomenological model. The evolutions of the total entropy per particle (e)-(f) display a reduction of degeneracy while the atom-number evolutions (g)-(h) indicate atom losses. The atom-loss is quantified with an exponential fit (dashed line).

equilibrium, due to an imperfect initial state preparation. With the complementary initial state, the transport dynamics displayed in Fig. 11.2(b), (d) suggest a stronger reduction of transported entropy per particle compared to Fig. 11.1, while increasing the dissipation seems to have a limited effect. The total entropy per particle and atom number displayed in Fig. 11.2(e)-(h) show that without dissipation the atom number is conserved, and the entropy is strictly increasing during transport but constant after. The spin-dependent dissipation imparted on the atoms inside the channel leads to the advective particle and entropy currents no longer directly reaching equilibrium but "overshooting" and subsequently relaxing diffusively (exponentially). This is in line with our previous observation in Fig 11.1 of an overshoot in the opposite direction where in both cases the origin of the effect seems to be a decreasing transported-entropy per particle. For the strongest dissipation (orange points in Fig. 11.2) the overshoot is less visible likely again due to a much stronger diffusive mode and weaker advective mode, reducing the peak response. The final state of the system (see Fig. 11.2(e)) with dissipation seems to be consistently indicating that without dissipation the diffusive mode is suppressed. This leads to a non-equilibrium steady-state (blue circles in Fig. 11.2(e)) similar to the one in the first experiment but much closer to equilibrium. In order to provide a quantitative description of the transport parameters we fit the data with the phenomenological model already described in the previous Ch. 10. The disparity between fit (red line) and data (red circles) in Fig. 11.2(d) stems from a systematic shift in the initial data point compared to the rest of the data-set. The fit generally performs well such that the χ_r^2 statistics are on the order of 1. This suggests that the previously assumed irreversibility of the transport process, i.e. Onsager"s reciprocal relations, also holds in the open system explored here.

11.3 PHENOMENOLOGICAL MODEL AND FITTING PROCEDURE

In this section the fit results from the phenomenological model to the data shown in Fig. 11.1, Fig. 11.2 as well as from additional datasets is discussed. The applied phenomenological model is given by

$$I_N = I_{exc} \tanh \frac{\Delta\mu + \alpha_c \Delta T}{\sigma} \tag{11.1}$$

$$I_S = \alpha_c I_N + G_T \Delta T / T \,. \tag{11.2}$$

The fit was performed separately for the data with strong confinement (Fig. 11.1) and for the data with weak confinement (11.2). In the case of the weak confinement a complementary dataset with a different initial state was fitted simultaneously in order to compare and differentiate effects of the initial state and reduce the effect of noisy data.

Fitting Procedure and Fit Parameters

In order to have a stable fit the respective datasets are fitted "simultaneously" meaning we calculate the residuals of all datasets and minimize the weighted sum of squared residuals, with the sum including all separate datasets, i.e. different dissipation strength or dissipation type. This procedure allows us to have fit parameters which are the same for all datasets ("globally" varying) and fit parameters which vary for each dataset independently ("locally" varying). This kind of procedure is necessary since there are parameters which have to be varied to be able to fit the data but are strongly correlated to other fit parameters, hence having them fitted globally puts less weight on a correlation stemming from one specific dataset. The full model we use for the fit is given by

$$-\frac{1}{2}\frac{d\Delta N(t)}{dt} = I_{\mathrm{exc}} \tanh\left(\frac{\Delta\mu + \alpha_c \Delta T}{\sigma}\right), \tag{11.3}$$

$$-\frac{1}{2}\frac{d\Delta S(t)}{dt} = -\alpha_c \frac{d\Delta N(t)}{2dt} + G_T \frac{\Delta T}{T}, \tag{11.4}$$

where the reservoir response is given by

$$\Delta\mu = \frac{(\ell_r + \alpha_r^2)\Delta N - \alpha_r \Delta S}{\ell_r \kappa}, \tag{11.5}$$

$$\Delta T = \frac{-\alpha_r \Delta N + \Delta S}{\ell_r \kappa}. \tag{11.6}$$

The initial values of this system of first order differential equations is fixed by the measurements and subsequently the equations are integrated in order to calculate the residuals using the measured entropy and atom number imbalances. For the weighting the average errorbars of the respective entropy and atom number imbalance is used in order to increase the stability of the fit. Without such averaging we observed that outliers with non-physical errorbars would skew the fit. In addition, using average error bars also allows more stable fitting of the global parameters which are also skewed by local outliers. Furthermore, since there are fluctuations of atom number and entropy between datasets which change the respective absolute value of α_r, ℓ_r and κ these parameters are not fitted directly. In order to preserve the differences between datasets due to fluctuations in preparation we only fit a scale to the measured reservoir parameters such that

$$\alpha_r = \alpha_s \alpha_m, \tag{11.7}$$

$$\ell_r = \ell_s \ell_m,$$

where the indices stand for scale s and measured m. The fit parameters for the fits we performed are given in Table 11.1

Scope of parameter	Fit Fig. 11.3, Fig. 11.5
locally optimized for each dataset	I_{exc}, α_c, G_T
globally optimized for all datasets	σ, α_s, ℓ_s

Table 11.1: Fit parameters used for fits of thermoelectric response with dissipation.

Initial Values of the Fit

Estimating the initial parameters for these fits is extremely useful since fitting the large datasets would otherwise be slow and would not necessarily converge. The excess current can be estimated via a fit of the initial atom number response of the system since in our system

$$I_N(0) \approx I_{\mathrm{exc}}. \tag{11.8}$$

For the data in this section there are not always enough measurements close to the initial state of the system, this is one of the main reasons why the fit cannot always determine the excess current as well as we would like. In addition, we can perform a fit of the exponential relaxation of the imbalances after the advective mode has relaxed. The exponential fit allows us to extract a timescale τ_T which is quantifying the diffusive mode, i.e. the linear thermal conductance. If the advective mode has relaxed, and it is much faster than the diffusive relaxation we find

$$-\frac{1}{2}\frac{d\Delta S}{dt} \approx G_T \frac{\Delta T}{T} = \frac{\ell_T \kappa}{2\tau_T}\Delta T\,. \tag{11.9}$$

Finally, for the Seebeck coefficient α_c we can perform a linear fit in the state-space ΔS, ΔN. Provided the diffusive mode is slow, or the system is prepared such that only an advective response is possible α_c can be approximated by s^* using

$$I_S = s^* I_N \iff d\Delta S = s^* d\Delta N\,. \tag{11.10}$$

11.4 COMPARISON OF SPIN-DEPENDENT AND SPIN-INDEPENDENT DISSIPATION

Figure 11.3 shows the fit results for the measurements shown in Fig. 11.1. The exponential decay constant shown in Fig. 11.3(a) shows that either type of dissipation – spin-dependent (circles in Fig. 11.3) or molecular (squares in Fig. 11.3) – have a similar effect on the overall atom loss. Interestingly, the loss due to the molecular dissipation is slower for low beam powers but shows less saturation behavior for higher powers and reaches a higher loss rate compared to the spin-dependent dissipation.

Excess Current and Thermal Conductance

Figure 11.3(b) shows the excess current in units of the unitary gap as a function of the fitted exponential decay constant. The unitary gap was calculated at the most degenerate point in the contacts to the channel, assuming they are in local equilibrium. We find that the excess current decreases due to the dissipation. Though, at stronger dissipation the molecular loss has a lesser effect on the excess current which seems to saturate to a constant value. The behavior of the exponential decay constant and the excess current indicate a conservation of currents in the junction, whenever the loss rate saturates the excess current doesn"t and vice versa.

Fig. 11.1 already indicated that the diffusive mode got faster due to the presence of dissipation which is reflected in the fitted value of the thermal conductance shown in Fig. 11.3(c). Here the thermal conductance has been normalized to the single mode, non-interacting QPC value $G_T^0 = \pi^2 k_B^2 T/3h$, given by the Wiedemann-Franz law. The thermal conductance behaves differently for the two dissipation types. The spin-dependent dissipation leads to a larger thermal conductance compared to the molecular loss. This could be related to the type of excitation created by the dissipation, where the spin-dependent dissipation creates spin and density excitations, the molecular loss can only create density excitations. Notably, the difference in behavior for the two dissipation types in the excess current – which apparently directly depends on the superfluid order parameter – is less clear. An explanation for the quantitative differences due to the different dissipation types are beyond the scope of this thesis. The overall increase of the thermal conductance with dissipation may be explained when comparing this

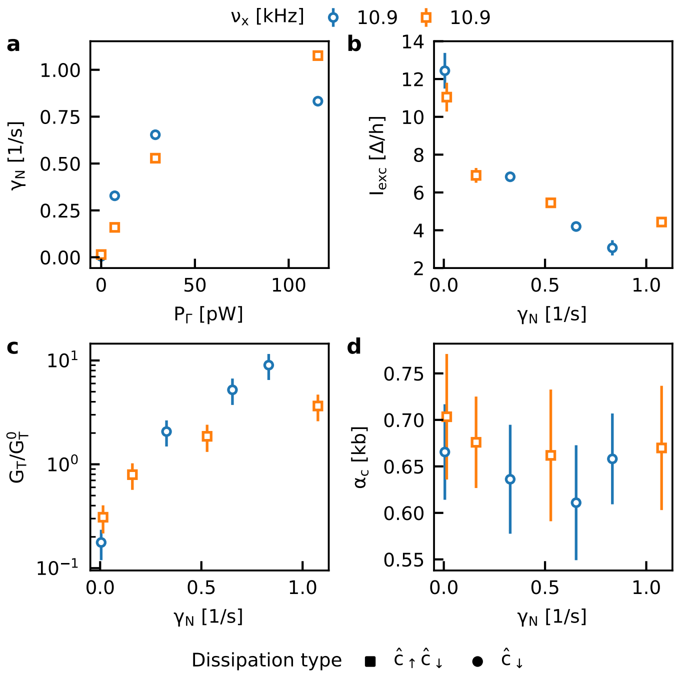

Figure 11.3: Parameters of the phenomenological model for the thermoelectric response. Fit results for spin-dependent (circles) and molecular (squares) dissipation are shown as a function of the dissipation strength, for strong transversal confinement (see Fig. 11.1). (a) shows the exponential decay constant extracted from a fit to the total atom number as a function of the beam power. The excess current (b) decreases as a function of the dissipation, for weak losses both types of dissipation have the same effect while for stronger losses the excess current seems to be much less affected by molecular loss. (c) displays the normalized thermal conductance which is increasing substantially due to dissipation, here the spin-dependent dissipation has a much bigger effect than the molecular dissipation for any dissipation strength. The enhanced thermoelectric response is reflected in the extracted Seebeck coefficient (d), the magnitude of which is increasing with dissipation.

observation to the increase of thermal conductance when reducing the channel confinement, as has been observed in Fig. 10.12. Here, the dissipation seems to compete with the many-body state of the strongly interacting system which leads to an increase of excitations to be transported diffusively.

Entropy Response – Comparison to Non-Interacting QPC

Figure 11.3(d) shows the Seebeck coefficient α_c as function of atom loss rate which follows the previously (see Fig. 11.1(a)-(d)) observed behavior that the peak thermoelectric response is increasing due to a reduction of the transported entropy per particle $\alpha_c = \alpha_r + \alpha$. The error bars are dominated by the uncertainty of the reservoir response coefficient α_r entering the calculation of $\alpha_c = \alpha_r + \alpha$. Comparing this behavior to the expectation from the non-interacting system allows us to show the peculiarity of this observation. Figure 11.4 shows the behavior of the transport coefficients of the linear transport model, the particle conductance G, the thermal conductance G_T and the Seebeck coefficient α_c when dissipation is present inside the QPC. From Fig. 11.4(c) we find that, independent of the gate potential, the transported entropy per particle α_c is always increasing with dissipation. This can be explained in a simple picture, where atoms spending

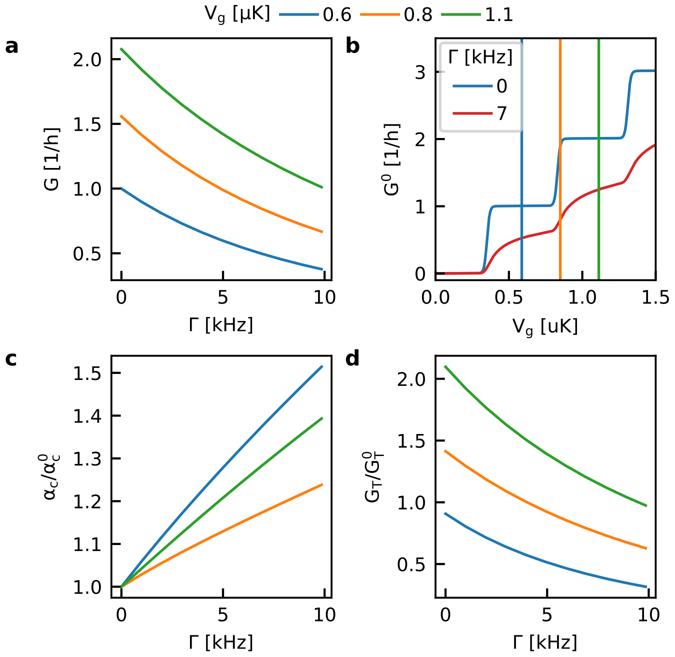

Figure 11.4: Landauer simulation of the non-interacting QPC with dissipation. In the non-interacting system particle conductance (a) decreases as a function of dissipation, independently of the applied gate potential. (b) shows the particle conductance without dissipation G^0 as a function of gate potential V_g. The transported entropy per particle (c) (normalized by its 0−dissipation value α_c^0) is increased by the dissipation, while the increase depends on the gate potential due to the energy dependent transmission. The thermal conductance G_T (d) is decreasing as a function on dissipation. G_T is normalized by its single-mode value $G_T^0 = \pi^2 k_B^2 T/3h$.

longer times in the dissipative beam are more likely to be dissipated and since in this non-interacting picture the low energy atoms also carry less entropy the dissipation preferentially removes low entropy currents. Thus, the transported entropy per particle increases. It is quite remarkable that the opposite happens in the superfluid regime since one would expect from the previous observations regarding the excess current and thermal conductance that dissipation reduces pairing which in turn would increase the transported entropy per particle due to the availability of more excitations. It is possible that the energy dependence of the dissipation changes due to interactions such that high entropy currents are more likely to be dissipated.

Moreover, we find that for dissipation in the non-interacting QPC the thermal conductance is strictly decreasing, contrary to what we have seen in the strongly interacting regime. The relation between G_T and the dissipation in the non-interacting QPC can be explained by the reduction of overall transmission with dissipation. In the strongly interacting system the excess current follows qualitatively the same behavior as the conductance in the non-interacting case. The thermal conductance on the other hand is strongly enhanced suggesting that the dissipation has a non-trivial effect on the many-body state,

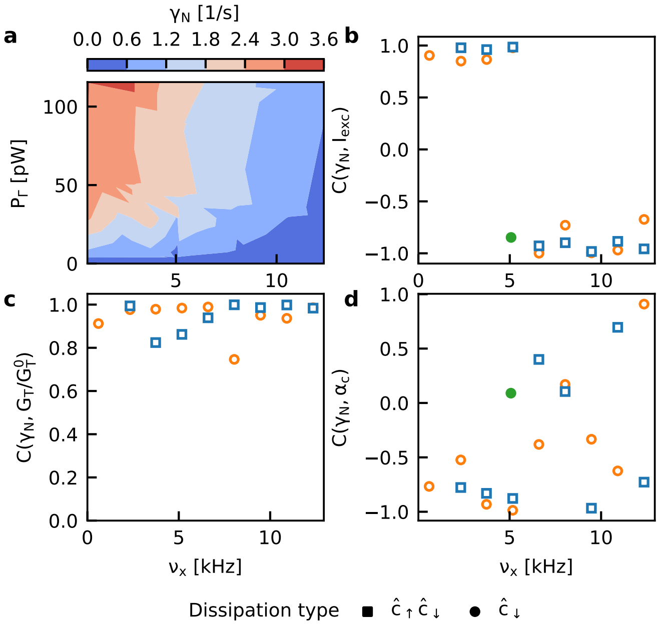

Figure 11.5: Correlations of the transport coefficients with dissipation strength. (a) The loss-rate γ_N extracted from an exponential fit to the total atom-number is presented as a function of confinement and dissipation beam power. The weighted Pearson correlation coefficient of γ_N with P_Γ is shown in the inset. (b)-(d) The weighted Pearson correlation coefficients are displayed as a function of transversal confinement. Open symbols correspond to data-sets where the initial state was a pure entropy imbalance. The closed symbol corresponds to the dataset presented in the left column of Fig. 11.2.

11.5 ENTROPY TRANSPORT WITH DISSIPATION IN THE 1D-2D CROSSOVER

In order to get a better picture of the effect of dissipation on our system we probe the system for varying transversal confinement ν_x. For the explored confinements the system is crossing over from the quasi-2D regime ($h\nu_x < k_B T$) to the quasi-1D regime. The measurement with an initially purely advective transport mode is called advective (filled circles in Fig. 11.5). The complementary measurement with an initially pure entropy imbalance is called diffusive (open symbols in Fig. 11.5). An exemplary measurement showing the advective response at an intermediate confinement is displayed in Figure 11.2. We fit the measured transport transients for both the molecular (square symbols in Fig. 11.5) and the spin-dependent (circle symbols in Fig. 11.5) dissipation and extract the transport coefficients. For each confinement frequency one dataset without dissipation and at least three data-sets with varying dissipation strength exist. In total 76 datasets are fitted using the previously described procedure. The datasets with molecular dissipation are all fitted simultaneously, the datasets with spin-dependent dissipation and the initial pure entropy bias are also fitted simultaneously, while the dataset shown in Fig. 11.2 is fitted separately. For this last dataset the diffusive response of the originally purely advective response is only visible with dissipation which made it not possible to correctly determine the thermal conductance.

Transport Coefficients

Figure 11.5 shows the result of the exponential fit to the total atom number and the weighted Pearson correlation coefficients $C(\gamma_N, Y)$ between the transport coefficients and the loss rate γ_N. Each transport coefficient Y used to calculate a correlation coefficient is weighed $w = 1/\Delta Y$ by its standard deviations ΔY. The loss-rate is displayed in a contour plot in Fig. 11.5(a) as a function of confinement ν_x and beam power P_Γ. We find that decreasing the confinement which increases the particle current in the system, even without dissipation (see Ch. 10), concurrently increases the atom loss rate γ_N. The same dependence is found for the beam power which increases γ_N as well.

Panels 11.5(b)-(d) display the different weighted Pearson correlation coefficient as a function of the confinement. These coefficients $C(X, Y)$ quantify the linear correlation between two variables X, Y and range from -1 to 1 where -1 corresponds to anti-correlated, 1 to correlated and 0 to uncorrelated variables, respectively. The markers in Fig. 11.5 correspond to correlation coefficients for different confinements, dissipation types and initial conditions. Moreover, we calculate the overall weighted correlation coefficient which provides the correlation between variables independent of the aforementioned measurement conditions. The overall correlation coefficient between the dissipation beam intensity P_Γ and the loss-rate γ_N is $C(\gamma_N, P_\Gamma) = 0.74(8)$ indicating an expected significant correlation. Due to the loss-rate γ_N not being linear (see Fig. 11.3(a)) as a function of P_Γ the correlation coefficient is not closer to 1.

The correlation between excess current I_{exc} and dissipation as a function of confinement presented in Fig. 11.5(b) suggests a transition from an anti-correlated behavior to a correlated behavior. This means for strong confinements the dissipation decreases the excess current while for the weakest confinements the opposite seems to be the case. The anti-correlation between dissipation and excess current has been previously observed [101] though only at strong confinements. In the limit of weak confinement there is a size miss-match between the dissipation beam and the channel width. Atoms can enter side-modes which propagate at the edge of the confinement potential thus circumventing the dissipation which reduces the absolute correlation coefficient between current and dissipation strength. The increase in excess current could then be a result of the decreased transported entropy per particle α_c, see Fig. 11.2. Reducing the transported entropy per particle will increase the overshoot thus effectively also increasing the initial current. The fit has difficulty to distinguish between the initial current and the excess current such that an apparent increase of the excess current is observed. On a technical level the estimation of the excess current for weak confinements is less trustworthy since the number of data-points in the initial response is smaller than for strong confinements. From Fig. 11.4(a) a decrease of I_{exc} would be expected from a reduction of the single-particle transmission of the channel. Further analysis is required to determine if the reduction of single-particle transmission is the only reason I_{exc} is decreasing or whether many-body effects are necessary to describe the decrease.

The diffusive response was already observed to be accelerated by the dissipation in Fig. 11.3. Calculating the correlation coefficient as function of confinement shown in Fig. 11.5(c) we find that this behavior is consistently observed in the quasi-1D and quasi-2D limit. The overall correlation coefficient between loss rate γ_N and thermal conductance G_T is $C(\gamma_N, G_T) = 0.75(8)$. Notably, in the non-interacting limit the thermal conductance is strictly de-

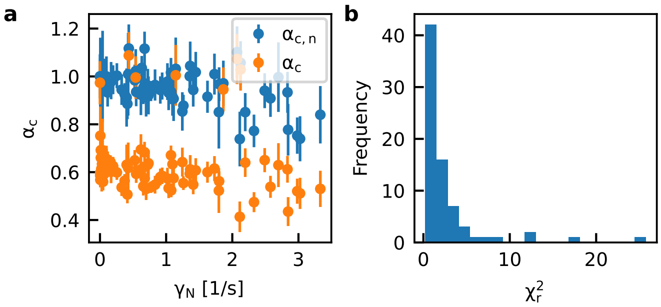

Figure 11.6: Measured Seebeck coefficient and reduced χ^2 statistic. (a) The transported entropy per particle α_c is displayed as function of the dissipation rate γ_N. The normalized $\alpha_{c,n}$ is calculated by dividing α_c by its value without dissipation. Both quantities show a clear trend, though the correlation coefficient of α_c would be dominated by the scale difference of the extracted value from the datasets with different initial states. (b) The reduced chi-square goodness of fit parameter is displayed in a histogram for the 76 different fits, which indicates that most of the fits have a reduced chi-square value close to 1. Excluding results of fits with $\chi^2_r \gg 1$ does not change our observations.

creasing as function of dissipation, see Fig. 11.4(d), due to a decrease of the overall transmission, see Fig. 11.4(b). Here, the thermal conductance is strongly correlated with the atom-loss rate indicating that the dissipation affects which type of excitations contribute to transport. Moreover, this directly shows that strong interactions are responsible for the suppression of G_T and it indicates that dissipation affects the many-body state. Generally we expect quasi-particles and Goldstone modes [136] to be responsible for entropy diffusion. Due to dissipation in the channel increasing G_T, we can conclude that the channel itself prevented these excitations from being transported in the quasi-1D limit without dissipation.

Figure 11.5(d) shows the correlation between the Seebeck coefficient α_c and the loss-rate. We determine that the two quantities are mostly anticorrelated or close to being uncorrelated. The overall correlation coefficient for all datasets $C(\gamma_N, \alpha_{c,n}) = -0.55(10)$ confirms a significant anticorrelation, as can be seen in Fig. 11.6(a). Implying that dissipation reduces the transported entropy per particle. For the overall correlation coefficient the datasets were scaled by α_c without dissipation in order to remove scale differences affecting the correlation coefficient. Figure 11.6(b) shows $\alpha_{c,n}$ and α_c as a function of the dissipation rate γ_N. The decrease in transported entropy per particle and the connection to the overshoot can be understood from the initial state which drives an advective response until it has relaxed. With an initial state with a pure entropy imbalance the number of particles needed to be transported to relax the advective mode is then directly proportional to α_c. We observe that this behavior is independent of the confinement.

We previously found that extracting the transport coefficient α_c is challenging in the presence of fast diffusion where the two transport modes compete, see Ch. 10 and Fig. 11.3(c). Here, we find that the overshoot observed at weak dissipation strengths – directly indicating α_c is decreasing – is suppressed by fast diffusion due to strong dissipation, see Fig. 11.1. The positive correlations found in Fig. 11.5(d) are biased by this behavior for strong dissipation strengths. Excluding the datasets with the strongest dissipation all datasets have a correlation coefficient $C(\alpha_c, \gamma_N) < 0.3$, where only one dataset has a positive correlation coefficient. In this limit the anti-correlation increases $C(\alpha_{c,n}, \gamma_N) = -0.61(11)$.

11.6 CONCLUSION AND OUTLOOK

In conclusion, we have found that spin-dependent and spin-independent dissipation has a clear effect on entropy transport between two superfluid gases. The main effects can be categorized into two behaviors. Firstly, the dissipation has shown to strongly affect transport parameters correlated to a decrease of the many-body enhancements generally associated with superfluidity. The excess current is suppressed with dissipation as previously observed [101], independent of initial state or geometry. Moreover, we find that the thermal conductance is enhanced when local dissipation is present. The locality of dissipation affecting the thermal conductance strongly suggests that the channel is responsible for filtering out excitations, which are able to diffusively transport entropy. This would also imply that the excitations have to be present in the channel region, contrary to previous interpretations [67]. A different explanation cloud be that the dissipation non-locally affects the many-body state in the regions around the channel. Secondly, the dissipation has shown to have an unexpected effect on the transported entropy per particle. We expect from the non-interacting system that dissipation increases the transported entropy per particle, since slow – low entropy – particles are more likely to be dissipated compared to fast – high entropy – particles. We find for the strongly interacting system that dissipation counterintuitively decreases α_c. Interestingly, assuming the low entropy superfluid contributes to transport we would expect that for strong dissipation α_c should increase by destroying the superfluidity. Since the observed heating is slow compared to the transport dynamics this effect could be another reason why α_c is non-monotonic for strong-confinements, where transport is generally also slower.

In order to shed light on these effects and understand our system better it is pertinent to understand the local spectral response of the system which could be measured via Raman- or Bragg spectroscopy [23], though both would require technical upgrades to the experiment. In addition, probing the effects of dissipation on spin conductance could give insights into the role of quasi-particles for the increased thermal conductance. Finally, a microscopic model beyond particle-hole symmetric systems, which has been studied in [38, 101], could sharpen our understanding of the entropy transport in our system.

12

CONCLUSION AND OUTLOOK

In this work we studied transport through different mesoscopic geometries observing entropy, spin and particle transport and their interplay. Our observations and theoretical models give valuable insight exemplified by the following results:

- **Robustness of conductance quantization to dissipation.** We found that quantized conductance through a ballistic channel affected by local particle dissipation retains its step of conductance at a reduced conductance value. Comparing our measurements to a simple extended Landauer-Büttiker model we find that this theoretical approach keeps its validity in the open system.

- **Spin-filtering in a weakly interacting QPC.** Employing a tightly focused beam inside the QPC we create a local effective Zeeman shift. The measurements show that fully polarized spin currents can be obtained and that the strength of the effective Zeeman shift can be larger than the Fermi energy. Varying the interactions we find that weakly interactions provide a measurable renormalization of the spin-dependent potential.

- **EIT in a strongly interacting Fermi gas.** We theoretically calculate that multiple three-level systems exist in the Paschen-Back regime. Upgrading the experiment to engineer atom-light interactions of three-levels we demonstrate EIT in a transport experiment. Non-linear particle transport in the unitary Fermi gas, superfluid in equilibrium, is getting linear under the influence of strong dissipation. We find that the particle currents can be restored by rendering the transported particles transparent with a second laser beam. Moreover, transport as a probe allows us to measure the optical potential of the three-level system away from the EIT resonance.

- **Entropy transport between two superfluids.** We measure non-linear particle currents between two strongly interacting Fermi gases, indicative of superfluidity. The concurrently observed increase of net entropy and the significant transported entropy per particle, show that the transported current is not a pure supercurrent and the transport process is irreversible. Comparing the measured transported entropy per particle to its local equilibrium value in the junction we conclude that the transport is not hydrodynamic. We find that said transported entropy per particle is independent of the geometry of the system, remaining constant when the channel is varied from quasi-1D to quasi-2D. In contrast, the variation of geometry has a strong effect on the transport timescales of the advective and the diffusive mode.

- **A phenomenological model describing irreversible, non-linear transport.** We derive a phenomenological model based on the non-linear response and the irreversibility of the observed currents. The model describes the observed particle imbalance, entropy imbalance and total entropy evolution. Using the model we can extract the transport coefficients from a fit. The coefficients show that both the excess current and the thermal conductance vary strongly with the transversal confinement while the Seebeck coefficient remains constant.

- **Dissipation reduces the Seebeck coefficient.** We measure the effects of dissipation on the non-linear entropy transport. The entropy and particle imbalance evolution show that dissipation enhances the magnitude of the advective response, implying that the transported entropy per particle is reduced. We find that our phenomenological model fits the observations even with dissipation. The extracted transport coefficients indicate that dissipation reduces the Seebeck coefficient. Moreover, dissipation reduces the excess current and increases the thermal conductance.

Based on the observations and technical upgrades outlined in this thesis possible new experiments are presented as well as some technical improvements.

12.1 ENTROPY TRANSPORT

A long-standing goal which has become feasible only now with the new temperature bias preparation method is the observation of quantized thermal conductance. We have shown that it is possible to prepare a temperature bias at low average temperatures which should enable us to study the quantization of the thermal conductance in the non-interacting QPC. The main challenge for the observation is the temperature broadening of the conductance steps by $4k_BT$. In previous preparation schemes the overall temperature was limited to $\gtrsim 170\,\text{nK}$ which easily blurs even the longest observed conductance plateaus $\sim 700\,\text{nK}$. The new preparation method has been demonstrated to preserve the non-linear transport characteristic in the strongly interacting limit which makes us confident the same can be done in the case of quantized conductance in the non-interacting regime. The quantization of thermal conductance has been observed in other systems [265–267] though not yet in an atom based mesoscopic system.

Another interesting field of study would be the transmission of collective excitations through different transport geometries. Collective excitations, only present in the superfluid phase, such as the second sound have been studied extensively [22, 24, 28] in different geometries. In a transport experiment there are open questions on how an entropy wave would contribute to transport [136]. The proposed experiment would entail first the excitation of a collective mode in one of the reservoirs and second the observation of its propagation through the transport region. The signal could possibly be enhanced by exciting collective modes in both reservoirs in and out-of-phase in order to observe possible interference effects. These experiments would not require any change in the experiment, the digital micro mirror device used in Ref. [61] can produce an elliptical beam in each reservoir and amplitude modulation is readily available via its amplitude stabilization.

12.2 MICROSCOPIC MANIPULATION

Advances in our understanding of the atom-light interaction at high magnetic fields and technical improvements in the projection of arbitrary potentials using spatial light modulation [149, 150] permit us to apply more complex structures to affect the transport system on a microscopic level.

12.2.1 Near-Resonant Atom-Light Interaction

We found that three-level systems can be addressed in the strongly interacting regime which opens several possible avenues of studies where transport is manipulated inside a quantum wire or QPC with light:

- **Subwavelength potentials as tunneling barriers.** The dark-state, arising from the three-level atom-light interactions, has non-adiabatic corrections to its energy when being subjected to fast changes of its internal state structure [102]. The subwavelength potential is given by the spatial derivative of the mixing angle of the dark-state $V_{DS}(y) = \frac{\hbar^2}{2m}\left(\partial\alpha(y)/\partial y\right)$ which can be varied on a subwavelength scale since $\tan\alpha = \Omega_c/\Omega_p$. The subwavelength potential used as an optical lattice has already been demonstrated [226]. We have theoretically calculated (see Ch. 9) that this allows for example the creation of a quantum dot. Importantly, the subwavelength structure enables large tunneling rates generally needed in the experiment in order to measure the transported currents. The main challenge in this context is the associated dissipation rate which can be reduced by large Rabi frequencies, though it is not clear how detrimental losses from molecular lines would be to this proposal.

- **Spin-Orbit coupling.** Spin-Orbit coupling in a BEC [54] or Fermi gas [205, 257] via a Raman transition has been demonstrated and used to observe the spin Hall effect [55]. Employing a Raman transition between the lowest- and second-lowest hyperfine state observed at strong interactions (see Ch. 9) would permit spin-orbit coupling in a quantum wire. The spin-orbit coupled superconducting quantum wire is the basis for the experimental realization of the Kitaev [268, 269] model and thus also for Majorana fermions [270]. Any realization of spin-orbit coupling would require technical upgrades in order to spatially separate the beams driving the Raman transition, preferably allowing for an adjustable angle between the beams. Alternatively, local rotations of the spins inside a superfluid QPC would provide a system similar to the Kondo effect [199], where a magnetic impurity is surrounded by a superconductor.

- **Local measurement of atoms.** The applicability of EIT as a density probe [53, 271] is a result of the phase shift of the light in a media. The slope of the susceptibility at the resonance determines the phase shift and is already widely used for measuring magnetic fields [272], while the slope itself is dependent on the density. The possible detection scheme of atoms in the QPC would be to continuously measure the slope of the EIT signal with a lock-in technique relying on frequency modulation. This technique would require technical changes to the experiment in order to enable a heterodyne detection of the phase. Another approach would be a single atom imaging technique in free space pioneered in Ref. [273]. This would require a different wall setup such that the density in the channel after transport is conserved and subsequently imaged. Both techniques would enable us to measure local densities and thus for example effects like the fermionic waiting time distribution in a QPC [206].

12.2.2 Two-Dimensional Structures

During this thesis we worked on improving the longitudinal potential landscape of the transport geometry to tolerate longer junctions. The main challenge in this respect is the Gaussian fall-off of the lightsheet which prevents structures longer than $\sim 20\,\mu\mathrm{m}$ [146]. It is planned to remedy this by applying a lightsheet with "top-hat" shape in longitudinal direction. The flat region of the top-hat will act as a box trap in transversal and longitudinal direction, while its Gaussian edges would conserve the adiabaticity required to limit interface resistances [70].

It would then be possible to project large structures in longitudinal and transversal direction. Interesting applications are triangular lattices exhibiting flat bands [274] which enhance the critical current in the DC Josephson effect. Moreover, while lattice experiments in the field of quantum gases rely primarily on microscopic observables the connection between the intrinsic (e.g. conductivity) and extrinsic (e.g. conductance) observables are less clear. Performing transport experiments through optical lattices would elucidate the extrinsic properties of said lattices. Notably, entropy transport is cumbersome to study in microscopic systems [239] but could be readily done via the external reservoirs providing a thermodynamic drain and source. The band-structure of a non-interacting 1D lattice [61] will invert the advective response of the entropy transport at the upper band-edge regime due to the suppression of transport in the gap. The entropy transport through a Fermi Hubbard model is more difficult to calculate and is subject of recent theoretical work [275, 276]. Finally, transport through shaken optical lattices would be an application combining the flexibility of spatial light modulation and the transport setup. The digital micro mirror device can already project potential landscapes changing at a rate of $\sim 20 \times 10^3$ FPS.

12.3 EXPERIMENTAL APPARATUS IMPROVEMENTS

The loading of atoms from the compressed MOT to the resonator dipole trap is the major limitation of the experiment in terms of atom-number. The reason is the limited depth of the dipole trap compared to the temperature of the compressed MOT which is above the Doppler temperature limit. There are two possibilities to resolve this:

- **Grey molasses cooling.** Gray molasses cooling has been established in ^{6}Li [277, 278] and provides an all optical way to reach temperatures below the Doppler limit. The implementation of gray molasses cooling would require a second laser setup addressing the D1 manifold, which would be readily available due to the recent upgrade of the MOT laser. In addition, since gray-molasses relies on the light shift of atoms for cooling it requires high intensities. In the current MOT setup the cooler and repumper beams are too large to reach the required intensities which would mean reducing their waist. Finding the correct waist requires finding a sweet spot between MOT loading and gray-molasses cooling. Importantly, laser cooling techniques reduce the phase-space density but usually with a reduction of density thus possibly worsening the overlap between the resonator mode and the cold cloud.

- **Enhancing the resonator trap.** The second possibility would be the addition of a high-power laser acting as a strong dimple in the resonator trap. A 30 W laser, already in the lab, could be focused to a 50 µm waist which would create a dimple trap deep enough ($U \approx 470\,\mu K$) to load the hot atoms from the compressed MOT.

BIBLIOGRAPHY

1. Rahmstorf, S. Ocean circulation and climate during the past 120,000 years. *Nature* **419,** 207–214. doi:10.1038/nature01090 (Sept. 2002) (cit. on p. 1).
2. Saba, V. S. *et al.* Enhanced warming of the Northwest Atlantic Ocean under climate change. *Journal of Geophysical Research: Oceans* **121,** 118–132. doi:10.1002/2015JC011346 (2016) (cit. on p. 1).
3. Callen, H. B. *Thermodynamics and an Introduction to Thermostatistics, 2nd Edition | Wiley* 2nd (Wiley, 1991) (cit. on pp. 1, 2, 22, 26, 172).
4. Balian, R. *From Microphysics to Macrophysics: Methods and Applications of Statistical Physics* (Springer, 2007) (cit. on p. 1).
5. Van Wees, B. J. *et al.* Quantized conductance of point contacts in a two-dimensional electron gas. *Physical Review Letters* **60,** 848–850. doi:10.1103/PhysRevLett.60.848 (Feb. 1988) (cit. on pp. 1, 25).
6. Krinner, S. *et al.* Observation of quantized conductance in neutral matter. *Nature* **517,** 64. doi:10.1038/nature14049 (Dec. 2014) (cit. on pp. 1, 2, 20, 25, 131).
7. Tinkham, M. *Introduction to superconductivity* 2nd ed (McGraw Hill, New York, 1996) (cit. on pp. 1, 53, 56, 58–61, 161, 201).
8. Likharev, K. K. Superconducting weak links. *Reviews of Modern Physics* **51,** 101–159. doi:10.1103/RevModPhys.51.101 (Jan. 1979) (cit. on pp. 1, 49, 54–56, 58, 59, 161).
9. Stormer, H. L., Tsui, D. C. & Gossard, A. C. The fractional quantum Hall effect. *Reviews of Modern Physics* **71,** S298–S305. doi:10.1103/RevModPhys.71.S298 (Mar. 1999) (cit. on p. 2).
10. Giamarchi, T. *Quantum physics in one dimension The international series of monographs on physics* **121** (Clarendon ; Oxford University Press, Oxford : New York, 2004) (cit. on p. 2).
11. Beenakker, C. Search for Majorana Fermions in Superconductors. *Annual Review of Condensed Matter Physics* **4,** 113–136. doi:10.1146/annurev-conmatphys-030212-184337 (2013) (cit. on pp. 2, 127, 158).
12. Carusotto, I. & Ciuti, C. Quantum fluids of light. *Rev. Mod. Phys.* **85,** 299–366. doi:10.1103/RevModPhys.85.299 (Feb. 2013) (cit. on p. 2).
13. Ramm, M., Pruttivarasin, T. & Häffner, H. Energy transport in trapped ion chains. *New Journal of Physics* **16,** 063062. doi:10.1088/1367-2630/16/6/063062 (June 2014) (cit. on p. 2).
14. Günter, G. *et al.* Observing the Dynamics of Dipole-Mediated Energy Transport by Interaction-Enhanced Imaging. *Science* **342,** 954–956. doi:10.1126/science.1244843 (2013) (cit. on p. 2).
15. Ketterle, W., Durfee, D. S. & Stamper-Kurn, D. M. in *Bose-Einstein Condensation in Atomic Gases* 67–176 (IOS Press, 1999). doi:10.3254/978-1-61499-225-7-67 (cit. on p. 2).
16. Ketterle, W. & Zwierlein, M. W. in *Ultra-cold Fermi Gases* 95–287 (IOS Press, 2007). doi:10.3254/978-1-58603-846-5-95 (cit. on pp. 2, 16, 52, 162).

17. Matthews, M. R. *et al.* Vortices in a Bose-Einstein Condensate. *Physical Review Letters* **83,** 2498–2501. doi:`10.1103/PhysRevLett.83.2498` (Sept. 1999) (cit. on p. 2).
18. Madison, K. W. *et al.* Vortex Formation in a Stirred Bose-Einstein Condensate. *Physical Review Letters* **84,** 806–809. doi:`10.1103/PhysRevLett.84.806` (Jan. 2000) (cit. on p. 2).
19. Kinast, J. *et al.* Evidence for Superfluidity in a Resonantly Interacting Fermi Gas. *Physical Review Letters* **92,** 150402. doi:`10.1103/PhysRevLett.92.150402` (Apr. 2004) (cit. on pp. 2, 60).
20. Zwierlein, M. W. *et al.* Vortices and superfluidity in a strongly interacting Fermi gas. *Nature* **435,** 1047–1051. doi:`10.1038/nature03858` (June 2005) (cit. on p. 2).
21. Chin, J. K. *et al.* Evidence for superfluidity of ultracold fermions in an optical lattice. *Nature* **443,** 961–964. doi:`10.1038/nature05224` (Oct. 2006) (cit. on p. 2).
22. Sidorenkov, L. A. *et al.* Second sound and the superfluid fraction in a Fermi gas with resonant interactions. *Nature* **498,** 78–81. doi:`10.1038/nature12136` (June 2013) (cit. on pp. 2, 53, 60, 216).
23. Hoinka, S. *et al.* Goldstone mode and pair-breaking excitations in atomic Fermi superfluids. *Nature Physics* **13,** 943–946. doi:`10.1038/nphys4187` (Oct. 2017) (cit. on pp. 2, 187, 200, 214).
24. Li, X. *et al.* Second sound attenuation near quantum criticality. *Science* **375,** 528–533. doi:`10.1126/science.abi4480` (Feb. 2022) (cit. on pp. 2, 53, 216).
25. Ramanathan, A. *et al.* Superflow in a Toroidal Bose-Einstein Condensate: An Atom Circuit with a Tunable Weak Link. *Physical Review Letters* **106,** 130401. doi:`10.1103/PhysRevLett.106.130401` (Mar. 2011) (cit. on p. 2).
26. Eckel, S. *et al.* Hysteresis in a quantized superfluid 'atomtronic' circuit. *Nature* **506,** 200–203. doi:`10.1038/nature12958` (Feb. 2014) (cit. on p. 2).
27. Sommer, A. *et al.* Universal spin transport in a strongly interacting Fermi gas. *Nature* **472,** 201–204. doi:`10.1038/nature09989` (Apr. 2011) (cit. on pp. 2, 23, 187).
28. Patel, P. B. *et al.* Universal sound diffusion in a strongly interacting Fermi gas. *Science* **370,** 1222–1226. doi:`10.1126/science.aaz5756` (Dec. 2020) (cit. on pp. 2, 53, 216).
29. Cheneau, M. *et al.* Light-cone-like spreading of correlations in a quantum many-body system. *Nature* **481,** 484–487. doi:`10.1038/nature10748` (Jan. 2012) (cit. on p. 2).
30. Fukuhara, T. *et al.* Quantum dynamics of a mobile spin impurity. *Nature Physics* **9,** 235–241. doi:`10.1038/nphys2561` (Apr. 2013) (cit. on p. 2).
31. Nichols, M. A. *et al.* Spin transport in a Mott insulator of ultracold fermions. *Science* **363,** 383–387. doi:`10.1126/science.aat4387` (Jan. 2019) (cit. on p. 2).
32. Ji, G. *et al.* Coupling a Mobile Hole to an Antiferromagnetic Spin Background: Transient Dynamics of a Magnetic Polaron. *Physical Review X* **11,** 021022. doi:`10.1103/PhysRevX.11.021022` (Apr. 2021) (cit. on p. 2).

33. Valtolina, G. *et al.* Josephson effect in fermionic superfluids across the BEC-BCS crossover. *Science* **350,** 1505–1508. doi:`10.1126/science.aac9725` (Dec. 2015) (cit. on pp. 2, 60, 162).

34. Del Pace, G. *et al.* Tunneling Transport of Unitary Fermions across the Superfluid Transition. *Physical Review Letters* **126,** 055301. doi:`10.1103/PhysRevLett.126.055301` (Feb. 2021) (cit. on pp. 2, 60, 162, 200).

35. Krinner, S. *et al.* Observation of a Fragmented, Strongly Interacting Fermi Gas. *Physical Review Letters* **115,** 045302. doi:`10.1103/PhysRevLett.115.045302` (July 2015) (cit. on p. 2).

36. Lebrat, M. *Microscopic Control and Mesoscopic Transport in Quantum Gases* PhD Thesis (ETH Zurich, Zurich, Mar. 2019) (cit. on pp. 2, 17, 65, 78).

37. Stadler, D. *et al.* Observing the drop of resistance in the flow of a superfluid Fermi gas. *Nature* **491,** 736–739. doi:`10.1038/nature11613` (Nov. 2012) (cit. on pp. 2, 3, 60, 196, 199).

38. Husmann, D. *et al.* Connecting strongly correlated superfluids by a quantum point contact. *Science* **350,** 1498–1501. doi:`10.1126/science.aac9584` (Dec. 2015) (cit. on pp. 2, 3, 49, 59, 60, 149, 162, 167, 172, 174, 199, 214).

39. Breuer, H.-P. & Petruccione, F. *The Theory of Open Quantum Systems* (Oxford University Press, Oxford ; New York, 2002) (cit. on pp. 2, 36, 131, 165, 201).

40. Ku, M. J. H. *et al.* Revealing the Superfluid Lambda Transition in the Universal Thermodynamics of a Unitary Fermi Gas. *Science* **335,** 563–567. doi:`10.1126/science.1214987` (Feb. 2012) (cit. on pp. 2, 3, 16, 161, 163–166, 170, 202).

41. Landau, L., Lifshitz, E. & Pitaevskii, L. *Statistical Physics Part II* Second Revised and Enlarged (Pergamon Press, 1969) (cit. on pp. 2, 49, 53, 161).

42. Andreev, A. F. The thermal conductivity of the intermediate state in superconductors. *Zhurnal Eksperimental'noj I Teoreticheskoj Fiziki* **46** (1964) (cit. on pp. 2, 49, 58–60, 201).

43. Shelly, C. D., Matrozova, E. A. & Petrashov, V. T. Resolving thermoelectric "paradox" in superconductors. *Science Advances* **2,** e1501250. doi:`10.1126/sciadv.1501250` (Feb. 2016) (cit. on pp. 2, 61).

44. Van Harlingen, D. J. Thermoelectric effects in the superconducting state. *Physica B+C. 16th International Conference on Low Temperature Physics, Part 3* **109-110,** 1710–1721. doi:`10.1016/0378-4363(82)90195-4` (July 1982) (cit. on pp. 2, 22, 201).

45. Fornieri, A. & Giazotto, F. Towards phase-coherent caloritronics in superconducting circuits. *Nature Nanotechnology* **12,** 944–952. doi:`10.1038/nnano.2017.204` (Oct. 2017) (cit. on p. 2).

46. Hussein, R. *et al.* Nonlocal thermoelectricity in a Cooper-pair splitter. *Physical Review B* **99,** 075429. doi:`10.1103/PhysRevB.99.075429` (Feb. 2019) (cit. on p. 2).

47. Radousky, H. B. & Liang, H. Energy harvesting: an integrated view of materials, devices and applications. *Nanotechnology* **23,** 502001. doi:`10.1088/0957-4484/23/50/502001` (Nov. 2012) (cit. on p. 2).

48. Sothmann, B., Sánchez, R. & Jordan, A. N. Thermoelectric energy harvesting with quantum dots. *Nanotechnology* **26,** 032001. doi:10.1088/0957-4484/26/3/032001 (Dec. 2014) (cit. on p. 2).

49. Mastomäki, J. *et al.* InAs nanowire superconducting tunnel junctions: Quasiparticle spectroscopy, thermometry, and nanorefrigeration. *Nano Research* **10,** 3468–3475. doi:10.1007/s12274-017-1558-7 (Oct. 2017) (cit. on p. 2).

50. Bradley, D. I. *et al.* Direct measurement of the energy dissipated by quantum turbulence. *Nature Physics* **7,** 473–476. doi:10.1038/nphys1963 (June 2011) (cit. on p. 2).

51. Ibabe, A. *et al.* Joule spectroscopy of hybrid superconductor–semiconductor nanodevices. *Nature Communications* **14,** 2873. doi:10.1038/s41467-023-38533-2 (May 2023) (cit. on p. 2).

52. Pekola, J. P. & Karimi, B. *Colloquium* : Quantum heat transport in condensed matter systems. *Reviews of Modern Physics* **93,** 041001. doi:10.1103/RevModPhys.93.041001 (Oct. 2021) (cit. on p. 2).

53. Fleischhauer, M., Imamoglu, A. & Marangos, J. P. Electromagnetically induced transparency: Optics in coherent media. *Reviews of Modern Physics* **77,** 633–673. doi:10.1103/RevModPhys.77.633 (July 2005) (cit. on pp. 2, 42, 45, 149, 155, 217).

54. Lin, Y.-J., Jiménez-García, K. & Spielman, I. B. Spin-orbit-coupled Bose-Einstein condensates. *Nature* **471,** 83–86. doi:10.1038/nature09887 (Mar. 2011) (cit. on pp. 2, 128, 145, 156, 217).

55. Beeler, M. C. *et al.* The spin Hall effect in a quantum gas. *Nature* **498,** 201–204. doi:10.1038/nature12185 (June 2013) (cit. on pp. 2, 217).

56. Müller, M. *et al.* in *Advances in Atomic, Molecular, and Optical Physics* (eds Paul Berman, E. A. & Lin, C.) 1–80 (Academic Press, 2012). doi:10.1016/B978-0-12-396482-3.00001-6 (cit. on pp. 2, 128).

57. Daley, A. J. Quantum trajectories and open many-body quantum systems. *Advances in Physics* **63,** 77–149. doi:10.1080/00018732.2014.933502 (Mar. 2014) (cit. on pp. 2, 128, 139).

58. Syassen, N. *et al.* Strong Dissipation Inhibits Losses and Induces Correlations in Cold Molecular Gases. *Science* **320,** 1329–1331. doi:10.1126/science.1155309 (June 2008) (cit. on pp. 2, 128).

59. Barontini, G. *et al.* Controlling the Dynamics of an Open Many-Body Quantum System with Localized Dissipation. *Physical Review Letters* **110,** 035302. doi:10.1103/PhysRevLett.110.035302 (Jan. 2013) (cit. on pp. 2, 201).

60. Tomita, T. *et al.* Observation of the Mott insulator to superfluid crossover of a driven-dissipative Bose-Hubbard system. *Science Advances* **3,** e1701513. doi:10.1126/sciadv.1701513 (Dec. 2017) (cit. on pp. 2, 128, 201).

61. Lebrat, M. *et al.* Band and Correlated Insulators of Cold Fermions in a Mesoscopic Lattice. *Physical Review X* **8,** 011053. doi:10.1103/PhysRevX.8.011053 (Mar. 2018) (cit. on pp. 2, 3, 78, 144, 216, 218).

62. Zupancic, P. *et al.* Ultra-precise holographic beam shaping for microscopic quantum control. *Optics Express* **24,** 13881–13893. doi:10.1364/OE.24.013881 (June 2016) (cit. on pp. 3, 14, 72, 80).

63. Häusler, S. *et al.* Scanning Gate Microscope for Cold Atomic Gases. *Physical Review Letters* **119,** 030403. doi:10.1103/PhysRevLett.119.030403 (July 2017) (cit. on pp. 3, 78, 143).

64. Chin, C. *et al.* Feshbach resonances in ultracold gases. *Reviews of Modern Physics* **82,** 1225–1286. doi:10.1103/RevModPhys.82.1225 (Apr. 2010) (cit. on p. 3).

65. *The BCS-BEC Crossover and the Unitary Fermi Gas* (ed Zwerger, W.) *Lecture notes in physics* **836** (Springer, Heidelberg, 2012) (cit. on pp. 3, 50, 54, 165).

66. Haussmann, R. *et al.* Thermodynamics of the BCS-BEC crossover. *Physical Review A* **75,** 023610. doi:10.1103/PhysRevA.75.023610 (Feb. 2007) (cit. on pp. 3, 50).

67. Krinner, S. *et al.* Mapping out spin and particle conductances in a quantum point contact. *Proceedings of the National Academy of Sciences* **113,** 8144–8149. doi:10.1073/pnas.1601812113 (July 2016) (cit. on pp. 3, 52, 187, 189, 214).

68. Brantut, J.-P. *et al.* A Thermoelectric Heat Engine with Ultracold Atoms. *Science* **342,** 713–715. doi:10.1126/science.1242308 (Nov. 2013) (cit. on pp. 3, 171, 172).

69. Häusler, S. *et al.* Interaction-Assisted Reversal of Thermopower with Ultracold Atoms. *Physical Review X* **11,** 021034. doi:10.1103/PhysRevX.11.021034 (May 2021) (cit. on pp. 3, 60, 162, 164, 169, 171, 172, 174, 184, 187, 190, 195, 196, 198, 199).

70. Krinner, S. J. *Quantum Transport of Ultracold Atoms* PhD Thesis (ETH Zurich, 2015). doi:10.3929/ethz-a-010556528 (cit. on pp. 7–9, 15, 19, 20, 74, 218).

71. Häusler, S. *Mesoscopic heat and particle transport in ultracold Fermi gases* Doctoral Thesis (ETH Zurich, 2020). doi:10.3929/ethz-b-000488517 (cit. on pp. 7, 20, 22, 23, 26, 51, 71, 75–77, 80, 81, 174, 176, 190).

72. Foot, C. J. *Atomic Physics Oxford master series in physics* **7** (Oxford University Press, Oxford ; New York, 2005) (cit. on pp. 7, 27, 36).

73. Zimmermann, B. *Microscopy of ultra-cold fermionic lithium* PhD Thesis (ETH Zurich, 2010). doi:10.3929/ethz-a-006212123 (cit. on pp. 7, 9, 65, 68, 73, 84, 92, 95).

74. Lee, S. K., Kim, J. J. & Cho, D. Transformable optical dipole trap using a phase-modulated standing wave. *Physical Review A* **74,** 063401. doi:10.1103/PhysRevA.74.063401 (Dec. 2006) (cit. on pp. 10, 98).

75. Zener, C. & Fowler, R. H. Non-adiabatic crossing of energy levels. *Proceedings of the Royal Society of London. Series A, Containing Papers of a Mathematical and Physical Character* **137,** 696–702. doi:10.1098/rspa.1932.0165 (Jan. 1997) (cit. on p. 11).

76. Landau, L. Theory of the Superfluidity of Helium II. *Physical Review* **60,** 356–358. doi:10.1103/PhysRev.60.356 (Aug. 1941) (cit. on pp. 11, 169).

77. Schunck, C. H. *et al.* Feshbach resonances in fermionic ^{6}Li. *Physical Review A* **71,** 045601. doi:10.1103/PhysRevA.71.045601 (Apr. 2005) (cit. on p. 11).

78. Hung, C.-L. *et al.* Accelerating evaporative cooling of atoms into Bose-Einstein condensation in optical traps. *Physical Review A* **78,** 011604. doi:`10.1103/PhysRevA.78.011604` (July 2008) (cit. on pp. 11, 70, 133).
79. Müller, T. *Microscopic probing and manipulation of ultracold fermions* PhD Thesis (ETH Zurich, 2011). doi:`10.3929/ethz-a-006492339` (cit. on pp. 14, 65, 66, 69, 71, 76, 84).
80. Mohan, J. *Reducing noise in thermodynamic measurements on interacting Fermi gases* MA thesis (ETH Zurich, 2018) (cit. on pp. 14, 101, 103, 104).
81. Horikoshi, M. *et al.* Appropriate Probe Condition for Absorption Imaging of Ultracold ^{6}Li Atoms. *Journal of the Physical Society of Japan* **86,** 104301. doi:`10.7566/JPSJ.86.104301` (Sept. 2017) (cit. on pp. 15, 101, 104, 165).
82. Reinaudi, G. *et al.* Strong saturation absorption imaging of dense clouds of ultracold atoms. *Optics Letters* **32,** 3143–3145. doi:`10.1364/OL.32.003143` (Nov. 2007) (cit. on pp. 15, 104).
83. Ockeloen, C. F. *et al.* Detection of small atom numbers through image processing. *Physical Review A* **82,** 061606. doi:`10.1103/PhysRevA.82.061606` (Dec. 2010) (cit. on pp. 15, 104, 164).
84. Guajardo, E. R. S. *et al.* Higher-nodal collective modes in a resonantly interacting Fermi gas. *Physical Review A* **87,** 063601. doi:`10.1103/PhysRevA.87.063601` (June 2013) (cit. on p. 15).
85. Thomas, J. E., Kinast, J. & Turlapov, A. Virial Theorem and Universality in a Unitary Fermi Gas. *Physical Review Letters* **95,** 120402. doi:`10.1103/PhysRevLett.95.120402` (Sept. 2005) (cit. on p. 15).
86. Husmann, D. *Mesoscopic transport phenomena in a unitary Fermi gas* Doctoral Thesis (ETH Zurich, 2018). doi:`10.3929/ethz-b-000336240` (cit. on p. 17).
87. Husmann, D. *et al.* Breakdown of the Wiedemann–Franz law in a unitary Fermi gas. *Proceedings of the National Academy of Sciences,* 201803336. doi:`10.1073/pnas.1803336115` (Aug. 2018) (cit. on pp. 18, 22, 60, 78, 162, 171, 174, 175, 184, 187, 188, 198, 199, 203).
88. Chien, C.-C., Di Ventra, M. & Zwolak, M. Landauer, Kubo, and microcanonical approaches to quantum transport and noise: A comparison and implications for cold-atom dynamics. *Physical Review A* **90,** 023624. doi:`10.1103/PhysRevA.90.023624` (Aug. 2014) (cit. on p. 20).
89. Rammelmüller, L. *et al.* Finite-Temperature Equation of State of Polarized Fermions at Unitarity. *Physical Review Letters* **121,** 173001. doi:`10.1103/PhysRevLett.121.173001` (Oct. 2018) (cit. on p. 23).
90. Glazman, L. I. *et al.* Reflectionless quantum transport and fundamental ballistic-resistance steps in microscopic constrictions. *ZhETF Pisma Redaktsiiu* **48,** 218 (Aug. 1988) (cit. on p. 24).
91. Büttiker, M. Absence of backscattering in the quantum Hall effect in multiprobe conductors. *Physical Review B* **38,** 9375–9389. doi:`10.1103/PhysRevB.38.9375` (Nov. 1988) (cit. on p. 25).
92. Datta, S. *Electronic transport in mesoscopic systems* (Cambridge University Press, Cambridge; New York, 1995) (cit. on pp. 25, 132).

93. Imry, Y. in *Directions in Condensed Matter Physics Series on Directions in Condensed Matter Physics* Volume 1, 101–163 (WORLD SCIENTIFIC, Aug. 1986). doi:10.1142/9789814415309_0004 (cit. on p. 25).

94. Wharam, D. A. *et al.* One-dimensional transport and the quantisation of the ballistic resistance. *Journal of Physics C: Solid State Physics* **21,** L209. doi:10.1088/0022-3719/21/8/002 (Mar. 1988) (cit. on p. 25).

95. Bartha, L. *Spin-dependent transport of lithium-6 atoms in near-resonant light fields* MA thesis (ETH Zurich, Apr. 2017) (cit. on pp. 27, 30).

96. Gehm, M. *Properties of 6 Li* in (2003) (cit. on pp. 28, 31).

97. Brog, K. C., Eck, T. G. & Wieder, H. Fine and Hyperfine Structure of the 2^2P Term of ^{6}Li and ^{7}Li. *Physical Review* **153,** 91–103. doi:10.1103/PhysRev.153.91 (Jan. 1967) (cit. on p. 28).

98. Breit, G. & Rabi, I. I. Measurement of Nuclear Spin. *Physical Review* **38,** 2082–2083. doi:10.1103/PhysRev.38.2082.2 (Dec. 1931) (cit. on p. 30).

99. Cohen-Tannoudji, C., Dupont-Roc, J. & Grynberg, G. *Photons and atoms: introduction to quantum electrodynamics* Nachdr. (Wiley, Weinheim, 2004) (cit. on p. 36).

100. Lindblad, G. On the generators of quantum dynamical semigroups. *Communications in Mathematical Physics* **48,** 119–130 (Jan. 1976) (cit. on pp. 36, 128, 131).

101. Huang, M.-Z. *et al.* Superfluid Signatures in a Dissipative Quantum Point Contact. *Physical Review Letters* **130,** 200404. doi:10.1103/PhysRevLett.130.200404 (May 2023) (cit. on pp. 38, 78, 144–146, 149, 151, 162, 167, 174, 201–203, 212, 214).

102. Łącki, M. *et al.* Nanoscale "Dark State" Optical Potentials for Cold Atoms. *Physical Review Letters* **117,** 233001. doi:10.1103/PhysRevLett.117.233001 (Nov. 2016) (cit. on pp. 42, 145, 153–155, 217).

103. Kasapi, A. *et al.* Electromagnetically Induced Transparency: Propagation Dynamics. *Physical Review Letters* **74,** 2447–2450. doi:10.1103/PhysRevLett.74.2447 (Mar. 1995) (cit. on p. 45).

104. Gonzalez, O. & A, D. Floquet dynamics in open quantum systems and the non-ideal lambda system. doi:10.3929/ethz-b-000617013 (2023) (cit. on p. 47).

105. Ommen, V. & Benjamin, H. *Magnetic Field Stabilisation System for the Lithium Experiment* MA thesis (ETH Zurich, Oct. 2021). doi:10.3929/ethz-b-000509713 (cit. on pp. 47, 110, 112).

106. Josephson, B. D. Possible new effects in superconductive tunnelling. *Physics Letters* **1,** 251–253. doi:10.1016/0031-9163(62)91369-0 (July 1962) (cit. on pp. 49, 54, 161).

107. Sauls, J. A. Andreev bound states and their signatures. *Philosophical Transactions of the Royal Society A: Mathematical, Physical and Engineering Sciences* **376,** 20180140. doi:10.1098/rsta.2018.0140 (Aug. 2018) (cit. on p. 49).

108. en. in *Nonequilibrium Electrons and Phonons in Superconductors: Selected Topics in Superconductivity* (eds Gulian, A. M. & Zharkov, G. F.) 213–254 (Springer US, Boston, MA, 2002). doi:10.1007/0-306-47087-X_9 (cit. on pp. 49, 59).

109. Goulko, O. & Wingate, M. Thermodynamics of balanced and slightly spin-imbalanced Fermi gases at unitarity. *Physical Review A* **82,** 053621. doi:10.1103/PhysRevA.82.053621 (Nov. 2010) (cit. on p. 50).

110. Haussmann, R. & Zwerger, W. Thermodynamics of a trapped unitary Fermi gas. *Physical Review A* **78,** 063602. doi:10.1103/PhysRevA.78.063602 (Dec. 2008) (cit. on pp. 52, 163, 165, 202).

111. Schirotzek, A. *et al.* Determination of the Superfluid Gap in Atomic Fermi Gases by Quasiparticle Spectroscopy. *Physical Review Letters* **101,** 140403. doi:10.1103/PhysRevLett.101.140403 (Oct. 2008) (cit. on pp. 52, 127, 145, 161, 200).

112. Bardeen, J., Cooper, L. N. & Schrieffer, J. R. Theory of Superconductivity. *Physical Review* **108,** 1175–1204. doi:10.1103/PhysRev.108.1175 (Dec. 1957) (cit. on p. 52).

113. Giorgini, S., Pitaevskii, L. P. & Stringari, S. Theory of ultracold atomic Fermi gases. *Reviews of Modern Physics* **80,** 1215–1274. doi:10.1103/RevModPhys.80.1215 (Oct. 2008) (cit. on pp. 52–54).

114. Shin, Y. *et al.* Observation of Phase Separation in a Strongly Interacting Imbalanced Fermi Gas. *Physical Review Letters* **97,** 030401. doi:10.1103/PhysRevLett.97.030401 (July 2006) (cit. on p. 52).

115. Behrle, A. *et al.* Higgs mode in a strongly interacting fermionic superfluid. *Nature Physics* **14,** 781–785. doi:10.1038/s41567-018-0128-6 (Aug. 2018) (cit. on p. 53).

116. Shimano, R. & Tsuji, N. Higgs Mode in Superconductors. *Annual Review of Condensed Matter Physics* **11,** 103–124. doi:10.1146/annurev-conmatphys-031119-050813 (Mar. 2020) (cit. on p. 53).

117. Bardeen, J. Critical Fields and Currents in Superconductors. *Reviews of Modern Physics* **34,** 667–681. doi:10.1103/RevModPhys.34.667 (Oct. 1962) (cit. on p. 53).

118. Schmidt, V. V. *The Physics of Superconductors* (eds Müller, P. & Ustinov, A. V.) doi:10.1007/978-3-662-03501-6 (Springer, Berlin, Heidelberg, 1997) (cit. on pp. 53, 54, 56–58, 60, 201).

119. Golubov, A. A., Kupriyanov, M. Y. & Il'ichev, E. The current-phase relation in Josephson junctions. *Reviews of Modern Physics* **76,** 411–469. doi:10.1103/RevModPhys.76.411 (Apr. 2004) (cit. on pp. 54, 55, 59).

120. Anderson, P. W. & Dayem, A. H. Radio-Frequency Effects in Superconducting Thin Film Bridges. *Physical Review Letters* **13,** 195–197. doi:10.1103/PhysRevLett.13.195 (Aug. 1964) (cit. on p. 54).

121. Levy Yeyati, A., Martín-Rodero, A. & García-Vidal, F. J. Self-consistent theory of superconducting mesoscopic weak links. *Physical Review B* **51,** 3743–3753. doi:10.1103/PhysRevB.51.3743 (Feb. 1995) (cit. on p. 55).

122. Martín-Rodero, A., García-Vidal, F. J. & Levy Yeyati, A. Microscopic theory of Josephson mesoscopic constrictions. *Physical Review Letters* **72,** 554–557. doi:10.1103/PhysRevLett.72.554 (Jan. 1994) (cit. on pp. 56, 174, 188).

123. Sols, F. & Ferrer, J. Crossover from the Josephson effect to bulk superconducting flow. *Physical Review B* **49,** 15913–15919. doi:10.1103/PhysRevB.49.15913 (June 1994) (cit. on p. 56).

124. Cuevas, J. C., Martín-Rodero, A. & Yeyati, A. L. Hamiltonian approach to the transport properties of superconducting quantum point contacts. *Physical Review B* **54,** 7366–7379. doi:`10.1103/PhysRevB.54.7366` (Sept. 1996) (cit. on pp. 57, 59–61, 174, 178, 188, 189).

125. Notarys, H. A. & Mercereau, J. E. Dynamics of small superconductors. *Physica* **55,** 424–431. doi:`10.1016/0031-8914(71)90284-9` (Oct. 1971) (cit. on pp. 57, 59).

126. Blonder, G. E., Tinkham, M. & Klapwijk, T. M. Transition from metallic to tunneling regimes in superconducting microconstrictions: Excess current, charge imbalance, and supercurrent conversion. *Physical Review B* **25,** 4515–4532. doi:`10.1103/PhysRevB.25.4515` (Apr. 1982) (cit. on pp. 58, 60, 189).

127. Klapwijk, T. M., Blonder, G. E. & Tinkham, M. Explanation of subharmonic energy gap structure in superconducting contacts. *Physica B+C. 16th International Conference on Low Temperature Physics, Part 3* **109-110,** 1657–1664. doi:`10.1016/0378-4363(82)90189-9` (July 1982) (cit. on pp. 58–60).

128. Pippard, A. B., Shepherd, J. G. & Tindall, D. A. Resistance of superconducting-normal interfaces. *Proceedings of the Royal Society of London. A. Mathematical and Physical Sciences* **324,** 17–35. doi:`10.1098/rspa.1971.0125` (Jan. 1997) (cit. on p. 59).

129. Skocpol, W. J., Beasley, M. R. & Tinkham, M. Phase-slip centers and nonequilibrium processes in superconducting tin microbridges. *Journal of Low Temperature Physics* **16,** 145–167. doi:`10.1007/BF00655865` (July 1974) (cit. on p. 59).

130. Langer, J. S. & Fisher, M. E. Intrinsic Critical Velocity of a Superfluid. *Physical Review Letters* **19,** 560–563. doi:`10.1103/PhysRevLett.19.560` (Sept. 1967) (cit. on p. 59).

131. Ambegaokar, V. & Halperin, B. I. Voltage Due to Thermal Noise in the dc Josephson Effect. *Physical Review Letters* **22,** 1364–1366. doi:`10.1103/PhysRevLett.22.1364` (June 1969) (cit. on p. 59).

132. McCumber, D. E. & Halperin, B. I. Time Scale of Intrinsic Resistive Fluctuations in Thin Superconducting Wires. *Physical Review B* **1,** 1054–1070. doi:`10.1103/PhysRevB.1.1054` (Feb. 1970) (cit. on p. 59).

133. Halperin, B. I., Refael, G. & Demler, E. Resistance in superconductors. *International Journal of Modern Physics B* **24,** 4039–4080. doi:`10.1142/S021797921005644X` (Aug. 2010) (cit. on pp. 59, 61, 200).

134. Varoquaux, E. Anderson's considerations on the flow of superfluid helium: Some offshoots. *Reviews of Modern Physics* **87,** 803–854. doi:`10.1103/RevModPhys.87.803` (Aug. 2015) (cit. on pp. 59, 161, 169, 170, 199).

135. Bartenstein, M. *et al.* Collective Excitations of a Degenerate Gas at the BEC-BCS Crossover. *Physical Review Letters* **92,** 203201. doi:`10.1103/PhysRevLett.92.203201` (May 2004) (cit. on p. 60).

136. Uchino, S. Role of Nambu-Goldstone modes in the fermionic-superfluid point contact. *Physical Review Research* **2,** 023340. doi:`10.1103/PhysRevResearch.2.023340` (June 2020) (cit. on pp. 60, 189, 199, 213, 216).

137. Luick, N. *et al.* An ideal Josephson junction in an ultracold two-dimensional Fermi gas. *Science* **369,** 89–91. doi:`10.1126/science.aaz2342` (July 2020) (cit. on p. 60).

138. Burchianti, A. *et al.* Connecting Dissipation and Phase Slips in a Josephson Junction between Fermionic Superfluids. *Physical Review Letters* **120,** 025302. doi:`10.1103/PhysRevLett.120.025302` (Jan. 2018) (cit. on p. 60).

139. Pershoguba, S. S. & Glazman, L. I. Thermopower and thermal conductance of a superconducting quantum point contact. *Physical Review B* **99,** 134514. doi:`10.1103/PhysRevB.99.134514` (Apr. 2019) (cit. on p. 61).

140. Bardeen, J., Rickayzen, G. & Tewordt, L. Theory of the Thermal Conductivity of Superconductors. *Physical Review* **113,** 982–994. doi:`10.1103/PhysRev.113.982` (Feb. 1959) (cit. on p. 61).

141. Mamin, H. J., Clarke, J. & Van Harlingen, D. J. Charge imbalance induced by a temperature gradient in superconducting aluminum. *Physical Review B* **29,** 3881–3890. doi:`10.1103/PhysRevB.29.3881` (Apr. 1984) (cit. on p. 61).

142. Swenumson, R. D. & Even, U. Continuous flow reflux oven as the source of an effusive molecular Cs beam. *Review of Scientific Instruments* **52,** 559–561. doi:`10.1063/1.1136639` (Apr. 1981) (cit. on p. 65).

143. Drullinger, R., Glaze, D. & Sullivan, D. *A Recirculating Oven for Atomic Beam Frequency Standards* in *39th Annual Symposium on Frequency Control* (IEEE, 1985), 13–17. doi:`10.1109/FREQ.1985.200811` (cit. on p. 65).

144. Merkel, B. *et al.* Magnetic field stabilization system for atomic physics experiments. *Review of Scientific Instruments* **90,** 044702. doi:`10.1063/1.5080093` (Apr. 2019) (cit. on pp. 68, 110).

145. Stadler, D. *Mesoscopic conduction in ultracold Fermi gases* PhD Thesis (ETH Zurich, 2014). doi:`10.3929/ethz-a-010139405` (cit. on p. 74).

146. Lebrat, M. *et al.* Quantized Conductance through a Spin-Selective Atomic Point Contact. *Physical Review Letters* **123,** 193605. doi:`10.1103/PhysRevLett.123.193605` (Nov. 2019) (cit. on pp. 78, 145, 146, 218).

147. Corman, L. *et al.* Quantized conductance through a dissipative atomic point contact. *Physical Review A* **100,** 053605. doi:`10.1103/PhysRevA.100.053605` (Nov. 2019) (cit. on pp. 78, 145, 146, 201, 202).

148. De Léséleuc, S. *Digital Micromirror Devices* tech. rep. (Aug. 2014) (cit. on p. 78).

149. Mohan, J. *Arbitrary 2D Optical Potentials with a Digital Micro Mirror Device* Semester Thesis (ETH Zurich, 2018) (cit. on pp. 78, 81, 216).

150. Rabec, F. *Generating Optical Lattices with a Digital Micromirror Device* MA thesis (ETH Zurich, 2021) (cit. on pp. 78, 216).

151. Lee, W.-H. Binary Synthetic Holograms. *Applied Optics* **13,** 1677–1682. doi:`10.1364/AO.13.001677` (July 1974) (cit. on p. 81).

152. Eismann, U. *et al.* An all-solid-state laser source at 671 nm for cold atom experiments with lithium. *Applied Physics B - Laser and Optics* **106,** 25. doi:`10.1007/s00340-011-4693-y` (2012) (cit. on p. 84).

153. Agrawal, G. P. en. in *Guided Wave Optical Components and Devices* (ed Pal, B. P.) 131–153 (Academic Press, Burlington, Jan. 2006). doi:`10.1016/B978-012088481-0/50010-3` (cit. on p. 84).

154. Boyd, R. W. *Nonlinear optics* 3rd ed (Academic Press, Amsterdam ; Boston, 2008) (cit. on pp. 84, 87).

155. Fejer, M. *et al.* Quasi-phase-matched second harmonic generation: tuning and tolerances. *IEEE Journal of Quantum Electronics* **28,** 2631–2654. doi:`10.1109/3.161322` (Nov. 1992) (cit. on p. 84).

156. Rabec, F. *A 671nm laser source, for a* ^{6}*Li cold atom experiment* Semester Thesis (ETH Zurich, 2020) (cit. on p. 84).

157. Woodbury, E. & Ng, W. Ruby laser operation in the near IR. *proc. IRE* **50,** 2347–2348 (1962) (cit. on p. 84).

158. Stolen, R., Ippen, E. & Tynes, A. Raman oscillation in glass optical waveguide. *Applied Physics Letters* **20,** 62–64. doi:`10.1063/1.1654046` (1972) (cit. on p. 84).

159. Chang, D. *et al.* Efficient cascaded Raman generation and signal amplification at 1.3 µm in GeO2-doped single-mode fibre. *Optics Communications* **142,** 289–293. doi:`10.1016/S0030-4018(97)00281-2` (1997) (cit. on p. 84).

160. Dianov, E. Raman fiber amplifiers for the spectral region near 1.3 µm. *Laser Physics* **6,** 579–581 (1996) (cit. on p. 84).

161. Chernikov, S. *et al.* High-gain, monolithic, cascaded fibre Raman amplifier operating at 1.3 µm. *Electronics Letters* **31,** 472–473. doi:`10.1049/el:19950312` (1995) (cit. on p. 84).

162. Stolen, R. H. & Ippen, E. P. Raman gain in glass optical waveguides. *Applied Physics Letters* **22,** 276–278. doi:`10.1063/1.1654637` (Oct. 2003) (cit. on pp. 84, 85).

163. Paschotta, R. *et al.* 82% Efficient continuous-wave frequency doubling of 1.06 µm with a monolithic MgO:LiNbO$_3$ resonator. *Optics Letters* **19,** 1325–1327. doi:`10.1364/OL.19.001325` (Sept. 1994) (cit. on p. 86).

164. Zhou, M. *et al.* 52% optical-to-optical conversion efficiency in a compact 1.5 W 532 nm second harmonic generation laser with intracavity periodically-poled MgO:LiNbO3. *Laser Physics* **20,** 1568–1571. doi:`10.1134/S1054660X10130232` (July 2010) (cit. on p. 86).

165. Schwesyg, J. R. *et al. Optical loss mechanisms in magnesium-doped lithium niobate crystals in the 300 to 2950 nm wavelength range* in *Advances in Optical Materials (2011), paper AIThE3* (Optica Publishing Group, Feb. 2011), AIThE3. doi:`10.1364/AIOM.2011.AIThE3` (cit. on p. 86).

166. Risk, W. P., Gosnell, T. R. & Nurmikko, A. V. *Compact Blue-Green Lasers* doi:`10.1017/CBO9780511606502` (Cambridge University Press, Cambridge, 2003) (cit. on p. 87).

167. Boyd, G. D. & Kleinman, D. A. Parametric Interaction of Focused Gaussian Light Beams. *Journal of Applied Physics* **39,** 3597–3639. doi:`10.1063/1.1656831` (July 1968) (cit. on p. 87).

168. Sellmeier, W. Ueber die durch die Aetherschwingungen erregten Mitschwingungen der Körpertheilchen und deren Rückwirkung auf die ersteren, besonders zur Erklärung der Dispersion und ihrer Anomalien. *Annalen der Physik* **223,** 386–403. doi:`10.1002/andp.18722231105` (1872) (cit. on p. 87).

169. Ghosh, G. Sellmeier coefficients and dispersion of thermo-optic coefficients for some optical glasses. *Applied Optics* **36,** 1540–1546. doi:`10.1364/AO.36.001540` (Mar. 1997) (cit. on p. 87).

170. Gayer, O. *et al.* Temperature and wavelength dependent refractive index equations for MgO-doped congruent and stoichiometric LiNbO3. *Applied Physics B* **91,** 343–348. doi:`10.1007/s00340-008-2998-2` (May 2008) (cit. on p. 87).

171. Armstrong, J. A. *et al.* Interactions between Light Waves in a Nonlinear Dielectric. *Physical Review* **127,** 1918–1939. doi:`10.1103/PhysRev.127.1918` (Sept. 1962) (cit. on p. 87).

172. Kumar, S. C. *et al.* High-efficiency, multicrystal, single-pass, continuous-wave second harmonic generation. *Optics Express* **19,** 11152. doi:`10.1364/OE.19.011152` (June 2011) (cit. on p. 88).

173. Glass, A. M. The Photorefractive Effect. *Optical Engineering* **17,** 470–479. doi:`10.1117/12.7972267` (Oct. 1978) (cit. on pp. 91, 92).

174. Li, G., Wang, J. & Cui, Y. The origin of inhibition of high power second harmonic generation in periodically poled lithium niobate crystal. *Journal of Optics* **17,** 105504. doi:`10.1088/2040-8978/17/10/105504` (Oct. 2015) (cit. on p. 92).

175. Schünemann, U. *et al.* Simple scheme for tunable frequency offset locking of two lasers. *Review of Scientific Instruments* **70,** 242–243. doi:`10.1063/1.1149573` (Jan. 1999) (cit. on p. 92).

176. Drever, R. W. P. *et al.* Laser phase and frequency stabilization using an optical resonator. *Applied Physics B* **31,** 97–105. doi:`10.1007/BF00702605` (June 1983) (cit. on p. 96).

177. Black, E. D. An introduction to Pound–Drever–Hall laser frequency stabilization. *American Journal of Physics* **69,** 79–87. doi:`10.1119/1.1286663` (Jan. 2001) (cit. on p. 96).

178. Zhang, W. *et al.* Reduction of residual amplitude modulation to 1×10^{-6} for frequency modulation and laser stabilization. *Optics Letters* **39,** 1980. doi:`10.1364/OL.39.001980` (Apr. 2014) (cit. on p. 96).

179. Li, Z. *et al.* Reduction of zero baseline drift of the Pound–Drever–Hall error signal with a wedged electro-optical crystal for squeezed state generation. *Optics Letters* **41,** 3331–3334. doi:`10.1364/OL.41.003331` (July 2016) (cit. on p. 96).

180. Donley, E. A. *et al.* Double-pass acousto-optic modulator system. *Review of Scientific Instruments* **76,** 063112. doi:`10.1063/1.1930095` (June 2005) (cit. on p. 96).

181. Neuhaus, L. *et al.* *PyRPL (Python Red Pitaya Lockbox) — An open-source software package for FPGA-controlled quantum optics experiments* in *2017 Conference on Lasers and Electro-Optics Europe & European Quantum Electronics Conference (CLEO/Europe-EQEC)* (June 2017), 1–1. doi:`10.1109/CLEOE-EQEC.2017.8087380` (cit. on pp. 100, 116).

182. Stenger, J. *et al.* Spin domains in ground-state Bose–Einstein condensates. *Nature* **396,** 345–348. doi:`10.1038/24567` (Nov. 1998) (cit. on p. 101).

183. Higbie, J. M. *et al.* Direct Nondestructive Imaging of Magnetization in a Spin-1 Bose-Einstein Gas. *Physical Review Letters* **95,** 050401. doi:`10.1103/PhysRevLett.95.050401` (July 2005) (cit. on p. 101).

184. Cumming, R. C. The Serrodyne Frequency Translator. *Proceedings of the IRE* **45,** 175–186. doi:`10.1109/JRPROC.1957.278387` (Feb. 1957) (cit. on pp. 114, 116).

185. Van Ommen, B. *High Transmission Optical Cleaning Cavity* Semester Thesis (ETH Zurich, 2021) (cit. on p. 114).
186. Black, E. D. An introduction to Pound–Drever–Hall laser frequency stabilization. *American Journal of Physics* **69,** 79–87. doi:`10.1119/1.1286663` (Dec. 2000) (cit. on p. 116).
187. Johnson, L. & Cox, C. Serrodyne optical frequency translation with high sideband suppression. *Journal of Lightwave Technology* **6,** 109–112. doi:`10.1109/50.3974` (Jan. 1988) (cit. on p. 116).
188. Johnson, D. M. S. *et al.* Broadband optical serrodyne frequency shifting. *Optics Letters* **35,** 745. doi:`10.1364/OL.35.000745` (Mar. 2010) (cit. on p. 116).
189. Holland, C. M., Lu, Y. & Cheuk, L. W. Synthesizing optical spectra using computer-generated holography techniques. *New Journal of Physics* **23,** 033028. doi:`10.1088/1367-2630/abe973` (Mar. 2021) (cit. on p. 116).
190. Peters, L. Servo-based mirror motor. doi:`10.3929/ethz-b-000605617` (2023) (cit. on p. 117).
191. Setiawan, W. *Fermi Gas Microscope* PhD Thesis (Harvard University, Aug. 2012) (cit. on p. 119).
192. Liu, Z. *An agile precision digital-to-analog converter board for quantum optics experiments* Semester Thesis (ETH Zurich, 2020) (cit. on p. 119).
193. Pahl, L. & Pahl, D. A low-noise, high-speed and scalable FPGA-based analog signal generator for quantum gas experiments. doi:`10.3929/ethz-b-000571612` (2022) (cit. on p. 119).
194. Dönmez, B. *Towards a Distributed Low-Noise Signal Generation System for Quantum Gas Experiments: A Scalable FPGA-Based Design* MA thesis (ETH Zurich, 2022). doi:`10.3929/ethz-b-000594182` (cit. on pp. 119, 121).
195. Pahl, D. *et al.* *A low-noise and scalable FPGA-based analog signal generator for quantum gas experiments* in *2021 IEEE International Conference on Quantum Computing and Engineering (QCE)* (Oct. 2021), 450–451. doi:`10.1109/QCE52317.2021.00073` (cit. on p. 121).
196. Mustafa, E. Real-time Laser Beam Stabilization using FPGA. doi:`10.3929/ethz-b-000565634` (2022) (cit. on p. 122).
197. Bisson, G. FPGA Based Fast Camera Readout and Laser Beam Profiling (May 2021) (cit. on p. 122).
198. Žutić, I., Fabian, J. & Das Sarma, S. Spintronics: Fundamentals and applications. *Reviews of Modern Physics* **76,** 323–410. doi:`10.1103/RevModPhys.76.323` (Apr. 2004) (cit. on p. 127).
199. Kondo, J. Resistance Minimum in Dilute Magnetic Alloys. *Progress of Theoretical Physics* **32,** 37–49. doi:`10.1143/PTP.32.37` (July 1964) (cit. on pp. 127, 158, 217).
200. Shiba, H. Classical Spins in Superconductors. *Progress of Theoretical Physics* **40,** 435–451. doi:`10.1143/PTP.40.435` (Sept. 1968) (cit. on p. 127).
201. Kane, C. L. & Mele, E. J. Z_2 Topological Order and the Quantum Spin Hall Effect. *Physical Review Letters* **95,** 146802. doi:`10.1103/PhysRevLett.95.146802` (Sept. 2005) (cit. on p. 127).

202. Carlini, F. & Stringari, S. Spin drag and fast response in a quantum mixture of atomic gases. *Physical Review A* **104,** 023301. doi:10.1103/PhysRevA.104.023301 (Aug. 2021) (cit. on p. 127).

203. Jessen, P. S. & Deutsch, I. H. en. in *Advances In Atomic, Molecular, and Optical Physics* (eds Bederson, B. & Walther, H.) 95–138 (Academic Press, Jan. 1996). doi:10.1016/S1049-250X(08)60099-3 (cit. on p. 128).

204. Mandel, O. *et al.* Coherent Transport of Neutral Atoms in Spin-Dependent Optical Lattice Potentials. *Physical Review Letters* **91,** 010407. doi:10.1103/PhysRevLett.91.010407 (July 2003) (cit. on p. 128).

205. Wang, P. *et al.* Spin-Orbit Coupled Degenerate Fermi Gases. *Physical Review Letters* **109,** 095301. doi:10.1103/PhysRevLett.109.095301 (Aug. 2012) (cit. on pp. 128, 145, 156, 217).

206. Haack, G., Albert, M. & Flindt, C. Distributions of electron waiting times in quantum-coherent conductors. *Physical Review B* **90,** 205429. doi:10.1103/PhysRevB.90.205429 (Nov. 2014) (cit. on pp. 128, 217).

207. Moiseyev, N. *Non-Hermitian quantum mechanics* (Cambridge University Press, Cambridge ; New York, 2011) (cit. on pp. 128, 131).

208. Miri, M.-A. & Alù, A. Exceptional points in optics and photonics. *Science* **363,** eaar7709. doi:10.1126/science.aar7709 (Jan. 2019) (cit. on p. 128).

209. Büttiker, M. Scattering theory of current and intensity noise correlations in conductors and wave guides. *Physical Review B* **46,** 12485–12507. doi:10.1103/PhysRevB.46.12485 (Nov. 1992) (cit. on p. 128).

210. Datta, S. Steady-state quantum kinetic equation. *Physical Review B* **40,** 5830–5833. doi:10.1103/PhysRevB.40.5830 (Sept. 1989) (cit. on p. 128).

211. Sols, F. Scattering, dissipation, and transport in mesoscopic systems. *Annals of Physics* **214,** 386–438. doi:10.1016/S0003-4916(05)80005-3 (Mar. 1992) (cit. on p. 128).

212. Amico, A. *et al.* Time-Resolved Observation of Competing Attractive and Repulsive Short-Range Correlations in Strongly Interacting Fermi Gases. *Physical Review Letters* **121,** 253602. doi:10.1103/PhysRevLett.121.253602 (Dec. 2018) (cit. on p. 128).

213. Gericke, T. *et al.* High-resolution scanning electron microscopy of an ultracold quantum gas. *Nature Physics* **4,** 949–953 (2008) (cit. on pp. 128, 143).

214. Wessels, P. *et al.* Absolute strong-field ionization probabilities of ultracold rubidium atoms. *Communications Physics* **1,** 1–9. doi:10.1038/s42005-018-0032-5 (July 2018) (cit. on p. 128).

215. Pfau, T. *et al.* Loss of Spatial Coherence by a Single Spontaneous Emission. *Physical Review Letters* **73,** 1223–1226. doi:10.1103/PhysRevLett.73.1223 (Aug. 1994) (cit. on p. 128).

216. Bouganne, R. *et al.* Anomalous decay of coherence in a dissipative many-body system. *Nature Physics* **16,** 21–25. doi:10.1038/s41567-019-0678-2 (Jan. 2020) (cit. on p. 128).

217. Landauer, R. Spatial Variation of Currents and Fields Due to Localized Scatterers in Metallic Conduction. *IBM Journal of Research and Development* **1,** 223–231. doi:10.1147/rd.13.0223 (July 1957) (cit. on p. 131).

218. Büttiker, M. Four-Terminal Phase-Coherent Conductance. *Physical Review Letters* **57,** 1761–1764. doi:`10.1103/PhysRevLett.57.1761` (Oct. 1986) (cit. on p. 131).

219. Meservey, R. & Tedrow, P. M. Spin-polarized electron tunneling. *Physics Reports* **238,** 173–243. doi:`10.1016/0370-1573(94)90105-8` (Mar. 1994) (cit. on p. 135).

220. Rössler, C. *et al.* Transport properties of clean quantum point contacts. *New Journal of Physics* **13,** 113006. doi:`10.1088/1367-2630/13/11/113006` (Nov. 2011) (cit. on p. 135).

221. Marrows, C. H. Spin-polarised currents and magnetic domain walls. *Advances in Physics* **54,** 585–713. doi:`10.1080/00018730500442209` (Dec. 2005) (cit. on p. 135).

222. Fröml, H. *et al.* Fluctuation-Induced Quantum Zeno Effect. *Physical Review Letters* **122,** 040402. doi:`10.1103/PhysRevLett.122.040402` (Feb. 2019) (cit. on pp. 139, 155, 201).

223. Moore, M. G., Bergeman, T. & Olshanii, M. Scattering in tight atom waveguides. *Journal de Physique IV (Proceedings)* **116,** 69–86. doi:`10.1051/jp4:2004116003` (Oct. 2004) (cit. on p. 139).

224. Bauer, G. E. W., Saitoh, E. & van Wees, B. J. Spin caloritronics. *Nature Materials* **11,** 391–399. doi:`10.1038/nmat3301` (May 2012) (cit. on p. 144).

225. Murthy, P. A. *et al.* High-temperature pairing in a strongly interacting two-dimensional Fermi gas. *Science* **359,** 452–455. doi:`10.1126/science.aan5950` (Jan. 2018) (cit. on pp. 145, 200).

226. Wang, Y. *et al.* Dark State Optical Lattice with a Subwavelength Spatial Structure. *Physical Review Letters* **120,** 083601. doi:`10.1103/PhysRevLett.120.083601` (Feb. 2018) (cit. on pp. 145, 153, 217).

227. Teo, B. K. *et al.* Autler-Townes spectroscopy of the 5S1/2-5P3/2-44D cascade of cold 85Rb atoms. **68,** 053407. doi:`10.1103/PhysRevA.68.053407` (Nov. 2003) (cit. on p. 149).

228. Vitanov, N. V. *et al.* Stimulated Raman adiabatic passage in physics, chemistry, and beyond. *Reviews of Modern Physics* **89,** 015006. doi:`10.1103/RevModPhys.89.015006` (Mar. 2017) (cit. on p. 153).

229. Fröml, H. *et al.* Ultracold quantum wires with localized losses: Many-body quantum Zeno effect. *Physical Review B* **101,** 144301. doi:`10.1103/PhysRevB.101.144301` (Apr. 2020) (cit. on p. 155).

230. Liu, X.-J. *et al.* Effect of Induced Spin-Orbit Coupling for Atoms via Laser Fields. *Physical Review Letters* **102,** 046402. doi:`10.1103/PhysRevLett.102.046402` (Jan. 2009) (cit. on pp. 156, 157).

231. Allen, J. F. & Jones, H. New Phenomena Connected with Heat Flow in Helium II. *Nature* **141,** 243–244. doi:`10.1038/141243a0` (Feb. 1938) (cit. on p. 161).

232. Amico, L. *et al.* Roadmap on Atomtronics: State of the art and perspective. *AVS Quantum Science* **3,** 039201. doi:`10.1116/5.0026178` (Sept. 2021) (cit. on pp. 161, 162).

233. Barenghi, C. F., Skrbek, L. & Sreenivasan, K. R. Introduction to quantum turbulence. *Proceedings of the National Academy of Sciences* **111,** 4647–4652. doi:`10.1073/pnas.1400033111` (Mar. 2014) (cit. on p. 161).

234. Regal, C. A., Greiner, M. & Jin, D. S. Observation of Resonance Condensation of Fermionic Atom Pairs. *Phys. Rev. Lett.* **92,** 040403. doi:10.1103/PhysRevLett.92.040403 (Jan. 2004) (cit. on p. 161).

235. Vale, C. J. & Zwierlein, M. Spectroscopic probes of quantum gases. *Nature Physics* **17,** 1305–1315. doi:10.1038/s41567-021-01434-6 (Dec. 2021) (cit. on pp. 162, 165).

236. Krinner, S., Esslinger, T. & Brantut, J.-P. Two-terminal transport measurements with cold atoms. *Journal of Physics: Condensed Matter* **29,** 343003. doi:10.1088/1361-648X/aa74a1 (2017) (cit. on p. 162).

237. Pavelka, M., Klika, V. & Grmela, M. *Multiscale thermo-dynamics: introduction to GENERIC* (De Gruyter, Berlin ; Boston, 2018) (cit. on pp. 162, 172, 173).

238. Ku, M. J.-H. *Thermodynamics and solitonic excitations of a strongly-interacting Fermi gas* PhD Thesis (Massachusetts Institute of Technology, 2015) (cit. on p. 165).

239. Kaufman, A. M. *et al.* Quantum thermalization through entanglement in an isolated many-body system. *Science* **353,** 794–800. doi:10.1126/science.aaf6725 (Aug. 2016) (cit. on pp. 165, 218).

240. Balian, R. *From Microphysics to Macrophysics: Methods and Applications of Statistical Physics* (Springer, 2007) (cit. on p. 165).

241. Gnezdilov, N. V. *et al.* Ultrafast dynamics of cold Fermi gas after a local quench. *Physical Review A* **107,** L031301. doi:10.1103/PhysRevA.107.L031301 (Mar. 2023) (cit. on p. 165).

242. Yao, J. *et al.* Controlled transport between Fermi superfluids through a quantum point contact. *Physical Review A* **98,** 041601. doi:10.1103/PhysRevA.98.041601 (Oct. 2018) (cit. on p. 167).

243. Kanász-Nagy, M. *et al.* Anomalous Conductances in an Ultracold Quantum Wire. *Physical Review Letters* **117,** 255302. doi:10.1103/PhysRevLett.117.255302 (Dec. 2016) (cit. on p. 169).

244. London, F. *Superfluids: Macroscopic theory of superfluid helium* (Wiley, 1954) (cit. on p. 169).

245. Khalatnikov, I. M. *An Introduction To The Theory Of Superfluidity* doi:10.1201/9780429502897 (CRC Press, Boca Raton, June 2019) (cit. on p. 169).

246. Hoskinson, E. *et al.* Transition from phase slips to the Josephson effect in a superfluid 4He weak link. *Nature Physics* **2,** 23–26. doi:10.1038/nphys190 (Jan. 2006) (cit. on pp. 170, 200).

247. Grenier, C., Kollath, C. & Georges, A. Thermoelectric transport and Peltier cooling of cold atomic gases. *Comptes Rendus Physique* **17,** 1161–1174. doi:10.1016/j.crhy.2016.08.013 (Dec. 2016) (cit. on p. 172).

248. Onsager, L. Reciprocal Relations in Irreversible Processes. I. *Physical Review* **37,** 405–426. doi:10.1103/PhysRev.37.405 (Feb. 1931) (cit. on p. 172).

249. Viljas, J. K. Multiple Andreev reflections in weak links of superfluid He 3 - B. *Physical Review B* **71,** 064509. doi:10.1103/PhysRevB.71.064509 (Feb. 2005) (cit. on p. 174).

250. Scheer, E. *et al.* Conduction Channel Transmissions of Atomic-Size Aluminum Contacts. *Physical Review Letters* **78,** 3535–3538. doi:10.1103/PhysRevLett.78.3535 (May 1997) (cit. on p. 188).

251. Grenier, C., Georges, A. & Kollath, C. Peltier Cooling of Fermionic Quantum Gases. *Physical Review Letters* **113,** 200601. doi:10.1103/PhysRevLett.113.200601 (Nov. 2014) (cit. on pp. 194, 198).

252. Ierley, G. & Kostinski, A. Universal Rank-Order Transform to Extract Signals from Noisy Data. *Physical Review X* **9,** 031039. doi:10.1103/PhysRevX.9.031039 (Sept. 2019) (cit. on p. 195).

253. D'Errico, C., Abbate, S. S. & Modugno, G. Quantum phase slips: from condensed matter to ultracold quantum gases. *Philosophical Transactions of the Royal Society A: Mathematical, Physical and Engineering Sciences* **375,** 20160425. doi:10.1098/rsta.2016.0425 (Oct. 2017) (cit. on p. 200).

254. Del Maestro, A. & Rosenow, B. Dissipation in mesoscale superfluids. *Physical Review B* **95,** 140507. doi:10.1103/PhysRevB.95.140507 (Apr. 2017) (cit. on p. 200).

255. Wlazłowski, G. *et al.* Dissipation Mechanisms in Fermionic Josephson Junction. *Physical Review Letters* **130,** 023003. doi:10.1103/PhysRevLett.130.023003 (Jan. 2023) (cit. on p. 200).

256. Setiawan, F. & Hofmann, J. Analytic approach to transport in superconducting junctions with arbitrary carrier density. *Physical Review Research* **4,** 043087. doi:10.1103/PhysRevResearch.4.043087 (Nov. 2022) (cit. on p. 200).

257. Cheuk, L. W. *et al.* Spin-Injection Spectroscopy of a Spin-Orbit Coupled Fermi Gas. *Physical Review Letters* **109,** 095302. doi:10.1103/PhysRevLett.109.095302 (Aug. 2012) (cit. on pp. 200, 217).

258. Shkedrov, C. *et al.* In situ momentum-distribution measurement of a quantum degenerate Fermi gas using Raman spectroscopy. *Physical Review A* **101,** 013609. doi:10.1103/PhysRevA.101.013609 (Jan. 2020) (cit. on p. 200).

259. Shapiro, S. Josephson Currents in Superconducting Tunneling: The Effect of Microwaves and Other Observations. *Physical Review Letters* **11,** 80–82. doi:10.1103/PhysRevLett.11.80 (July 1963) (cit. on p. 200).

260. Averin, D. V. & Likharev, K. K. en. in *Modern Problems in Condensed Matter Sciences* (eds Altshuler, B. L., Lee, P. A. & Webb, R. A.) 173–271 (Elsevier, Jan. 1991). doi:10.1016/B978-0-444-88454-1.50012-7 (cit. on p. 200).

261. Zhu, B. *et al.* Suppressing the Loss of Ultracold Molecules Via the Continuous Quantum Zeno Effect. *Physical Review Letters* **112,** 070404. doi:10.1103/PhysRevLett.112.070404 (Feb. 2014) (cit. on p. 201).

262. Hagenmüller, D. *et al.* Cavity-assisted mesoscopic transport of fermions: Coherent and dissipative dynamics. *Physical Review B* **97,** 205303. doi:10.1103/PhysRevB.97.205303 (May 2018) (cit. on p. 201).

263. Partridge, G. B. *et al.* Molecular Probe of Pairing in the BEC-BCS Crossover. *Physical Review Letters* **95,** 020404. doi:10.1103/PhysRevLett.95.020404 (July 2005) (cit. on pp. 201, 202).

264. Junker, M. *et al.* Photoassociation of a Bose-Einstein Condensate near a Feshbach Resonance. *Physical Review Letters* **101,** 060406. doi:`10.1103/PhysRevLett.101.060406` (Aug. 2008) (cit. on p. 202).

265. Schwab, K. *et al.* Measurement of the quantum of thermal conductance. *Nature* **404,** 974–977. doi:`10.1038/35010065` (Apr. 2000) (cit. on p. 216).

266. Meschke, M., Guichard, W. & Pekola, J. P. Single-mode heat conduction by photons. *Nature* **444,** 187–190. doi:`10.1038/nature05276` (Nov. 2006) (cit. on p. 216).

267. Mosso, N. *et al.* Heat transport through atomic contacts. *Nature Nanotechnology* **12,** 430–433. doi:`10.1038/nnano.2016.302` (May 2017) (cit. on p. 216).

268. Leijnse, M. & Flensberg, K. Introduction to topological superconductivity and Majorana fermions. *Semiconductor Science and Technology* **27,** 124003. doi:`10.1088/0268-1242/27/12/124003` (Nov. 2012) (cit. on p. 217).

269. Kitaev, A. Y. Fault-tolerant quantum computation by anyons. *Annals of Physics* **303,** 2–30. doi:`10.1016/S0003-4916(02)00018-0` (Jan. 2003) (cit. on p. 217).

270. Jiang, L. *et al.* Majorana Fermions in Equilibrium and in Driven Cold-Atom Quantum Wires. *Physical Review Letters* **106,** 220402. doi:`10.1103/PhysRevLett.106.220402` (June 2011) (cit. on p. 217).

271. Lukin, M. D. *et al.* Spectroscopy in Dense Coherent Media: Line Narrowing and Interference Effects. *Physical Review Letters* **79,** 2959–2962. doi:`10.1103/PhysRevLett.79.2959` (Oct. 1997) (cit. on p. 217).

272. Qu, W. *et al.* Sub-Hertz resonance by weak measurement. *Nature Communications* **11,** 1752. doi:`10.1038/s41467-020-15557-6` (Apr. 2020) (cit. on p. 217).

273. Bergschneider, A. *et al.* Spin-resolved single-atom imaging of ^{6}Li in free space. *Physical Review A* **97,** 063613. doi:`10.1103/PhysRevA.97.063613` (June 2018) (cit. on p. 217).

274. Pyykkönen, V. A. J. *et al.* Flat-band transport and Josephson effect through a finite-size sawtooth lattice. *Physical Review B* **103,** 144519. doi:`10.1103/PhysRevB.103.144519` (Apr. 2021) (cit. on p. 218).

275. Wang, W. O. *et al. Quantitative assessment of the universal thermopower in the Hubbard model* en. arXiv:2302.13169 [cond-mat]. Feb. 2023 (cit. on p. 218).

276. Ulaga, M., Mravlje, J. & Kokalj, J. *The thermoelectric effect on diffusion in the two-dimensional Hubbard model* en. arXiv:2307.05320 [cond-mat]. July 2023 (cit. on p. 218).

277. Grier, A. T. *et al.* Λ -enhanced sub-Doppler cooling of lithium atoms in D 1 gray molasses. *Physical Review A* **87.** doi:`10.1103/PhysRevA.87.063411` (June 2013) (cit. on p. 218).

278. Burchianti, A. *et al.* Efficient all-optical production of large ^{6}Li quantum gases using D_1 gray-molasses cooling. *Physical Review A* **90,** 043408. doi:`10.1103/PhysRevA.90.043408` (Oct. 2014) (cit. on p. 218).

ACKNOWLEDGEMENTS

Doing a PhD in experimental physics in particular with Quantum Gases which no only present technological but also theoretical challenges has many ups and downs along the way. Here I would like to acknowledge the people who helped me along the way and their impact on the work presented here.

Firstly, I would like to thank Tilman for letting me do my PhD in the Quantum Optics Group. The group atmosphere he fosters to make everyone happy and motivated enabled us to overcome the challenges presented by the experiment. His intuitive way of understanding physics and his desire to understand complicated phenomena in this way often challenged us but lead to a better understanding for everyone in the long run. Finally, I would like him for allowing us to realize all the exotic ideas we had in mind even though it took years for some of the projects to be finished.

Regarding the members of the Lithium team I would like to acknowledge them in chronological order. When I started in the team Laura was the PostDoc. Her deep knowledge of physics helped me tremendously to understand the experiment and the underlying theory. She was always curious and happy to discuss ideas and gave the team a well organized structure which I appreciated a lot. I also would like to thank Martin, Samuel and Dominik who were the senior PhDs at the experiment around the time I started and thus had the biggest impact on me. Martin was always happy to answer questions with an impressive knowledge of formulas while Samuel had the patience to explain concepts extensively no matter how long it took. Dominik was writing his thesis when I started but still was willing to discuss physics and lightened the mood in the team with his wit on many occasions. Moreover, we had fun in the lab like building glasses from Thorlabs components or listening to every online radio channel from KEXP to FM4.

The most time in the team I spent with Jeff who started his PhD shortly after me but was already a Semester and subsequently Master student when I started. Jeff had probably the biggest impact on my PhD since we went together through the bad times and the good times. I still remember the moment we realized, shortly after the Covid shutdown was over, that our atomic beam oven ran out of Lithium and we both had the confidence and naivety to think we could replace it in no time. It took as over 3 months, but Jeff's unwavering positivity helped a lot to not get overly frustrated. Furthermore, his drive and interest to understand and discuss physics helped us tremendously to finish the projects we were working on over the last years. Mohsen who started a year after Jeff in the team, right at the beginning of Covid, also helped in furthering our understanding of the experiment and the theory behind it. His desire to deeply understand what we do also pushed me to get better knowledge of our system and helped us find new models for the transport we observe. Myles is the current PostDoc, and he started shortly after Covid and helped immediately with his technical skills. At the time we were upgrading the experiment and were struggling with our resonator lock when Myles came in and could immediately solve our problems with his knowledge of the RedPitaya. Also in the following Myles was driving the experiment forward by fixing all the small imperfections along the way. I also appreciate the precision Myles brings to the team, always finding and fixing the small mistakes we make whether its in the experiment or on a paper. Finally, I would like to thank Simon who is the last PhD I had overlapped with in the Lithium team. He could integrate very quickly in the team and learned the experiment in no time which helped us a lot with the projects we were working on. Simon's desire to understand the experiment and challenge our old understanding led to many interesting and unexpected results which we are still trying to understand. I think him, Mohsen and Myles are a great team for the future of the Lithium experiment. I would also like to thank the current members of the Lithium team, i.e. Jeff, Myles, Mohsen and Simon, for proofreading this thesis.

Besides the team I worked with I also would like to thank Alexander Frank our electric engineer was always extremely helpful in solving our problems with electronics, repairing our equipment and answering my questions. Also, his limitless stock of electronics parts simplified our lives massively. I also like to thank Steffi, our administrator, who was always very helpful with all the organizational and administrative questions and challenges, such as export and importing lasers or organizing visits.

I also want to acknowledge the other people from the group who I worked with over the years and who made the Quantum Optics group what it is. I'm grateful to everyone from the Lattice, Impact and Cavity team, in no particular order Michael, Frederik, Remi, Kilian, Anne-Sophie, Joaquin, Tobi, Fabian, Rodrigo, Manuele, Nishant, Lorenz, Katrin, Nicola, Francesco, Panos, Dalila, Jacob, Justyna, Alex, Simon, Davide, Andrea, Philip, Marius, Giacomo, Zijie, Samuel and Konrad. In addition, I would like to thank the many Semester and Master students who helped us realized many different projects over the years again in no particular order Franco, Benjamin, Enis, Shijia, Stefano, Kevin, David, Lukas, Lisa, Jeremie, Pratyiush, Moritz, Giacomo and Zhenning.

Beyond the lab I had a great time in Zurich during my PhD and would like to thank the people who making it this good. What first come to mind are our nighttime visits to the Langstrasse and surrounding bars/clubs with Frederik, Andrea, Joaquin, Davide, Kilian, Norbert and Anne-Sophie who were always a lot of fun. In particular, I would like to thank Frederik for immediately integrating me in the group and also his activities outside the lab. The same goes for Anne-Sophie, Davide, Jeff and Joaquin who started in the group around the same time I did and were always willing to go out and experience things beyond the lab like legendary visits to the opening of a mezcaleria. In addition, our hikes and mountaineering tours to the swiss alps with Kilian, Simon, Laura, Wilfried, Anne-Sophie, Leah, Florina and Martin where we climbed the Weissmies or the walls at the Kletterzentrum in Wädi. I also appreciated the sporting events in the group such as the Sola and Boltzmann Cup where Dominik, Fabian, Joaquin, Kilian, Michael, Philip, Martin, Anne-Sophie were always pushing our teams to new limits. Another fond memory are the visits to concerts organized and often played by Konrad, Simon and Philip. Finally, a big part of the fun was eating out whether in Zurich or Napels with Davide, Alex and Jeff or the wine bar visits with Laura and Wilfried who show us the next best natural wine or some freshly fermented vegetable.

Zu guter Letzt möchte ich mich noch von ganzem Herzen bei meiner Familie und meinen Verwandten bedanken. Meine Eltern, meine Schwester und Ihre Familie sowie meine Oma haben mir immer Rückhalt gegeben und mich unterstützt. Bei meinen Onkels, Tanten, Cousinen/Cousins und meinem Patenkind möchte ich mich auch bedanken für Ihre Unterstützung und Interesse an dem was ich tue sowie für die grossartigen Familientreffen.

LIST OF PUBLICATIONS

1. L. Corman, P. Fabritius, S. Häusler, J. Mohan, L. H. Dogra, D. Husmann, M. Lebrat, and T. Esslinger
   Quantized conductance through a dissipative atomic point contact
   Phys. Rev. A **100**, 053605 (2019)

2. M. Lebrat, S. Häusler, P. Fabritius, D Husmann, L. Corman, and T. Esslinger
   Quantized conductance through a spin-selective atomic point contact
   Phys. Rev. Lett. **123**, 193605 (2019)

3. S. Häusler, P. Fabritius, J. Mohan, M. Lebrat, L. Corman, and T. Esslinger
   Interaction-Assisted Reversal of Thermopower with Ultracold Atoms
   Phys. Rev. X **11**, 021034 (2021)

4. V. Pyykkönen, S. Peotta, P. Fabritius, J. Mohan, T. Esslinger, and P. Törmä
   Flat-band transport and Josephson effect through a finite-size sawtooth lattice
   Phys. Rev. B **14**, 144519 (2021)

5. D. Pahl, L. Pahl, E. Mustafa, Z. Liu, P. Fabritius, J. Mohan, P. Clements, A. Akin, and T. Esslinger
   A low-noise and scalable FPGA-based analog signal generator for quantum gas experiments
   IEEE Conference on Quantum Computing and Engineering (2021)

6. M.-Z. Huang, J. Mohan, A.-M. Visuri, P. Fabritius, M. Talebi, S. Wili, S. Uchino, T. Giamarchi, and T. Esslinger
   Superfluid Signatures in a Dissipative Quantum Point Contact
   Phys. Rev. Lett. **130**, 200404 (2023)

7. S. Marti, E. Mustafa, G. Bisson, P. Anand, P. Fabritius, T. Esslinger and A. Akin
   FPGA-based real-time laser beam profiling and stabilization system for quantum simulation applications
   Accepted for Publication in 26th Euromicro Conference on Digital System Design (2023)

8. P. Fabritius, J. Mohan, M. Talebi, S. Wili, W. Zwerger, M.-Z. Huang and T. Esslinger
   Irreversible Entropy Transport Enhanced by Fermionic Superfluidity
   ArXiv:2309.04359 (2023)

CURRICULUM VITÆ

PERSONAL

born January 25th, 1993, in Stuttgart, Germany
citizen of Germany

E-mail: fabritius@phys.ethz.ch

EDUCATION

2017 – 2023	Ph.D. thesis under the supervision of T. Esslinger: *Entropy and Particle Transport in Quantum Gases Manipulated with Near-Resonant Light*. ETH Zurich, Switzerland
2016 – 2017	Master thesis under the supervision of S. Whitlock: *Equilibrium and quench dynamics in a Fermi-Hubbard ladder*. University of Heidelberg, Germany
2015 – 2017	Master of Science at University Heidelberg, Germany
2014 – 2015	Semester abroad Univ. Joseph-Fourier Grenoble, France
2014	Bachelor thesis under the supervision of M. Weidemüller: *Coherent excitation of ultracold Rydberg atoms*. University of Heidelberg, Germany
2011 – 2014	Bachelor of Science at University Heidelberg, Germany
2011	*Abitur* at Droste-Hülshoff Gymnasium, Meersburg, Germany

COLOPHON

The design of this thesis is largely inspired by Robert Bringhurst's seminal book on typography *"The Elements of Typographic Style"*. It was typeset in XeLaTeX with a style that is partly based on `classicthesis.sty` by André Miede, `arsclassica.sty` by Lorenzo Pantieri and the dissertation of Thomas Uehlinger.

ComponentLibrary by Alexander Franzen was used to illustrate some of optical setups in this thesis and is licensed under a Creative Commons Attribution-NonCommercial 3.0 Unported License.